Centennial AMOC variability : mechanism and impacts

Weimin Jiang

Thèse de doctorat

DE SORBONNE UNIVERSITÉ

ECOLE DOCTORALE Nº129 : Sciences de l'Environnement d'Ile de France
Spécialité : océanographie physique, climatologie, modélisation climatique

Préparée au
UMR LOCEAN, Laboratoire d'Océanographie et du Climat: Expérimentations et Approches Numériques

par
Weimin JIANG

Centennial AMOC variability: mechanism and impacts

Thèse présentée et soutenue à Paris, le 28 juin 2022
Composition du jury :

Professeur	Hervé Le Treut	Président
Professeur associé	David Ferreira	Rapporteur
Chercheur	Yohan Ruprich-Robert	Rapporteur
Professeur	Sarah Kang	Examinatrice
Chercheur	Rym Msadek	Examinatrice
Professeur	Francis Codron	Directeur de thèse
Maître de conférences	Guillaume Gastineau	Co-directeur de thèse

Acknowledgement

First of all, I would like to express my sincere gratitude to my supervisor Francis Codron and co-supervisor Guillaume Gastineau for their continuous trust and support throughout my PhD. The project is dedicated to exploring the North Atlantic and this PhD adventure is also like a navigation in the ocean. Francis has been always in charge of the right direction in the journey, especially when the mist of failures came. Guillaume has taught me patiently and carefully from the very beginning, step by step, and guided me to grow as a scientist. They have made countless discussions with me in the past three years. My research cannot be completed without the nurturing of them.

I would like to thank all the members of my jury for their comments on my work and their agreement to award me the title of Ph.D. Thanks a lot to Hervé Le Treut, David Ferreira, Yohan Ruprich Robert, Sarah Kang, Rym Msadek. I also acknowledge reviewers Yohan Ruprich-Robert and David Ferreira for coping with this manuscript.

I am truly indebted to Julie Deshayes and Christophe Cassou, who were members of the committee for the first and second years. They made many suggestions not only for the research project but also about my career plans. They encouraged me to attend more conferences, to interact with other researchers and to think about future plans.

The same gratitude belongs to Gurvan Madec for pointing out the appropriate salinity and temperature for the NEMO model. This saved us a lot of time in finding errors in our experiments and helped to implement our proposed method.

My thanks must go to the Make Our Planet Great Again (MOPGA) project, which funded my study the study and gave me the opportunity to experience life in Paris. This PhD has been completed in the Laboratoire d'océanographie et du climat : expérimentations et approches numériques (LOCEAN). I am happy to be a part of this laboratory. Many thanks to Juliette Mignot for gathering people in the VARCLIM team and making us have regular exchanges.

I am also grateful to other lovely PhD students in the laboratory, Yang, Lucie, Yona, Gina, Carla, Han, Sara, Clovis, Antoine, Leonard, Constantin, Georges, and many others. They shared with me their passion and experience in research, and of course, after-work entertainments.

Finally, I would like to thank my parents in China, who have always given me solid support in all kinds of forms whenever I need it. It has been three years since the last time I saw them. But they never complained about my absence in the family reunion moments and always encouraged me to do what I wanted to do.

Finally, I would like to thank my parents in China, who have always given me solid support in all kinds of forms whenever I need it. It has been three years since the last time I saw them. But they never complained about my absence in the family reunion moments and always encouraged me to do what I wanted to do.

Abstract

The mechanisms driving the Atlantic meridional overturning circulation (AMOC) low-frequency variability and the climate impact are investigated in the atmosphere-ocean coupled general circulation model (AOGCM) IPSL-CM6A-LR. A centennial to multi-centennial variability of the AMOC emerges in this model, which increases the uncertainties associated with internal variability in the climate projections. We isolate the low-frequency variations in a 2000-yr preindustrial control simulation and show the dominant role of the freshwater exchanges between the Arctic Ocean and the North Atlantic in controlling the AMOC intensity.

As the AMOC increases, the ocean transports heat northward, which leads to the sea-ice melting in the Arctic Ocean. Combined with the weakened southward East Greenland Current, the freshwater export from the Arctic reduces, and a progressive accumulation of freshwater occurs in the central Arctic. Meanwhile, the saltier Atlantic inflow through the Barents Sea results in a positive salinity anomaly in the Eastern Arctic subsurface. The mean transpolar drift across the Arctic towards the Lincoln Sea tends to transport the positive salinity in the Eastern Arctic subsurface to the central Arctic and the central freshwater anomaly to the Lincoln Sea north of Greenland. In parallel, a cyclonic circulation anomaly is simulated around Greenland, which competes with the tendency of the transpolar drift transporting freshwater southward towards Greenland. This competition leads to the relatively long retainment of a surface freshwater anomaly in the Arctic Ocean. When this accumulated freshwater finally reaches the Lincoln Sea, the oceanic currents around Greenland reorganize, leading to the export of the anomalous Arctic freshwater to the North Atlantic, enhancing the stratification in deep convection sites. The AMOC then decreases, positive salinity anomalies appear in the Central Arctic, and the variability switches to the opposite phase.

We further examine the climate responses to this low-frequency AMOC and associated oceanic meridional energy transport (OMET) variability using AOGCM sensitivity experiments. The underlying mechanism is also revealed by comparison to a slab ocean model (SOM) coupled with the same atmospheric module as in IPSL-CM6A-LR. In the AOGCM experiments, we constrain the AMOC anomalies using a novel scheme modifying online the baroclinic current of the AMOC in the North Atlantic Ocean. These simulations do not use any flux correction into the climate system, so that the climate responses to an intensified AMOC can be investigated in the framework of energy flow diagnostics in the climate system.

A strengthening of the AMOC is found to be responsible for a wide warming in the Northern Hemisphere and a northward displacement of the intertropical convergence zone (ITCZ). According to Bjerknes compensation, at the decadal time scale and beyond, a decreasing atmospheric meridional energy transport (AMET) should compensate for the AMOC-associated

increasing OMET. Such compensation is verified when the AMOC increases, as the ocean heat storage changes are small, and the energy balance at the top of the atmosphere (TOA) is hardly modified. Therefore, the northward OMET anomaly due to strong AMOC is balanced by a southward AMET. In the tropics, the abnormal southward AMET is completed by an anomalous equatorial Hadley circulation through its upper branch. Thus, the moisture and heat are transported northward via its lower limb, leading to the shift of ITCZ. The anomalous wind stress associated with the Hadley cell also leads to the formation of an overturning cell transporting heat northward in the Indo-Pacific Ocean. In contrast, in analogous SOM experiments, where the ocean is motionless, the imposed increase in Atlantic OMET is therefore solely balanced by a decrease in AMET. The resulting climate variations in SOM experiments are similar to that in AOGCM but with much larger amplitudes. In addition, the SOM atmospheric circulation changes are further amplified by more intense radiative changes at the TOA than that in AOGCM, which are driven by the tropical low cloud changes.

Résumé

Les mécanismes à l'origine de la variabilité à basse fréquence de la circulation méridienne de retournement de l'Atlantique (AMOC, pour Atlantic Meridional Overturning Circulation) et la réponse du climat à cette variabilité, basée sur le modèle de circulation générale atmosphère-océan (AOGCM, pour atmosphere ocean general circulation model) IPSL-CM6A-LR. Une forte variabilité centennale à multi-centennale de l'AMOC apparaît dans le modèle, ce qui engendre de fortes incertitudes pour les projections climatiques. Nous isolons les variations à basse fréquence dans une simulation de contrôle préindustrielle de 2000 ans et avons trouvons que les échanges d'eau douce entre l'océan Arctique et l'Atlantique Nord jouent un rôle déterminant.

Lors d'une intensification de l'AMOC, le transport de chaleur vers le nord réalisé par l'océan augmente. Ceci entraîne la fonte de la banquise dans l'océan Arctique. Nous trouvons également que le courant Est du Groenland orienté vers le sud s'affaiblit. Ainsi, l'export d'eau douce de l'Arctique diminue, entrainant une accumulation progressive d'eau douce dans le centre de l'Arctique. Parallèlement, l'afflux d'eau salée provenant de l'Atlantique Nord à travers les détroits bordant la mer de Barents entraîne la formation d'une anomalie de salinité positive de sous-surface au niveau de l'Arctique orientale. La dérive transpolaire à travers l'Arctique vers la mer de Lincoln tend à transporter cette anomalie de salinité positive de vers l'Arctique central, tandis que l'anomalie centrale d'eau douce de surface se propage vers la mer de Lincoln au nord du Groenland. En parallèle une anomalie de circulation cyclonique est simulée autour du Groenland, alors que des anomalies positives de salinité se forme le long des côtes du Groenland. Les courants générés entrent en compétition avec le renforment du transport d'eau douce vers le sud de de la dérive transpolaire. Cette compétition conduit à une rétention relativement longue de l'anomalie d'eau

douce de surface dans l'océan Arctique. Lorsque cette eau douce accumulée atteint finalement la mer de Lincoln, un seuil est alors atteint. Les courants océaniques autour du Groenland se réorganisent alors, entraînant un export massif de l'eau douce de l'Arctique anormale vers l'Atlantique Nord. L'AMOC diminue alors, et des anomalies positives de salinité apparaissent dans le centre de l'Arctique, alors que la phase opposée de la variabilité se met en place.

Nous examinons en détail les réponses climatiques aux anomalies de l'AMOC se formant à basse fréquence en utilisant des expériences de sensibilité avec le même AOGCM. Les mécanismes sous-jacents sont également mis en évidence par comparaison avec un modèle analogue utilisant une couche de mélange océanique (SOM, pour slab ocean model) couplé au même modèle atmosphérique que celui utilisé dans IPSL-CM6A-LR. Dans les expériences AOGCM, les courants barocline associés à l'AMOC dans l'océan Atlantique Nord sont contraint par une méthode innovante ne modifiant que la dynamique océanique. Ces simulations n'utilisent pas de correction de flux et les réponses climatiques à une intensification de l'AMOC peuvent être étudiées en étudiant les bilan et flux d'énergie dans le système climatique.

Le renforcement de l'AMOC conduit à un fort réchauffement de l'hémisphère nord et déplace vers le nord de la zone de convergence intertropicale (ITCZ, pour Intertropical convergence zone). Selon la compensation de Bjerknes, à l'échelle décennale et au-delà, un transport méridien d'énergie dans l'atmosphère (AMET, pour atmopheric meridional energy transport) vers le sud doit se former pour compenser l'OMET (pour ocean merdional energy transport) vers le nord engendré par une intensification de l'AMOC. Cette compensation est vérifiée dans nos simulations car le contenu de chaleur océanique varie peu, de même que le bilan radiatif au sommet de l'atmosphère. L'anomalie de l'OMET vers le nord due à une forte AMOC est ainsi compensée par un AMET vers le sud. Dans les tropiques, l'anomalie de l'AMET vers le sud est réalisée par une cellule de Hadley anormale au niveau de l'équateur transportant de l'énergie dans sa branche supérieure. L'humidité et la chaleur sont en revanche transportées vers le nord par sa branche inférieure, ce qui est cohérent avec le déplacement de la ITCZ. La modification des vents alizées associée entraîne également la formation d'une cellule de circulation océanique superficielle transportant de la chaleur vers le sud dans l'océan Indo-Pacifique. En revanche, dans les expériences SOM, le changement de l'OMET imposé dans l'océan Atlantique est uniquement équilibré par un changement de l'AMET. Ainsi, les variations climatiques dans les expériences SOM sont similaires à celles du AOGCM, mais avec des amplitudes beaucoup plus grandes. Les changements de la circulation atmosphérique dans les expériences SOM sont également amplifiés par une rétroaction positive liée aux changements des nuages bas, entrainant une variation du bilan radiatif au sommet de l'atmosphère.

List of abbreviations

(A/O) GCM	(Atmosphere/Ocean) general circulation model
AOGCM	Atmosphere-ocean general circulation model
AMET	Atmosphere meridional energy transport
AMOC	Atlantic meridional overturning circulation
AMV/O	Atlantic multidecadal variability/Oscillation
(D)WBC	(Deep) western boundary current
EAP	East Atlantic pattern
ENSO	El Niño– Southern Oscillation
IPO	Interdecadal Pacific Oscillation
ITCZ	Intertropical convergence zone
LFC	Low frequency component
LFP	Low frequency pattern
MET	Meridional energy transport
MMC	Mean meridional circulation
MSE	Moist static energy
NADW	North Atlantic Deep Water
NAO	North Atlantic Oscillation
OHT	Ocean heat transport
OLR	Outgoing longwave radiation
OMET	Ocean meridional energy transport
PDO/V	Pacific Decadal Oscillation
piControl	pre-industrial control
PNA	Pacific/North America
SAT	Surface air temperature
SLP	Sea level pressure
SOM	Slab ocean model
SSS	Sea surface salinity
SST	Sea surface temperature
STN	Stationary planetary waves
TOA	Top of the atmosphere
TRS	Transient eddies

List of models and datasets

20CR	20th Century Reanalysis
CERES	Clouds and the Earth's Radiant Energy System
CESM	Community Earth System Model
CMIP	Coupled Model Intercomparison Project Phase
CNRM CM	Centre National de Recherches Météorologiques coupled global climate model
ECMWF	European Centre for Medium-Range Weather Forecasts
ERA	European Centre for Medium-Range Weather Forecasts Re-Analyses
ERA-Interim	ECMWF-Interim Re-Analysis (ERA-Interim)
ERBE	Earth Radiation Budget Experiment
GFDL CM	Geophysical Fluid Dynamics Laboratory coupled model
HadCM3	Hadley Centre Coupled Model
HadISST	Hadley Centre Sea Ice and Sea Surface Temperature data set
IPSL	Institut Pierre Simon Laplace
MPI	Max-Planck-Institute for Meteorology
JRA	Japanese Re-Analyses
KCM	Kiel Climate Model
LMDZ	Laboratoire de Météorologie Dynamique
MPI	Max-Planck-Institute
NCAR	National Center for Atmospheric Research
NCEP	National Center for Environmental Prediction
NEMO	Nucleus for European Models of the Ocean
NRA	NCAR-NCEP Reanalyses
OSNAP	Overturning in the subpolar North Atlantic Program
RAPID-MOCHA	Rapid Climate Change–Meridional Overturning Circulation and Heatflux Array
SAMBA	South Atlantic meridional overturning circulation basin-wide array

Contents

1 OCEAN AND ATMOSPHERE ENERGY BUDGET AND TRANSPORTS 1

1.1 ENERGY BUDGET 1
1.2 ATMOSPHERIC AND OCEANIC ENERGY TRANSPORT 3
1.3 DECOMPOSITION OF THE ATMOSPHERIC MERIDIONAL ENERGY TRANSPORT 7
1.4 OCEANIC TRANSPORT 12
1.4.1 WIND-DRIVEN SURFACE CURRENTS 14
1.4.2 DEEP THERMOHALINE CIRCULATION 18
1.4.3 MESOSCALE EDDIES 21

2 ATLANTIC MERIDIONAL OVERTURNING CIRCULATION 22

2.1 THE OBSERVED AMOC 22
2.2 THE SIMULATED AMOC 24
2.3 DRIVERS OF THE AMOC VARIABILITY 26
2.3.1 ATMOSPHERIC FORCING 28
2.3.2 INTRINSIC OCEANIC DYNAMICS 31
2.4 WHAT DOES THE AMOC VARIABILITY DRIVE? 36
2.4.1 THE ATLANTIC OCEAN 39
2.4.2 THE ARCTIC 43
2.4.3 THE PACIFIC OCEAN 45
2.5 SUMMARY 48

3 CENTENNIAL VARIABILITY OF THE AMOC IN COUPLED IPSL MODEL 49

3.1 INTRODUCTION 49
3.2 IPSL-CM6A-LR MODEL 49
3.3 ARTICLE 51
3.4 CONCLUSION AND DISCUSSIONS 77
3.5 SIMPLIFIED MODEL FOR THE FRESHWATER RECHARGE MECHANISM 78

4 EXPERIMENTAL DESIGN TO INVESTIGATE THE INFLUENCE OF LOW-FREQUENCY AMOC VARIABILITY ON CLIMATE 82

4.1 INTRODUCTION 82
4.2 A METHOD TO IMPLEMENT A FLOW FIELD CORRECTION 84
4.3 ADJUSTMENT OF THE PARAMETERS 86
4.3.1 CORRECTION STRENGTH: α 86
4.3.2 LOCALIZATION OF β 90
4.3.3 CUTOFF DEPTH 92
4.4 PERFORMANCE OF CONTROL RUN 94

5 RESPONSE OF CLIMATE TO AMOC LOW-FREQUENCY VARIATIONS..... 100

5.1 INTRODUCTION 100
5.2 ARTICLE 100
5.3 DISCUSSION 146

6 CONCLUSIONS AND PERSPECTIVES..... 147

6.1 CONCLUSIONS 147
6.2 PERSPECTIVES 153
6.2.1 REALISM OF MULTI-CENTENNIAL VARIABILITY 153
6.2.2 TOOLS TO UNDERSTAND AMOC VARIABILITY 154
6.2.3 POSSIBLE IMPROVEMENTS IN FLOW-FIELD CONSTRAINT METHOD 157
6.2.4 CONSTRAINING FLOWS TO STUDY CLIMATE CHANGE 158
6.2.5 TELECONNECTIONS WITH OTHER BASINS 159

Chapter 1

Contents

1 OCEAN AND ATMOSPHERE ENERGY BUDGET AND TRANSPORTS 1

1.1 ENERGY BUDGET 1
1.2 ATMOSPHERIC AND OCEANIC ENERGY TRANSPORT 3
1.3 DECOMPOSITION OF THE ATMOSPHERIC MERIDIONAL ENERGY TRANSPORT 7
1.4 OCEANIC TRANSPORT 12
1.4.1 WIND-DRIVEN SURFACE CURRENTS 14
1.4.2 DEEP THERMOHALINE CIRCULATION 18
1.4.3 MESOSCALE EDDIES 21

1 Ocean and atmosphere energy budget and transports

1.1 Energy budget

The energy that drives climate systems is almost entirely from the radiative shortwave flux coming from the sun. In this thesis, we focus on the atmosphere and ocean components of the climate system. For a climate of equilibrium, the incoming shortwave (or solar) radiation needs to be balanced by a radiative flux returned to outer space. From the top of the atmosphere (TOA), part of the incoming solar radiation is firstly reflected and scattered by Rayleigh scattering, clouds, and aerosols or absorbed in the atmosphere. The net shortwave radiation designates the incoming minus reflected shortwave radiation. At the earth surface, the remaining incoming radiation is then either reflected or absorbed by the Earth's surface. The Outgoing longwave radiation (OLR) is the radiative longwave (or thermal) flux emitted by the earth surfaces and the atmosphere at the TOA. The OLR necessarily balances the net shortwave radiation so that the energy of the climate system remains stable. The partitioning of the energy fluxes in the climate system to achieve this balance is usually referred to as Earth's energy budget.

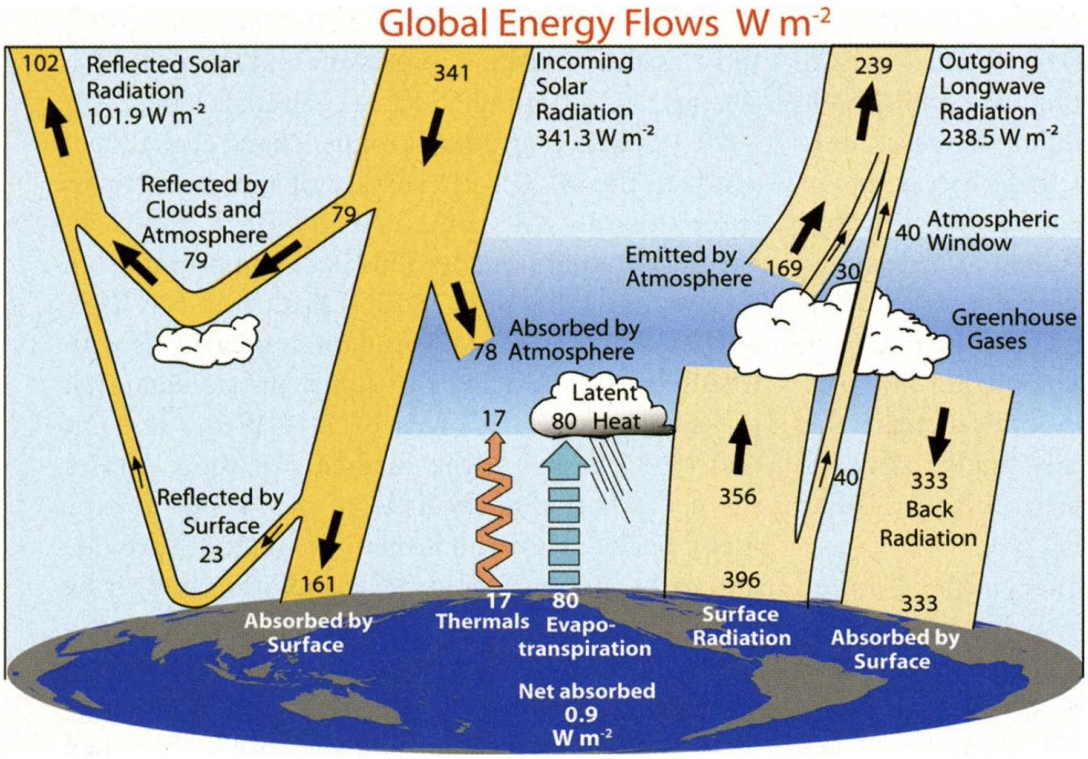

Figure 1.1. The global annual mean Earth's energy budget for Mar 2000 to May 2004 (W m-2). The broad arrows indicate the schematic flow of energy in proportion to their importance. The yellow arrows indicate the shortwave fluxes. The beige arrows indicate the longwave fluxes. The orange and blue arrows are the sensible and latent heat flux. Reprinted from Trenberth et al. (2009).

There is a long history of attempts to understand and estimate this budget, at least dating back to Dines (1917). Dines (1917) provided a global annual mean surface-atmosphere energy budget for the earth. Over the years, improvements in estimating the global annual mean energy budget due to the application of remote sensing have been made by numerous research (e.g., Hunt et al., 1986; Kiehl and Trenberth, 1997; Stephens et al., 2012; Trenberth et al., 2009). Trenberth et al. (2009) constructed a delicate global mean energy budget based on various measurements, models, and previous estimations. The TOA terms use satellite retrievals from the Earth Radiation Budget Experiment (ERBE) and the Clouds and the Earth's Radiant Energy System (CERES) datasets. The global atmospheric temperature and moisture fields are available from the reanalyses datasets of the National Centers for Environmental Prediction (NCEP) – National Center for Atmospheric Research (NCAR) Reanalyses (NRA), and European Centre for Medium-Range Weather Forecasts (ECMWF) Re-Analyses (ERA) and Japanese Re-Analyses (JRA). Figure 1.1 shows the global annual mean earth's energy budget for 2000–2005. The incoming shortwave radiation is 341 W m^{-2}, and part of it, 102 W m^{-2}, is reflected or scattered by the atmosphere and the Earth surface. The albedo of the earth is thus approximately 0.3. The surface absorbs most of the shortwave radiation, 161 Wm^{-2}, and 78 W m^{-2} is absorbed by the water vapor and ozone in the

atmosphere. OLR consists of the emission from the atmosphere (169 W m^{-2}) and the clouds (30 W m^{-2}). Another small component is also emitted at the surface and transmitted through the atmospheric window (40 W m^{-2}), where a range of wavelengths of the electromagnetic spectrum can pass through the atmosphere.

Nevertheless, even if the OLR and the net shortwave radiation are almost balanced globally, such fluxes are not balanced locally, i.e., for a specific location. This regional imbalance induces oceanic and atmospheric motions. The storage, transport of the energy, and conversion among different types, lead to motions in the atmosphere and ocean, driving the weather on the earth.

A similar balance also needs to be achieved for the energy entering and leaving the atmosphere. The shortwave energy absorbed by the atmosphere (78 W m^{-2}), the absorbed longwave radiation from the earth's surface (356 W m^{-2}), the sensible heat flux (17 W m^{-2}), and the latent heat flux (80 W m^{-2}) are the source of the incoming energy. The outgoing energy includes the longwave emission by the atmosphere and clouds to outer space (169 Wm^{-2} and 30 Wm^{-2}) and to the earth's surface by the atmosphere (333 W m^{-2}). Similarly, for the surface, the longwave radiation (396 W m^{-2}), the sensible (17 W m^{-2}), and latent heat fluxes (80 W m^{-2}) cancel the absorbed shortwave radiation from the sun (161 W m^{-2}) and the longwave back radiation from the greenhouse gases in the atmosphere (333 W m^{-2}).

Over the 2000-2005 period, the OLR and net shortwave radiation were not balanced. The rising greenhouse gas concentration leads to the increasing longwave radiation absorption in the atmosphere, decreasing the OLR and giving rise to a global imbalance at the TOA of 0.9 W m^{-2}. This imbalance is usually estimated through the changing ocean heat content, the principal reservoir of energy in the climate system (Hansen et al., 2005; Levitus et al., 2000; Meyssignac et al., 2019), as the accuracy of remote sensing estimates, is insufficient to provide this value.

This thesis aims at exploring the intrinsic variability emerging from the atmosphere, the ocean, and their interactions and how it affects the energy flows within the climate system. Therefore, in the following, we focus on the mean energy flows within the climate system rather than track changes in the earth's energy budget caused by external forcings.

1.2 Atmospheric and oceanic energy transport

As noted before, the uneven distribution of the radiative fluxes induces the transport of energy by the atmospheric and oceanic circulations. Due to the sphericity of the earth, high latitudes receive less shortwave radiation than low latitudes. Therefore, the atmosphere and the ocean transport energy from the equator to the poles, forming the Earth's climate as we know it today and maintaining its stability. Such a mode of transport is called meridional energy transport.

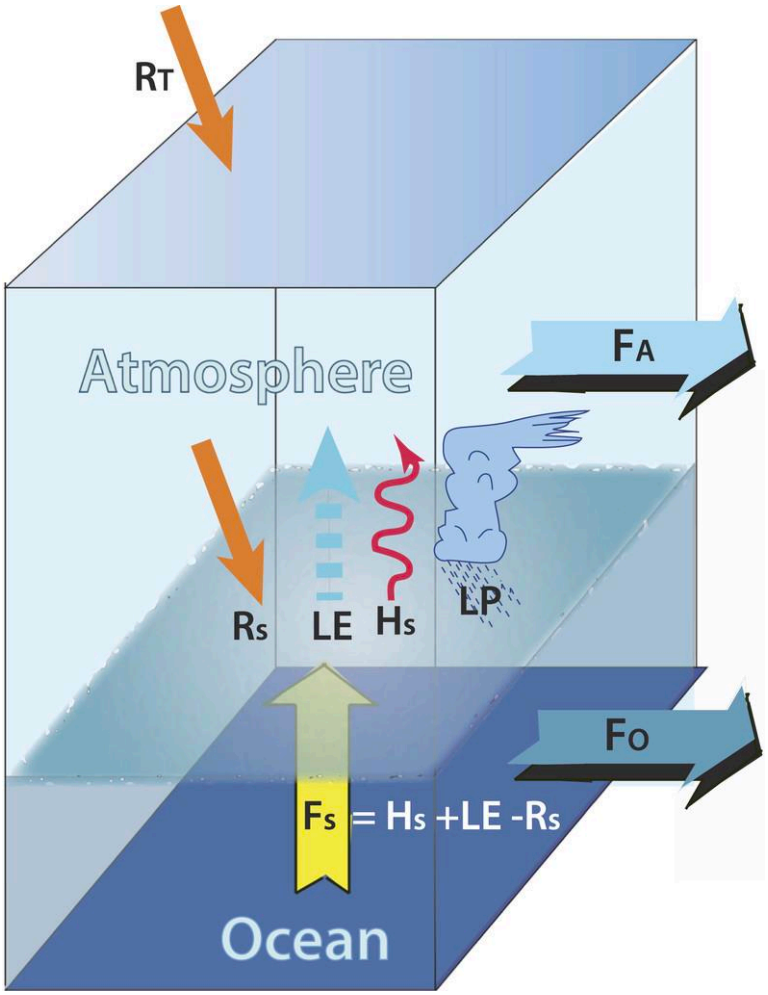

Figure 1.2. Schematic of the main flows of energy through the climate system for the atmosphere and ocean, including net radiation at the top and surface R_T and Rs, surface sensible heat flux Hs, and surface latent heat flux LE. The last three terms combine to give the surface flux Fs. Latent heat is realized in the atmosphere as precipitation LP. The vector transports of total energy in the atmosphere F_A and ocean F_O are indicated. Reprinted from Trenberth et al. (2019).

The meridional energy transport in the climate system has been assessed in much research. Heat transport is often used as a shorthand for what is really energy transport (Warren, 1999). Based on the definition, heat transport is computed from the velocity and temperature fields. For instance, the ocean heat transport (OHT) can be adequately approximated as (Yang and Xu, 2015; Zhang et al., 2002):

$$OHT = \int_{x_w}^{x_e} \int_{-H}^{z} \rho c_{pw} \theta v_w dz dx, \qquad (1.1)$$

where v_w is the meridional velocity of oceanic current perpendicular to the cross-section from the western (x_w) to the eastern (x_e) boundaries, and z indicates the vertical coordinate. ρ is the density of seawater, andc_{pw} is the density and specific heat capacity of the seawater at constant pressure. θ is the potential temperature. w in c_{pw} and v_w denotes seawater.

In the ocean, heat transport is dominant in energy transport, despite in some cases where the transport of latent heat by sea ice and icebergs needs to be considered at high latitudes. The meridional ocean heat transport thus approximately equals the OMET in most cases. While for the AMET, heat, latent heat, and geopotential energy must be taken into account. The significant cancellation among these individual components leads to a smooth meridional transport of total MSE by the MMC (Trenberth and Stepaniak, 2003).

However, considering the sparse observations and uncertainties for the dynamic and thermal structures in the atmosphere and ocean, heat transport is often derived from the heat fluxes. The total meridional heat transport is usually calculated by integrating the radiative flux, defined as the difference between the net shortwave radiation and the OLR at the TOA. The OMET can be estimated instead as an integration of the net surface heat flux entering the ocean, and the atmospheric energy transport is obtained by subtracting the OMET from the total (Hsiung, 1985; Wunsch, 2005). Reversely, some studies treat the OMET as a residual of the TOA radiation and the atmospheric energy budget (Fasullo and Trenberth, 2008; Vonder Haar and Oort, 1973; Oort and Vonder Haar, 1976; Trenberth and Caron, 2001). The method of computing OMET or AMET as a residual is referred to as the indirect approach in the following.

Figure 1.2 presents a schematic of the indirect methodology (Trenberth et al., 2019). The climate system is simplified as two layers: the (top) atmosphere and (bottom) ocean. The main flows of energy through the climate system include radiation at the TOA (R_T) and the surface (R_S) and surface sensible heat flux H_S. The surface latent heat flux is given by LE, where L is the latent heat of vaporization, and E the evaporation. The combination of the last three terms provides the total surface flux F_S, although a small precipitation enthalpy term can also be included. Latent heat is realized in the atmosphere by the formation of precipitation, so that in the atmosphere, latent heat is given by LP, where P is the precipitation. The vertically integrated energy transport in the atmosphere and ocean, namely AMET and OMET, are indicated by the vectors named as F_A and F_O. Either AMET or OMET is computed as a residual. For instance, the OMET is computed as a residual:

$$F_O = R_T - S - F_a, \qquad (1.2)$$

where *S* denotes the energy stored in the atmosphere, ocean, land, and ice. The most dominant heat reservoir is the ocean, as the ocean heat capacity is much larger than the one of the atmosphere or the land surfaces. In the ocean, energy is stored through the ocean heat content, which is defined as the vertical integration of heat:

$$S = OHC = \int_{-H}^{0} \rho \; C_{pw} T_w dz, \qquad (1.3)$$

with the same notations as in Equation 1.1. T_w is the conservative temperature of the seawater in °C and H is the ocean's depth. The widely adopted indirect computation of AMET and OMET assumes that the changes in the ocean heat content are negligible. The horizontal ocean circulations balance all net surface flux into the ocean.

Energy transport takes place in various ways in the atmosphere. For example, the annual mean energy transport by the atmosphere from ocean to land regions is 2.2 ± 0.1 PW (Petawatts = 10^{15} W), as the air is drier and the OLR is larger over land than over the ocean. This transport is especially pronounced in the Northern Hemisphere winter, when the transport exceeds 5 PW (Fasullo and Trenberth, 2008). This manuscript will focus on the meridional energy transport, carried mainly by the oceanic and the atmospheric large-scale overturning circulations, including the Hadley cell in the tropics, or by baroclinic storms in extratropics. The atmospheric and oceanic meridional energy transports are referred to as AMET and OMET, respectively. Although the heat capacity of the global atmosphere only corresponds to that of the ocean to a depth of 3.5 m (Trenberth and Stepaniak, 2004), AMET is a dominant contributor to the mean poleward transport of energy outside the tropics.

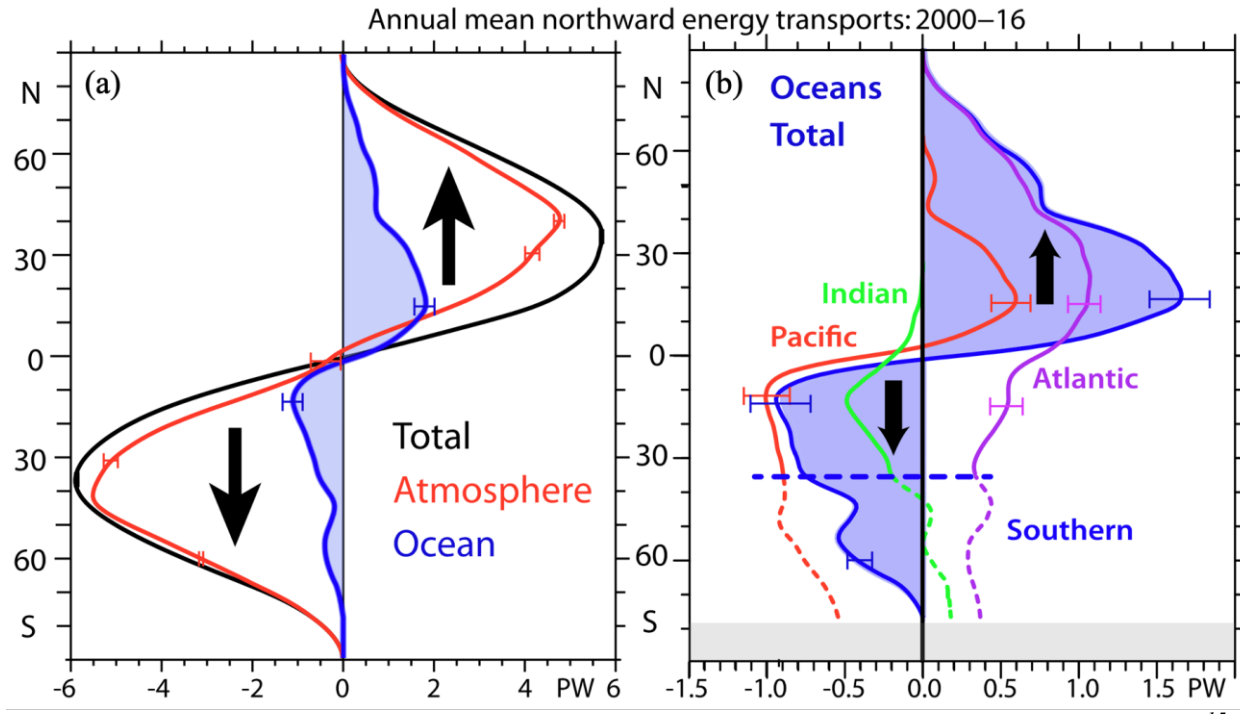

Figure 1.3. Long-term averaged zonal-mean annual meridional transports in PW (1PW = 10^{15} W) for the period 2000-2016. (a) Those inferred from TOA radiation (black), within the atmosphere from ERA-I (red), and the residual for the oceans (blue). (b) The breakdown for the oceans for the Atlantic (purple), Pacific (red), and Indian (green) and combined for the Southern Ocean south of 35°S (blue) in PW. Error bars denote the standard errors. Reprinted from Trenberth et al. (2019).

The indirect estimation of AMET/OMET dates back to the beginning of the satellite era. Vonder Haar and Oort (1973) firstly estimated the OMET as a residual in the atmospheric energy balance using radiosonde data. Over the past decades, calculations using satellite measurements and reanalysis data have been made by many studies (Liu et al., 2020; Oort and Haar, 1976; Peters et al., 2008; Trenberth and Caron, 2001; Wunsch, 2005). Using ERBE measurements at the TOA in the mid-1980s, a complete picture of AMET and OMET is given by Trenberth and Caron (2001). They found the annual mean AHT peak at 5.0 PW at around 40°N/S. At 35° latitudes, where the total meridional energy transport peaks in both hemispheres, the contribution of AMET is as high as 78% in the Northern Hemisphere and 92% in the Southern Hemisphere (Figure 1.3). The OMET is comparable to AMET only in the tropics.

Afterward, rapid progress has been made using similar methodology and new observational data sets (Ganachaud and Wunsch, 2003; Mayer and Haimberger, 2012; Wunsch, 2005; Zheng and Giese, 2009). The TOA radiation measurements from the ERBE in Trenberth and Caron (2001) have been replaced by higher-quality CERES observations since March of 2000 (Loeb et al., 2009). The atmospheric reanalysis data from ECMWF also has been improved with the advances in assimilation techniques and updates in the general circulation model formulation (Dee et al., 2011). In particular, ECMWF-Interim Re-Analysis (ERA-Interim) has proven the most stable and reliable (Trenberth et al., 2011; Trenberth and Fasullo, 2013). Trenberth and Fasullo (2018) made further improvements in this methodology, providing adjustments for the inevitable spurious mass imbalance and accounting for the enthalpy associated with precipitation. Nevertheless, these improvements do not significantly change the results shown in Trenberth and Caron (2001).

1.3 Decomposition of the atmospheric meridional energy transport

The estimations of heat transport presented above use the indirect approach. However, one of AMET and OMET is computed as residual so that they are not obtained independently. The indirect approach fails in studying the relationship between the changes in the AMET and OMET. The improvements in numerical models and the increased coverage of the observational data have facilitated the ‘direct computation’ of heat transport, using the observed state variables in the ocean and atmosphere together with the velocity field. As there is no radiation imbalance at TOA for a stable climate, the transports given by the residual methodology and direct computation should be consistent.

The atmospheric circulation is highly variable both in space and time domains and understanding the roles of different physical processes in the meridional energy transports is interesting. Partitioning of AMET and OMET is thus a subject of much research (Trenberth et al.,

2011; Trenberth and Fasullo, 2013). The direct estimations also allow decomposing energy transport into the contribution by mean circulations, eddies, and dissipation (Nummelin et al., 2017; Yang et al., 2015).

For the tropic-to-pole horizontal transport, only synoptic scale systems such as mid-latitude (anti) cyclones, planetary scale systems such as planetary-scale waves, and slow general circulations extending over thousands of kilometers make significant contributions. The total energy per unit mass in the atmosphere is defined as:

$$E = \underbrace{C_{pa}T_a + Lq + gZ}_{MSE} + \frac{1}{2}V^2, \qquad (1.4)$$

where C_{pa} is the specific heat capacity of the air at constant pressure (J kg^{-1} K^{-1}). T_a is the absolute air temperature (K), L is the specific heat of condensation (J kg^{-1}), q is the specific humidity (kg kg^{-1}), g is the gravitational acceleration (kg m^{-1} s^{-2}), Z is the geopotential height (m), and V is the wind velocity (m s^{-1}). The four terms on the right-hand side are internal energy, latent heat, geopotential energy, and kinetic energy, respectively. The internal energy accounts for 70% of the total energy, and the potential energy accounts for 27%. The kinetic energy makes a minor contribution (0.05%) and is thus neglected in AMET calculation (Hartmann, 2015). The sum of the first three terms is commonly referred to as moist static energy (MSE).

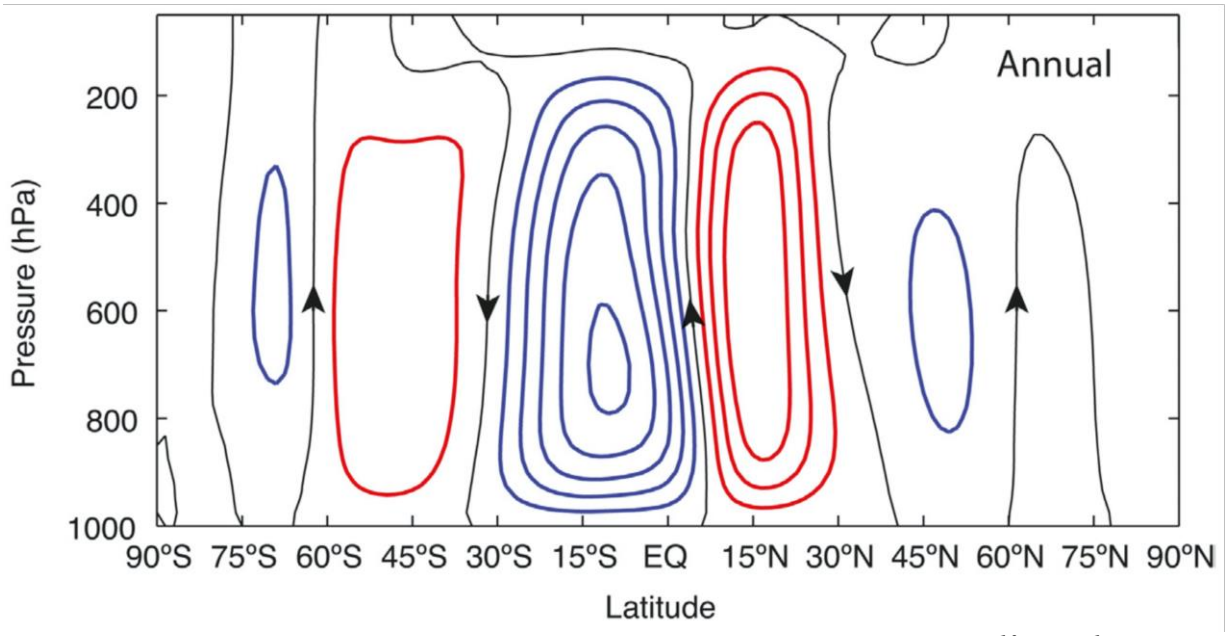

Figure 1.4. Atmospheric annual mean meridional mass stream function, in 10^{10} kg s^{-1}. Contour interval is 2 × 10^{10} kg s$^{-1,}$ and the arrows on the zero contour indicate the directions of vertical motion. Red is positive, and blue is negative. Reprinted from Hartmann (2015).

At the latitude φ, the atmospheric meridional energy transport (AMET) is given by the vertically integrated energy in the atmosphere:

$$AMET(\varphi) = \frac{-2\pi a \cos\varphi}{g} \int_{p_s}^{0} [\overline{vMSE}]dp \qquad (1.5)$$

with a indicating the radius of the earth, and p_s denoting the pressure at the surface. Note that v designates the meridional velocity of air. The overbar represents the time average, and square brackets denote the zonal average. Zonal average captures a physically meaningful subset of the climate and simplifies the computation of the general circulations of the atmosphere, as the net radiation is independent of longitude. Averaging over time removes the consideration of weather variations.

The product $[\overline{vMSE}]$ is traditionally decomposed into:

$$[\overline{vMSE}] = \underbrace{[\bar{v}][\overline{MSE}]}_{MMC} + \underbrace{[v^*MSE^*]}_{STN} + \underbrace{[\overline{v'MSE'}]}_{TRS} \qquad (1.6)$$

where primes and stars denote deviations from time and zonal averages, respectively, following the conventions in Lorenz (1967). The first term on the right-hand side represents the energy transport associated with the mean meridional circulations (MMC). It represents the transport due to the Hadley cells in the tropics (30°S-30°N) and the minor contribution of the Ferrel cells in mid-latitudes. The MMC can be described by the meridional streamfunction characterizing the zonal mean meridional and vertical velocities, which are much slower than the zonal wind. Figure 1.4 shows the annual-averaged mean meridional mass stream function, with the two tropical Hadley cells visible between 30°S and 30°N.

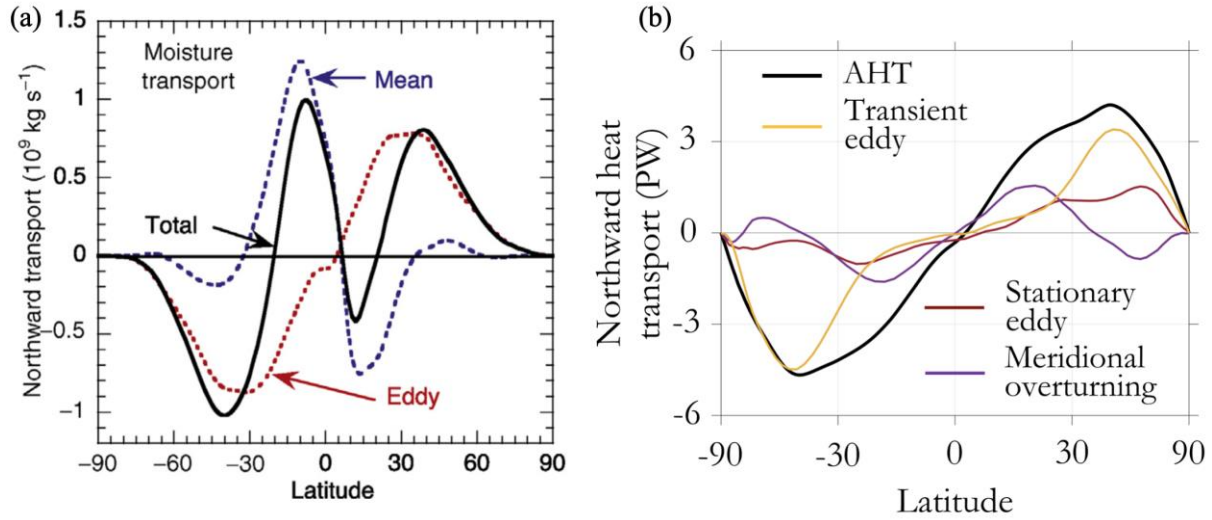

Figure 1.5. (a) Annual average meridional transport of moisture by the atmosphere in 10^9 kg s^{-1}; totals and contributions by the mean meridional circulation and eddies are shown. Reprinted from Hartmann (2015). (b) Annual average northward meridional energy transport (in PW); totals and contributions by the mean meridional circulation, transient and stationary eddies are shown. CERES satellite observations and ERA-Interim data are used. Reprinted from Armour et al. (2019).

In the tropics, the troposphere is heated by the ocean and land. Warm air rises near the equator and flows poleward in the upper atmosphere. Compensating downwelling occurs in the subtropical latitudes and then moves equatorward. The near-surface flow brings air back to the equator and forms northeasterly trade winds in the Northern Hemisphere and southeasterly trade winds in the Southern Hemisphere due to the Coriolis effect. This resulting MMC is the so-called Hadley cell, which George Hadley proposed in 1735 to explain the trade winds. Hadley cell plays a central role in the global circulation of the atmosphere and is associated with the formation of intertropical convergence zone (ITCZ), subtropical deserts, and jet streams. The descending branches of the two cells locate at about 30°S and 30°N, respectively (Figure 1.4). The annual mean Hadley cell is slightly more substantial in the Southern Hemisphere than in the Northern Hemisphere. The southern cell extends in the Northern Hemisphere to about 7°N, likely attributing to a weak net energy transport from the Northern to the Southern Hemisphere in the atmosphere, as shown by the negative AMET at the equator calculated from radiation budget measurements (Figures 1.3a and 1.5b).

If one focuses on moisture transport, the moisture transport by MMC mainly occurs within the Hadley cells between 30°S and 30°N and is equatorward. The location of maximum transport coincides with the position of the trade winds over the oceans. The water vapor then condenses, and heavy precipitation occurs as warm moist air converges at the ITCZ. The release of latent heat provides the energy for the ascent of air in the upward branch of the Hadley cell. During ascending, latent heat and internal energy are converted into potential energy.

Therefore, in the low troposphere, the lower branch of the Hadley cell transports warm and moist air from the subtropical oceans to the ITCZ (Figure 1.5a). Conversely, geopotential energy is exported poleward in the upper branch. The poleward flow of potential energy in the upper branch of the Hadley cell exceeds the sum of the equatorward flow of latent and sensible energy in the lower branch, leading to a poleward AMET in the Hadley cell. The maximum AMET by the MMC is around 1.5 PW at 20°S and 15°N, dominating the total local transport of around 2 PW (Armour et al., 2019). In the mid-latitudes, eddies are responsible for most poleward atmospheric water vapor transport (Figure 1.5a). The heat transport by eddies also dominates the mid-latitude AMET, as the eddies hardly transport the geopotential energy.

The transport by stationary planetary waves (STN) and transient eddies (TRS) is denoted by the second and third terms in Equation 1.6, respectively. Transient eddies represent the rapid development and decay of weather fluctuations in the mid-latitudes, which generally move eastward along with the prevailing flow and contribute to the wind and temperature variations, especially during winter. These disturbances are very apparent on weather maps and have a typical duration of 2 to 10 days.

Cyclones and anticyclones are the major transient eddies. They are fundamental in modern meteorology and synoptic climatology due to their crucial contribution to the wind and temperature variations. The growth and decay of these mid-latitude weather systems can be understood based on baroclinic instability theory. The tendency of the temperature wave to be displaced westward relative to the pressure wave, especially in the lower troposphere, leads to a positive correlation between poleward velocity and temperature in large-scale atmospheric waves. Thus, the available potential energy in the meridional temperature gradient associated with vertical shear of the mean flow is converted to the kinetic energy of waves. Cyclone waves whose amplitude increases rapidly with time have a large zonal phase shift between their pressure and temperature waves and thus produce efficient poleward transports of heat and moisture. As the temperature gradient is strongest during winter and weakest during summer, cyclones are usually most active during winter. Such a seasonal cycle is observed in the Atlantic (Nakamura, 1992). Nevertheless, the annual mean TRS transport peaks at about 45°N of 3.2 PW. The corresponding maximum in the Southern Hemisphere is even larger than the total transport, with a value of -4.5 PW (Figure 1.5b). Furthermore, the transient component exhibits a considerable local variability with sporadic extreme episodes exceeding the mean transport values by orders of magnitude (Messori et al., 2017; Messori and Czaja, 2013).

Stationary waves do not move around much and are fixed in specific geographic locations. It is computed by the departures of the time average from zonal symmetry (Equation 1.6). Indeed, stationary waves, such as the eddies of wavenumbers of 1-3 in the Northern Hemisphere, mainly result from zonal asymmetries in topography and land-sea thermal contrast. The structure and amplitude of the stationary waves depend on the structure of the seasonally varying zonal-mean zonal winds, i.e., the jet stream. TRS fluxes dominate the meridional flux of temperature except in the Northern Hemisphere during winter, when STN contributes up to half of the flux (Hartmann, 2015).

The maximum STN transport occurs at 70°N in the Northern Hemisphere, of ~1.5 PW, and the minimum occurs at 25°S in the Southern Hemisphere, of -1PW (Figure 1.5b). It is more robust in the Northern Hemisphere than in the Southern Hemisphere as the Himalayas and Rocky Mountain ranges provide mechanical forcing of zonal variations in the time mean winds and temperatures. In particular, the thermal contrast between the warm waters of the Kuroshio and

Gulf Stream ocean currents and the cold temperatures in the interiors of the continents also provides strong thermal forcing of STN during winter. The poleward transport of moisture by stationary and transient eddies peaks at about 30° of latitude in two hemispheres in the lower part of the troposphere (Figure 1.5a).

We have introduced the roles of three individual components in AMET. However, the seamless nature of the AMET also directly relates to the interactions between these components. The latent heating in the upward branch and the radiative cooling in the downward branch are regarded as the main driver of the Hadley circulation. While, as shown by some simulation studies deliberately exploring the possible atmospheric states without eddies (e.g., Kim and Lee, 2001), these eddies also force a large part of the Hadley circulation. The absence of eddies leads to a reduction of 75% in the Hadley cell (Kim and Lee, 2001). The cooling of the downward branch is more fundamentally caused by the transient baroclinic eddies advecting cooler air into the region. These eddies also strengthen the Hadley cells by interacting with other processes such as surface friction. The zonal asymmetries in topography are the leading cause of the STN. In addition, the heat and momentum fluxes by TRS also contribute to shaping the stationary flows. The preferred regions of baroclinic eddies are organized into storm tracks that are symbiotic with the quasi-stationary waves as the location and activity in storm tracks are determined by and, in turn, help maintain through eddy transports, the quasi-stationary flow.

1.4 Oceanic transport

The global ocean plays several critical roles in the Earth's climate system, mainly due to its low albedo and large heat capacity. Oceans provide a perfectly wet surface, with a low albedo except over the sea ice in polar regions. Therefore, the majority of the solar heat is absorbed by the ocean, particularly in tropical waters. The evaporative cooling of oceans balances much of the solar energy absorbed by the oceans, making them the primary source of water vapor and heat for the atmosphere. The world ocean is thus the boiler that drives the global hydrologic cycle. It also provides the bulk of thermal inertia of the climate system on time scales from weeks to centuries. The great capacity of oceans to store heat reduces the magnitude of the seasonal cycle in surface temperature by storing heat in summer and releasing it in winter. Because seawater is a fluid, currents in the ocean can move water over large distances and carry heat and other ocean properties from one geographic area to another. Oceanic currents transport substantial amounts of heat from lower latitudes, where heat is absorbed by the upper ocean, to higher latitudes, where heat is released into the atmosphere. The OMET plays an essential role in reducing the pole-to-equator temperature gradient. Horizontal and vertical energy transport in the ocean can also alter the regional climates by controlling the local sea surface temperature (SST). The effective heat content of the ocean and the function of the deep ocean as a reservoir of excessive heat are of significant

importance for the transient warming of the climate system in response to changing external forcing, such as the increase in greenhouse gases associated with human activities.

We have introduced that the annual mean OMET is usually estimated as residual of the TOA radiation and the atmospheric energy budget. The ocean heat transport represents OMET well in most cases. This estimation shows that the maximum OMET in the Northern hemisphere is only 1/3 of the AHT and occurs at a lower latitude, peaking in the tropical rather than the middle latitudes (Figure 1.3a). The maximum OMET in the Northern Hemisphere (1.7 PW at 15°N) is nearly twice that in the Southern Hemisphere (0.9 PW at 10°S). This asymmetry may result from the different topography in the two hemispheres. The transports by the ocean and atmosphere are comparable in the tropics.

Efforts have also been made to distinguish the OMET in each basin (e.g., Boccaletti et al., 2005; Hsiung, 1985; Trenberth et al., 2019; Trenberth and Caron, 2001). Despite the disagreement in magnitudes, the direction of transport from different studies is consistent. As shown in Figure 1.3b, the transport in the Pacific Ocean is poleward in both hemispheres, centered on 10° of latitude, with the peak value of 0.5 PW in the Northern Hemisphere and ~ 1 PW in the Southern Hemisphere. While in the Atlantic basin, the transport is northward in both hemispheres, with a peak of 1.1 PW at 20°N. As discussed next, this is associated with the shallow subtropical cells and the Atlantic Meridional Overturning Circulation (AMOC; Trenberth and Caron, 2001). The Indian Ocean transports energy southward, with a maximum of ~0.4 PW at 15°S.

Model simulations reveal that the absence of OMET would cool the high latitudes, and polar ice packs would spread. The Earth might freeze further as the profound influence on climate exerted by the ocean is likely through its crucial role in forming radiatively important sea ice and low oceanic cloud cover (Winton, 2003). In addition, for a time scale of several decades, AMET and OMET usually offset the changes of each other to achieve the energy balance at the TOA. This straightforward scenario is known as Bjerknes compensation (Bjerknes, 1964), indicating the significance of OMET in maintaining the earth's energy balance. For instance, the northward-oriented OMET at the equator needs to be balanced by a southward-oriented AMET. In the tropics, atmospheric energy transport is mainly achieved by the Hadley circulation through the geopotential transport in the upper branch. Thus, a total southward AMET corresponds to a northward flow in the lower branch, transporting heat and water vapor and forming the rainfall belt. Therefore, the northward OMET contributes to the northward shift in the mean position of the ITCZ (Frierson et al., 2013; J. Marshall et al., 2014). Then, what processes drive this important OMET?

Ocean circulation can be conceptually divided into two main components: a fast and energetic wind-driven surface circulation and a slow and sizeable density-driven circulation that

dominates the deep ocean, although the ocean circulation is not a simple addition of the effects of these two types of forcings. Winds also play a significant role in thermohaline circulation (Shrestha et al., 2014). Wind-driven or tidal mixing are key components of the global thermohaline circulations (Oka and Niwa, 2013; Wunsch and Ferrari, 2004). Wind-driven and deep-oceanic circulations are responsible for a significant part of the OMET, the former having a central influence in the tropics. The role of the oceanic eddies is less well-known, but they can be significant in the Southern Ocean (Marshall and Speer, 2012), where eddies feed energy and momentum back into the mean flow and help drive the deep ocean circulation (M. Susan Lozier, 1997; Morrow et al., 1994).

1.4.1 Wind-driven surface Currents

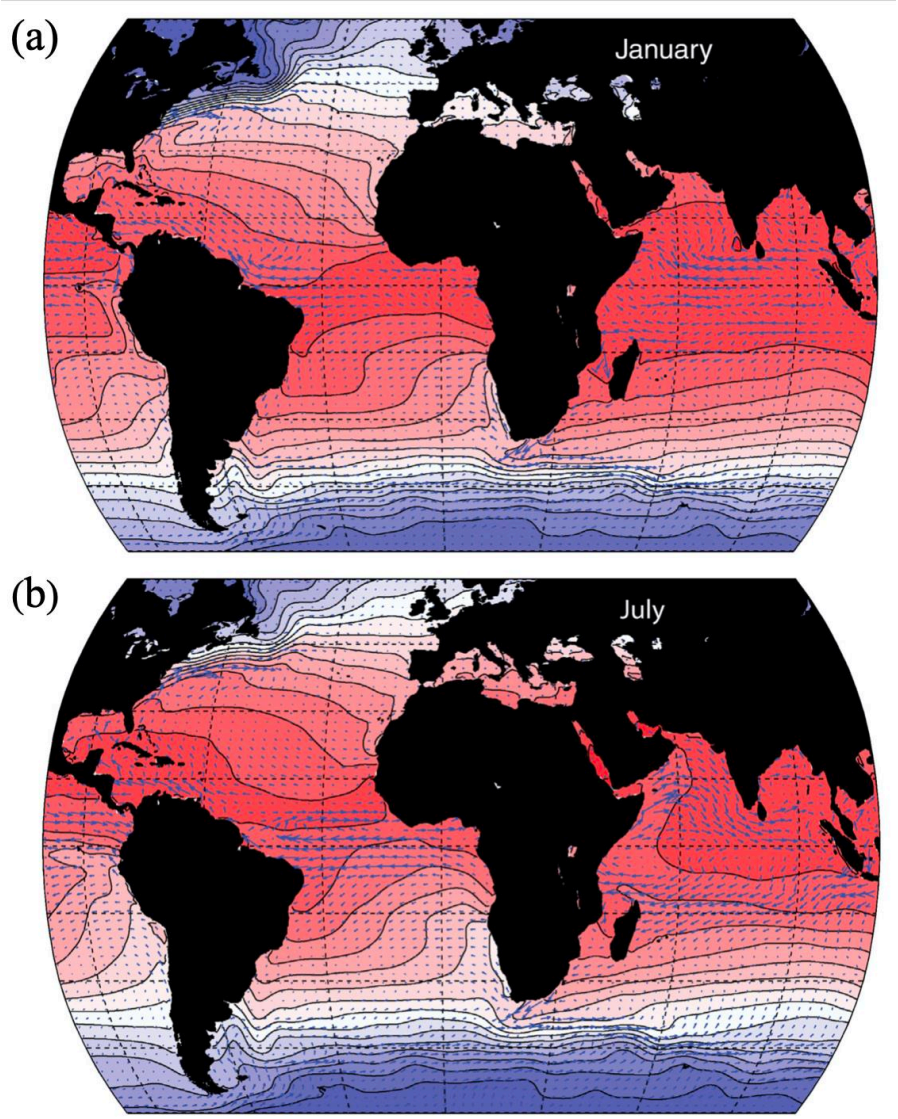

Figure 1.6. Surface ocean current vectors and sea surface temperature (SST) for (a) January and (bb) July. SST data is from ERA-Interim. Current vectors are from the OSCAR data set. Reprinted from Hartmann (2015).

The wind blows across the ocean surface and moves the sea water due to its frictional drag on the surface. The large-scale global wind field consists of the westerlies in the mid-latitudes and the easterly trade winds in the tropics. The wind stress acting on the ocean resembles the near-surface winds and transfers momentum to the ocean. Figure 1.6 shows the global distribution of large-scale surface ocean currents in the Atlantic and Indian basins. Due to the presence of continental barriers, the trades and westerlies result in currents forming loops called the subtropical and subpolar gyres. The surface currents in the subtropical gyres are intensified along the western boundaries of the oceans, forming well-known western boundary currents (WBCs), such as the Gulf Stream off the eastern coast of North America and the Kuroshio Current off Japan. At higher latitudes in the Northern Hemisphere, there are weaker subpolar gyres. While in the Southern Ocean, the absence of continents and the strong westerlies induces the formation of the eastward flowing Antarctic Circumpolar Current that connects all the ocean basins. The Antarctic Circumpolar Current at about 60°S is one of the strongest currents on Earth, with a mass transport of about 130 Sv (1 Sv = $10^6\ m^3 s^{-1}$). These currents and gyres circulate in almost the same direction as the applied wind stress (Figure 1.7). In contrast, the position of the ITCZ north of the equator induces the formation of equatorial countercurrents and thermoclines in all ocean basins, which flow in the direction opposite to trade winds.

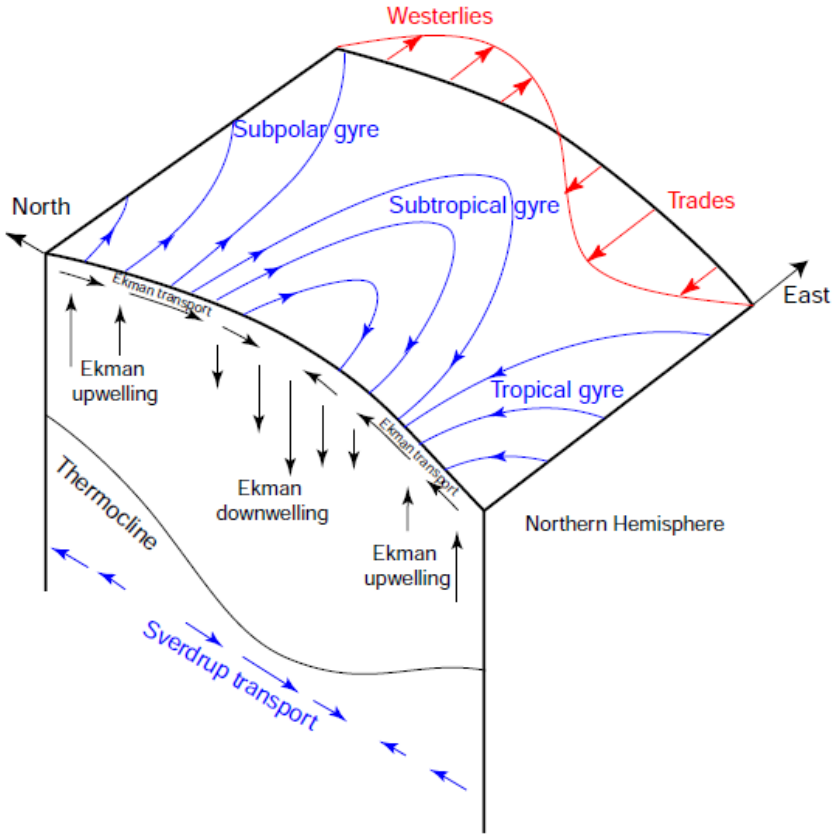

Figure 1.7. Schematic of the westerly and trade winds and associated Ekman transport and wind-driven surface gyres. Reprinted from (Talley et al., 2011).

As shown in Figure 1.8a, the balance between Coriolis and turbulent drag forces leads to a vertically integrated transport in the ocean surface layer normal to the applied wind stress (to the right in the Northern Hemisphere, to the left in the Southern Hemisphere). This transport, known as the horizontal Ekman transport, plays an important role in explaining the path of the wind-driven surface currents. Furthermore, conservation of mass requires vertical motions in the ocean to compensate for the surface convergence/divergence caused by the horizontal Ekman transport. For instance, the coastal upwelling results from the offshore Ekman transport driven by the alongshore winds (Figure 1.8c). The cold tongue of SST in the eastern equatorial Pacific Ocean results from the coastal upwelling of the deep cold seawater.

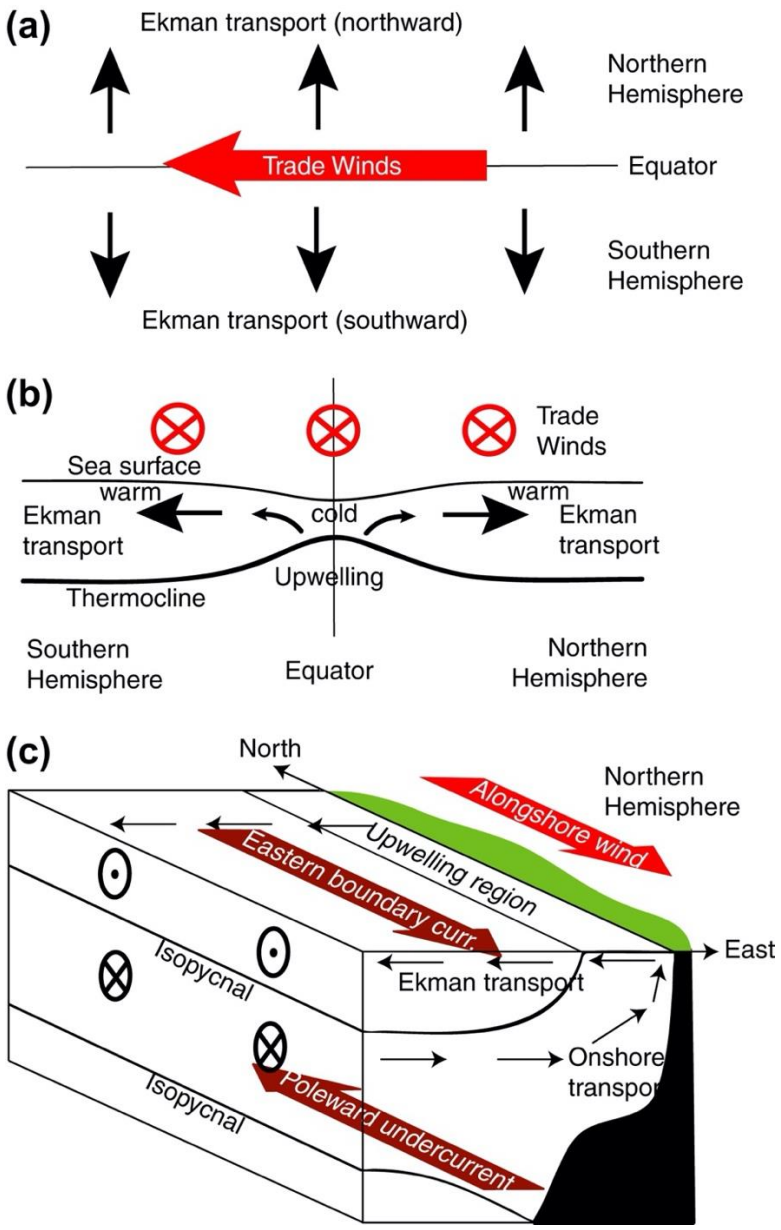

Figure 1.8. Ekman transport divergence near the equator driven by easterly trade winds. (a) Ekman transports. (b) Meridional cross-section showing effects on the thermocline and surface temperature. (c) Coastal upwelling system due to an alongshore wind with offshore Ekman transport (Northern Hemisphere). The accompanying isopycnal deformations and equatorward eastern boundary current and poleward undercurrent are also shown. Reprinted from (Talley et al. 2011).

In addition, as the trade wind converges toward the ITCZ, the Ekman transport diverges at the equator. The resulting divergence at the equator is compensated by an upwelling there (Figure 1.8b), leading to a pair of shallow meridional overturning cells on both sides of the equator, known as the shallow tropical cells (McCreary and Lu, 1994). It consists of poleward surface Ekman transport that subducts in the subtropics and flows in the subsurface layers equatorward to the

equator, where it upwells to close the cell. These two subtropical cells are shallow, extending from the surface to about 500-m depth.

Figure 1.3a shows the equal importance of the atmosphere and ocean in the meridional energy transport in the tropical regions (0-10°), of about 1.5 PW for each. Many studies have suggested that both the wind-driven ocean circulation and the deep overturning cells are responsible for the considerable OMET (Klinger and Marotzke, 2000; Talley, 2003). Note that the heat transport depends on the surface winds that drive the mass transport and the surface heat fluxes that shape the temperature distribution. Hence the OMET cannot be explained uniquely with ocean mass transport. Although the mass transport in the WBCs is much stronger than the Ekman mass transport (31.4 Sv versus 3.8 Sv; see details in Chapter 2.1), between the equator to 10°N/S, the zonal temperature gradient is not as strong as that at subtropical regions (30°- 40°; Figure 1.6). The horizontal tropical gyre associated with WBCs might not contribute a large fraction to the meridional energy transport in the tropics (Figure 1.8). The shallow tropical overturning related to Ekman transport may be mainly responsible for the mean ocean heat transport within ~25° of the equator (Levitus, 1987).

Numerical simulations indicate that in the Atlantic Ocean, heat transport by the subtropical cell peaks at 10°N/S, of about 0.1 PW. Due to the higher meridional temperature contrast in the South Indian Ocean, the shallow subtropical overturning transport is about 0.23 PW (Klinger and Marotzke, 2000). This transport in the broader Pacific Ocean in both hemispheres is around 0.3 PW. Meanwhile, between 10°N and 10°S, the maximum total OMET is ~0.9 PW in the Atlantic, ~ 0.4 PW in the Pacific, and ~0.3 PW in the Indian Ocean (Figure 1.3b). Therefore, the contribution of subtropical cell transport is minor in the Atlantic Ocean but plays an important role in the Pacific and Indian Oceans. This is consistent with the hydrographic measurements, which show that in the North Atlantic, the OMET is dominated by the meridional overturning circulation associated with deep flows (Bryden et al., 1991; Hall and Bryden, 1982; Roemmich and Wunsch, 1985).

The importance of Ekman transport in the OMET is also reflected by its contribution to driving the subtropical gyres and WBCs. The subtropical gyre and the WBCs such as the Gulf Stream in the Atlantic Ocean and the Kuroshio in the Pacific Ocean carry large amounts of heat poleward. For instance, the Gulf stream and the associated eastward North Atlantic Current lead to relatively high temperatures along their pathway compared to other oceanic regions at the same latitude. The atmospheric circulation then brings relatively warm air of oceanic origin to Europe, causing the different winter temperatures in Eastern Canada and Western Europe.

1.4.2 Deep thermohaline circulation

The thermohaline circulation, sometimes used to refer to the overturning circulation, is driven by the water density gradients, which are in turn related to sources and sinks of heat (thermo) and salt (haline). However, the term overturning circulation is preferred in this manuscript as the wind is another key component driving the deep currents. The overturning designates the presence of current in opposite directions for different depths of the ocean. Specifically, we will focus on the meridional overturning circulation, which refers to the overturning due to meridional flow. Figure 1.9 presents a strongly simplified sketch of the global oceanic circulation. The wind-driven gyres and the associated WBCs, such as Gulf Stream, carry warm and salty water poleward from the equatorial regions, losing water vapor and heat to the atmosphere along its path. Sea ice forms in the polar regions as the ocean surface loses heat during winter and melts in summer, discharging salt into the ocean where the sea ice grows and adding freshwater where the sea ice melts. Surface water may then be dense enough to sink. The resultant deep water moves equatorward through the deep western boundary current (DWBC). The conventional view is that the sinking process, often called deep ocean convection, only occurs in a few places, mainly in the Labrador Sea and Nordic Seas in the Atlantic basin and the Southern Ocean. Nevertheless, based on observations from OSNAP, some recent work pointed out that the conversion of warm, salty, shallow Atlantic waters into colder, fresher, deep waters occurs in the eastern than western subpolar gyre (Lozier et al., 2019; Menary et al., 2020).

In the North Atlantic, the hydrography defines the North Atlantic Deep Water (NADW) formed by mixing the deep water of different origins in the Atlantic basin. The NADW flows southward along the western boundary of the Atlantic and eventually reaches the Southern Ocean. In the Southern Ocean, it then blends with other ambient water masses and then forms the circumpolar deep water. Next, this circumpolar deep water slowly upwells towards the thermocline in all oceanic basins. Although sinking is confined to very small regions, the upwelling is broadly distributed throughout the ocean. The return flow to the North Atlantic downwelling regions is achieved through the surface and intermediate-depth circulation.

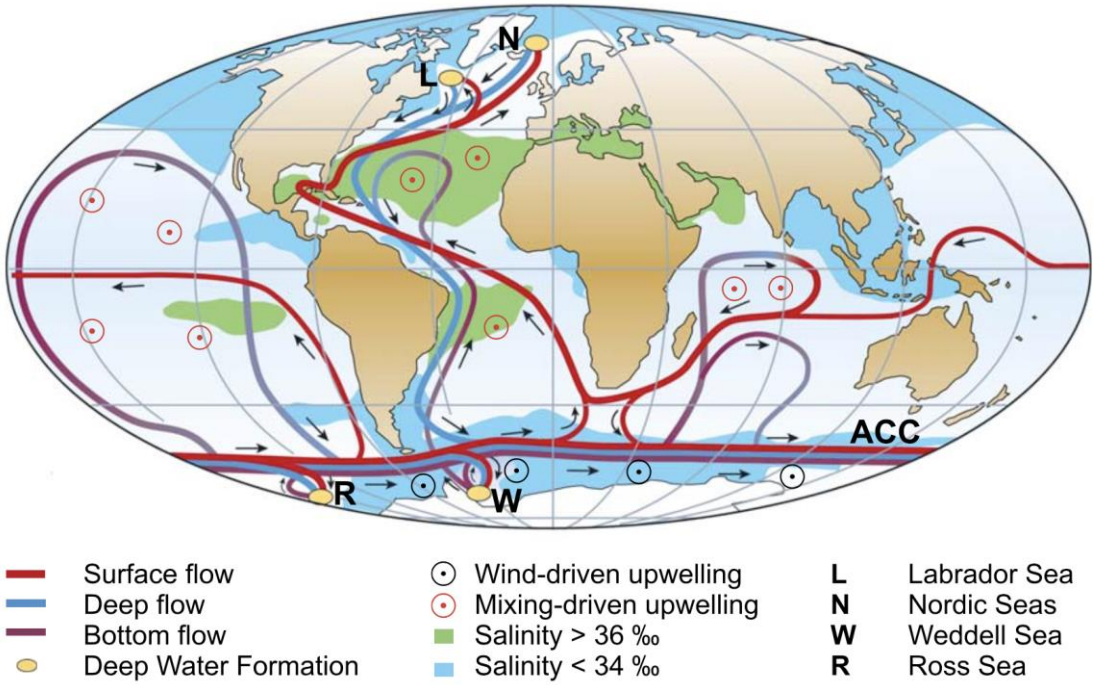

Figure 1.9. Sketch of the global overturning circulation system. In the Atlantic, warm and saline waters flow northward all the way from the Southern Ocean into the Labrador and Nordic Seas. By contrast, there is no deepwater formation in the North Pacific, and its surface waters are fresher. Deep waters formed in the Southern Ocean become denser and thus spread to deeper levels than those from the North Atlantic. Note the small, localized deep water formation areas compared to the broad zones of mixing-driven upwelling. Wind-driven upwelling occurs along the Antarctic Circumpolar Current. Reprint from (Kuhlbrodt et al., 2007).

In the Southern Ocean, Antarctic Bottom Water is mainly produced in the Weddell and Ross Seas. This water mass is colder and denser than NADW and thus flows below it. Therefore, the AMOC (Figure 1.9), the most prominent branch of the global meridional overturning circulation (Kuhlbrodt et al., 2007), consists of two primary overturning cells: (1) an upper cell in which warm ocean waters are transported northward in the upper 1,000 m and lose buoyance gradually during the path, leading to the formation of the NADW, which returns southward at depths of approximately 1,500-4,500 m and (2) an abyssal cell in which Antarctic Bottom Water flows northward below depths of about 4,500 m west of the Mid-Atlantic Ridge and gradually rises into the lower part of the southward-flowing NADW (Clark, 2009).

The AMOC connects northward flowing warm waters on the surface and southward flowing cold waters at great depths in the entire basin. In the South Atlantic, the northward heat transported by this deep overturning cell overwhelms the shallow subtropical cell transport, leading to a positive OMET along the whole latitude range from 30°S to 80°N in the Atlantic (Figure 1.3b). The Pacific Ocean does not support a significant deep-reaching overturning cell; the transports are mainly due to near-surface subtropical overturning cells and gyre circulations. Therefore, the

OMET is symmetrically poleward in two hemispheres. Because of the unique geometry, the transport by the cross-equatorial cell in the Indian Ocean is southward due to the Ekman flow driven by the southwesterly summertime monsoon winds (Lutsko et al., 2019).

The heat transported by the AMOC at 26°N is around 1.3 PW, calculated with the short-term (about four years) observational data (Johns et al., 2011). There is a discrepancy between the observed AMOC transport and the total OMET in the Atlantic computed with the indirect approach. The AMOC transport should be smaller than the total transport as the wind-driven transport is also northward. This difference might be explained by the different temporal coverage of these estimations.

The significant heat transport achieved by the deep overturning circulation in the Atlantic Ocean has a broader impact beyond the Atlantic sector. For example, the northward cross-equatorial Atlantic OMET due to the AMOC is important to determine the mean position of the ITCZ north of the equator (Chapter 1.4). More details of its impact on climate are given in Chapter 2.5.

1.4.3 Mesoscale eddies

Although the history of computing the time mean OMET is long, with hydrographic observations and different estimations of surface fluxes, our understanding of its temporal variability is not sufficient, partly due to limited observations of mesoscale processes in many regions. In addition, the role of eddies in OMET is sometimes thought to be minor because of their small spatial scales compared with the scale of the oceans. These oceanic eddy structures are smaller than the eddies in the atmosphere approximately by a factor of 100. Indeed, the eddy heat transport is generally weak in the central gyres. However, some observations and eddy-permitting models have indicated that eddy heat transport is intense near the WBC extensions and the Antarctic Circumpolar Current (Dong et al., 2014; Jayne and Marotzke, 2002; Volkov et al., 2008). The Argo data reveals that the eddy transport reaches 0.12 PW in the northwestern boundary current band and −0.38 PW in the Antarctic Circumpolar Current band, respectively (Zhang et al., 2014). The eddy transport is confined to the upper 1000 m of the ocean (Jayne and Marotzke, 2002; Zhang et al., 2014). These results are likely beneficial to improving the parameterization scheme in models.

Chapter 2

Contents

2 ATLANTIC MERIDIONAL OVERTURNING CIRCULATION 22

2.1 THE OBSERVED AMOC 22
2.2 THE SIMULATED AMOC 24
2.3 DRIVERS OF THE AMOC VARIABILITY 26
2.3.1 ATMOSPHERIC FORCING 28
2.3.2 INTRINSIC OCEANIC DYNAMICS 31
2.4 WHAT DOES THE AMOC VARIABILITY DRIVE? 36
2.4.1 THE ATLANTIC OCEAN 39
2.4.2 THE ARCTIC 43
2.4.3 THE PACIFIC OCEAN 45
2.5 SUMMARY 48

2 Atlantic Meridional Overturning Circulation

2.1 The observed AMOC

As the AMOC plays a significant role in the Earth's climate, the continuous instrumental records of the AMOC and associated heat transport have existed since 2004, by the Rapid-MOCHA-WBTS project (RAPID array in the following), which developed and maintained an observing system at 26.5°N in the Atlantic (Cunningham et al., 2007). RAPID concentrates on western boundaries and owns the longest temporal coverage, available from April 2004 to March 2020, compared to other AMOC observing arrays in the trans-basin areas: OSNAP in the subpolar North Atlantic since 2014 (Li et al., 2017; Lozier et al., 2017) and SAMBA in the South Atlantic at 34.5°S since 2009. Next, we give an overview of the results retrieved from the AMOC observations, mainly from RAPID data.

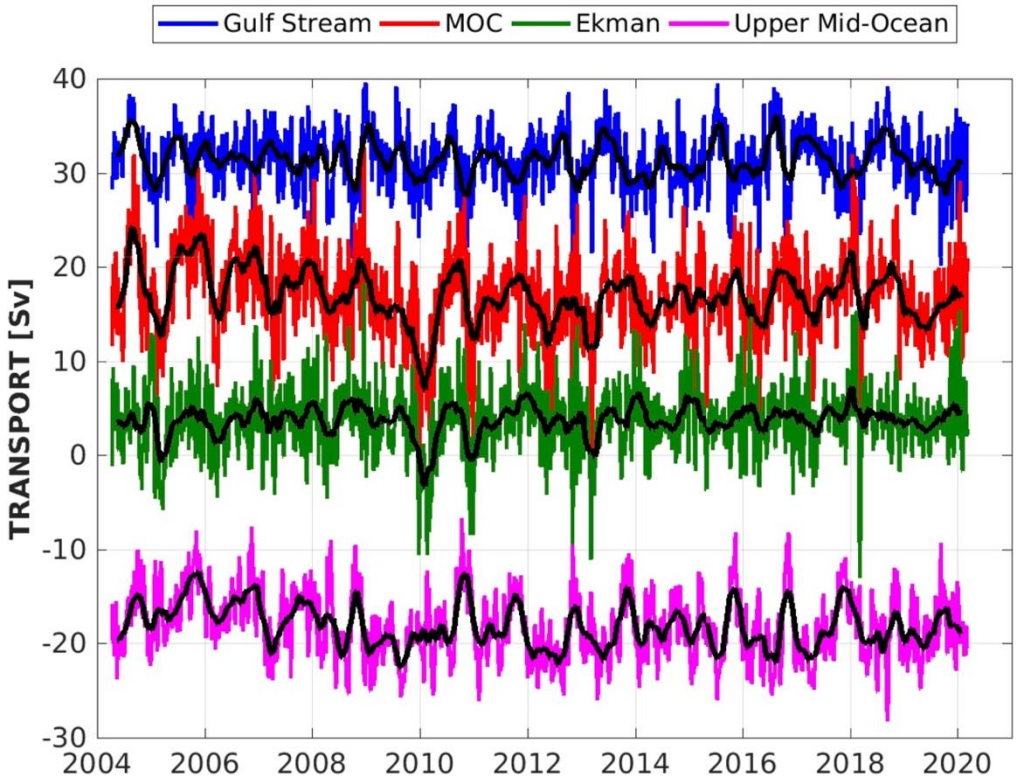

Figure 2.1. Observational Atlantic meridional overturning circulation (AMOC) transport from RAPID array data from 2nd April 2004 to 9th March 2020. Ten-day (colors) and three-month (black) low-pass filtered timeseries of Florida Straits transport (blue), Ekman transport (green), upper mid-ocean transport (magenta), and overturning transport (red). Positive transports correspond to northward flow. The same figure but with data from April 2004 to October 2012 is provided by McCarthy et al. (2015). This figure calculates the transports in the same way, but the data is updated by the RAPID array team.

The AMOC is commonly described by the overturning streamfunction:

$$\Psi(z) = \int_{x_w}^{x_e} \int_{-H}^{z} v(x,z)dzdx \qquad (2.1)$$

with the same notations as in Chapter 1. Ψ is the zonally and vertically integrated meridional volume transport in a unit of Sv. The AMOC strength at a given latitude is defined as the maximum vertical value of the streamfunction.

Figure 2.1 shows the AMOC timeseries (red line) at 26.5°N from RAPID. The meridional overturning circulation is computed as the sum of the three different components derived through different observational data: the Gulf stream transport (Florida cable; blue line) through the Florida Straits, the wind-driven Ekman transport (atmospheric reanalysis; black line), and the mid-ocean transport (RAPID array hydrography; pink line) in the upper mid-Ocean. The mid-ocean transport is derived from the differences between vertical density profiles from the eastern and western

boundaries. The strength of meridional overturning circulation is 16.9 ± 4.6 Sv. The Gulf stream transport, Ekman transport, and upper mid-ocean transport are 31.4 ± 3.2 Sv, 3.8 ± 3.5Sv, and -18.1 ±3.5Sv, respectively.

Many other features of the AMOC have been explored with the observational data. Johns et al. (2011) showed that the overturning carries 88% of the total OMET in the Atlantic Ocean, while the rest, 12%, is due to the gyre circulation. On seasonal time scales, the peak-to-peak amplitude of the AMOC was found to be 6.7 Sv, with important contributions from the geostrophic mid-ocean transports (Kanzow et al., 2010). They also suggested that the seasonal cycle is dominated by wind stress at the eastern boundary, while Chidichimo et al. (2010) showed that the changes in the eastern-boundary densities give rise to 5.2 Sv peak-to-peak transport variability. At the western boundary, the variability of the DWBC was studied by Johns et al. (2008), who showed that the DWBC is −26.5 Sv and is divided nearly equally between upper and lower NADW. The 30% decline in the annual mean AMOC caused by unusually low AMOC in winter 2009/2010 was attributed by McCarthy et al. (2012) to anomalous Ekman transports from December 2009 to March 2010 and the intensification of the geostrophic mid-ocean transports. Using the relatively short OSNAP data (2014 - 2018), Li et al. (2021) proposed that DWBC variability is not firmly related to AMOC variability. Indeed, they found that the observed wintertime deep water formation in the interior basin has minimal impact on density changes in the DWBC, suggesting a dominant role in the overflows connecting the Nordic Seas to the North Atlantic.

The wealth of information from the RAPID array calls for a comparison with results from general circulation models (GCMs), as presented in the next section.

2.2 The simulated AMOC

Because the observations of the AMOC are limited in terms of sampling, numerous studies investigated the AMOC using numerical modeling. Figures 2.2 show the AMOC stream function from various models, including non-eddy and eddy-rich simulations, high- and low-resolution runs, atmosphere-ocean GCM (AOGCM) simulations and ocean-only GCM (OGCM) runs. In addition, we show an estimation of the observed AMOC from Lumpkin and Speer (2007) in Figure 2.3. It is a zonally averaged mean AMOC stream function with an inversion of multiple observational data (air-sea fluxes of heat and freshwater, recent hydrographic sections, and direct current measurements) that Buckley and Marshall (2016) converted into depth coordinate.

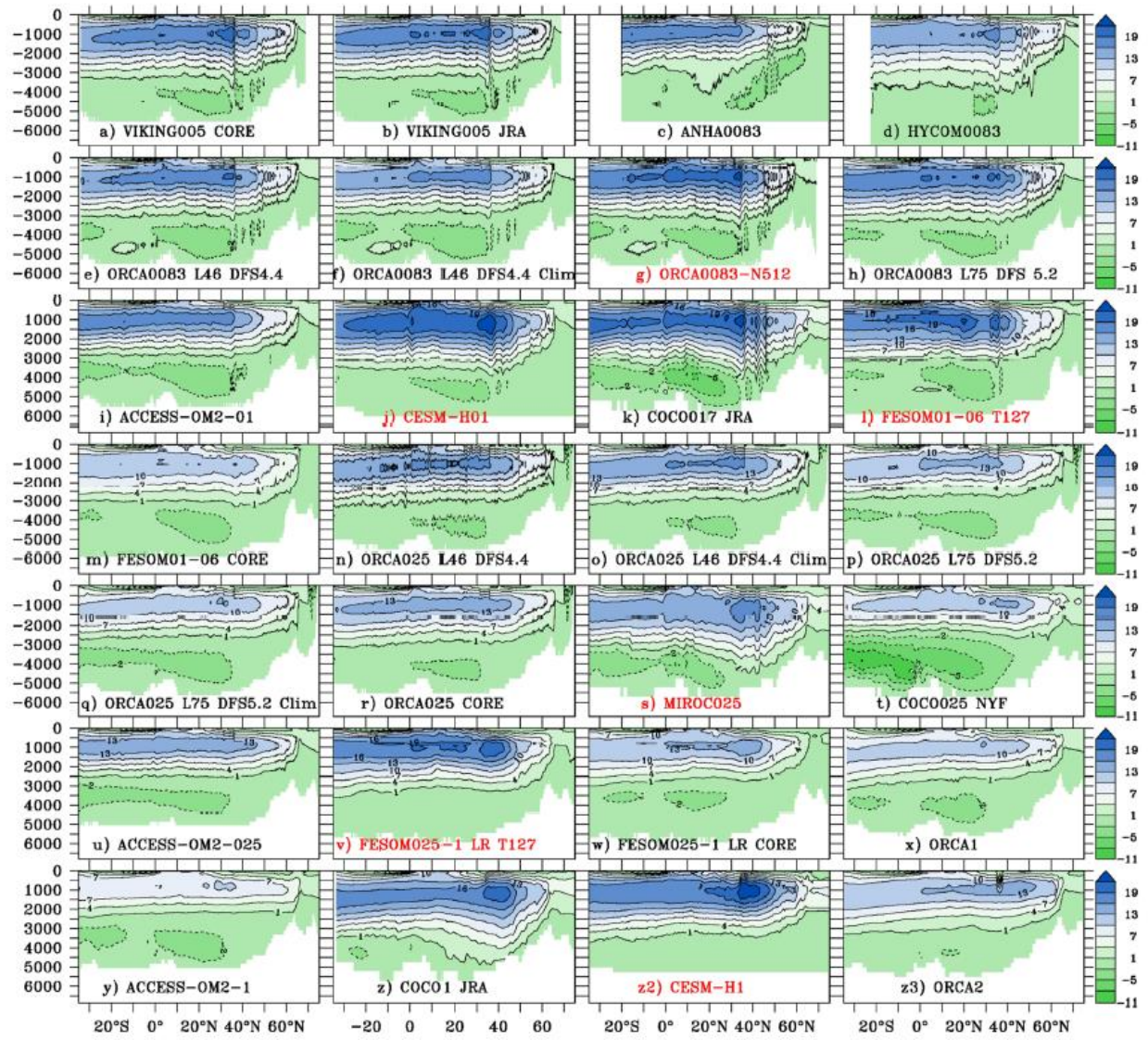

Figure 2.2. AMOC stream functions in the depth coordinate in models from non-eddying to eddy-rich simulations. The highest resolutions are shown in the top row and the lowest in the bottom. Ocean-atmosphere coupled models are indicated in red. Reprinted from Hirschi et al. (2020).

The models present different strengths and structures of the AMOC from the observed AMOC. The maximum stream function occurs at around 24°N in observations (Figure 2.3), while in the models, the maximum values are generally located at about 40°N (Figure 2.2). The strength of the simulated AMOC varies by a factor of 2 between the strongest and the weakest simulations. The coupled version of the model tends to present a stronger AMOC than the ocean-only configurations (Hirschi et al., 2020). Improvement in oceanic resolution also usually leads to a stronger simulated AMOC due to the stronger air-sea interactions (Grist et al., 2018; Roberts et al., 2016). Nevertheless, significant differences exist among the different models, even for those of similar resolution and configuration.

Simulating a realistic AMOC structure and associated Atlantic OMET remains challenging (Zhang et al., 2019). The simulated weak AMOC is linked to a pronounced cold SST bias in the mid-latitude North Atlantic in many AOGCMs (Wang et al., 2014). It is also related to a fresh bias of the North Atlantic sea surface salinity (SSS), especially over the NADW formation sites (Drews et al., 2015; T. Park et al., 2016; Talandier et al., 2014).

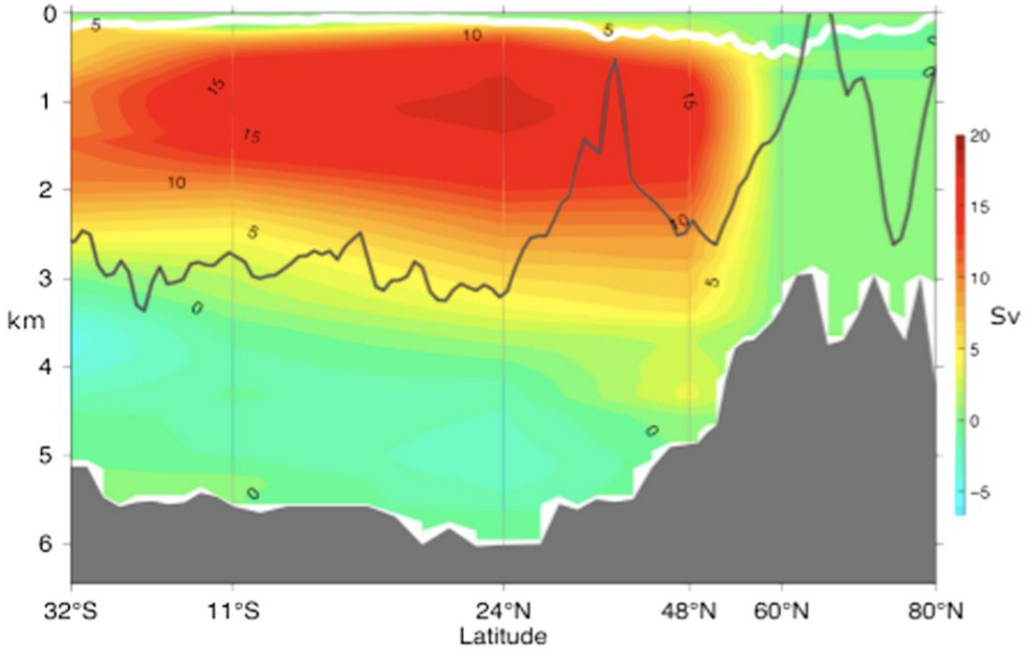

Figure 2.3. Mean Atlantic Meridional Overturning Circulation (AMOC) stream function in depth coordinates estimated from tracer inversion by Lumpkin and Speer (2007). Grey shading indicates the ocean bottom (maximum depth in the Atlantic at each latitude), and the black line indicates the crest of the Mid-Atlantic Ridge. The thick white line near the topography represents the deepest (climatological) mixed layer depth. Reprinted from Buckley and Marshall (2016).

2.3 Drivers of the AMOC variability

Under the background of climate change, the long-term trend of the AMOC has been a concern in the climate community for decades. Numerical simulations with double atmospheric CO_2 suggest a slowdown of the AMOC in response to global warming through radiative warming and freshening due to sea ice melting (Swingedouw et al., 2007; Zhu et al., 2015). The palaeo-proxy evidence suggests a slowdown of the AMOC started in the nineteenth century and enhanced during the mid-twentieth century (Caesar et al., 2021). Some other palaeo-proxy studies also found a reduction in AMOC in the twentieth century (Rahmstorf et al., 2015; Thornalley et al., 2018). The continuous observation by the RAPID array reveals a substantial decline in the AMOC between 2004 and 2012 (Smeed et al., 2014). Studies simulating a dramatic collapse of the AMOC with internal perturbations or external forcings have suggested a cooling at least in the Northern

Hemisphere resulting from the weakened AMOC (e.g., Brunnabend and Dijkstra, 2017; Drijfhout, 2015; Vellinga and Wood, 2002). The potential global cooling related to the shutdown of the AMOC may obliterate global warming (Drijfhout, 2015).

On the other hand, based on a comprehensive set of palaeo-proxy data, a recent work argues that the strength of AMOC over recent centuries is poorly constrained, and the projected slowdown in response to global warming may not have started yet (Kilbourne et al., 2022). Jackson et al. (2016) also proposed that the recent slowing of Atlantic overturning circulation is a recovery from earlier strengthening. However, it is difficult to distinguish the influence of global warming on the AMOC from its natural variability without a proper understanding of the underlying mechanisms of AMOC variability on different time scales. In particular, the low-frequency variations have an important influence on the long-term trend of the AMOC.

Fluctuations in the AMOC have been linked to changes in essential ocean variables, such as SST and subsurface temperature (Zhang, 2008), sea level (Bingham and Hughes, 2009; Frajka-Williams, 2015; Park and Latif, 2008), deep density gradients (Zanna et al., 2011), and Arctic sea ice (Mahajan et al., 2011; Park and Latif, 2008). These associations can enable the prediction or attribution of SST or Arctic sea ice variations in response to AMOC changes. A robust variability mechanism can provide appropriate ocean initial conditions for use in the decadal prediction experiments, where the AMOC and upper-ocean temperatures are crucial to assess the decadal climate forecast skills (Cassou et al., 2018). Moreover, we have shown the scarcity of instrumental measurements of the AMOC both in temporal and spatial domains. Understanding the mechanism of the AMOC variability helps figure out the key regions where the local variations drive the rest of the Atlantic and facilitate the design of observational networks.

The variability of the AMOC on different timescales, ranging from interannual to multi-centennial, has been widely explored in many previous studies. We have briefly shown the seasonal to decadal variability investigated with observational data in Chapter 2.1. Whereas for multi-decadal to multicentennial variations, instrumental records are not enough. Some paleo-proxy studies have shown the existence of low-frequency variability in the North Atlantic (Nyberg et al., 2002; Sicre et al., 2008) or in the Northern Hemisphere (Ayache et al., 2018; Laepple and Huybers, 2013; Mann et al., 1995). Nyberg et al. (2002) and Farmer et al. (2008) found centennial variations of SST in the North Atlantic in the Holocene. Centennial to millennial-scale variability also has been found in the North Atlantic Ocean circulation in the surface and deep layers (Bond et al., 2001; I. R. Hall et al., 2004; Kissel et al., 2013). A reconstruction of past AMOC based on multiple proxy-derived SST records suggested a multi-centennial variability over the Holocene (Ayache et al., 2018). However, it is difficult to distinguish this internal variability from external forcings, such as solar irradiance and volcanic aerosol variations (Mann et al., 2021). Therefore, even though the simulated cold and fresh bias in North Atlantic SST/SSS might lead to the

underestimation of the low-frequency AMOC variability at multidecadal timescales (Park et al., 2016) and the deficiencies in models may alter our understanding of the role of AMOC in climate, numerical models remain the main method to explore a large spectrum of AMOC variability, at the interannual, decadal, multidecadal or multi-centennial time scales.

In the following, we will present the dominant mechanisms of the AMOC variability. Firstly, we will present the direct role of the atmospheric variations. Secondly, we will investigate the oceanic mechanism which can drive AMOC variations in models.

2.3.1 Atmospheric forcing

The AMOC variability is largely regulated by atmospheric variations. The linkage between the atmospheric forcing and the AMOC variations is usually examined with OGCM forced by the historical atmospheric forcing estimated during the last decades. Such runs are also called ocean hindcasts and use the so-called bulk formulae to estimate the fluxes exchanged between the ocean and the atmosphere. The ocean hindcast simulations used to investigate the AMOC variability adopts, for instance, NCEP reanalysis (Kalnay et al., 1996) or ERA-40 (Uppala et al., 2005). The Coordinated Ocean-ice Reference Experiment framework defines protocols for performing these simulations, for example, using inter-annually varying atmospheric forcing over the 60 years from 1948 to 2007 to force the ocean and sea-ice model (Danabasoglu et al., 2014). Based on these ocean hindcast simulations, the role of buoyancy fluxes and wind stress can be investigated on interannual to decadal time scales, even if a salinity restoring has to be used.

The North Atlantic Oscillation (NAO), associated with a large-scale atmospheric pressure see-saw at sea level in the North Atlantic region between the Azores islands (the subtropical high) and low pressure centered over Iceland (the subpolar low), is the most prominent atmospheric mode that can drive the AMOC fluctuations. The NAO index is defined by the sea level pressure (SLP) difference between these two regions and is most dominant in the winter. The observed winter NAO index has been available since 1864, provided by the Hurrell North Atlantic Oscillation Index from NCAR. Fluctuations of the NAO-related surface fluxes are found to increase the deep water formation in the subpolar regions, which then intensifies the AMOC (e.g., Danabasoglu et al., 2016; Xu et al., 2019). The AMOC variations are often detected in the subpolar gyre by changes in temperature, salinity, and, hence, density anomalies (Häkkinen et al., 2011), particularly in deep-water formation regions. Xu et al. (2013) found that the observed decadal variability of wintertime NAO index leads the boundary current transport in the subpolar gyre by 2 years and leads the simulated AMOC by about 1 year. Böning et al. (2006) reported that the NAO weakens subpolar gyre intensity, consistent with sea surface height observations. The associated volume transport changes in the DWBC off the Labrador Sea reflect the variations of AMOC. The gyre circulation variations connect the NAO and the AMOC oscillations.

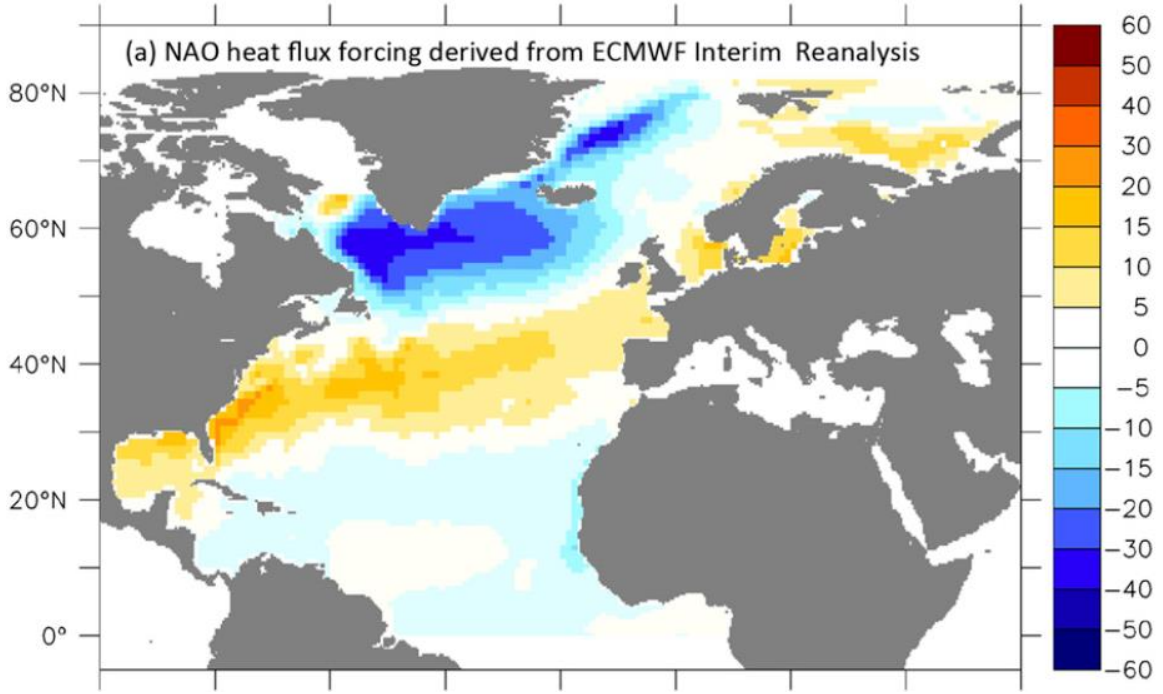

Figure 2.4. Winter (from December to March) heat flux anomalies (W m^{-2}) that correspond to a one-standard-deviation anomaly of the North Atlantic Oscillation (NAO). Negative values indicate a flux of heat from the ocean to the atmosphere. Heat flux data is from ECMWF ERA-Interim. The NAO index uses the station-based index provided by the NCAR–UCAR climate data guide. Reprinted from (Delworth and Zeng, 2016).

More specifically, during the positive phase of the NAO, both the subpolar low and the subtropical high are higher than average. The intensified pressure contrast between the two regions leads to stronger westerlies manifested by the Atlantic jet stream. Intensified westerlies can extract more heat from the ocean to the atmosphere in the subpolar gyre regions through increased turbulent fluxes (Marshall et al., 2001). Anomalous heat is released from the ocean to the atmosphere in the subpolar gyre and the Nordic Seas (Figure 2.4). The convection in the deep water formation sites increases due to the buoyancy loss. The lower branch of the AMOC (NADW) intensifies concomitantly. Some studies found that the enhanced convection occurs in the Labrador Sea associated with the WBCs (Danabasoglu et al., 2012; Delworth and Zeng, 2016; Kwon and Frankignoul, 2012; Yeager and Danabasoglu, 2014). However, other studies suggested other key regions. For instance, Deshayes and Frankignoul (2008) found that the increased deep water formation driven by the interannual-to-decadal variability of the NAO occurs in the Irminger Sea instead of the Labrador sea. The subpolar gyre is weakened in the south and strengthened in the north by the anomalous Ekman pumping associated with NAO-related wind stress anomalies. The buoyancy loss in the Labrador sea increases in smaller amplitude than that in the Irminger Sea. Therefore, the subpolar gyre and the AMOC intensifications are initialized in the Irminger Sea.

Some other work based on the short-term observations (OSNAP since 2014) instead found that buoyancy anomalies driving AMOC variability do not occur in the Labrador Sea. The changes in the Irminger and Iceland basins are important (Lozier et al., 2019). The comparison between OSNAP observations and models further reveal that the eastern subpolar gyre plays a more prominent role in the AMOC variability (Menary et al., 2020).

Although the debate on the role of currents in the Labrador or the Irminger Seas exists, another crucial source of the NADW is found related to the Nordic Seas (Greenland Sea, Norwegian Sea, and Iceland Sea) outflow, which is the cold/dense water from the Nordic Seas returning southward in the form of bottom-attached gravity currents (Darelius et al., 2015). However, the variability in the Labrador Sea and the Nordic Seas convection driven by decadal air-sea fluxes in the convective region are related to opposite phases of the NAO. The enhanced convection in the Labrador Sea tends to be favored by cold and dry air masses during the positive NAO. The increasing Labrador Sea sea-ice extent also contributes to the convection via brine release. Similar effects of the air-sea fluxes are seen in the Nordic Seas during a negative phase of NAO when fewer warm and moist air masses are brought into the region by reduced storms (Medhaug et al., 2012). The Labrador Sea convection driven by NAO primarily regulates the variability in AMOC. Connections between the outflows in the Nordic Seas and the AMOC are less direct and more complicated due to the barrier of the Greenland-Scotland Ridge.

In summary, although whether the interannual-to-decadal AMOC variability is a dynamic ocean response to the atmospheric forcing is still under debate, a consensus is achieved that anomalous surface buoyancy fluxes over the subpolar gyre driven by the NAO through modifications in the air-sea fluxes of heat, water, and momentum, are significant to the variations of the NADW formation and associated AMOC variability.

Apart from NAO, the East Atlantic pattern (EAP), which has a similar configuration as NAO but displaces southeastward to the approximate nodal lines of the NAO pattern, is found to play a role in affecting the AMOC decadal to multidecadal variability (Msadek and Frankignoul, 2009; Ruprich-Robert and Cassou, 2015; Song et al., 2019). In the IPSL-CM4 model, Msadek and Frankignoul (2009) found that during the negative EAP phase, the associated anomalous cyclonic atmospheric circulation over the subpolar gyre increases the heat released from the ocean to the atmosphere, leading to negative SST anomalies at high latitudes. The subpolar gyre and the North Atlantic Current hence intensify, and the warm salty water is advected to the subpolar convection site south of Iceland. The positive density anomalies generate in the deep convection sites, and the AMOC is enhanced. Ruprich-Robert and Cassou (2015) also suggested that the EAP should be included a forcing in addition to NAO for the multidecadal AMOC variability, using the CNRM-CM5 model. With Kiel Climate Model (KCM), Song et al. (2019) proposed that under Large

Glacial Maximum conditions, multidecadal AMOC variability is mainly forced by EAP while NAO dominates under the preindustrial conditions.

2.3.2 Intrinsic oceanic dynamics

In the mechanism for atmosphere-driven AMOC variations, the density anomalies in the subpolar gyre result from the NAO or EAP-related fluxes cooling the ocean surface. Meanwhile, many studies have suggested that AMOC variability over multi-decadal to multi-centennial time scales tends to be intrinsic to the ocean rather than forced by the atmosphere. Most of these studies emphasize the importance of salinity on the density changes (Ba et al., 2014; Delworth and Zeng, 2012; Jackson and Vellinga, 2013). For instance, the AMOC variations are found to be driven by the salinity anomalies from the Arctic (Jungclaus et al., 2005), primarily due to an anomalous freshwater export, or from the Southern Ocean through a slow propagation (Delworth and Zeng, 2012; W. Park and Latif, 2008), or a combined contribution of the salinity anomalies from the Arctic and the tropical North Atlantic (Jackson and Vellinga, 2013; Vellinga and Wu, 2004). We focus on the time scales greater than 50-yr in this subsection.

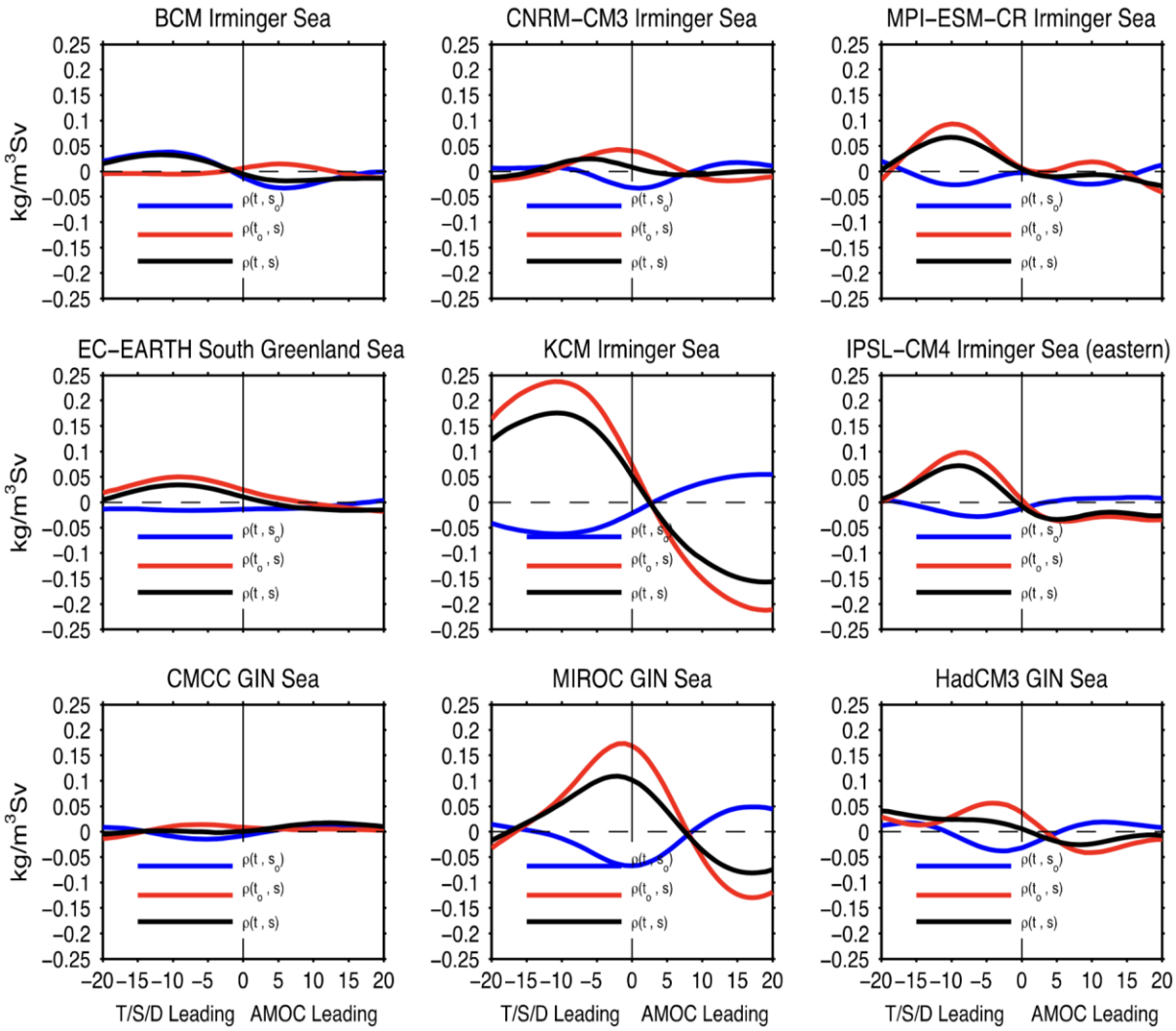

Figure 2.5. Lagged regressions between the AMOC at 30°N and the density (black) and corresponding contribution of temperature (blue) and salinity (red) anomaly in convection sites of nine AOGCMs. An 11-year running mean is applied to all variables before the regression. In each model, the relationships are calculated in the regions where increased mixed layer depth significantly precedes AMOC changes. Reprinted from Ba et al. (2014).

Figure 2.5 shows the density anomalies in the sinking regions where a significant deepening of the mixed layer leads the AMOC variations in nine models. The density anomalies are decomposed into anomalies induced by the salinity and temperature. Most of the models show that the sign of the density anomalies is the same as the salt contribution. The density anomaly induced by temperature changes has the opposite sign and acts as a damping effect for the density anomaly. Similar results are also found in other studies (Delworth and Zeng, 2012; Jackson and Vellinga, 2013). Although Jungclaus et al. (2005) found that the temperature variations might be important in the Greenland Sea, the salinity variations still dominate in the Labrador sea, where most of the deep convection occurs in their AOGCM. The positive (negative) upper layer salinity anomalies in the subpolar North Atlantic strengthen (weaken) the AMOC by regulating upper ocean density

and vertical stratification. Nevertheless, the source and propagation of these prominent salinity and concurrent density anomalies differ in various model studies.

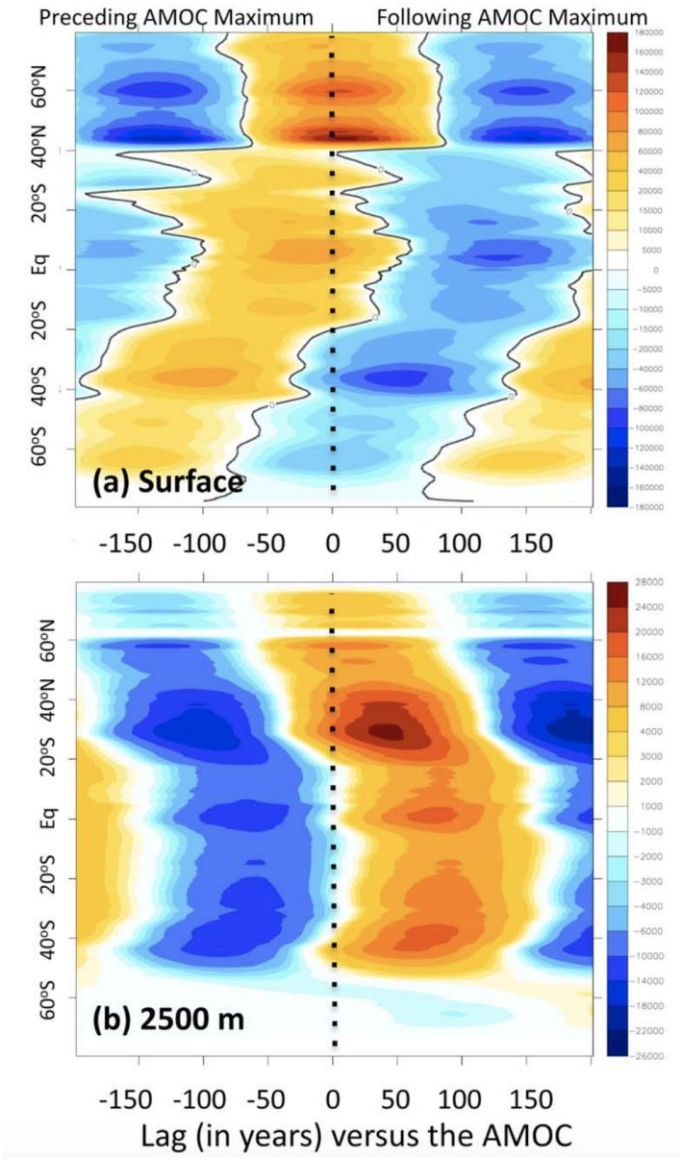

Figure 2.6. Zonal integral of the regression coefficients of salinity in the Atlantic versus the AMOC time series in the GFDL CM2.1 climate model. Units are in PSU m Sv $^{-1}$. Negative (positive) values on the time axis indicate periods before (after) a maximum AMOC (occurring at lag 0). (a) Values at sea surface. (b) Values at 2500 m depth. Reprinted from Delworth and Zeng (2012).

With a 4000-year control simulation of the Geophysical Fluid Dynamics Laboratory coupled model (GFDL CM2.1), Delworth and Zeng (2012) found that the AMOC variability at low frequencies is linked to a century-scale (approximately 100–150 years) propagation of salinity anomalies from the Southern Ocean to the subpolar North Atlantic (Figure 2.6). The upper-ocean

positive salinity anomalies propagate northward in the Atlantic, and resultant intensified convection in the North Atlantic leads to a positive salinity anomaly at depth, which then propagates southward. Transport variations in the upper and deeper layers (2500m) in the Atlantic Ocean are in the opposite directions. This slow propagation appears to set the time scale of the low-frequency AMOC variations. Park and Latif (2008) pointed out that in the KCM, the important freshwater anomalies originating in the Southern Ocean are linked to the sea ice extent changes.

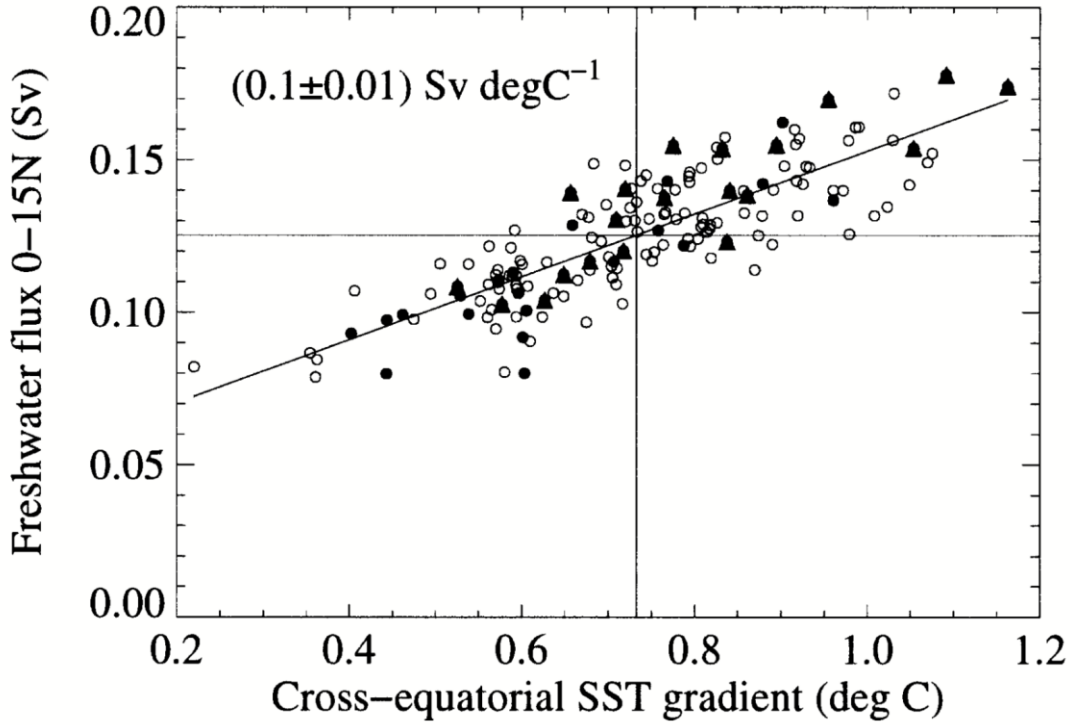

Figure 2.7. Net surface freshwater flux into the tropical North Atlantic (between 0° and 15°N) versus cross-equatorial Atlantic SST gradient (0°– 15°N minus 0°–15°S) in the HadCM3 model. Solid triangles (circles) denote decades lagging (preceding) the 20 decades with the strongest (weakest) AMOC by 60 yr. Reprinted from Vellinga and Wu (2004).

Using the Hadley Centre Coupled Model (HadCM3) simulations, Vellinga and Wu (2004) showed that the salinity anomalies are transported from the subtropical North Atlantic to the subpolar Atlantic. In a strong phase of the AMOC oscillation, the increased northward OMET leads to a cross-equatorial SST gradient. This temperature gradient causes an intensification and a northward displacement of the ITCZ. The anomalous ITCZ results in extra precipitation and hence imposes a positive freshwater anomaly in the tropical North Atlantic (Figure 2.7). In five to six decades, these substantial freshwater anomalies are advected toward the subpolar Atlantic.

However, some studies argue that the variations come from the Arctic. Jungclaus et al. (2005) suggested that the anomalous export of freshwater from the Arctic center and anomalous

circulations in the Nordic Seas are responsible for the 70–80-year variability in the Max-Planck-Institute for Meteorology global atmosphere-ocean–sea ice model (MPI coupled model). The anomalous northward heat transport associated with a strong AMOC leads to a warming in the subpolar North Atlantic and the Greenland Sea. A relatively light water pool forms and is associated with anticyclonic circulation anomalies in the Norwegian and Greenland Seas (not in the Iceland Sea). The anomalous northward East Greenland Current inhibits the freshwater export from the Arctic so that the freshwater anomaly accumulates in the central Arctic for a relatively long period. Eventually, this freshwater anomaly from the Arctic overwhelms the northward abnormal East Greenland Current and is released through the Fram Strait, propagating southward toward the Labrador Sea and decreasing the convection. In addition to the salinity, the temperature changes contribute to the overall oscillation cycle, with positive temperature anomalies in the subpolar North Atlantic propagating westward into the Labrador Sea and initiating the decay of convection. The mechanism suggesting the importance of the freshwater exchanges between the Arctic and North Atlantic regions is also proposed in other studies (Hawkins and Sutton, 2007; Jahn and Holland, 2013; Pardaens et al., 2008).

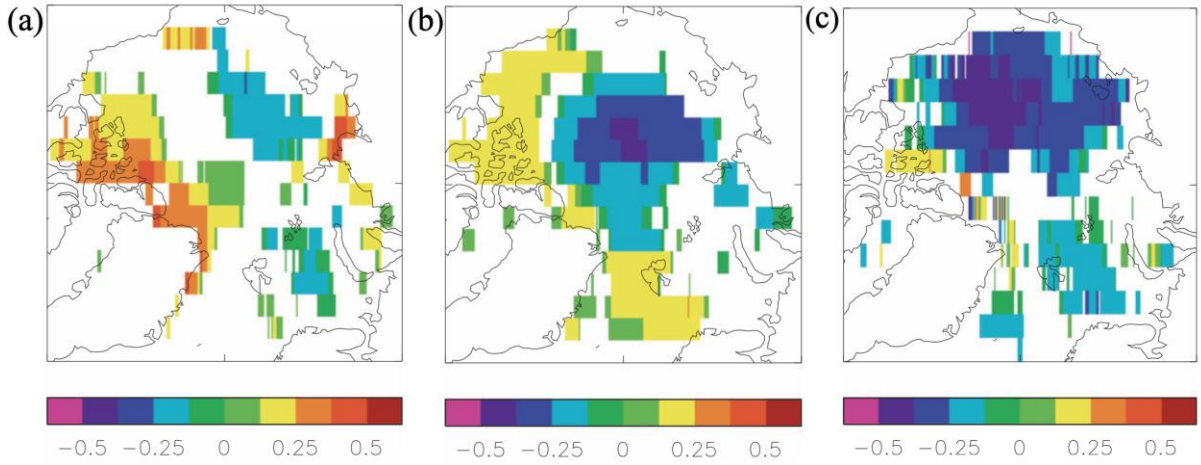

Figure 2.8. Simultaneous correlations of (a) upper layer (averaged from the surface to a depth of 535 m) salinity, (b) rate of change of upper layer saliniy, and (c) wind stress curl, with a Beaufort gyre SLP index (average of 70°–90°N, 90°–270°E). All fields are from the HadCM3 model. Only regions that are considered significant are shaded. Reprinted from Jackson and Vellinga (2013).

With an ensemble of perturbed physics based on HadCM3, Jackson and Vellinga (2013) proposed that the salinity anomalies in the deep convection sites originate in the tropical North Atlantic and the Arctic Ocean. The mechanism involved with tropical salinity anomalies is described in Vellinga and Wu (2004). The Arctic salinity anomaly is suggested to be driven by the stochastic atmospheric forcing. When there is a high SLP anomaly over the Arctic basin, the associated anticyclonic wind stress leads to downwelling in the basin's center and upwelling at the coasts (Figure 2.8c). This results in a freshening in the middle of the gyre, and salinization at the

coasts, as surface water is colder and fresher than the subsurface (Fig. 2.8b). Therefore, the positive salinity anomalies at the coast, particularly in the north of Greenland, are further salinized, as shown by the positive rate of change of the salinity (Figure 2.8b). Thus, the SLP plays a role in the salinity anomaly in the Arctic, which is important to AMOC variations in the HadCM3.

The precise mechanisms driving the AMOC variability on the decadal to multi-centennial scale remain open questions. We have presented that at multidecadal (longer than 50 yr) to multi-centennial timescales, the propagation of salinity anomalies might dominate the AMOC variability. The impact of NAO on AMOC variability mostly occurs on the decadal time scale. However, the relatively low-frequency variability of AMOC does not necessarily relate to the atmospheric forcing or oceanic salinity anomalies. Many model studies also suggest that the AMOC variability at decadal to bi-decadal timescales arises from variations in the subpolar North Atlantic through westward propagation of subsurface temperature anomalies in the North Atlantic (Escudier et al., 2013; Gastineau et al., 2018; Ortega et al., 2015; Sévellec and Fedorov, 2013). Muir and Fedorov (2017) examined this mode with 25 CMIP5 (Coupled Model Intercomparison Project Phase 5) models and found this westward propgation of temperature anomalies in more than half of the models.

The AMOC variability presented above plays an important role in climate not only over the North Atlantic and surrounding landmass but also globally, mainly because of the associated basin-scale heat and salt transport. Next, we introduce its impacts on climate.

2.4 What does the AMOC variability drive?

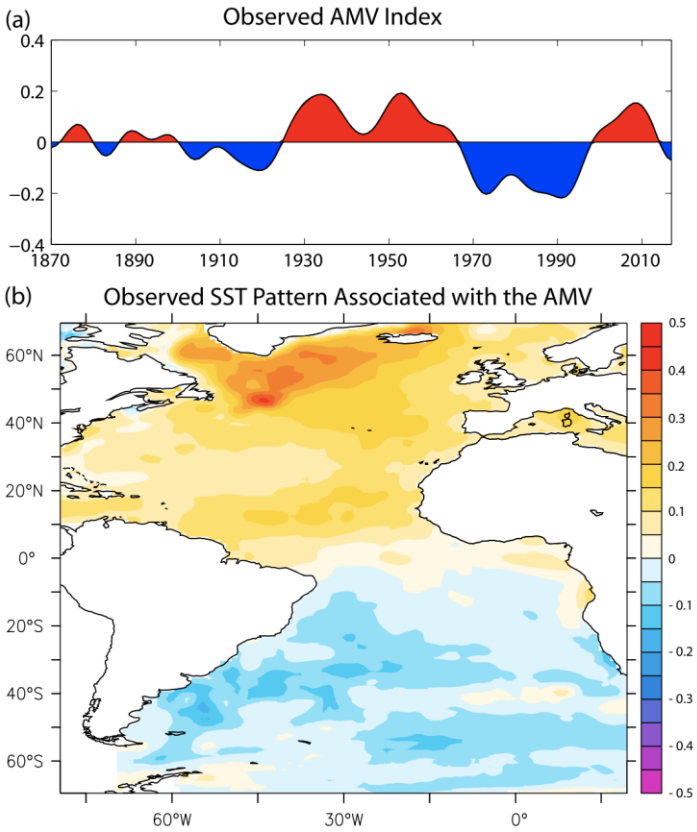

Figure 2.9. Observed AMV index and SST pattern associated with AMV derived from Hadley Centre Sea Ice and Sea Surface Temperature (HadISST) data set. (a) Observed AMV index, defined as the 10-year low-pass-filtered area-weighted average of SST anomalies over the North Atlantic (80°W to 0°E, 0–65°N). The effect of global warming was first removed using a regression of the SST at each grid point on the global mean SST. (b) Observed SST pattern associated with AMV computed as regression of SST anomalies on the AMV index shown in (a). Reprinted from Zhang et al. (2019).

The influence of AMOC variability on climate occurs on a range of timescales with significant societal and economic implications. On interannual to decadal timescales, the AMOC fluctuations in the subtropical Atlantic likely influence the coastal sea level off North America (Little et al., 2017). On the multidecadal scale, numerous studies have suggested that the AMOC variability is often linked to the pattern of SST changes, known as the Atlantic Multidecadal Variability (AMV), with a range of climate implications (e.g., Buckley and Marshall, 2016; Muir and Fedorov, 2015; Zhang et al., 2019). The AMV is defined as averaged SST in the North Atlantic sector, lowpass filtered using a cutoff period typically of 10-yr. The pattern associated with the AMV is basin-wide SST anomalies in the North Atlantic, with a maximum over the subpolar region (Figure 2.9b; e.g., Danabasoglu et al., 2016; Zhang, 2008). AMV is previously known as the Atlantic multidecadal oscillation (AMO; Kerr, 2000), but recently the term “AMV” has been preferred in

the community as the observed SST anomalies do not oscillate at a single frequency but consist of a broader band of low-frequency signals (Sutton et al., 2018; Zhang, 2017).

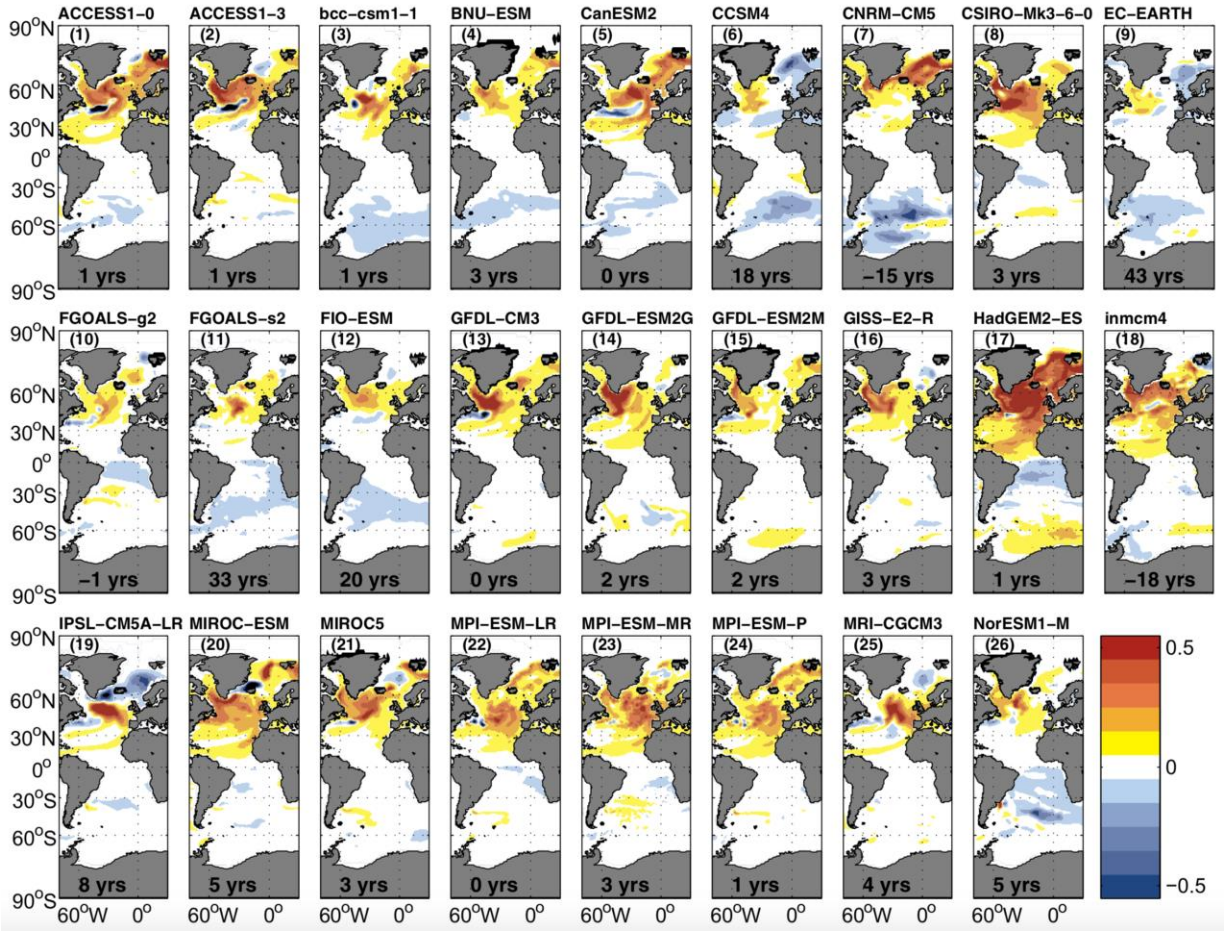

Figure 2.10. SST anomalies (in °C Sv^{-1}) associated with AMOC in 26 climate models. SST is regressed onto the AMOC index (evaluated at 30°N) at the lag corresponding to the maximum correlation between the AMOC and the Atlantic Dipole index (the best lag). The Atlantic Dipole index refers to the SST difference between the Northern Hemisphere Atlantic (60°W-10°W, 40°N-60°N) and Southern Hemisphere Atlantic (50°W-0°E, 60°S-40°S) by subtracting the latter from the former. Numbers at the top of the panels indicate the model number. Numbers at the bottom indicate the lag (in years) of the SST Index with respect to AMOC variations. Reprinted from Muir and Fedorov (2015).

The instrumental observations of AMV reveal a possible dominant variability of about 50-70 yr, while more sampling is needed to better quantify the periodicity (Figure 2.9a). Although the direct instrumental observations of the AMOC only started in 2004 (see Chapter 2.1), reconstructed historical AMOC multidecadal variability using tropical North Atlantic subsurface temperature anomaly shows close connections with the observed AMV signal (Zhang, 2007; Zhang et al., 2019). These connections are usually explained through the heat and salt transported by the AMOC in the upper North Atlantic Ocean.

Figure 2.10 illustrates the regression of SST onto the AMOC index at the lag corresponding to the maximum correlation between the AMOC and the Atlantic SST index in 25 CMIP5 models. A warming pattern in the North Atlantic, with the largest anomalies occurring between 40°N and 60°N, is shown in all models. Models No. 2, 6, 9, 19, 21, and 25 also present a cooling in the Nordic Seas. Given the multi-model average, SST changes of about 0.3 °C per 1 Sv of AMOC anomaly (Muir and Fedorov, 2015).

On the other hand, comparing North Atlantic SST anomaly patterns in AOGCMs versus that in slab ocean models, Clement et al. (2015) proposed that SST changes associated with the AMV are a direct red noise response to stochastic atmosphere-induced surface heat flux forcing. Nevertheless, this view is disputed by Zhang et al. (2016), where the anomalous OMET convergence is the main driver, and the air-sea heat flux variations on a multidecadal scale do not drive the AMV but damp the effect of the convergence over the North Atlantic subpolar gyre. This negative correlation is consistent with observations (Gulev et al., 2013) and many other recent model studies (Drews and Greatbatch, 2016; O'Reilly et al., 2016). In the following subsection, we illustrate the climate response to low-frequency (multidecadal to multi-centennial) AMOC variability in terms of the regions.

2.4.1 The Atlantic Ocean

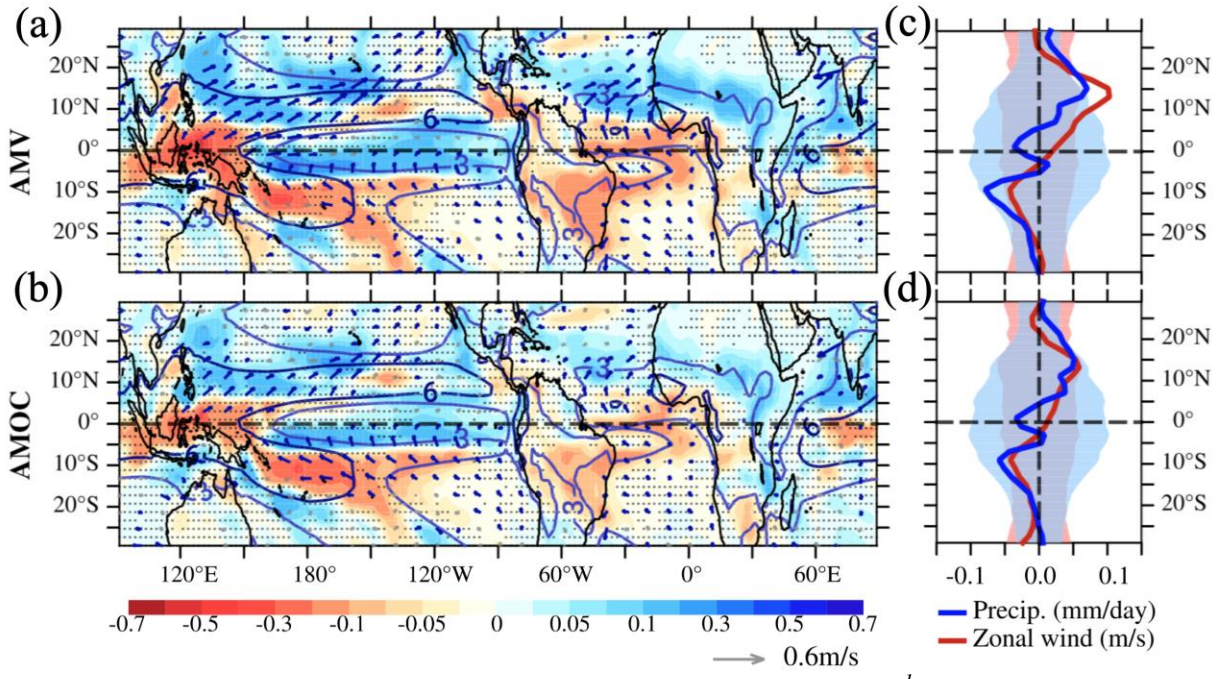

Figure 2.11. Anomalous annual mean precipitation (shading; mm day^{-1}) and wind arrows (m s^{-1}) anomalies at 1000 hPa between years above and below one standard deviation in the 10-year smoothed time series of (a) the AMV and (b) the AMOC, in GFDL CM2.1 climate model. Contours indicate climatological precipitation. Stippling masks statistically non-significant anomalies in precipitation at the 5% level, whereas blue arrows highlight statistically significant anomalies. (c) and (d) are the zonally averaged anomalies in precipitation (blue) and wind (red) in (a) and (b). Blue and red shading, respectively, mask anomalies in precipitation and zonal wind that are nonsignificant at the 5% level. Reprinted from Moreno-Chamarro et al. (2019).

Moreno-Chamarro et al. (2019) computed the precipitation and surface wind anomalies between years above and below one standard deviation in the 11-yr running mean smoothed AMV and AMOC indices with the GFDL model. Overall, a strong AMOC and a positive AMV result in more precipitation in the Northern Hemisphere and less in the tropical Southern Hemisphere in the tropics (Figures 2.11c and d), associated with a northward shift of the ITCZ. The increasing rainfall mostly occurs in the tropical North Atlantic and North Pacific, and the Sahel. Negative precipitation anomalies take place in the tropical South Pacific and Brazil and the equatorial Atlantic (Figures 2.11a and b). Based on the Bjerknes compensation, the northward OMET anomaly induced by a stronger AMOC and resulting in a positive AMV needs to be balanced by an anomalous southward AMET. As introduced in Chapter 1.3, in the tropical and subtropical regions, the AMET is primarily due to the geopotential transport in the upper branch of the Hadley circulation. Therefore, an intensified AMOC leads to a southward transport of the upper branch of the Hadley cell, while the transport of moisture is northward in the lower branch. The increased northward moisture transport can be seen with the strengthening (weakening) trade winds in the Southern (Northern) Hemisphere (Figure 2.11). These changes displace the ITCZ northward.

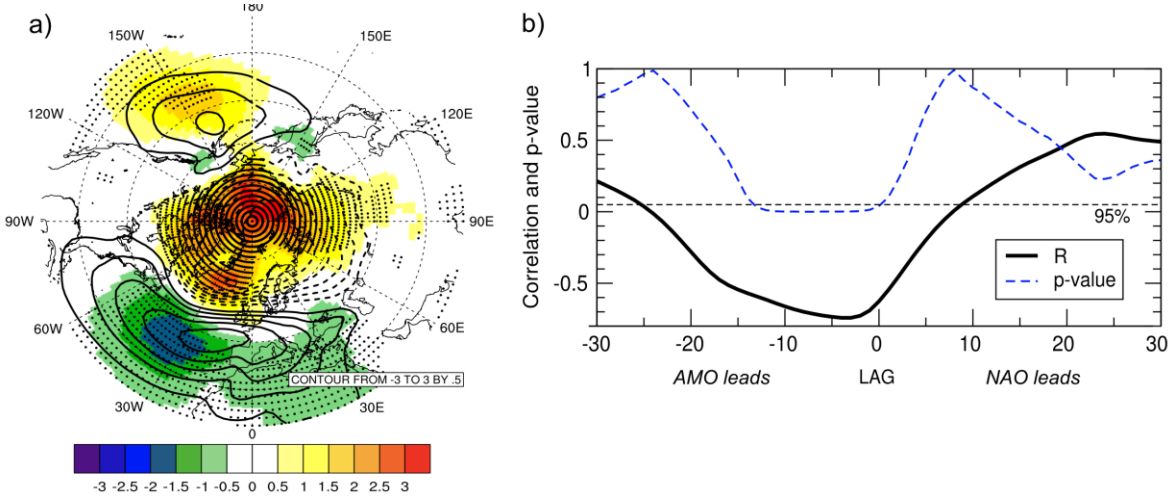

Figure 2.12. Relationship between the AMV and the winter NAO. (a) DJFM (December, January, February, and March) SLP anomalies associated with the AMO signal (positive AMV phase minus negative AMV phase) in the 20th-century reanalysis data (20CR) over 1901–2010 (shading in hPa). Contours indicate the first empirical orthogonal function of the SLP north of 20°N using the 20CR SLP data (in hPa). Anomalies significant at the 95% confidence level are stippled. (b) Lead–lag correlations (black curve) between the DJFM AMO and the DJFM decadal NAO indices over 1901–2010. Blue and black dashed lines indicate statistical significance of the correlation and 95% confidence level, respectively. Winter AMV index is constructed over 1870- 2012 period using Hadley Centre Sea Ice and Sea Surface Temperature data set. Reprinted from Peings and Magnusdottir (2014).

An intensified AMOC may also induce negative NAO-like SLP anomalies in winter over the North Atlantic region on the multidecadal scale, with dipolar pressure anomalies weakening the subtropical high and the subpolar low (Gastineau and Frankignoul, 2012). This relationship is consistent with that found between the AMV and the SLP, as shown in Figure 2.12a. The correlation between the AMV and NAO is negative, and the minimum occurs when the AMV leads the NAO by a decade (Figure 2.12b). A negative NAO following the positive AMV on the multidecadal scale has been found in many studies (e.g., Frankignoul et al., 2015; Gastineau et al., 2013; Msadek et al., 2011). Gastineau et al. (2016) showed the winter NAO response to the AMV with AGCM (Atmospheric general circulation model) simulations forced by the prescribed AMOC-SST signature obtained from AOGCMs, consistent with observational/reanalysis data analysis (Gastineau and Frankignoul, 2015; Peings andMagnusdottir, 2014). Even though both the observations and model simulations exhibit a statistical relationship between the AMV and the decadal fluctuations of the atmospheric circulation (NAO), the underlying mechanism remains an open question. One possible explanation is that an intensification of the AMOC and associated warm AMV-like SST anomalies leads to an enhanced heat loss over the subpolar North Atlantic. The lower tropospheric baroclinicity over the SST gradient anomalies shifts northward, resulting in fewer eddy activities in the North Atlantic storm track and weakened westerly, and thus a negative wintertime NAO phase (Figure 2.13b). A warm AMV also increases the upward

propagation of planetary waves, leading to the weakening of the stratospheric polar vortex and warming in the high-latitude stratosphere, which in turn propagates downward to the troposphere and enhances the negative NAO response in winter (Gastineau et al., 2016; Omrani et al., 2014).

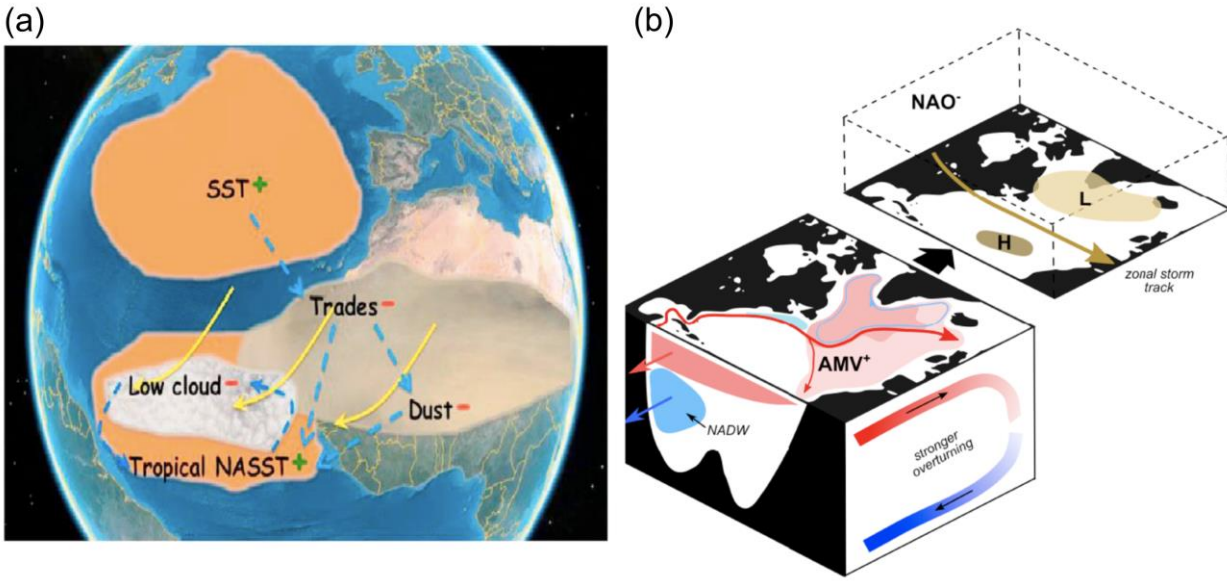

Figure 2.13. Schematic diagrams of impacts of the positive AMV-like SST anomalies induced by a strong AMOC. Reprinted from Zhang et al. (2019).

The NAO associated with the AMV and AMOC likely modulates the pathway of the Atlantic storm track and the probability of blocking events, largely regulating the temperature and precipitation patterns over Western Europe and the Eastern United States. Atmospheric blocking is a quasi-stationary high-pressure system involving the isolation of large regions of air from the westerly circulation for 5 days or more. Blocking events are known for their contribution to the extremely cold winter temperatures in Europe (Sillmann et al., 2011). Häkkinen et al. (2011) suggested that increased Greenland and western Europe blockings occur when the North Atlantic is in a warm state. The wind stress and heat flux associated with blockings, in turn, sustains the warm AMV. It is hard to separate cause and effect between increased blocking activity and the warm Atlantic surface. Such a relationship between blocking and AMV or NAO is also shown in other studies (Davini et al., 2015; Woollings et al., 2008, 2010; Yao and Luo, 2015). Rimbu et al. (2014) found that the correlation between the blocking and the AMV peaks when the AMV leads by 5-10 years. But in general, the causality remains an open question.

In addition, as the meridional temperature gradient decreases, the Atlantic jet stream formed by the thermal wind relation is weakened and presents a more west-to-east orientation. The reduced temperature and pressure gradients also result in fewer and weaker winter storms through this more west-east pathway, leading to reduced storminess, less precipitation, and lower temperatures in northern Europe. In contrast, southern Europe experiences increased storminess, more

precipitation, and warmer temperatures. In eastern North America, the negative phase of NAO generally brings lower air pressure, a condition associated with stronger cold-air outbreaks and increased storminess.

Some studies pointed out a southward propagation of the AMOC-induced AMV SST signal from the subpolar to the tropical North Atlantic (Smirnov and Vimont, 2012; Yuan et al., 2016). The warm ocean surface in the mid-latitude induces a cyclonic circulation over lower latitudes and weakens the trade winds (Figures 2.11a and b). The dust emission over the Sahara reduces, and the transport of dust from the Sahara to the tropical Atlantic weakens. Therefore, the low cloud cover over the tropical North Atlantic decreases, likely leading to the increase in the tropical North Atlantic SST (Figure 2.13a; Yuan et al., 2016).

2.4.2 The Arctic

Observations reveal a significant multidecadal variability of the surface air temperature (SAT) over the Greenland ice sheet correlated with the observed AMV index (Drinkwater et al., 2014). The mass loss from the Greenland ice sheet quadrupled from 1992 to 200l. This change was partly attributed to the warming in the subpolar gyre consistent with multidecadal ocean variability and partly attributed to a long-term increase in the North Atlantic's upper ocean heat content since the 1950s (Straneo and Heimbach, 2013). On the multidecadal scale, sea ice extent and the duration of the iceberg season fluctuations off the Eastern Newfoundland are associated with a combination of the NAO and the AMV signals. Positive ice anomalies lag the negative AMV by several years (Peterson et al., 2015).

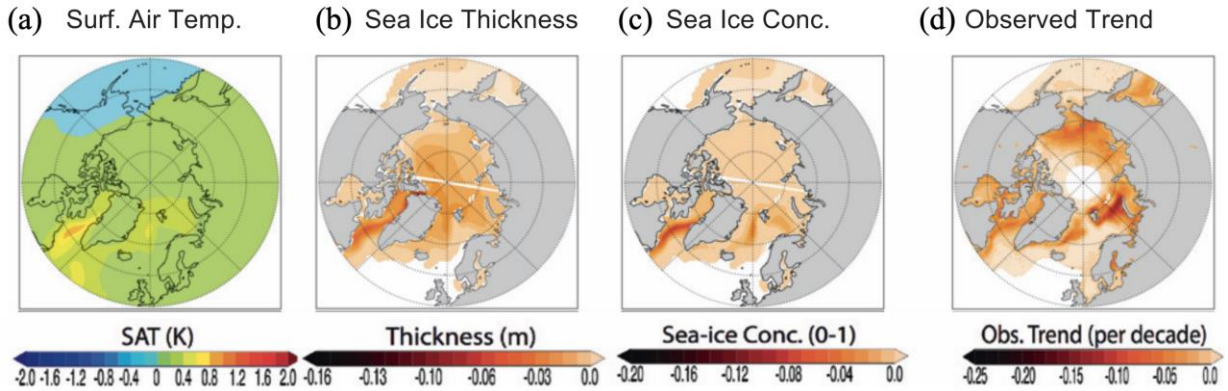

Figure 2.14. Regression of 10-year lowpass filtered (a) Arctic surface air temperature, (b) sea ice thickness, and (c) concentration on standardized lowpass filtered AMOC index. (d) Linear trend (per decade) of satellite-observed Arctic sea ice concentration from 1979–2008 derived from National Snow and Ice Data Center. Data in (a)-(c) is from GFDL CM2.1 model. Reprinted from Mahajan et al. (2011).

The AMOC variability and AMV are also associated with the Arctic SAT and sea ice variations on the multidecadal time scale (Figure 2.14; Mahajan et al., 2011). Figures 2.14b and c show simulated winter Arctic sea ice decline induced by an intensification of the AMOC in a climate model simulation. The pattern obtained resembles the observed winter Arctic sea ice decline over the past decades (Figure 2.14d), suggesting that the intensified AMOC has contributed to the observed decline in winter Arctic sea ice. This anticorrelation between the Arctic sea ice and the AMOC on a multidecadal timescale is also found in other model studies (Day et al., 2012; R. Zhang, 2015).

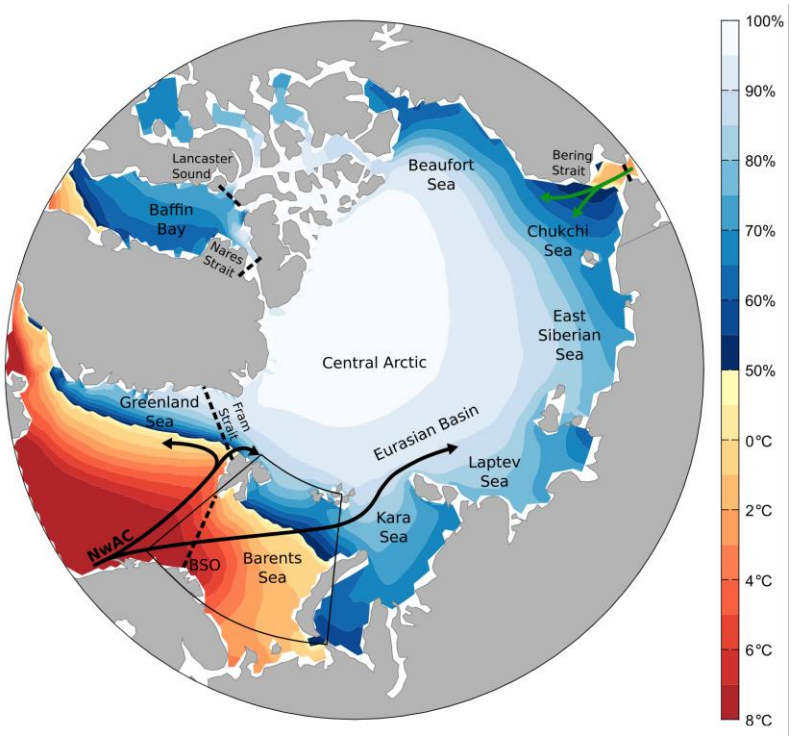

Figure 2.15. The Arctic Ocean and its marginal seas. Shading shows annual mean sea ice concentration and sea surface temperature in Community Earth System Model (CESM) model from 2010 to 2019. The black arrows show the main pathways of Atlantic water toward the Arctic Ocean. The black dashed lines indicate two main sections through which the Atlantic Water enters the Arctic Ocean. BSO denotes Barents Sea Opening and NwAC stands for Norwegian Atlantic Current. Reprinted from Årthun et al. (2019).

The warm Atlantic water enters the Arctic Ocean mainly through the Fram Strait and the Barents Sea Opening (Figure 2.15). With the GFDL model, Zhang (2015) found that at the multidecadal timescale, the AMOC and associated heat transport entering the Arctic Ocean lead the Atlantic inflow temperature by several years and anticorrelates with Arctic summer sea ice extent (Zhang, 2015). Using five CMIP3 models, Day et al. (2012) suggested that the anticorrelations between AMV/AMOC and the Arctic sea ice extent occur in both summer and

winter and are stronger in winter than in summer. Delworth et al. (2016) further attributed this correlation to the changes in the AMOC heat transport driven by the NAO.

In addition to oceanic processes, atmospheric teleconnections driven by the SST anomalies associated with AMV lead to adjustments in atmospheric circulation patterns, driving the low-frequency Arctic sea ice variations through both dynamic and thermodynamic effects, even without any influence of OMET changes (Castruccio et al., 2019). The weakening of the Beaufort Sea high and the increased prevalence of an Arctic dipole–like SLP pattern in late winter/early spring lead to anomalous winds that drive anomalous ice motions (dynamic effect). Warmer surface temperatures resulting from increased low cloud cover reduce winter sea ice formation (thermodynamic effect). The combined effects lead to thinner and more vulnerable sea ice in the Arctic. These atmospheric teleconnections that occur after a phase shift to positive AMV may produce a decadal Arctic sea ice thinning on the order of 8% to 16% of the reconstructed long-term trend and a decadal decline in September Arctic sea ice extent of up to 21% of the observed long-term trend (Castruccio et al., 2019). Lastly, the multidecadal variations in the Antarctic SAT are anticorrelated with the SAT fluctuations in the Arctic. The low-frequency AMOC variability and associated AMV are invoked as a key player in the bipolar seesaw, i.e., antiphase changes in Arctic and Antarctic climates, through the AMOC-related OMET variations (Chylek et al., 2010; Skinner et al., 2007).

2.4.3 The Pacific Ocean

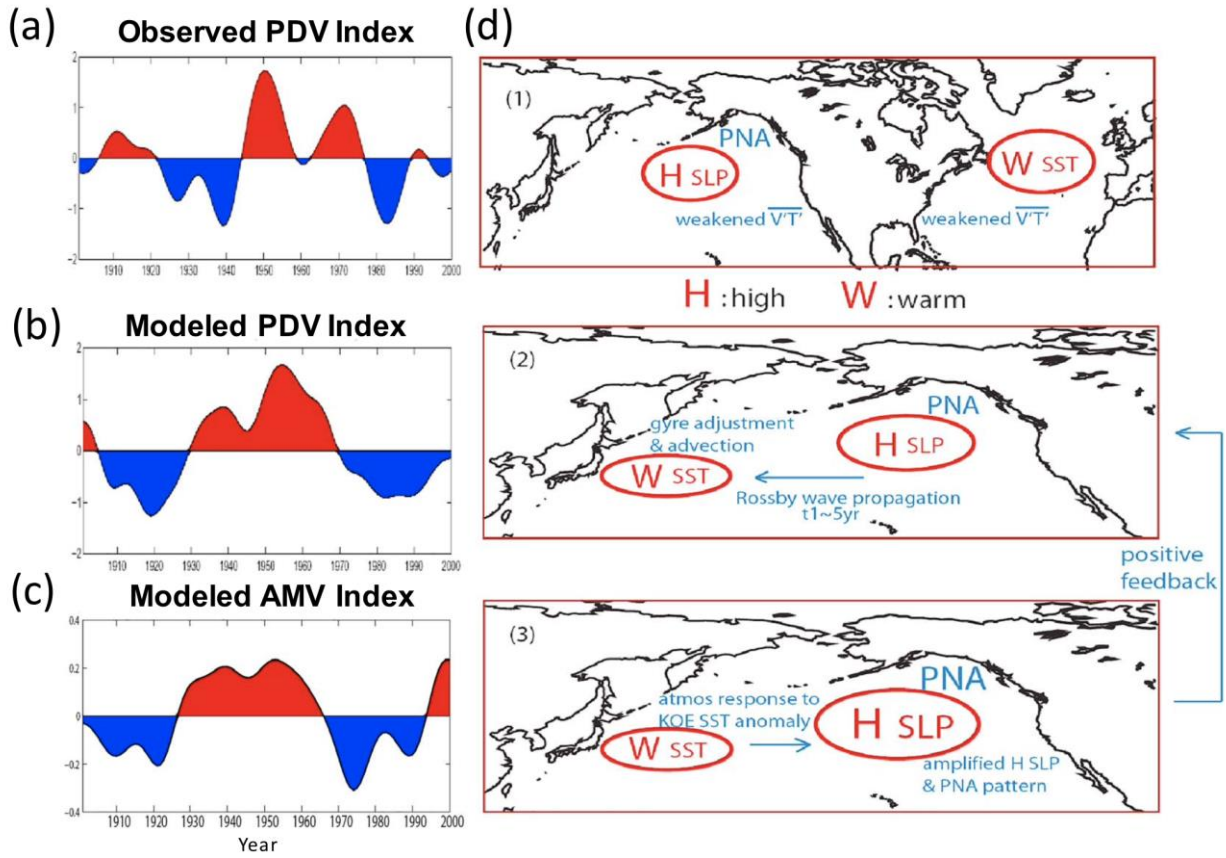

Figure 2.16. (a) Observed 20th century PDV index derived from HadISSST data set. (b) Modeled (GFDL CM2.1) PDV index in response to the prescribed AMV-like forcing. PDV indices in (a, b) are 10-year low-pass filtered. (c) Modeled (GFDL CM2.1) AMV index induced by the prescribed AMV-like forcing. (d) Schematic diagram of the interactions between the PDV and AMV. H stands for "high" and W indicates "warm". Reprinted from Zhang et al. (2019).

Many observational and model studies suggest a teleconnection between the AMV and the climate variations in the Pacific. The Pacific Decadal Oscillation (PDO) or Pacific Decadal Variability (PDV) is the leading mode of SST variability in the North Pacific. The PDV and Interdecadal Pacific Oscillation (IPO) are sometimes described as a long-lived El Niño-like pattern of Pacific climate variability. The PDV refers to the SST anomalies in the Northern Hemisphere, while the IPO rather designates the Pacific-wide pattern. The positive (or warm) phase of PDV corresponds to horseshoe-shaped warm anomalies along the west coast of North America and into the tropical Pacific, concurrent with an anomalous cooling in the interior North Pacific. A warm PDV is accompanied by lower SLP over the North Pacific, reinforcing the Aleutian low. Analyses using observational data indicate the multidecadal component of PDV is strongly correlated with the AMV, following the AMV by approximately 13 years or preceding the AMV by 17 years (d'Orgeville and Peltier, 2007). AOGCM simulations with prescribed AMV-related surface heat flux anomalies induced by the AMOC variations also suggested that the AMV contributes to the multidecadal component of PDV and the associated Pacific/North America (PNA) pattern (Zhang

and Delworth, 2007), which is defined by opposite mid-troposphere height anomalies over the Aleutian low and northwestern Canada. The AMV leads the PDV by several years (Figures 2.16 a-c).

The mechanism of Zhang and Delworth (2007) relies on the impacts of the AMV on the storm tracks over the Pacific and Atlantic Oceans. During a strong AMOC/positive AMC, the enhanced Atlantic OMET reduces the northward atmospheric eddy energy transport and mid-latitude storms in the Northern Hemisphere (see Chapter 2.4.1). The weakening of the mid-latitude winter storm track results in a poleward shift of the westerly wind, and thus a weekend Aleutian Low and associated positive PNA pattern (Figure 2.16 d1). The associated negative wind stress curl leads to a warming over the western North Pacific through the westward oceanic Rossby wave propagation (Figure 2.16 d2). The atmospheric response to the warm western North Pacific amplifies the weakening of the Aleutian Low and PNA pattern over the North Pacific (Figure 2.16 d3). Therefore, the AMV contributes to the multidecadal variability in the North Pacific via atmospheric teleconnections, which are enhanced by the ocean dynamics and coupled air-sea interactions in the North Pacific.

Some studies also find the impacts on the Pacific Ocean through a tropical pathway. The positive AMV drives a northward shift of the ITCZ, and associated rainfall anomalies leads to a reorganization of the Walker circulation through diabatic heating. The perturbed Walker circulation, with an anomalous rising branch over the North Atlantic and descending motion over the central tropical Pacific, can trigger a stationary Rossby wave pattern extending northward into the extratropics. The stationary wave increases subsidence over the northeastern Pacific by the abnormal advections of vorticity and temperature. The enhanced descending motion leads to the weakened Aleutian low and the intensified subtropical high over the eastern North Pacific (Lyu et al., 2017).

The model simulations also indicate that the AMV regulates the tropical Pacific variability to some extent. The positive AMV leads to La Niña-like cooling over the eastern tropical Pacific through stronger trade winds and a reorganization of the Walker circulation (Polo et al., 2015; Ruprich-Robert et al., 2017), which further results in stronger vertical wind shear and reduced tropical cyclone frequency over the western North Pacific (Zhang et al., 2018), and a northward displacement of the Pacific ITCZ (Levine et al., 2018; Ruprich-Robert et al., 2017). Moreover, the AMV can modulate the amplitude of the El Niño– Southern Oscillation (ENSO) variability on multidecadal timescales (Levine et al., 2017; Ruprich-Robert et al., 2017). A warm AMV damps the ENSO variations through the background cooling over the central equatorial Pacific (Kang et al., 2014). The weakening of the Aleutian low and the strengthening of the subtropical high over the eastern North Pacific associated with the positive AMV extend to the central equatorial Pacific through the wind-evaporation-SST feedback and strengthen the trade wind over the central

equatorial Pacific (Yu et al., 2015). This leads to a more frequent occurrence of the central Pacific type of El Niño events characterized by a westward shift of the warm SST anomaly from the eastern Pacific to the central Pacific. Therefore, the positive AMV phase may contribute to the observed shift of El Niño events to the central Pacific type in recent decades (Yu et al., 2015).

In some AOGCM experiments, the response to the AMV exist in both the tropical and North Pacific, i.e., anomalous SST over the central tropical Pacific and the PNA pattern in the mid-troposphere over the North Pacific. The North Pacific response may be amplified by the tropical Pacific response through the Rossby wave propagation into the North Pacific (Ruprich-Robert et al., 2017). The relative contribution of the two different pathways (the tropical and the extratropical paths) for the North Atlantic and North Pacific teleconnection likely depends on the different models and the detailed structure of the Atlantic forcing used in various experiments.

In summary, the AMOC multidecadal variability has a profound impact on global and regional climate. Its impact is primarily realized by the heat transport and associated AMV-like SST anomalies, regardless of whether the AMOC/ocean circulation is the major driver of the AMV.

2.5 Summary

We have introduced the inadequate ocean observations (Chapter 2.1), the mechanisms of the AMOC low-frequency variability (Chapter 2.3) and associated impacts on climate (Chapter 2.4). Climate models are one of the main tools to investigate the variabilities and impacts especially on long time scales. However, mechanisms vary in different models. CMIP provides a framework for comparison among models performing common sets of experiments. Advances in numerical modelling enables better representation of various oceanic and atmospheric fields and better understanding of the mechanism driving their variations. In the following chapter, we will investigate the AMOC variability in a AOGCM called IPSL-CM6A-LR that participates the latest CMIP phase 6. Then, in Chapter 4, the impacts of the AMOC variability studied in Chapter 3 on climate will be explored with dedicated sensitivity experiments in the same model.

Chapter 3

Contents

3 CENTENNIAL VARIABILITY OF THE AMOC IN COUPLED IPSL MODEL 49

3.1 INTRODUCTION 49
3.2 IPSL-CM6A-LR MODEL 49
3.3 ARTICLE 51
3.4 CONCLUSION AND DISCUSSIONS 77
3.5 SIMPLIFIED MODEL FOR THE FRESHWATER RECHARGE MECHANISM 78

3 Centennial variability of the AMOC in coupled IPSL model

3.1 Introduction

As presented in previous chapters, the AMOC is a key player in the climate system and exhibits variations on different time scales ranging from seasonal to multi-centennial. In this context, I have been involved in investigating the low-resolution CMIP6 version of the IPSL model. This IPSL-CM6A-LR model was under development as I started my PhD. Boucher et al. (2020) presented the emergent properties of this climate model and pointed out a low-frequency variability of the AMOC with a period of around 200 years in this model. The aim of the first part of my PhD then was to explore the underlying mechanism of this low-frequency fluctuation. The following section will present this model in more detail.

3.2 IPSL-CM6A-LR model

The IPSL (Institut Pierre Simon Laplace) model participates in the CMIP6 (Eyring et al., 2016), which provides a framework for comparison among models performing common sets of experiments. In this thesis, we use the low resolution (LR) of the coupled ocean-atmosphere model, as the development of versions using higher resolutions was not finished at the start of the PhD. The IPSL-CM6A-LR consists of the atmospheric model LMDZ (Laboratoire de Météorologie Dynamique; Z standing for Zoom) version 6A-LR (Hourdin et al., 2020), the ocean component

NEMO (Nucleus for European Models of the Ocean) version 3.6 and the ORCHIDEE land surface model Version 2.0 (Cheruy et al., 2020).

The LMDZ model has 144 points in longitude and 142 in latitude with a corresponding resolution of $2.5° \times 1.3°$. The number of vertical levels is 79, and the upper boundary is 80 km in height. Thus, it is a "high-top" model that has a well-resolved stratosphere compared to the "low-top" models with a lower top boundary and a fairly coarse vertical resolution in the stratosphere. The ocean model NEMO consists of three sub-modules, i.e., the ocean physics NEMO-OPA, the sea ice dynamics and thermodynamics NEMO-LIM3, and the ocean biogeochemistry NEMO-PISCES. NEMO model is based on the eORCA1 grid, the quasi-isotropic global tripolar grid with a 1° nominal resolution. The coupling between the ocean and the atmosphere models is performed with the OASIS3-MCT coupler.

Compared to the CMIP5 version named CM5A, IPSL-CM6A-LR includes many improvements and simulates more realistic ocean physics. Boucher et al. (2020) evaluated and presented the performance of IPSL-CM6A-LR. We show here three main advances related to our work.

- Structure of the AMOC: all versions of IPSL models underestimate the AMOC maximum at 26°N compared to the RAPID array observations, likely due to the biases in the North Atlantic and the representation of the Nordic Seas overflow and the WBCs. The Atlantic meridional streamfunction reverses the sign at around 2800 m in IPSL-CM6A-LR but at 4500 m in observations (see the depth of the zero-isoline in Figure 2.3). Nevertheless, the strength of the deep cell is realistic. The maximum of the upper AMOC cell is around 14 Sv in the IPSL-CM6A-LR and is more realistic than in previous versions. This improvement is closely linked to the changed location of the deep water formation site, as shown by the mixed layer depth. In IPSL-CM6A-LR, large values for the winter depth are located in the Nordic Seas and the Labrador Sea, while CM5A simulates maximum mixed layer depth south of Iceland and in the subpolar gyre. The new location of the deep water formation site is more consistent with the observations.

- Heat transport: both the global and the Atlantic OMET in IPSL-CM6A-LR are closer to the observations than in previous versions. However, a likely unrealistic feature remains in the IPSL-CM6A-LR: a northward global heat transport of ~0.5 PW at 40°S. There are no direct observations at that latitude, but the consensus is that the global OMET is southward in the entire Southern Hemisphere (Trenberth et al., 2019). This discrepancy might result from the excessive mode water formation in the Atlantic Ocean, leading to a strong convergence of heat at 40°S. Although OMET in the Atlantic Ocean is still underestimated at all latitudes, especially in the tropics, the biases are largely reduced in IPSL-CM6A-LR.

This improvement in simulating heat transport might be partly responsible for the alleviation of the SAT bias over Europe and North Africa due to the increase in the amount of heat carried to the high-latitude Atlantic Ocean.

- Multidecadal variability: the AMV in IPSL-CM6A-LR presents a pattern with warm SST anomalies from the subpolar North Atlantic to the subtropical regions comparable to observations. The anomalous SST associated with the AMV in previous versions was restricted to the subpolar region and the eastern Atlantic (model No. 19 in Figure 2.10; Zhang and Wang, 2013). In addition, a relatively clear teleconnection between the AMV and the Pacific is found in IPSL-CM6A-LR, with a negative IPO-like pattern linked to a positive AMV, consistent with observations. This teleconnection is not simulated in previous CM5A models. However, as instrumental observation has been available since 1850, the sampling remains relatively limited to thoroughly investigating the multidecadal relationships, especially for the AMV/IPO connections.

3.3 Article

As pointed out in Boucher et al. (2020), the AMV index seems to oscillate with a period of about 200 years in IPSL-CM6A-LR. This multi-centennial variability is robust but weakens toward the end of the 1200-year pre-industrial control (*piControl*) simulation. The AMOC also exhibits a predominant variability at centennial time scales. To explore the exact origin of this new low-frequency variability emerging in the North Atlantic, statistical analyses of the 2000-y piControl simulation in coupled IPSL-CM6A-LR model are used to investigate the involved mechanism and also its impact on the climate. The results were published in the Journal of Advances in Modeling Earth System and dedicated to the special collection 'The IPSL Climate Model Used in CMIP6' in 2021 (Jiang et al., 2021).

The primary driving mechanism is that this multicentennial variability is driven by delayed freshwater changes between the Arctic and Atlantic oceans. The increased heat transport associated with an intensified AMOC leads to the warming of the North Atlantic. The lower troposphere in the Northern Hemisphere warms promptly, especially in winter over the Arctic, with an amplitude of 1.5°C near the surface. This fast warming in the atmosphere, in turn, contributes to the sea ice melting over the Arctic, leading to the formation of anomalous freshwater in the surface Arctic Ocean. Positive salinity anomalies around Greenland and weakened East Greenland Current lead the AMOC by around 40 years. The sea ice export through the Fram Strait via East Greenland Current reduces and further contributes to the freshwater anomaly on the Arctic surface. This freshwater anomaly builds up progressively in thermal wind balance with an anomalous anticyclonic circulation that helps maintain it inside the Arctic. Meanwhile, the saltier

Atlantic inflow enters the Arctic through the Barents Ocean Opening and leads to a positive salinity anomaly, opposite to the freshwater anomaly on the surface. The freshwater content in the upper layer (the top 150 m) is almost in phase with the AMOC with a short lag. The surface freshwater anomalies in the Arctic extend for four to five decades until they reach the Lincoln Sea north of Greenland. Then, the salinity anomalies around Greenland change the sign to become negative when lagging the AMOC by 30-40 years. Eventually, the anomalous freshwater propagates to the Nordic and Labrador Seas, inhibiting the deep convection and weakening the AMOC. The oscillation enters the opposite phase.

JAMES | Journal of Advances in Modeling Earth Systems

RESEARCH ARTICLE
10.1029/2020MS002366

Special Section:
The IPSL climate model used in CMIP6**

Multicentennial Variability Driven by Salinity Exchanges Between the Atlantic and the Arctic Ocean in a Coupled Climate Model

Weimin Jiang[1], **Guillaume Gastineau**[1], **and Francis Codron**[1]

[1]UMR LOCEAN, Sorbonne Université/CNRS/IRD/MNHN, Paris, France

Key Points:

- A centennial to multicentennial variability emerges from the North Atlantic and Arctic Ocean in the IPSL-CM6A-LR model
- AMOC oscillations are driven by freshwater build-up and release in the Arctic
- The interplay between sea ice and oceanic freshwater export modulates the salinity anomalies in the Arctic

Supporting Information:

Supporting Information may be found in the online version of this article.

Correspondence to:

W. Jiang,
weimin.jiang@locean.ipsl.fr

Citation:

Jiang, W., Gastineau, G., & Codron, F. (2021). Multicentennial variability driven by salinity exchanges between the Atlantic and the arctic ocean in a coupled climate model. *Journal of Advances in Modeling Earth Systems*, *13*, e2020MS002366. https://doi.org/10.1029/2020MS002366

Received 14 OCT 2020
Accepted 17 FEB 2021

Abstract The IPSL-CM6-LR atmosphere-ocean coupled model exhibits a pronounced multicentennial variability of the Atlantic meridional overturning circulation (AMOC), driven by delayed freshwater accumulation and release in the Arctic. The AMOC fluctuations are preceded by salinity-driven density anomalies in the main deep convection sites in the Labrador and Greenland seas. During a strong AMOC, a combination of reduced sea ice volume and anomalous currents reduces the freshwater export from the Arctic and leads instead to a slow accumulation of freshwater in the central Arctic. Simultaneously, the saltier Atlantic inflow through the Barents Sea results in a positive salinity anomaly in the Eastern Arctic subsurface. When the surface Central Arctic freshwater pool finally reaches the Lincoln Sea, the oceanic currents around Greenland reorganize, leading to the export of the anomalous Arctic freshwater to the North Atlantic, enhancing the stratification in deep convection sites. The AMOC then decreases, positive salinity anomalies appear in the Central Arctic, and the variability switches to the opposite phase. These AMOC and sea ice fluctuations have broader climate impacts, with a strong AMOC leading to a mean warming of about 0.4°C north of 20°N, reaching up to 1°C in the Arctic lower troposphere during winter. In all seasons, a northward displacement of the intertropical convergence zone is also simulated.

Plain Language Summary The North Atlantic Ocean is known to have large climate fluctuations emerging from the different components of the climate system and their interactions. These fluctuations play a crucial role in the North American and European climate or the Arctic sea ice. A proper understanding of such internal variations is key to attribute the observed climate changes to anthropogenic activities or to assess the skill of decadal forecast systems. However, investigations of the long-term basin-scale variations are restrained by the limited instrumental observations. Therefore, an atmosphere-ocean general circulation model is used here to explore the low-frequency variability. This model simulates a large variability in the North Atlantic with a period between 1 century and 1 millennium. We found that this variability owes its existence to the freshwater exchanges between the North Atlantic and Arctic. Such North Atlantic variability has important impacts, as typical positive anomalies of the Atlantic oceanic northward heat transport reduce the sea ice, warm up the whole Northern Hemisphere by 0.4°C, and shift northward the intertropical convergence zone.

1. Introduction

The North Atlantic exhibits a pronounced variability on different timescales, ranging from interannual to multicentennial. A proper understanding of the low-frequency intrinsic variability is essential for detecting the anthropogenic climate change and assessing decadal climate forecast skills (Cassou et al., 2018). Besides, since the scarcity of instrumental measurements hampers research on variations on a multidecadal or longer timescale (Vellinga & Wu, 2004), this knowledge is also important for designing observational networks.

The Atlantic Meridional Overturning Circulation (AMOC) consists of a warm northward near-surface current and a colder southward return flow, extending over the full latitude range. It has a significant influence on climate over the North Atlantic and peripheral land masses due to the associated basin-scale meridional heat transport: a strengthening of the AMOC increases the oceanic northward heat transport and leads to a warming in the North Atlantic, extending into the Arctic (Jackson et al., 2015; Mahajan et al., 2011). The low-frequency fluctuations of the AMOC also have impacts in the Tropics and the Southern Hemi-

sphere: a stronger AMOC and cross-equatorial northward heat transport often lead to a northward shift of the Intertropical convergence zone (ITCZ; Frierson et al., 2013; Vellinga & Wu, 2004) and a cooling of the Southern Hemisphere (Muir & Fedorov, 2015; Stocker, 1998). The AMOC has also been linked in climate models to the multidecadal variability of the basin-wide North Atlantic sea surface temperature (SST; Knight et al., 2005; Roberts et al., 2013), known as the Atlantic multidecadal variability (AMV), although other mechanisms have a large role, such as the atmospheric stochastic forcing (Cane et al., 2017; Clement et al., 2015) or the changes associated to external forcings (Murphy et al., 2017; Qin et al., 2020).

Most previous studies of the North Atlantic climate variability (e.g., Brown et al., 2016; Colfescu & Schneider, 2020; Danabasoglu, 2008; Kerr, 2000; Nigam et al., 2011; Zhang et al., 2017) mainly focused on periods within 10–70 years, in agreement with the variability observed in the instrumental period since 1850. Here, we concentrate instead on the centennial to multicentennial periods. Several paleoproxy records have suggested the existence of a centennial to multicentennial variability in the North Atlantic (Nyberg et al., 2002; Sicre et al., 2008) or in the Northern Hemisphere (Ayache et al., 2018; Laepple & Huybers, 2013; Mann et al., 1995). However, the relative significance of internal variability compared to the external forcing from solar irradiance and volcanic aerosol variations remains unknown.

The potential mechanisms for low-frequency variability in the North Atlantic (multidecadal to multicentennial) remain an open question due to the limited availability of instrumental records. The AMOC observing systems have both short temporal and sparse spatial coverage. Continuous observations of the AMOC conducted by the Rapid Climate Change (RAPID) program only started in 2004 and are confined in the subtropical North Atlantic (Cunningham et al., 2007). Hence, models are needed to explore the low-frequency variability of the AMOC, even if biases in the simulated AMOC and its associated heat transport remain in most general circulation models (GCMs; Xu et al., 2019; Zhang et al., 2019). Variability of the North Atlantic on multidecadal (particularly referring to scale longer than 70 years hereafter) to multicentennial scale is found in a number of models. Delworth and Zeng (2012) found connections between the Southern Ocean and the subpolar North Atlantic through the propagation of salinity anomalies in the GFDL CM2.1. Park and Latif (2008) also emphasized in the KCM model the importance of freshwater anomalies from the Southern Ocean, associated with sea ice cover anomalies. Vellinga and Wu (2004) proposed that the subtropical salinity anomaly generated by the AMOC-driven northward shift of the ITCZ was the source of the AMOC oscillations in the model HadCM3. The freshwater anomaly is advected toward the subpolar Atlantic in five to six decades. On the other hand, some studies argue that the variations come from the Arctic. Jungclaus et al. (2005) suggested that the anomalous export of freshwater from the Arctic center and anomalous circulations in the Nordic Seas were responsible for the 70–80-year variability in the MPI coupled model. A dominant role of freshwater exchanges between the Arctic and North Atlantic regions also appears in other studies (Hawkins & Sutton, 2007; Jahn & Holland, 2013; Pardaens et al., 2008). With an ensemble of perturbed physics based on HadCM3, Jackson and Vellinga (2013) proposed that the salinity anomalies in the deep water formation sites not only originated in the tropical North Atlantic as described previously in Vellinga and Wu (2004), but also originated in the Arctic Ocean, probably driven by the stochastic sea level pressure.

In the present study, we explore the centennial variability emerging in the North Atlantic in the IPSL (Institut Pierre Simon Laplace) atmosphere-ocean model developed for CMIP6 (Coupled Model Intercomparison Project Phase 6, Eyring et al., 2016). Boucher et al. (2020) identified that in the multicentennial preindustrial control simulation of this model, both the AMOC and AMV fluctuate with an approximate period of 200 years. We will show that these oscillations are generated by a slow build-up of freshwater anomalies in the central Arctic when the AMOC is intensified, resulting from reduced sea ice export. This freshwater is eventually flushed into the Nordic Seas and the North Atlantic with a delay of four to five decades, reversing the sign of the AMOC anomalies.

2. Data and Methodology

2.1. Model Description

IPSL-CM6A-LR is the low resolution (LR) version of the IPSL-CM6A model developed by the IPSL for CMIP6. A complete description of this model is provided in Boucher et al. (2020), and we will focus below on the main characteristics relevant to the investigation of the low-frequency climate variability. The

atmospheric component is LMDZ6 and has a resolution of $1.26° \times 2.5°$ and 79 levels in the vertical (up to 1 Pa). The oceanic model NEMO has 75 vertical levels and a nominal resolution of about 1° in the horizontal, refined up to 1 / 3° in the equatorial and polar regions (ORCA1 grid). The sea ice module is LIM3.6 and adopts five sea ice thickness categories. We use the outputs from a 2,000-year preindustrial control simulation performed for CMIP6. This run follows a 100-year spin-up and uses preindustrial land use and atmospheric concentration of greenhouse gases, aerosols, and stratospheric ozone. A cooling drift exists in this simulation, although it remains small at about 0.2 K in 2,000 years. This drift was approximated by a quadratic trend, which was removed from all data before analysis.

2.2. Assessment of the Arctic Ocean in the Model

To evaluate the simulated salinity and temperature fields in the Arctic and the North Atlantic, we use the World Ocean Atlas 2018 (WOA18) data set (Locarnini et al., 2018; Zweng et al., 2018) for comparison. In this study, the regions of interest are the Arctic and the North Atlantic (Figure S1). The Arctic is defined as being enclosed by the Fram, Bering, and Davis straits and the Barents Sea. The location of the four cross sections is given in Figure S1. In the top 200 m, the simulated Arctic temperature has a good agreement with the WOA18 data set (Figure S1d). However, the warm and salty North Atlantic inflow, shown by the ~1°C potential temperature maximum at 400 m in WOA (Figure S1a), is absent in the model. Instead, IPSL-CM6-LR simulates a uniform water mass at ~0.2°C from 300 to 2,000 m, suggesting either an underestimation of the inflow of Atlantic water or an unrealistic mixing of the North Atlantic inflow with the Arctic deeper water. In addition, the salinity in the top 200 m is overestimated in the Arctic, especially in the Eastern Arctic over the shallow continental shelf (Figure S1c), suggesting an underestimated runoff from the Eurasian continent or a bias resulting from the coarse resolution of the steep continental slope. The same diagnostics in the North Atlantic, from 30°N to the Fram Strait and Barents Sea Opening cross section, also show that the simulated upper North Atlantic Deep Water is too cold between 300 and 800 m (Figure S1b). This bias is associated with a relatively weak AMOC in IPSL-CM6A-LR, with a mean Atlantic meridional streamfunction at 30°N of 10.8 Sv (from 6.5 to 15.4 Sv), while the deep oceanic convection is underestimated in the Labrador Sea and overestimated in the Nordic Seas (see Boucher et al., 2020). The model also simulates a cold and fresh bias in the subpolar gyre (Figures S1c and S1d), as the Gulf Stream and North Atlantic current are not well resolved when using a low-oceanic resolution (Flato et al., 2013; Wang et al., 2014).

Figure S2a shows the mean oceanic currents and salinity in the top 150 m. The Atlantic water inflow through the Barents Sea is well simulated in the model, while the intensity of the West Spitzbergen Current in the Eastern Fram Strait is underestimated compared to observations (Aksenov et al., 2011). This may contribute to the bias of the simulated Atlantic water in the Arctic, as discussed above. The fresh Beaufort Gyre located in the Canadian Basin is generally present in IPSL-CM6A-LR, but the associated anticyclonic circulation is not fully developed. Besides, the transpolar drift near 150°E and toward the Fram Strait is shifted west toward the north of the Canadian Archipelago in the Lincoln Sea (Petty et al., 2016; Pnyushkov et al., 2015). This might lead to an overestimation of the current north of Greenland and of the Atlantic inflow penetrating the Beaufort Gyre.

To further explore the origin of the broad positive salinity bias in the Arctic, we quantify the freshwater exchanges between the Arctic and the Atlantic. Freshwater can exit the Arctic in liquid form or as sea ice. The liquid freshwater transport is computed on the four cross sections previously identified, from the monthly mass transport and salinity fields. The mass transport used includes resolved and parameterized advective transport. As the mean Arctic salinity in our model and observations is about 34.8 (Figure S1), we take 34.8 as reference salinity. These sections are along the ocean grid to facilitate the calculation. We use the sea ice-mass transports provided by the CMIP6 outputs, at slightly different locations (given in Notz et al., 2016) from that shown in Figure S1, but still through the same passages. We assume a constant sea ice salinity of 7.2 psu to compute the freshwater proportion in the sea ice mass transport. Table 1 compares the freshwater transport in IPSL-CM6A-LR to various observational estimates (summarized by Lique et al., 2009). The liquid export of Arctic freshwater occurs mainly through the Davis and Fram Straits, and the model underestimates the export through Fram to some extent. The freshwater input from the Bering Strait is realistic and leads to a relatively fresher Beaufort Gyre and a salinity gradient in the Arctic from the Pacific sector to the Atlantic sector (Figure S2a). The liquid freshwater transport at the Barents Sea Opening is smaller

Table 1
Mean Freshwater Budget in the Arctic Ocean

	Freshwater transport (mSv)					Freshwater fluxes (mSv)	
	Fram strait	Bering strait	Barents section	Davis strait	Total	Runoff	P-E
IPSL-CM6-LR							
Liquid	−32.6 ± 23.3	71.2 ± 15.0	10.6 ± 13.2	−112.8 ± 33.3	−63.5 ± 32.2	108.9 ± 5.6	46.1 ± 5.2
Sea ice	−63.1 ± 14.9	−0.63 ± 4.0	−11.7 ± 5.9	−8.9 ± 3.4			
Observations							
Liquid	−63/−95/−28	57/79	−18	−92		94/102	65/31
Sea ice	−56/−88	3.00	−3.9	−12.9			

Reference salinity is 34.8 psu. Transport and fluxes are positive when entering the Arctic. Uncertainty in IPSL-CM6-LR is one standard deviation and is calculated from yearly outputs.

compared with the other three sections. It has a sign opposite to that of observations, with considerable uncertainty, which possibly leads to the underestimation of salinity in the Arctic between 200 and 600 m (Figure S1a). The flux due to precipitation minus evaporation (P-E) is underestimated, which may explain the occurrence of the positive surface salinity bias in comparison with WOA dataset. Nevertheless, the freshening caused by the runoff seems to be well simulated and results in the salinity minimum apparent in the coastal seas of the eastern Arctic (Figure S2a). Therefore, the large positive bias in this region is more likely to result from the bottom topography (Figure S1c). Lastly, an overwhelming majority of the sea ice export is realized through the Fram Strait, and the model simulates well this export.

2.3. Statistical Methods

2.3.1. Empirical Orthogonal Function and Low-Frequency Component Analysis

To characterize the centennial variability, we first compute the empirical orthogonal functions (EOF) of the Atlantic yearly meridional stream function from 30°S to 80°N, after weighting the data by the square root of the grid cell thickness. Hereafter, the principal components (PC) time series are standardized, while the EOFs shown are the regressions onto the PCs. The resulting first EOF (Figure S3, left) explains 21% of the variance and has largest loadings in the Tropics between 10°S and 10°N. The corresponding first PC shows some centennial to multicentennial variability, but it also includes some variations with a period smaller than 10 years. Conversely, the second EOF explains 16% of the variance and has large loadings between 40°N and 50°N. The associated second PC also shows a clearer centennial to multicentennial variability (Figure S3, right). The two PCs are positively correlated over a broad range of nonzero lags (with PC2 leading by a decade); this illustrates that standard EOF analysis, designed to maximize the variance, fails in our case to isolate a multicentennial variability with large meridional coherence. Therefore, we use instead a low-frequency component analysis (LFCA). The LFCA looks for the linear combination of the EOFs that maximizes the ratio of low frequency to total variance (Wills et al., 2018). The LFCA then provides the spatial pattern, called low-frequency pattern (LFP), that explains most of the low-frequency variance. The associated time series, called low-frequency component (LFC), is found by projecting the original unfiltered data onto the LFP. Here, we apply the LFCA using the first 8 EOFs, explaining 73.8% of the total variance, and the low-frequency time series are calculated using a third-order Butterworth filter with a 20-year cutoff period. The first LFP then explains 50.6% of the low-frequency variance (Figure 1, top) and is a meridional coherent overturning cell extending from 30°S to 80°N, with a typical variability of 0.8 Sv between 30°N and 50°N. The associated LFC1 shows a clear multicentennial variability. Using 10 years as the cutoff period in the Butterworth filter applied does not lead to significant differences. In the following, LFC1 is used as an index of centennial AMOC fluctuations.

2.3.2. Regression and Significance Test

The regression of various fields onto the LFC1 AMOC index is used to investigate the mechanisms of the centennial to multicentennial variability. The statistical significance of the correlated time series is estimat-

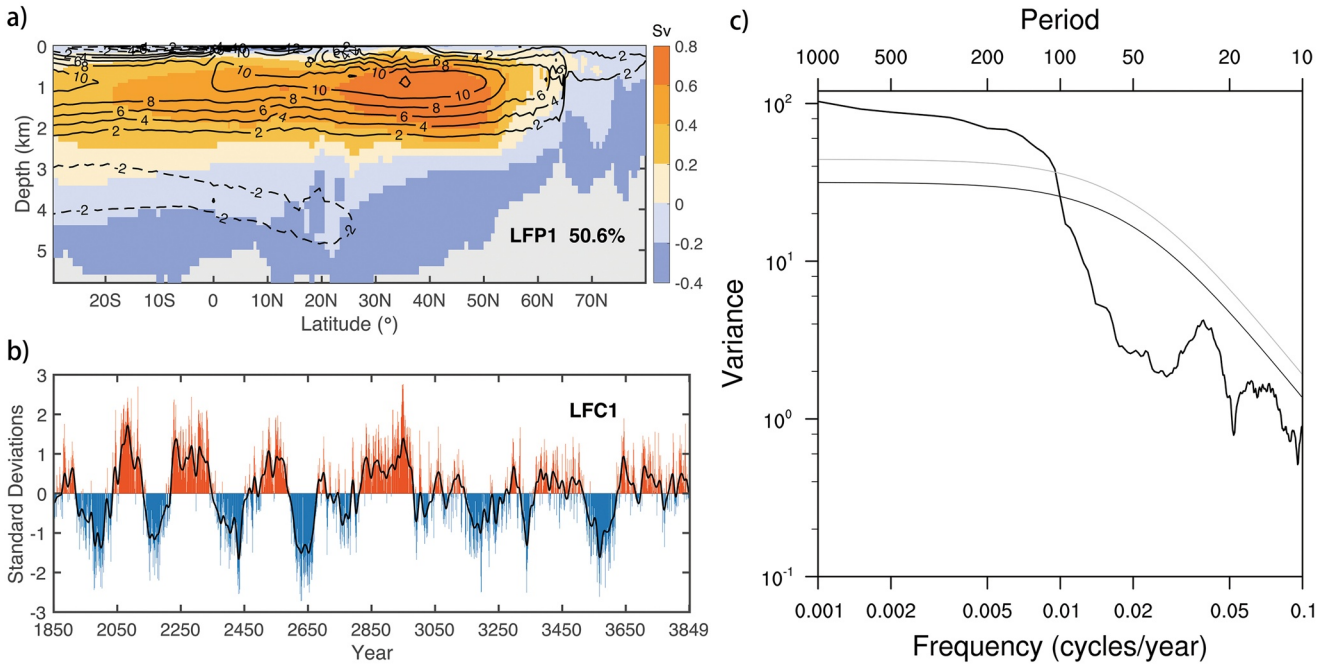

Figure 1. (a) First low-frequency pattern (LFP1) of the meridional stream function in the Atlantic basin from 30°S to 80°N (colors) and the climatological mean meridional stream function (contours), in Sv. The stream function is positive for clockwise rotation. LFP1 accounts for 50.6% of the low-frequency variance sampled by the first eight empirical orthogonal functions. (b) (Colors) standardized first low-frequency component (LFC1). The black line shows the maximum of the Atlantic meridional stream function at 30°N, after applying a third-order Butterworth lowpass filter with a cutoff period of 20 years. (c) The variance-frequency spectrum of LFC1 (in black). The best-fit first-order Markov red noise spectrum (lower gray curve) and its 95% (upper gray curve) confidence bounds are also indicated.

ed by a nonparametric method (Ebisuzaki, 1997). We create a large number of surrogate time series with the same power spectra as the AMOC LFC1 time series but with randomized phases in Fourier space. The original correlation between the AMOC index and the field of interest is compared to the distribution of correlations with the surrogate time series. The statistical significance level is the fraction of surrogate time series with a larger correlation than the actual value. One hundred surrogate time series are used in our case to estimate the significance. To ease the calculation of the regression maps, we convert the annual mean data into decadal time series, replacing every 10-year blocks by their time average. Only few differences were found when using annual mean data.

In the following text, the sign convention is that the AMOC leading the regressed fields is positive. For instance, "at lag −10 years" means that the AMOC lags by 10 years.

3. Results

3.1. Role of Salinity

As previously illustrated by the LFCA, a clear multicentennial variability is found in LFC1 (Figure 1). For comparison, the black line in Figure 1b is the standardized time series of maximum AMOC stream function at 30°N smoothed with a lowpass filter using 20 years as cutoff period. We find that LFC1 captures many characteristics of the raw AMOC time series. As noted in Boucher et al. (2020), the first 1,000 years of the preindustrial control run shows some variability with an approximate period of 200 years, but the last 1,000 years shows a less regular variability. A spectrum analysis of LFC1(Figure 1c) indeed shows a broad maximum emerging for periods longer than 100 years, without any clear peak. We also note a small peak at 30 year, which could be similar to the variability produced in the previous version of the IPSL model, IPSL-CM5A-LR (Escudier et al., 2013; Ortega et al., 2015). But this peak has less variance than the multicentennial variability and remains below the fitted red noise spectrum.

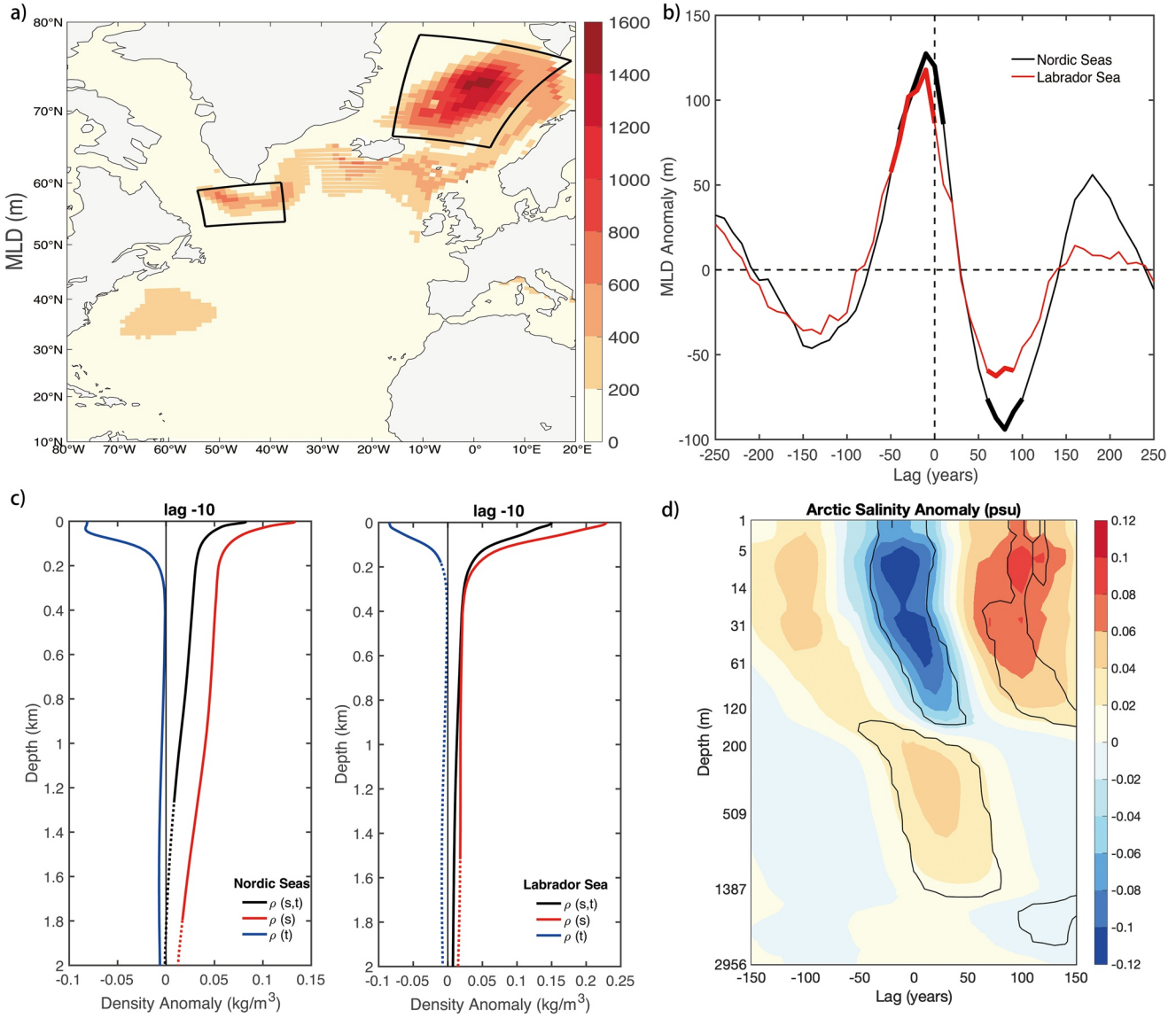

Figure 2. (a) Mean mixed layer depth (MLD), in m, in February, March, and April (FMA). Two convective sites: the Nordic Seas (the upper one) and Labrador Sea (the lower one) are outlined with black boxes. (b) Lagged regression of FMA MLD onto AMOC LFC1. The lag is positive when the AMOC leads. The thick lines indicate significance level below 5%. (c) Density anomaly (in black), in kg m^{-3}, regressed onto AMOC when the AMOC lags by 10 years, in the Nordic Seas and Labrador Sea convection sites. The density anomaly $\rho(s,t)$ caused by salinity anomaly $\rho(s)$ or temperature anomaly $\rho(t)$ is given in red and blue, respectively. Full (dashed) lines indicate the significance level below (above) 5%. (d) Vertical section of the lagged regression of the Arctic-wide averaged salinity. Black lines indicate significance level of 5%. The vertical scale is proportional to the mean size of the model vertical levels.

In IPSL-CM6A-LR, the mean mixed layer depth (MLD) in February-March-April (FMA) depicts one dominant deep water formation site in the Nordic seas, with mean MLD of ~1,400 m; and a smaller one in the Labrador Sea (Figure 2a), with mean MLD of ~600 m. The lagged regression of the FMA MLD in these two sites onto LFC1 reaches a maximum anomaly of ~120 m at both sites at lag −10 years (Figure 2b). To figure out the relative importance of salinity and temperature anomalies in driving the convection at those two sites, we calculate the density anomalies caused by anomalous salinity and temperature, while keeping the other field as its mean value. The results show that the upper (0–200 m) density anomalies are dominated by salinity anomalies and slightly balanced by temperature's impacts. The effect of temperature also decreases with depth and becomes negligible below 200 m (Figure 2c). The deepening of the MLD preceding the AMOC is therefore mainly induced by salinity anomalies. We also note that these salinity-driven density anomalies occur almost simultaneously in the Nordic and Labrador Seas (Figure 2b).

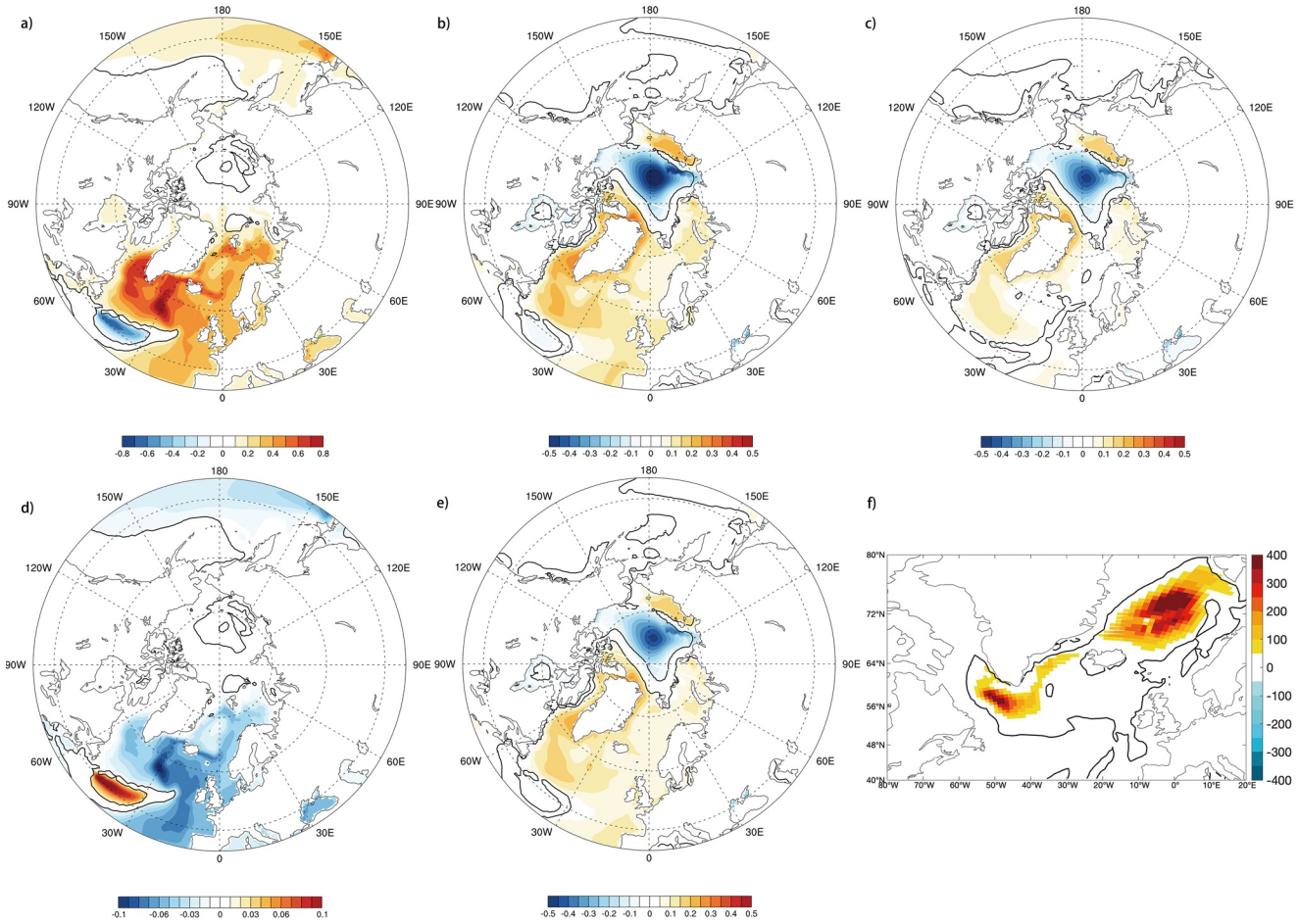

Figure 3. Oceanic fields regressed onto AMOC LFC1 when the AMOC lags by 10 years. (a) Regressed temperature (in °C), (b) salinity (in psu), and (c) density (in kg m^{-3}) in the top 150 m. (d) Thermal and (e) haline components (in kg m^{-3}) contributing to the density anomaly in (c). Note the difference in color scale for (d) when compared to (c) or (e). (f) Regressed MLD in FMA (in m). The black lines in (a–f) indicate the significance level at 5%. The red lines in (a) indicate the locations of transects and the blue points indicate each section's starting position.

Figures 3a–3c show maps of temperature, salinity, and density anomalies in the top 150 m at lag −10 years, corresponding to the deepest MLD. In the subpolar gyre, the warming and salinization pattern is coherent with that found in other studies of low-frequency Atlantic variations (e.g., Drews & Greatbatch, 2017; Roberts et al., 2013), with a southward extension of the subpolar gyre. The similarity between the density and salinity anomaly patterns clearly reveals the solid impact of salinity on density. The corresponding thermal and haline components of the density anomalies, shown in Figures 3d and 3e, further illustrate that the Arctic density anomaly is almost entirely determined by the abnormal salinity. The temperature slightly influences the eastern part of the Nordic seas and subpolar gyre since the Atlantic Ocean warms when the AMOC is strong. But its impact is smaller than that of salinity. Despite a smaller density anomaly in the Nordic Seas compared to the Labrador Sea, the anomalous MLD at these two sites are of comparable amplitudes (Figure 3f), and even the Nordic Seas anomalies have a broader extent. This may be linked to deeper mean MLD in the Nordic Seas.

Farther from the convection sites, we find a sizeable negative salinity anomaly in the Central Arctic, contrasting with the positive salinity anomalies located around Greenland and in the East Siberian Sea (Figure 3b). The regression of the basin-averaged salinity shows that this Central Arctic freshwater anomaly is located above 200m and is present from lag −40 years to 40 years (Figure 2d). This fresh anomaly is balanced by a smaller positive salinity anomaly between 200 and 1,400 m. As the top ~150 m presents an opposite salinity anomaly with the underlying ocean, in the following, we use the mean of the upper 150 m to characterize the Arctic salinity anomalies.

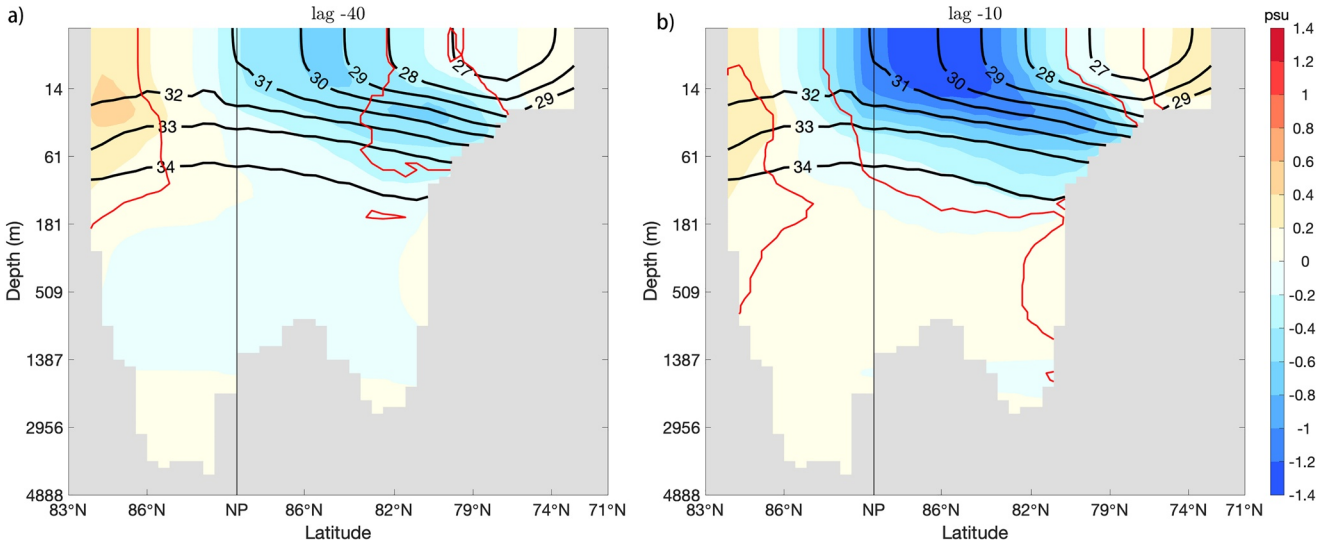

Figure 4. Salinity, in psu at the Arctic cross section, from (left) Northern Greenland to (right) the East Siberian Sea. (a) Anomalous (in colors) and mean (in black contours) salinity along the section, leading AMOC by 40 years. (b) Same as (a) but for leading AMOC by 10 years. Red contours indicate the significance level at 5%. The vertical scale is proportional to the mean size of the model vertical levels. AMOC, Atlantic meridional overturning circulation.

To better illustrate the salinity anomalies in the Arctic Ocean, we regress the salinity onto AMOC LFC1 in a cross section across the Arctic from northern Greenland to the coast of northern Siberia (see Figure 3a for location). At lag −40 years, the AMOC strengthens from the neutral state. While salty anomalies are present at the north coast of Greenland, a fresh anomaly occupies the top 60 m in the rest of the Arctic. Its structure suggests both a deepening and poleward extension of the surface freshwater pool found off the Siberian coast. At lag −10 years (Figure 4b), corresponding to a strong AMOC, this initial fresh anomaly has grown and extended toward Greenland, where the positive anomalies have decreased. Small positive salinity anomalies have appeared at the continental slope of northern Siberia, and below 180 m.

Before investigating the link between the Arctic and North Atlantic salinity anomalies, we briefly inspect other possible drivers, such as atmospheric forcing or the propagation of salinity anomalies from the tropics (e.g., Vellinga & Wu, 2004) or the Southern Ocean (e.g., Delworth & Zeng, 2012). To characterize the variations of anomalous salinity in the Atlantic Ocean, we show the Hovmöller diagram of the regression of the Atlantic zonal-mean salinity (0–150 m) onto LFC1 (Figure 5a). Indeed, the positive salinity anomalies occurring in the North Atlantic between 20°N and 60°N are associated with fresh anomalies between the equator and 15°N, as noticed by Vellinga and Wu (2004). However, these tropical fresh anomalies do not seem to propagate northward. Furthermore, few anomalies appear south of 40°S in the Southern Ocean, unlike previous studies (Delworth & Zeng, 2012; Park & Latif, 2008). The positive salinity anomalies in the middle-latitude North Atlantic seem instead to follow positive anomalies North of 60°N. Even if cause and effect cannot be fully distinguished, this suggests a stable linkage between the Arctic Ocean and the salinity anomalies driving the AMOC centennial variability. Finally, we investigate the potential role of the atmospheric forcing, showing the regression of the sea level pressure (SLP) onto AMOC LFC1 when the SLP leads the AMOC LFC1 by 10 years (Figures 5b and 5c). The SLP decreases over the subpolar Atlantic during a strong AMOC, but the magnitude of the anomalies is small: about 40 Pa at maximum. As we will show in the following, the associated geopotential height anomalies at higher altitudes have the opposite sign. Such a baroclinic structure contrasts with the barotropic modes of atmospheric variability previously identified as driving the AMOC (Eden & Willebrand, 2001; Häkkinen et al., 2011). Moreover, the SLP anomalies over the Arctic are not statistically significant, nor are surface wind anomalies (not shown). Therefore, it is likely that the SLP anomalies and the tropical salinity anomalies are the results of the strong AMOC, not the cause of the AMOC changes. In the following, we will investigate how salinity anomalies coming from the Arctic regulate the AMOC.

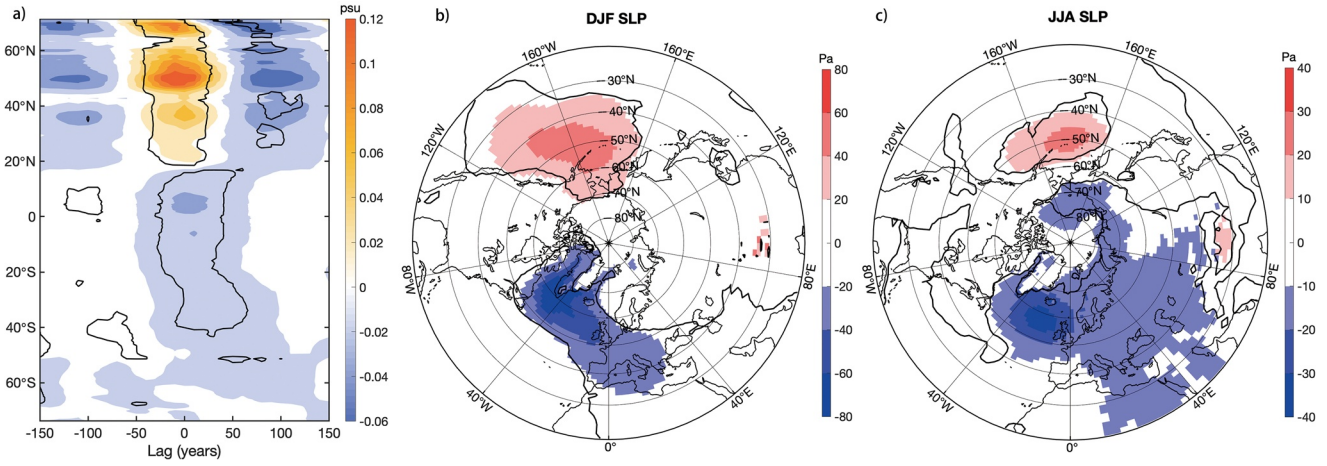

Figure 5. (a) Zonal-mean salinity anomalies in the Atlantic basin regressed onto AMOC LFC1 (in colors). Black lines illustrate the significance level at 5%. (b) Anomalous sea level pressure (SLP), in Pa, in December, January, February (DJF) and (c) June, July, and August (JJA) regressed onto AMOC LFC1, when the AMOC lags by 10 years. AMOC, Atlantic meridional overturning circulation; LFC, low-frequency component.

3.2. Life Cycle of the Salinity Anomalies

To investigate the propagation of salinity anomalies and understand the associated mechanisms, Figure 6 shows lagged regression maps of the top 150 m salinity and currents in the Arctic. From lags −80 years to −60 years, positive salinity anomalies occur in the Arctic center then propagate to the coast of Greenland, especially the Lincoln Sea and the Fram Strait. Minor negative anomalies appear in the East Siberian and the Laptev Seas. However, most of those anomalies are not significant at the 5% level. By lag −40 years, the salty anomaly around Greenland has grown and spread into the Nordic Seas, while a fresh anomaly appeared in the Central Arctic. These salinity anomalies are associated with an anomalous anticyclonic circulation in the central Arctic, and a cyclonic one around Greenland, with weakened West Greenland Current (WGC) in the Baffin Bay and East Greenland Current (EGC) through the Fram Strait, closed by a westward anomalous current north of Greenland.

From lags −20 years to 0 years, the AMOC gradually reaches its maximum value. The fresh anomaly in Central Arctic intensifies to about −0.5 psu. The gradual accumulation of freshwater leads to the reinforcement of the associated anticyclonic geostrophic flow. This anomalous circulation likely contributes in turn to maintaining this fresh anomaly in the central Arctic instead of it flushing through Fram Strait, as observed in the recent decades (Petty et al., 2016; Proshutinsky et al., 2009). Both the abnormal freshwater pool and anticyclonic circulation peak together with the AMOC (lag 0 year), while the salty anomaly around Greenland has started to decrease.

When the AMOC leads by 10 years, the Central Arctic freshwater finally reaches the Lincoln Sea and quickly spreads around Greenland. The accumulated freshwater is then gradually exported toward the Atlantic Ocean through the Fram straight from lag 20 years to lag 40 years, presumably through advection by the mean current, as well as by a stronger southward WGC. We notice that the negative salinity anomaly decays before exiting the Arctic (lag 30), probably due to the advection of the positive anomalies from the Eastern coastal Arctic to the Central Arctic (Figure 4b). When the freshwater has completely disappeared from the Central Arctic (lag 40 years to lag 70 years), an anomalous anticyclonic circulation sets up around Greenland, together with negative salinity anomalies. Simultaneously, a positive salinity anomaly initially located in the East Siberian and Laptev Seas at lag 30 years builds up and expands into the Central Arctic from lag 30 years to lag 70 years . This salty anomaly is associated with an anomalous cyclonic flow. The pattern shown at lag 70 years is of the opposite sign when compared to that found during the strong AMOC (lag 0 year). We can note during this cycle alternating near-surface salinity anomalies between the Central Arctic and at the Greenland coasts, with positive anomalies around Greenland leading the AMOC by 40 years to 0 year and negative anomalies lagging the AMOC by 40 to 70 years, while the central Arctic anomalies are more in phase. This relatively uniform distribution around Greenland could result from a fast adjustment

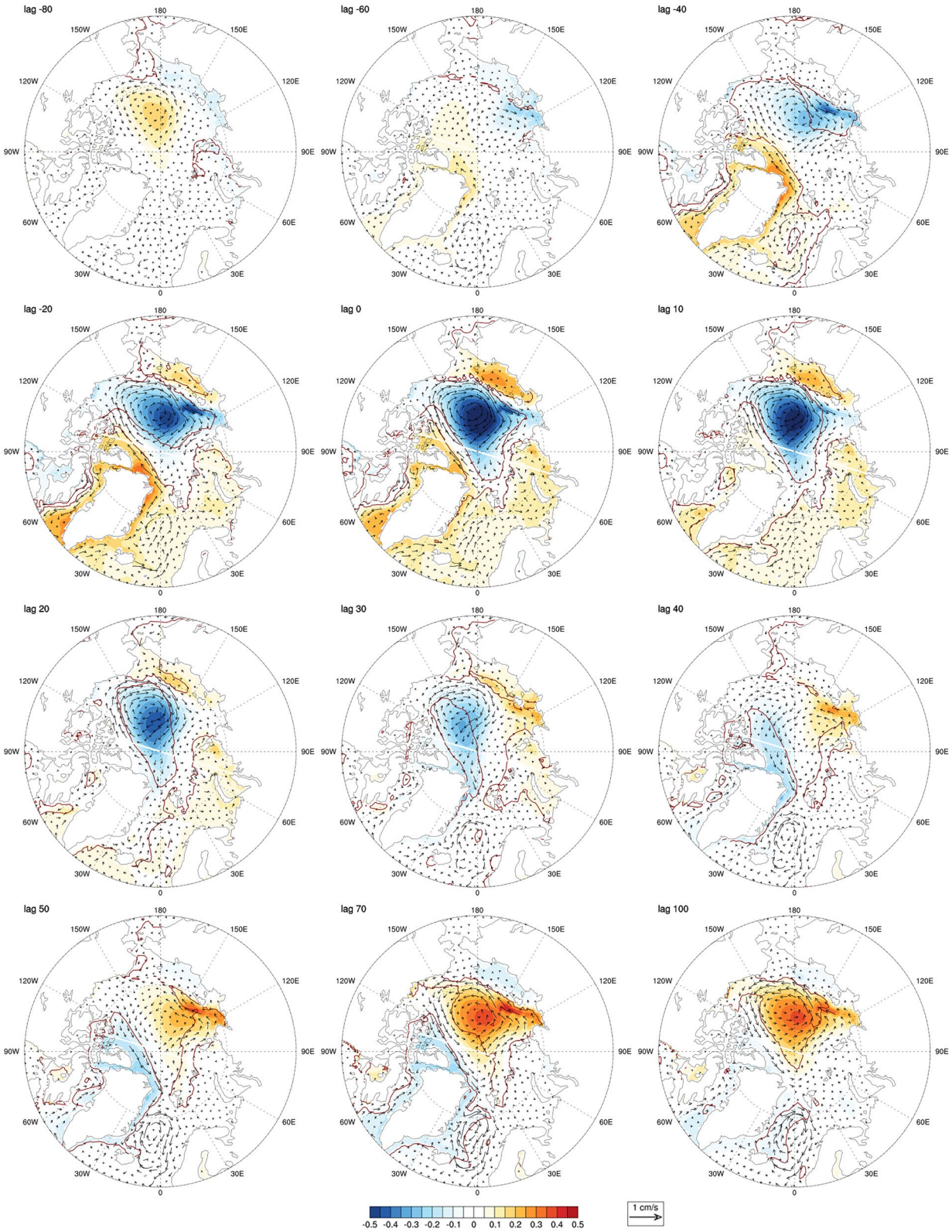

Figure 6. Regression onto AMOC LFC1 of the top 150 m salinity (colors), in psu, and currents (arrow), in cm s^{-1}, onto AMOC LFC1. Red contours indicate the significance level at 5% for the salinity regression. The lag is positive when the AMOC leads. AMOC, Atlantic meridional overturning circulation; LFC, low-frequency component.

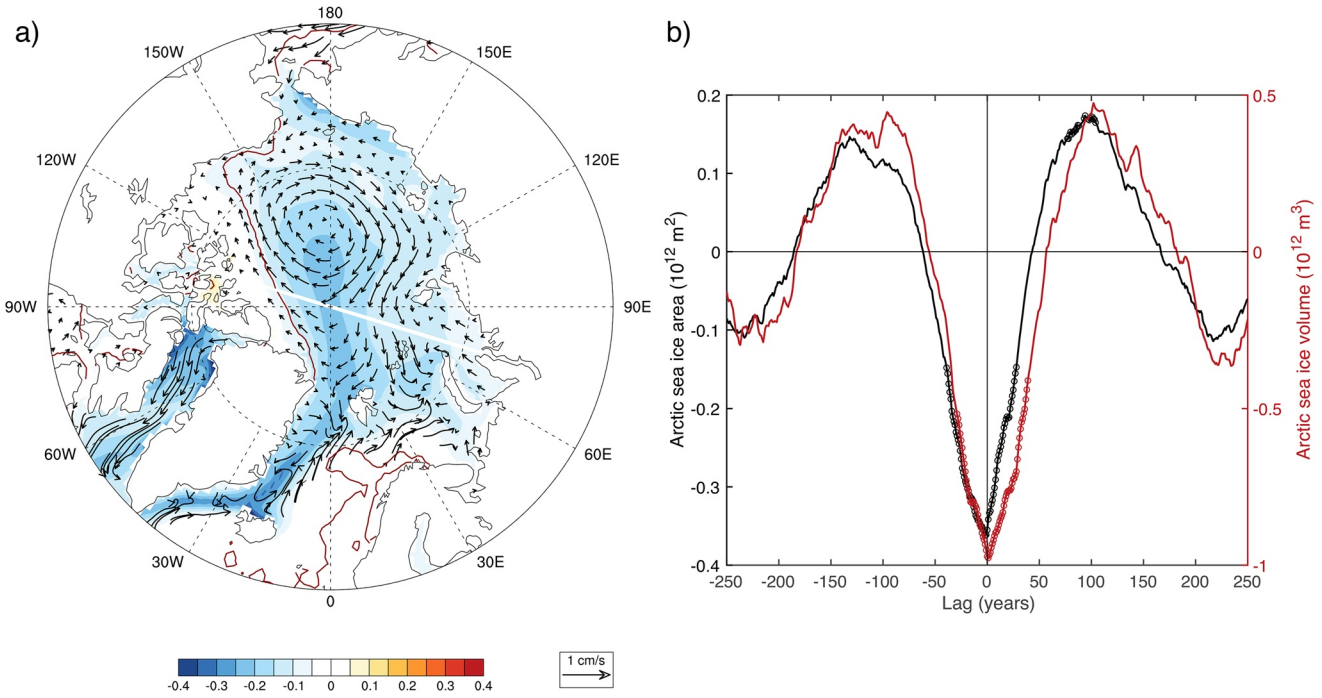

Figure 7. (a) Sea ice thickness in March (in colors), in m, and sea ice velocity (in black curved arrows), in cm s^{-1}, when the AMOC lags by 10 years. Red contours indicate the significance level at 5% of sea ice thickness. (b) The lagged regression of Arctic sea ice extent (in black line), in 10^{12} m^2, and the lagged regression of equivalent freshwater of Arctic sea ice volume (in red line), in 10^{12} m^3. The lag is positive when the AMOC leads. Circles indicate significance level below 5%. AMOC, Atlantic meridional overturning circulation.

of salinity and current anomalies trapped around Greenland, associated with opposite anomalous EGC and WGC.

To trace the source of the surface freshwater, we inspect the variations of sea ice thickness (Figure 7a), volume (Figure 7b, red line), and area (Figure 7b, black line). The reduction of sea ice in all aspects is simultaneous with the AMOC. This is consistent with a sea ice loss associated with the persistent warming linked to the increased northward oceanic heat transport, as previously found in models simulating a substantial multidecadal Atlantic variability with a period larger than 40 years (Frankcombe et al., 2010; Mahajan et al., 2011). As we discussed before, the atmospheric circulation above the Arctic Ocean is not significantly modified by the multicentennial variability, while the oceanic anticyclonic oceanic currents anomalies increase at lag −10 years (Figure 6). This results in a clockwise sea ice velocity anomaly (see arrows in Figure 7a).

In summary, the anomalous salinity anomalies located in the central Arctic grow gradually with the AMOC, associated with anomalous oceanic currents and sea ice velocity. Conversely, the main convection sites located in the Nordic and Labrador Seas show salinity and density anomalies more linked to large salinity anomalies forming all around Greenland, that lead the AMOC. These anomalies around Greenland in turn result from the delayed propagation of the anomalies located over the Arctic.

3.3. Source of Salinity Anomalies

To understand the freshwater exchanges between the Arctic and the North Atlantic, we quantify the liquid freshwater and sea ice transports across the boundaries of the Arctic, as well as the contribution from the sea ice melting/freezing and surface fluxes due to runoff and precipitation minus evaporation (see Section 2.2 for details).

Figure 8a reveals that in phase with a strong AMOC (and a maximum accumulated freshwater in the top 150 m of the Arctic), there is a large compensation between a freshwater input from sea ice and surface

fluxes (Figure 8a, black line), and an export by oceanic transport through the straits (Figure 8a, red line). Among the different contributors to the surface and freshwater fluxes, sea ice is by far the largest (~9 mSv at lag 0; Figure 8b, red line). Increased runoff (~1.5 mSv at lag 0) also contributes marginally to the positive surface input. The impact of precipitation and evaporation is negligible (Figure 8b, orange line). As we will show in the following subsection, the strong AMOC-driven heat transport warms the Northern Hemisphere high latitudes, especially in the lower troposphere in winter over the Arctic (up to ~1.5°C near the surface). This warming is almost simultaneous with the AMOC due to the fast response of the atmosphere, and leads to sea ice melt all over the Arctic—possibly with some feedbacks. In addition, sea ice export decreases (~5.5 mSv at lag 0; Figure 8d, black line), in line with the decreased volume and weaker currents, mostly at the Fram Strait (~4.5 mSv Figure 8d, red line) with a small contribution from the Barents Sea (~1.5 mSv at lag 0; Figure 8d, blue line).

To better understand the oceanic freshwater transport, we also detail in Figure 8c the oceanic transport at each cross section delimiting the Arctic boundaries. Anomalous transports at the Fram and Davis Straits precede the AMOC by 30–40 years. They are opposite in sign and balance each other to a large extent, with a slightly larger magnitude at Davis (Figure 8c). These transports are consistent with the cyclonic (anticyclonic) circulation and positive (negative) salinity anomalies trapped around Greenland at lag −40 years (50 years), as illustrated in Figure 6. The total oceanic transport is however in phase with the AMOC (Figure 8c, black line) and is mainly driven by the saltier Atlantic inflow through the Barents Sea (Figure 8c, blue line).

The oceanic transport anomalies are further decomposed into the advection of salinity anomalies by the mean current, and the anomalous advection of the mean salinity (Figure 8c). Both contributions are equally important at the Fram Strait (Figure 8c, dashed and dotted black lines). The current anomalies dominate at the Davis Strait, and the mean advection of anomalous salinity at the Barents Sea opening.

In order to link these freshwater fluxes with the salinity anomalies, we also compute a simple integrated freshwater budget:

$$\Delta FWC = \int_{t'=0}^{t'=t} F_S dt' + \int_{t'=0}^{t'=t} F_{Oce} dt' + R \quad (1)$$

where F_S denotes the surface and sea ice freshwater fluxes, and F_{Oce} is the total freshwater fluxes at the straits. ΔFWC is the anomaly of Arctic-integrated freshwater content (FWC). R is a small residue due to the off-line calculation of freshwater transports from monthly outputs. The regression of the terms of Equation 1 shows that the total Arctic FWC (Figure 8a, solid black line) continuously decreases from lag −70 to 50 years, and is a residual of a large cancelation between the two terms on the right-hand side of Equation 1. The oceanic transport, dominated by the inflow of North Atlantic water through Barents (Figure 8e, red line), decreases the total Arctic FWC (Figure 8e, solid black line), resulting in the subsurface positive salty anomalies found below 150 m in Figure 2d or Figure 4b. Meanwhile, the surface and especially sea ice fluxes (Figure 8e, blue line) bring freshwater to the surface, damping the total FWC variations. Although these two terms thus largely cancel each other on average, their impacts on the vertical structure differ, resulting in opposite salinity anomalies in the surface layer and at depth (Figure 2d). Indeed, the FWC anomaly restricted to the top 150 m (Figure 8e, dashed black line) is positive in phase with a strong AMOC or with a short lag, consistent with the surface freshwater input and with the salinity anomalies shown in Figure 6. The results suggest that the changes of the accumulated oceanic transport dominate the total and deep FWC anomalies while the surface freshwater fluxes dominate the near-surface FWC, with a contribution from transport anomalies.

Lastly, we compare the FWC variation in the top 150 m (Figure 8f, black line) to the accumulated contribution from cross-neutral diffusion (Figure 8f, red line). The impact of diffusion is negligible. The internal wave-driven vertical mixing scheme produces low mixing in the polar region (de Lavergne et al., 2016), which is consistent with the little role played by the diffusion in IPSL-CM6A-LR.

The salinity and current at the three main boundaries of the Arctic Ocean are shown in Figure 9, at the lags when the respective transport anomalies peak (preceding the AMOC by 40 years for Fram and Davis, lag 0 for Barents Sea Opening). At Fram Strait, salty anomalies (largest above the halocline) and a weaker

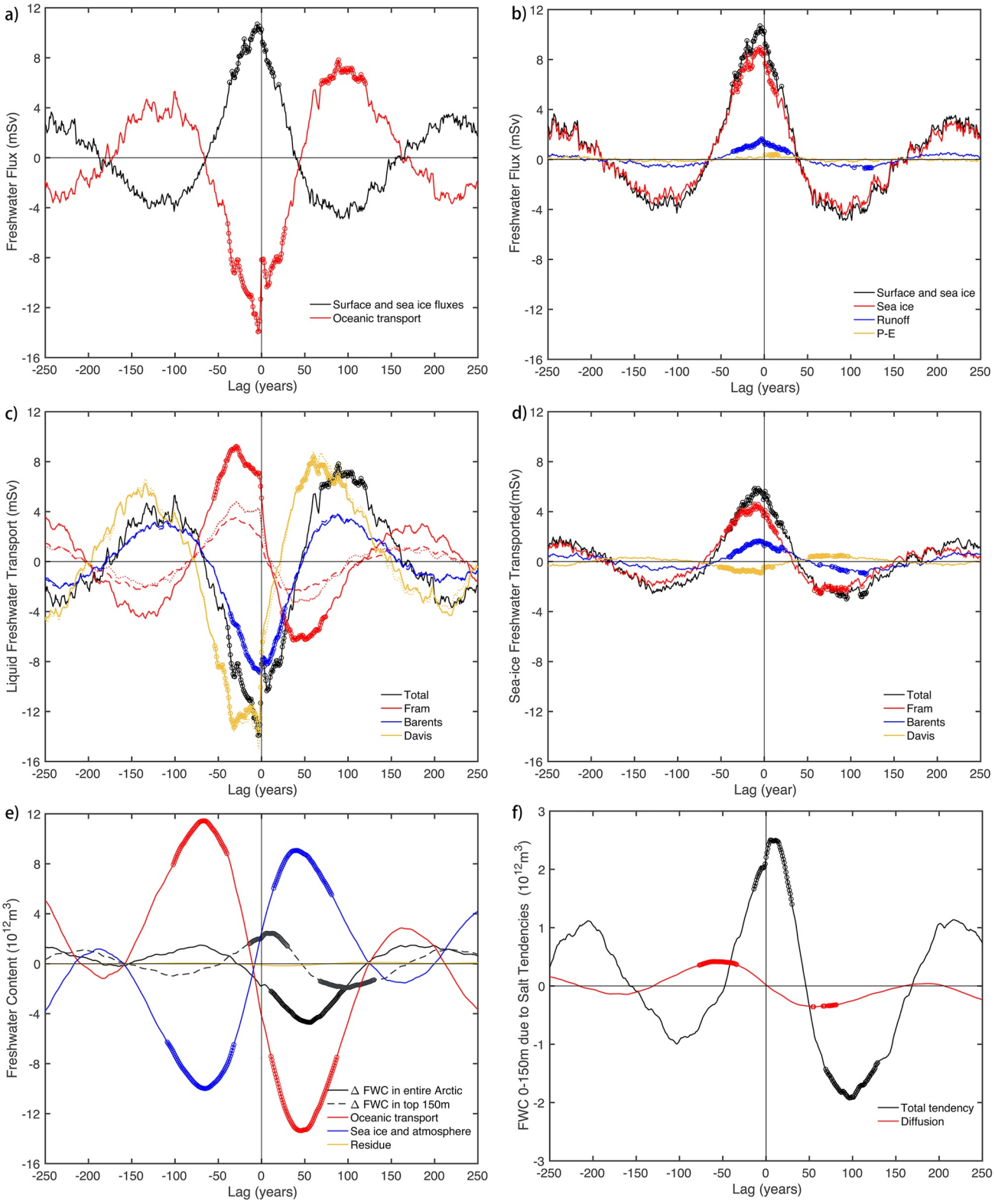
a)
Freshwater Flux (mSv)
Lag (years)
Surface and sea ice fluxes
Oceanic transport
b)
Freshwater Flux (mSv)
Lag (years)
Surface and sea ice
Sea ice
Runoff
P-E
c)
Liquid Freshwater Transport (mSv)
Lag (years)
Total
Fram
Barents
Davis
d)
Sea-ice Freshwater Transported(mSv)
Lag (year)
Total
Fram
Barents
Davis
e)
Freshwater Content ($10^{12}m^3$)
Lag (years)
Δ FWC in entire Arctic
Δ FWC in top 150m
Oceanic transport
Sea ice and atmosphere
Residue
f)
FWC 0-150m due to Salt Tendencies ($10^{12}m^3$)
Lag (years)
Total tendency
Diffusion

EGC appear near the Greenland coast (Figures 9c and 9d). These changes are in thermal wind balance, and both acts to reduce the freshwater export from the Arctic with a similar magnitude (Figure 8d, dashed and dotted black lines). The Davis Strait shows anomalous southward flow, consistent with the anomalous cyclonic circulation around Greenland. The salinity anomalies are more complicated, with salty anomalies near Greenland and fresh ones on the other side (Figure 9b). They correspond to outflow of saltier water from the Lincoln Sea through the Nares Strait and of fresher water from the Beaufort Sea through the Barrow Strait. These opposite salinity anomalies compensate, so the changes of current velocity transporting climatological mean freshwater southward dominate. In the Barents Sea, during strong AMOC conditions (lag 0 year), the smaller northward freshwater transport is mainly caused by an increase of the salinity of the water entering the Arctic where the mean current is oriented northward (Figure 9e). This saltier Atlantic inflow enters the Arctic through the Barents Sea Opening and propagates below the halocline toward the Eastern Arctic (Figure 4b).

Next, we will evaluate the global impacts of the North Atlantic multicentennial variability.

3.4. Climate Impacts of the Multicentennial Variability

The atmospheric changes associated with the AMOC variations are quite similar from lag −10 years to lag 10 years. To better evaluate the atmosphere's response to the AMOC variations and separate it from the atmospheric forcing, we show in Figure 10 the regressions when the AMOC leads by 10 years, but the results presented next are hardly modified for lag 0 year and lag −10 years.

Associated with the strong AMOC and increased northward heat transport, the Arctic warms by ∼1.5°C in winter and ∼0.8°C in summer. The amplification of the warming in winter is likely linked to the anomalous heat release from the ocean to the atmosphere associated with sea ice loss (Deser et al., 2015) and to the North Atlantic warming. The Arctic atmosphere being more stable near the surface in winter, the warming is confined to the lower troposphere (Pithan & Mauritsen, 2014), while it reaches 400 hPa or 300 hPa in summer. Aside from the polar region, the entire Northern Hemisphere north of 20°N also warms by ∼0.5°C, and the tropics between 20°S and 20°N show a weak warming of ∼0.05°C (Figures 10a and 10e). The zonal-mean tropospheric temperature shows a local warming maximum in the tropical upper troposphere (Figures 10b and 10f), following changes in the moist adiabat (Chiang & Bitz, 2005; Zhang et al., 2017). It is larger in summer, as the SST anomalies are warmer, and possibly because deep convection occurs more frequently in the Northern Hemisphere. These tropospheric temperature anomalies resemble the “mini global warming” pattern found in many modeling works simulating the Arctic sea ice loss (e.g., Deser et al., 2015; Liu & Fedorov, 2019; Screen et al., 2018; Sun et al., 2018). However, in those cases, sea ice loss is imposed, and the resulting warming and freshwater release lead to an AMOC decrease. In IPSL-CM6A-LR, the intrinsic variability shows instead simultaneous AMOC increase and Arctic sea ice extent decrease.

In summer, the geopotential height at 500-hPa increases uniformly in the Northern Hemisphere, with a larger amplitude at high latitudes (Figures 10c and 10g). At the same time, the SLP anomalies are negative over the Arctic and North Atlantic Ocean (not shown at lag 10, but similar to Figure 5c at lag −10), indicating a thermal low structure resulting from the heating of the lower troposphere. The situation is similar in winter, apart from some small positive SLP anomalies over the Arctic sea ice edges (not shown). An exception to this baroclinic structure is the SLP and geopotential height increase over the Aleutians. This

Figure 8. Freshwater content (FWC), in 10^{12} m^3, and fluxes, in mSv, regressed onto AMOC LFC1 in the Arctic ocean. (a) Regression of the freshwater flux into the Arctic caused by surface and sea ice thermodynamics fluxes (black line) and liquid freshwater fluxes (red line). (b) Regression of the surface and sea ice fluxes (black line), sea ice only flux (red line), the precipitation and evaporation (orange line) and runoff (blue line). (c) Regression of the total liquid freshwater transport (black line) and individual freshwater transport at each section: Fram (red lines), Davis (orange lines), and Barents (blue lines). Solid lines indicate FW transport anomalies; dashed lines represent anomalies caused by mean currents transporting salinity anomalies; dotted lines are anomalies due to mean salinity transported by anomalous currents. (d) Regression of freshwater flux due to sea ice export in total (black line) and through each passage Fram (red line), Davis (blue line) Straits, and Barents Sea Opening (orange line). (e) Regression of the Arctic Ocean FWC variation (solid black line) and FWC variation of the top 150 m (dashed black line), and corresponding variation due to accumulated oceanic transport (red line) and freshwater fluxes including sea ice thermodynamics and surface fluxes (solid blue line) and residual (orange line). (f) Regression of the FWC variation in the top 150 m (black line), and contribution from cross-neutral diffusion (red line). In (a–f), the significance level below 5% is shown in circles. AMOC, Atlantic meridional overturning circulation; LFC, low-frequency component.

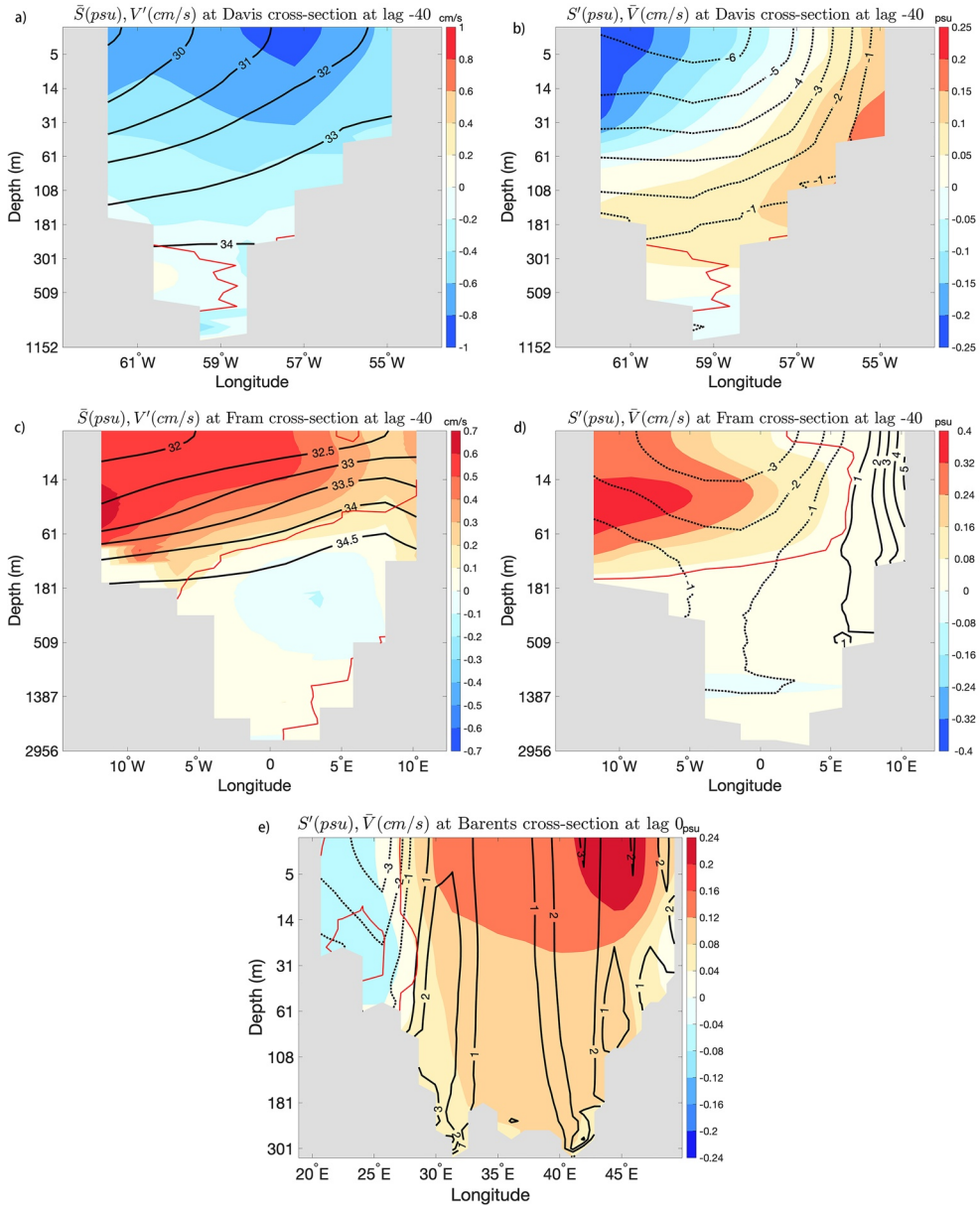

Figure 9. Salinity, in psu, and cross-section current, in cm s^{-1}at the Davis and Fram straits and Barents Sea Opening. (a and c) The mean salinity (in black contours) and anomalous currents (in colors); (b, d, and e) the mean currents (in black contours) and anomalous salinity (in colors). Note that the depth axis and scale in each plot is different. Red lines indicate the significance level at 5%.

could be related to the relative cooling of the Equatorial Pacific in winter, itself possibly a consequence of the warm surface anomalies in the Atlantic Ocean driving La Niña-like anomalies through a reorganization of the Walker circulation (Polo et al., 2015; Ruprich-Robert et al., 2017).

Another typical pattern associated with a warming Northern Hemisphere and an intensified AMOC is the northward shift of the ITCZ. Precipitation indeed increases north of the equator and decreases south of the equator, especially over the tropical Atlantic in summer (Figure 10h) and over the Indo-Pacific in winter (Figure 10d). This displacement causes more summertime rainfall in the Caribbean, African Sahel, and the Indian and Asian monsoon regions but less in Brazil (Figure 10h). Similar responses of rainfall to a strong AMOC are found in other models (Folland et al., 2001; Smith et al., 2017; Sutton & Hodson, 2005)

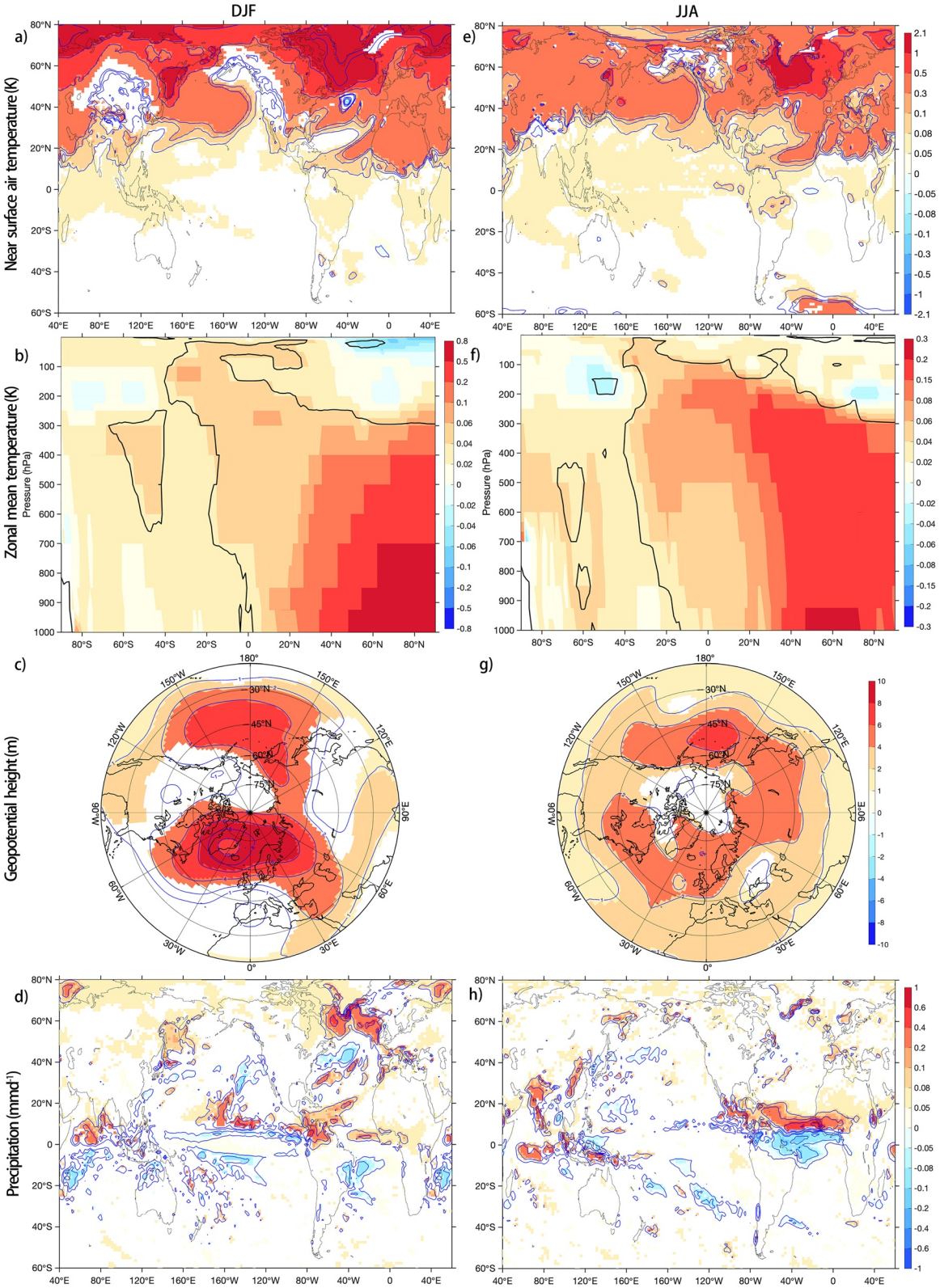
DJF
JJA
a)
e)
b)
f)
c)
g)
d)
h)
Near surface air temperature (K)
Zonal mean temperature (K)
Pressure (hPa)
Geopotential height (m)
Precipitation (mmd⁻¹)

as well as in observations (Folland et al., 1986; Zhang & Delworth, 2006). An explanation involving the energy budget was put forward in atmospheric model simulations coupled to a mixed layer ocean (Frierson et al., 2013; L'Hévéder et al., 2015; Kang et al., 2008; Tomas et al., 2016): to balance the anomalous northward cross-equatorial energy transport by a stronger AMOC, the atmosphere needs to transport energy southward. In the Tropics, this is accomplished by a cross-equatorial Hadley circulation, transporting total energy in the direction of its upper branch. The anomalous near-surface circulation is then northward, transporting more moisture into the northern hemisphere and leading to a northward shift of the ITCZ.

4. Discussion and Conclusions

The variability emerging from the North Atlantic and Arctic oceans in the 2,000 years IPSL-CM6-LR preindustrial control simulation is dominated by multicentennial fluctuations, as previously noted in Boucher et al. (2020). We show that this multicentennial variability is caused by delayed oceanic freshwater exchanges between the North Atlantic and the Arctic, with little influence of the atmospheric forcing. The AMOC changes are driven by density anomalies in the deep convective regions, caused by salinity anomalies. The cycle starts with the build-up of a positive salinity anomaly around Greenland, increasing the surface seawater density and the deep convection in the Labrador and Nordic Seas. This leads to an intensified AMOC, and the associated heat transport causes a surface warming in the North Atlantic. The associated warming of the lower troposphere then warms the ocean and melts the sea ice. A negative salinity anomaly thus appears at the surface in the Central Arctic. This freshwater anomaly builds up progressively, in thermal wind balance with an anomalous anticyclonic circulation that helps to maintain it inside the Arctic. Meanwhile, the advection of the positive salt anomaly by the mean inflow of Atlantic water leads to a positive salinity anomaly over the Laptev and East Siberian seas. The freshwater anomalies in Central Arctic broaden during four to five decades until they reach the Lincoln Sea north of Greenland. Then, the salinity anomalies around Greenland change sign to become negative, associated with a faster anticyclonic circulation. Eventually, the anomalous freshwater spreads to the convection sites in the Nordic and Labrador Seas, the AMOC decreases and the oscillation shifts to the opposite phase, with positive salt anomalies propagating from Eastern Arctic to Central Arctic.

The investigation of salt tendencies reveals that the parameterized diffusion does not play a significant role, as expected from the low mixing in polar region (de Lavergne et al., 2016). Thus, we suggest that the multicentennial timescale emerges mostly from the freshwater holding capacity in the central Arctic, and the interplay between this central freshwater pool and the circulation circling Greenland. Besides, we speculate that the salt anomalies advected by the Atlantic inflow into the Eastern Arctic are acting as a negative feedback, reversing the sign of the Arctic freshwater content anomalies. The oceanic circulation over the continental shelf in the East Siberian Sea and the Laptev Sea might bring the subsurface salty Atlantic water to reach the surface. However, the actual pathway of the salt anomaly remains to be fully understood with tools such as Lagrangian tracers. More work is also needed to quantify the advective time scales involved to fully understand this Arctic freshwater holding capacity as well as the mixing processes in the Laptev and East Siberian Seas.

The primary driving mechanism in our study reminds of the one proposed by Jungclaus et al. (2005, J05), in which the anomalous freshwater exchanges between the Arctic and North Atlantic are also the key driving factor, but with some important differences. First, their period is shorter, about 70–80 years, and the deep convection is not in phase in the Labrador and Nordic Seas. The initial reduction in sea ice export results from anticyclonic circulation anomalies in the Greenland Sea caused by ocean warming, and the geopotential height difference between the Greenland Sea and the Arctic Ocean. But in our study, the influence of temperature does not contribute to the density anomalies in the regions of interest. We also find that current and salinity anomalies are in phase in the EGC, unlike in Jungclaus et al. (2005). Besides, in our case, the

Figure 10. Regression onto AMOC LFC1 of various climate fields in winter (DJF, [a–d]) and summer (JJA, [e–h]), when the AMOC leads by 10 year: (a) Air temperature at 2 m height, in K, (b) zonal-mean air temperature, in K, (c) geopotential height at 500 hPa, in m. (d) Precipitation, in mm d^{-1}. In (a, b, and d), colors are shown if anomalies are statistically significant at 5% level, while blue contours intervals correspond to that shown in color bar. In (d), black contours indicate significance level at 5%. (e–h) are the same as (a–d), but for summer. Note the different color scale in (b and f). AMOC, Atlantic meridional overturning circulation; LFC, low-frequency component; DJF, December, January, February; JJA, June, July, and August.

atmospheric circulation anomalies remain small and hardly statistically significant. More generally, the accumulation of freshwater in the central Arctic seems to play a larger role in our case, rather than circulation changes in the Nordic Seas.

We did not find significant salinity anomalies propagating from the Southern Ocean, which is the key mechanism proposed in Delworth and Zeng (2012). Some negative salinity anomalies in the subtropical Atlantic are found associated with the ITCZ northward shift, as in Vellinga and Wu (2004) or Jackson and Vellinga (2013), but these anomalies are much weaker than those propagating from the Arctic. Therefore, we suggest that they do not have an active role in the centennial variability.

A strong AMOC phase shows significant climate impacts, with a Northern Hemisphere warming, maximum in winter. The warming is mainly baroclinic over North Atlantic and Arctic, with only a few sea level-pressure changes, as found in a previous study focusing on the impacts of North Atlantic warming (Ruprich-Robert et al., 2017). We also found an important northward shift of the ITCZ, influencing both the West African and Indian monsoon. All these impacts are consistent with a Northern Hemisphere warming caused by Arctic sea ice reduction and AMOC intensification. Further work would be needed to distinguish the specific role for climate of the AMOC from the sea ice loss and polar amplification feedbacks.

Although such multicentennial variability is not as dominant as the multidecadal variability, climate proxies indicate that a centennial to multicentennial North Atlantic variability exists (Ayache et al., 2018; Laepple & Huybers, 2013; Mann et al., 1995). More work is still needed to further assess the realism of the variability found in IPSL-CM6A-LR with proxy data. Similar centennial variability also occurs in other climate models participating in CMIP6. CNRM-CM6 (Voldoire et al., 2019) has an even more dominant centennial variability, while EC-Earth3.3 has a comparable one (Ruprich-Robert, personal communication). As EC-Earth3.3 and CNRM-CM6 share the same oceanic component as IPSL-CM6-LR, that is, NEMOv6 with a 1° nominal resolution, but with a different embedded sea ice module in the case of CNRM-CM6, the question about the properties within the ocean favoring the emergence of such centennial variability remains open. Our results suggest that such variability is characterized by an alternating salinity anomaly between the Central Arctic and at the coast of Greenland. A better understanding of the freshwater budget over these specific locations is needed to investigate the relevant evolution. Besides, the rapid adjustment of salinity anomalies around Greenland could be exacerbated by an over-simplistic bathymetry around Greenland, with the Nares strait being too deep (Figure S2b). However, multicentennial sensitivity experiments would be required to further assess the role of bathymetry.

Lastly, human activities are estimated to have caused approximately 1°C of global warming above preindustrial levels (IPCC, 2018). The presence of such centennial variability might potentially regulate and cover up the anthropogenic-driven climate change. Therefore, ongoing efforts aim to assess the signature of centennial to multicentennial variability in the warming climate and investigate how it impacts the historical and scenario simulation in terms of spread or uncertainty.

Acknowledgments
We thank two anonymous reviewers for their constructive suggestions and comments. We also acknowledge the developers of SOSIE version 3.0 and CDFTOOLS package, that we used to rotate the current from the tripolar ORCA grid to the geographic domain (SOSIE), calculate the oceanic transports through sections and approximate geographical sections with proper adjacent grid points (CDFTOOLS). Guillaume Gastineau and Francis Codron were supported by the Blue-Action project (European Union's Horizon 2020 research and innovation program, Grant No. 727852), Weimin Jiang by a grant from the MOPGA project and EUR-IPSL. This work used the HPC resources of TGCC under the allocations 2016-A0030107732, 2017-R0040110492, and 2018-1293R0040110492 (project gencmip6) provided by GENCI (Grand Equipement National de Calcul Intensif). This study benefited from the ESPRI (Ensemble de Services Pour la Recherche à l'IPSL) computing and data center (https://mesocentre.ipsl.fr) which is supported by CNRS, Sorbonne Université, Ecole Polytechnique and CNES and through national and international grants.

Data Availability Statement

The data of the simulation presented here are available on ESGF-CMIP6 (https://doi.org/10.22033/ESGF/CMIP6.1534).

References

Aksenov, Y., Ivanov, V. V., Nurser, A. J. G., Bacon, S., Polyakov, I. V., Coward, A. C., et al. (2011). The Arctic Circumpolar Boundary Current. *Journal of Geophysical Research*, *116*(C9), C09017. https://doi.org/10.1029/2010JC006637

Ayache, M., Swingedouw, D., Mary, Y., Eynaud, F., & Colin, C. (2018). Multi-centennial variability of the AMOC over the Holocene: A new reconstruction based on multiple proxy-derived SST records. *Global and Planetary Change*, *170*, 172–189. https://doi.org/10.1016/j.gloplacha.2018.08.016

Boucher, O., Servonnat, J., Albright, A. L., Aumont, O., Balkanski, Y., Bastrikov, V., et al. (2020). Presentation and evaluation of the IPSL-CM6A-LR climate model. *Journal of Advances in Modeling Earth Systems*, *12*, e2019MS002010. https://doi.org/10.1029/2019MS002010

Brown, P. T., Lozier, M. S., Zhang, R., & Li, W. (2016). The necessity of cloud feedback for a basin-scale Atlantic Multidecadal Oscillation. *Geophysical Research Letters*, *43*(8), 3955–3963. https://doi.org/10.1002/2016GL068303

Cane, M. A., Clement, A. C., Murphy, L. N., & Bellomo, K. (2017). Low-pass filtering, heat flux, and Atlantic multidecadal variability. *Journal of Climate*, *30*(18), 7529–7553. https://doi.org/10.1175/JCLI-D-16-0810.1

Cassou, C., Kushnir, Y., Hawkins, E., Pirani, A., Kucharski, F., Kang, I.-S., & Caltabiano, N. (2018). Decadal climate variability and predictability: Challenges and opportunities. *Bulletin of the American Meteorological Society*, *99*(3), 479–490. https://doi.org/10.1175/BAMS-D-16-0286.1

Chiang, J. C. H., & Bitz, C. M. (2005). Influence of high latitude ice cover on the marine Intertropical Convergence Zone. *Climate Dynamics*, *25*(5), 477–496. https://doi.org/10.1007/s00382-005-0040-5

Clement, A., Bellomo, K., Murphy, L. N., Cane, M. A., Mauritsen, T., Rädel, G., & Stevens, B. (2015). The Atlantic multidecadal oscillation without a role for ocean circulation. *Science*, *350*(6258), 320–324. https://doi.org/10.1126/science.aab3980

Colfescu, I., & Schneider, E. K. (2020). Decomposition of the Atlantic multidecadal variability in a historical climate simulation. *Journal of Climate*, *33*(10), 4229–4254. https://doi.org/10.1175/JCLI-D-18-0180.1

Cunningham, S. A., Kanzow, T., Rayner, D., Baringer, M. O., Johns, W. E., Marotzke, J., et al. (2007). Temporal variability of the Atlantic meridional overturning circulation at 26.5°N. *Science*, *317*(5840), 935–938. https://doi.org/10.1126/science.1141304

Danabasoglu, G. (2008). On multidecadal variability of the Atlantic meridional overturning circulation in the community climate system model version 3. *Journal of Climate*, *21*(21), 5524–5544. https://doi.org/10.1175/2008JCLI2019.1

De Lavergne, C., Madec, G., Le Sommer, J., Nurser, A. G., & Naveira Garabato, A. C. (2016). The impact of a variable mixing efficiency on the abyssal overturning. *Journal of Physical Oceanography*, *46*(2), 663–681.

Delworth, T. L., & Zeng, F. (2012). Multicentennial variability of the Atlantic meridional overturning circulation and its climatic influence in a 4000 year simulation of the GFDL CM2.1 climate model: Multicentennial climate variability. *Geophysical Research Letters*, *39*, L13702. https://doi.org/10.1029/2012GL052107

Deser, C., Tomas, R. A., & Sun, L. (2015). The role of ocean-atmosphere coupling in the zonal-mean atmospheric response to Arctic Sea Ice Loss. *Journal of Climate*, *28*(6), 2168–2186. https://doi.org/10.1175/JCLI-D-14-00325.1

Drews, A., & Greatbatch, R. J. (2017). Evolution of the Atlantic multidecadal variability in a model with an Improved North Atlantic Current. *Journal of Climate*, *30*(14), 5491–5512. https://doi.org/10.1175/JCLI-D-16-0790.1

Ebisuzaki, W (1997). A method to estimate the statistical significance of a correlation when the data are serially correlated. *Journal of Climate*, *10*(9), 2147–2153. https://doi.org/10.1175/1520-0442(1997)010<2147:AMTETS>2.0.CO;2

Eden, C, & Willebrand, J (2001). Mechanism of interannual to decadal variability of the North Atlantic circulation. *Journal of Climate*, *14*(10), 2266–2280. https://doi.org/10.1175/1520-0442(2001)014<2266:MOITDV>2.0.CO;2

Escudier, R., Mignot, J., & Swingedouw, D. (2013). A 20-year coupled ocean-sea ice-atmosphere variability mode in the North Atlantic in an AOGCM. *Climate Dynamics*, *40*(3), 619–636. https://doi.org/10.1007/s00382-012-1402-4

Eyring, V., Bony, S., Meehl, G. A., Senior, C. A., Stevens, B., Stouffer, R. J., & Taylor, K. E. (2016). Overview of the coupled model intercomparison project phase 6 (CMIP6) experimental design and organization. *Geoscientific Model Development*, *9*(5), 1937–1958. https://doi.org/10.5194/gmd-9-1937-2016

Flato, G., Marotzke, J., Abiodun, B., Braconnot, P., Chou, S. C., Collins, W., et al. (2013). Evaluation of climate models. In T. F. Stocker, et al. (Eds.), *Climate change 2013: The physical science basis. Contribution of working Group I to the fifth assessment report of the intergovernmental panel on climate change* (pp. 741–882). Cambridge, UK: Cambridge University Press. https://doi.org/10.1017/CBO9781107415324.020

Folland, C. K., Colman, A. W., Rowell, D. P., & Davey, M. K. (2001). Predictability of Northeast Brazil Rainfall and real-time forecast skill, 1987–98. *Journal of Climate*, *14*(9), 1937–1958. https://doi.org/10.1175/1520-0442(2001)014<1937:PONBRA>2.0.CO2

Folland, C. K., Palmer, T. N., & Parker, D. E. (1986). Sahel rainfall and worldwide sea temperatures, 1901–85. *Nature*, *320*(6063), 602–607. https://doi.org/10.1038/320602a0

Frankcombe, L. M., von der Heydt, A., & Dijkstra, H. A. (2010). North Atlantic multidecadal climate variability: An investigation of dominant time scales and processes. *Journal of Climate*, *23*(13), 3626–3638. https://doi.org/10.1175/2010JCLI3471.1

Frierson, D. M. W., Hwang, Y.-T., Fučkar, N. S., Seager, R., Kang, S. M., Donohoe, A., et al. (2013). Contribution of ocean overturning circulation to tropical rainfall peak in the Northern Hemisphere. *Nature Geoscience*, *6*(11), 940–944. https://doi.org/10.1038/ngeo1987

Häkkinen, S., Rhines, P. B., & Worthen, D. L. (2011). Atmospheric blocking and Atlantic multidecadal ocean variability. *Science*, *334*(6056), 655–659. https://doi.org/10.1126/science.1205683

Hawkins, E., & Sutton, R. (2007). Variability of the Atlantic thermohaline circulation described by three-dimensional empirical orthogonal functions. *Climate Dynamics*, *29*(7–8), 745–762. https://doi.org/10.1007/s00382-007-0263-8

IPCC (2018). Global Warming of 1.5°C. An IPCC Special Report on the impacts of global warming of 1.5°C above pre-industrial levels and related global greenhouse gas emission pathways. In V. Masson-Delmotte, et al. (Eds.), *The context of strengthening the global response to the threat of climate change, sustainable development, and efforts to eradicate poverty*. In press. IPCC.

Jackson, L., & Vellinga, M. (2013). Multidecadal to centennial variability of the AMOC: HadCM3 and a perturbed physics ensemble. *Journal of Climate*, *26*(7), 2390–2407. https://doi.org/10.1175/JCLI-D-11-00601.1

Jackson, L. C., Kahana, R., Graham, T., Ringer, M. A., Woollings, T., Mecking, J. V., & Wood, R. A. (2015). Global and European climate impacts of a slowdown of the AMOC in a high resolution GCM. *Climate Dynamics*, *45*(11), 3299–3316. https://doi.org/10.1007/s00382-015-2540-2

Jahn, A., & Holland, M. M. (2013). Implications of Arctic sea ice changes for North Atlantic deep convection and the meridional overturning circulation in CCSM4-CMIP5 simulations. *Geophysical Research Letters*, *40*, 1206–1211. https://doi.org/10.1002/grl.50183

Jungclaus, J. H., Haak, H., Latif, M., & Mikolajewicz, U. (2005). Arctic-North Atlantic interactions and multidecadal variability of the meridional overturning circulation. *Journal of Climate*, *18*(19), 4013–4031. https://doi.org/10.1175/JCLI3462.1

Kang, S. M., Held, I. M., Frierson, D. M. W., & Zhao, M. (2008). The response of the ITCZ to extratropical thermal forcing: Idealized slab-ocean experiments with a GCM. *Journal of Climate*, *21*(14), 3521–3532. https://doi.org/10.1175/2007JCLI2146.1

Kerr, R. A. (2000). A North Atlantic climate pacemaker for the centuries. *Science*, *288*(5473), 1984–1985. https://doi.org/10.1126/science.288.5473.1984

Knight, J. R., Allan, R. J., Folland, C. K., Vellinga, M., & Mann, M. E. (2005). A signature of persistent natural thermohaline circulation cycles in observed climate. *Geophysical Research Letters*, *32*, L20708. https://doi.org/10.1029/2005GL024233

Laepple, T., & Huybers, P. (2013). Reconciling discrepancies between Uk37 and Mg/Ca reconstructions of Holocene marine temperature variability. *Earth and Planetary Science Letters*, *375*, 418–429. https://doi.org/10.1016/j.epsl.2013.06.006

L'Hévéder, B., Codron, F., & Ghil, M. (2015). Impact of anomalous Northward oceanic heat transport on global climate in a slab ocean setting. *Journal of Climate*, *28*(7), 2650–2664. https://doi.org/10.1175/JCLI-D-14-00377.1

Liu, W., & Fedorov, A. V. (2019). Global impacts of Arctic Sea Ice loss mediated by the Atlantic meridional overturning circulation. *Geophysical Research Letters*, *46*, 944–952. https://doi.org/10.1029/2018GL080602

Lique, C., Treguier, A. M., Scheinert, M., & Penduff, T. (2009). A model-based study of ice and freshwater transport variability along both sides of Greenland. *Climate Dynamics*, *33*(5), 685–705. https://doi.org/10.1007/s00382-008-0510-7

Locarnini, R. A., Mishonov, A. V., Baranova, O. K., Boyer, T. P., Zweng, M. M., Garcia, H. E., et al. (2018). *World Ocean Atlas 2018, Volume 1: Temperature*. In A. Mishonov (Ed.). NOAA Atlas NESDIS 81 (p. 52).

Mahajan, S., Zhang, R., & Delworth, T. L. (2011). Impact of the Atlantic meridional overturning circulation (AMOC) on Arctic surface air temperature and sea ice variability. *Journal of Climate*, *24*(24), 6573–6581. https://doi.org/10.1175/2011JCLI4002.1

Mann, M. E., Park, J., & Bradley, R. S. (1995). Global interdecadal and century-scale climate oscillations during the past five centuries. *Nature*, *378*(6554), 266–270. https://doi.org/10.1038/378266a0

Muir, L. C., & Fedorov, A. V. (2015). How the AMOC affects ocean temperatures on decadal to centennial timescales: The North Atlantic versus an interhemispheric seesaw. *Climate Dynamics*, *45*(1), 151–160. https://doi.org/10.1007/s00382-014-2443-7

Murphy, L. N., Bellomo, K., Cane, M., & Clement, A. (2017). The role of historical forcings in simulating the observed Atlantic multidecadal oscillation. *Geophysical Research Letters*, *44*(5), 2472–2480. https://doi.org/10.1002/2016GL071337

Nigam, S., Guan, B., & Ruiz-Barradas, A. (2011). Key role of the Atlantic Multidecadal Oscillation in 20th century drought and wet periods over the Great Plains. *Geophysical Research Letters*, *38*, L16713. https://doi.org/10.1029/2011GL048650

Notz, D., Jahn, A., Holland, M., Hunke, E., Massonnet, F., Stroeve, J., et al. (2016). The CMIP6 Sea-Ice Model Intercomparison Project (SIMIP): understanding sea ice through climate-model simulations. *Geoscientific Model Development*, *9*(9), 3427–3446. https://doi.org/10.5194/gmd-9-3427-2016

Nyberg, J., Malmgren, B. A., Kuijpers, A., & Winter, A. (2002). A centennial-scale variability of tropical North Atlantic surface hydrography during the late Holocene. *Palaeogeography, Palaeoclimatology, Palaeoecology*, *183*(1), 25–41. https://doi.org/10.1016/S0031-0182(01)00446-1

Ortega, P., Mignot, J., Swingedouw, D., Sévellec, F., & Guilyardi, E. (2015). Reconciling two alternative mechanisms behind bi-decadal variability in the North Atlantic. *Progress in Oceanography*, *137*, 237–249. https://doi.org/10.1016/j.pocean.2015.06.009

Pardaens, A., Vellinga, M., Wu, P., & Ingleby, B. (2008). Large-Scale Atlantic salinity changes over the last half-century: A model-observation comparison. *Journal of Climate*, *21*(8), 1698–1720. https://doi.org/10.1175/2007JCLI1988.1

Park, W., & Latif, M. (2008). Multidecadal and multicentennial variability of the meridional overturning circulation. *Geophysical Research Letters*, *35*, L22703. https://doi.org/10.1029/2008GL035779

Petty, A. A., Hutchings, J. K., Richter-Menge, J. A., & Tschudi, M. A. (2016). Sea ice circulation around the Beaufort Gyre: The changing role of wind forcing and the sea ice state. *Journal of Geophysical Research: Oceans*, *121*, 3278–3296. https://doi.org/10.1002/2015JC010903

Pithan, F., & Mauritsen, T. (2014). Arctic amplification dominated by temperature feedbacks in contemporary climate models. *Nature Geoscience*, *7*(3), 181–184. https://doi.org/10.1038/ngeo2071

Pnyushkov, A. V., Polyakov, I. V., Ivanov, V. V., Aksenov, Y., Coward, A. C., Janout, M., & Rabe, B. (2015). Structure and variability of the boundary current in the Eurasian Basin of the Arctic Ocean. *Deep Sea Research Part I: Oceanographic Research Papers*, *101*, 80–97. https://doi.org/10.1016/j.dsr.2015.03.001

Polo, I., Martin-Rey, M., Rodriguez-Fonseca, B., Kucharski, F., & Mechoso, C. R. (2015). Processes in the Pacific La Niña onset triggered by the Atlantic Niño. *Climate Dynamics*, *44*(1), 115–131. https://doi.org/10.1007/s00382-014-2354-7

Proshutinsky, A., Krishfield, R., Timmermans, M.-L., Toole, J., Carmack, E., McLaughlin, F., et al. (2009). Beaufort Gyre freshwater reservoir: State and variability from observations. *Journal of Geophysical Research*, *114*, C00A10. https://doi.org/10.1029/2008JC005104

Qin, M., Dai, A., & Hua, W. (2020). Quantifying contributions of internal variability and external forcing to Atlantic multidecadal variability since 1870. *Geophysical Research Letters*, *47*, e2020GL089504. https://doi.org/10.1029/2020GL089504

Roberts, C. D., Garry, F. K., & Jackson, L. C. (2013). A multimodel study of sea surface temperature and subsurface density fingerprints of the Atlantic meridional overturning circulation. *Journal of Climate*, *26*(22), 9155–9174. https://doi.org/10.1175/JCLI-D-12-00762.1

Ruprich-Robert, Y., Msadek, R., Castruccio, F., Yeager, S., Delworth, T., & Danabasoglu, G. (2017). Assessing the climate impacts of the observed Atlantic multidecadal variability using the GFDL CM2.1 and NCAR CESM1 global coupled models. *Journal of Climate*, *30*(8), 2785–2810. https://doi.org/10.1175/JCLI-D-16-0127.1

Screen, J. A., Deser, C., Smith, D. M., Zhang, X., Blackport, R., Kushner, P. J., et al. (2018). Consistency and discrepancy in the atmospheric response to Arctic sea-ice loss across climate models. *Nature Geoscience*, *11*(3), 155–163. https://doi.org/10.1038/s41561-018-0059-y

Sicre, M.-A., Yiou, P., Eiríksson, J., Ezat, U., Guimbaut, E., Dahhaoui, I., et al. (2008). A 4500-year reconstruction of sea surface temperature variability at decadal time-scales off North Iceland. *Quaternary Science Reviews*, *27*(21), 2041–2047. https://doi.org/10.1016/j.quascirev.2008.08.009

Smith, D. M., Dunstone, N. J., Scaife, A. A., Fiedler, E. K., Copsey, D., & Hardiman, S. C. (2017). Atmospheric response to Arctic and Antarctic Sea Ice: The importance of ocean-atmosphere coupling and the background state. *Journal of Climate*, *30*(12), 4547–4565. https://doi.org/10.2307/26388076

Stocker, T. F. (1998). The seesaw effect. *Science*, *282*(5386), 61–62. https://doi.org/10.1126/science.282.5386.61

Sun, L., Alexander, M., & Deser, C. (2018). Evolution of the global coupled climate response to Arctic Sea Ice Loss during 1990–2090 and its contribution to climate change. *Journal of Climate*, *31*(19), 7823–7843. https://doi.org/10.1175/JCLI-D-18-0134.1

Sutton, R. T., & Hodson, D. L. R. (2005). Atlantic Ocean forcing of North American and European summer climate. *Science*, *309*(5731), 115–118. https://doi.org/10.1126/science.1109496

Tomas, R. A., Deser, C., & Sun, L. (2016). The role of ocean heat transport in the global climate response to projected Arctic Sea Ice Loss. *Journal of Climate*, *29*(19), 6841–6859. https://doi.org/10.1175/JCLI-D-15-0651.1

Vellinga, M., & Wu, P. (2004). Low-latitude freshwater influence on centennial variability of the Atlantic thermohaline circulation. *Journal of Climate*, *17*(23), 4498–4511. https://doi.org/10.1175/3219.1

Voldoire, A., Saint-Martin, D., Sénési, S., Decharme, B., Alias, A., Chevallier, M., et al. (2019). Evaluation of CMIP6 DECK Experiments With CNRM-CM6-1. *Journal of Advances in Modeling Earth Systems*, *11*, 2177–2213. https://doi.org/10.1029/2019MS001683

Wang, C., Zhang, L., Lee, S.-K., Wu, L., & Mechoso, C. R. (2014). A global perspective on CMIP5 climate model biases. *Nature Climate Change*, *4*(3), 201–205. https://doi.org/10.1038/nclimate2118

Wills, R. C., Schneider, T., Wallace, J. M., Battisti, D. S., & Hartmann, D. L. (2018). Disentangling global warming, multidecadal variability, and El Niño in Pacific temperatures. *Geophysical Research Letters*, *45*(5), 2487–2496. https://doi.org/10.1002/2017GL076327

Xu, X., Chassignet, E. P., & Wang, F. (2019). On the variability of the Atlantic meridional overturning circulation transports in coupled CMIP5 simulations. *Climate Dynamics*, *52*(11), 6511–6531. https://doi.org/10.1007/s00382-018-4529-0

Zhang, L., Delworth, T. L., & Zeng, F. (2017). The impact of multidecadal Atlantic meridional overturning circulation variations on the Southern Ocean. *Climate Dynamics*, *48*(5), 2065–2085. https://doi.org/10.1007/s00382-016-3190-8

Zhang, R., & Delworth, T. L. (2006). Impact of Atlantic multidecadal oscillations on India/Sahel rainfall and Atlantic hurricanes. *Geophysical Research Letters*, *33*, L17712. https://doi.org/10.1029/2006GL026267

Zhang, R., Sutton, R., Danabasoglu, G., Kwon, Y., Marsh, R., Yeager, S. G., et al. (2019). A review of the role of the Atlantic meridional overturning circulation in atlantic multidecadal variability and associated climate impacts. *Reviews of Geophysics*, *57*, 316–375. https://doi.org/10.1029/2019RG000644

Zweng, M. M., Reagan, J. R., Seidov, D., Boyer, T. P., Locarnini, R. A., Garcia, H. E., et al. (2018). World Ocean Atlas 2018, Volume 2: Salinity. In A. Mishonov (Technical Ed.), NOAA Atlas NESDIS 82 (p. 50).

Journal of Advances in Modeling Earth Systems

Supporting Information for

Multi-centennial variability driven by salinity exchanges between the Atlantic and the Arctic Ocean in a coupled climate model

Weimin Jiang[1], Guillaume Gastineau[1], Francis. Codron[1]

[1]UMR LOCEAN, Sorbonne Université/CNRS/IRD/MNHN, Paris, France

Contents of this file

Figures S1 to S3

Introduction

Our analysis is based on a 2000-yr pre-industrial control simulation of the low-resolution atmosphere-ocean model developed by the IPSL for CMIP6 (CMIP6.CMIP.IPSL.IPSL-CM6A-LR; doi:10.22033/ESGF/CMIP6.1534). The mean simulated salinity and currents in the North Atlantic at high latitudes and the Arctic are shown, and the World Ocean Atlas 2018 (WOA18) dataset is used to assess the salinity and temperature fields in the model. We use empirical orthogonal functions (EOF) to analyze the Atlantic yearly meridional streamfunction from 30°S to 80°N, after weighting the data by the square root of the grid cell thickness. The principal components (PC) time-series are standardized, and the EOFs are the regressions onto the PCs. A small cooling drift of about 0.2K in 2000 years exists in this simulation. We approximated this drift as a quadratic trend and removed it from all data before analysis.

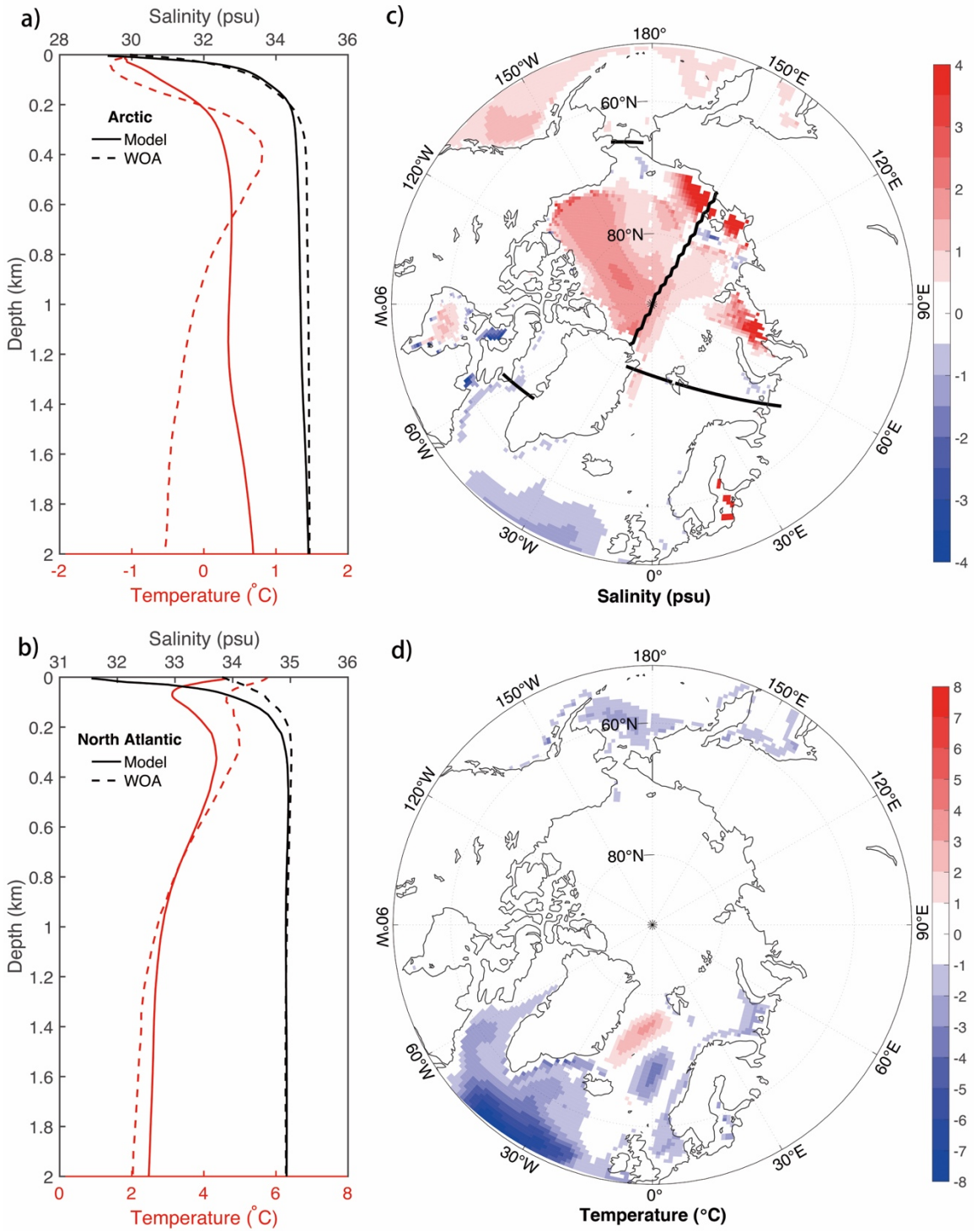

Figure S1. Comparison between model results and World Ocean Atlas 2018 (WOA18) dataset. Mean salinity and temperature in (a) the Arctic and (b) the North Atlantic. The Arctic is enclosed by four cross-sections at the Bering Strait, the Fram Strait, the Davis Strait and the Barents Sea Opening, indicated with black lines in (c). The cross-section across the north pole is called the Arctic cross-section. The North Atlantic is from 30°N to the Fram Strait and Barents open ocean cross-section. Difference of (c) salinity, in psu, and (d) temperature, in °C, between model and WOA18 (model minus WOA18) integrated over top 200 meters.

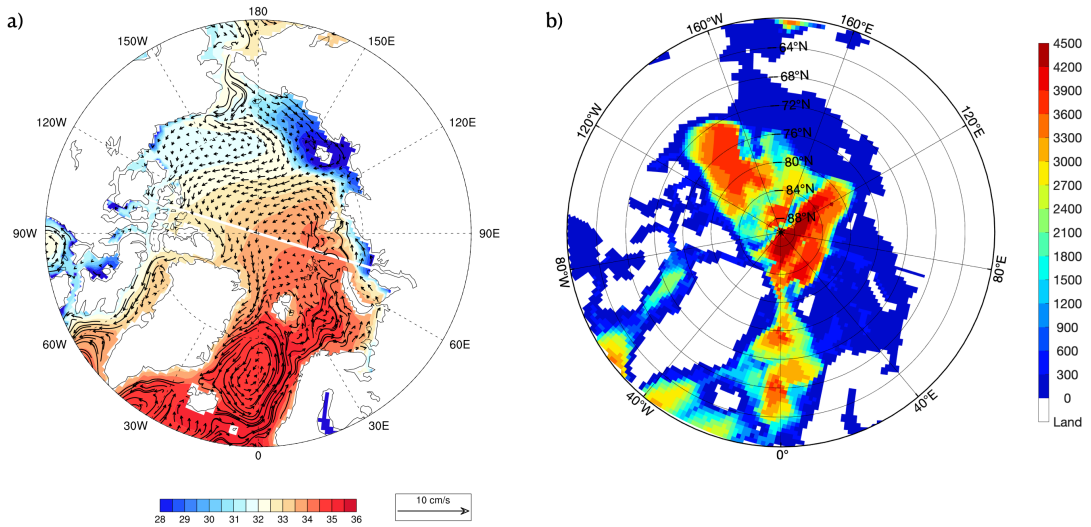

Figure S2. (a) Top 150m mean salinity (in colors), in psu, and current (in black curved arrows), in $cm \cdot s^{-1}$. (b) The bathymetry of the model, in m.

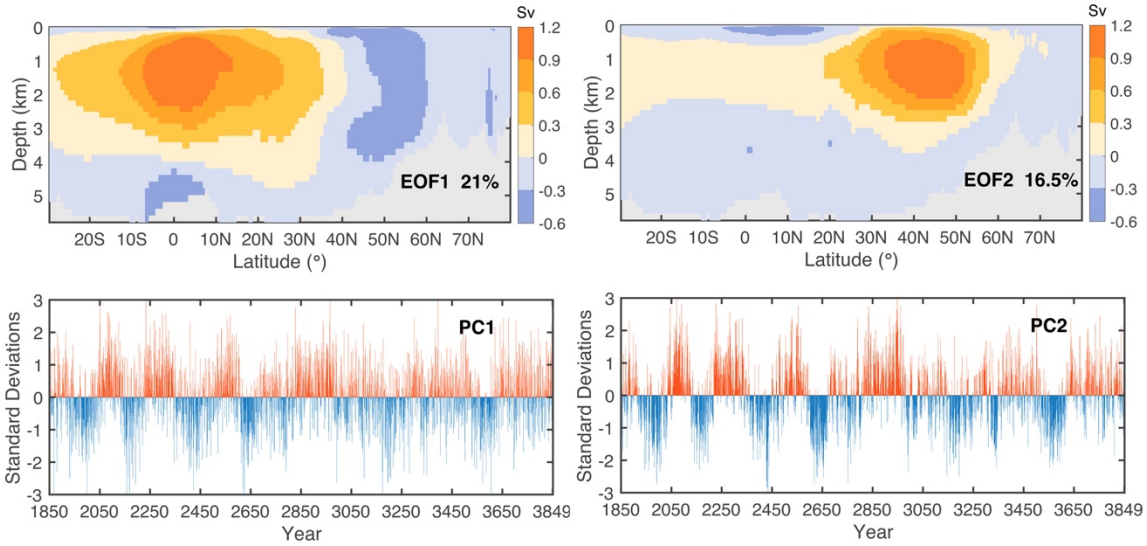

Figure S3. (Top left) First empirical orthogonal function (EOF1) of the Atlantic meridional streamfunction, in Sv, and (bottom left) associated normalized principal component (PC1). Right panels are the same as left panels, but for the second EOF and PC. The variance explained (in %) is provided by the numbers in top panels.

3.4 Conclusion and discussions

In Chapter 2.3.2, we have introduced that some studies attribute the AMOC variability on multidecadal timescales (longer than 50 yr) to the salinity anomalies originating in the tropical Atlantic or the Southern Ocean. Our study found that salinity anomalies associated with AMOC changes are confined to the Atlantic north of 20°N and not significantly related to the tropical Atlantic or the South Atlantic (Figure 5a in the article). Jackson and Vellinga (2013) also suggested the importance of the salinity anomalies in the Arctic Ocean driven by the stochastic SLP (see Chapter 2.3.2 and Figure 2.8). We, however, proposed that the atmospheric forcing is minor as the amplitude of SLP anomalies is small, at 40 Pa at maximum (Figures 5b and c in the article). Here, we further examined the wind field over the Arctic Ocean. The climatological mean summer winds are anticyclonic and up to ~ 1 m s^{-1}, especially over the Beaufort Sea (Figure 3.1). The mean wintertime winds are strongly westward. But the wind anomalies in both seasons are weak (~5 cm s^{-1}) compared to the mean winds, and they are nowhere statistically significant. Therefore, we believe that in IPSL-CM6A-LR, the atmosphere plays a marginal role in driving the AMOC variations.

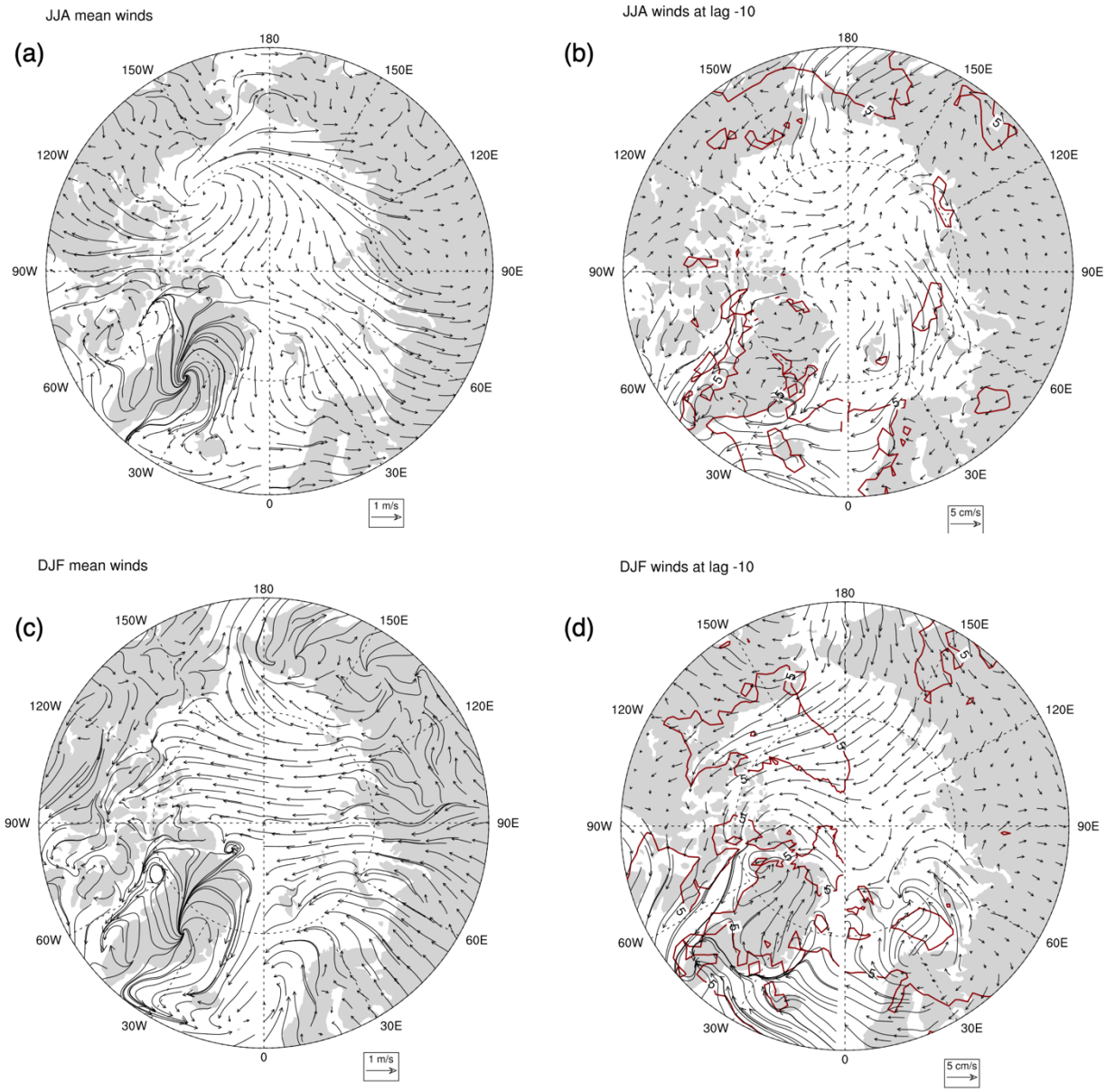

Figure 3.1. (a) Climatological mean winds, in ms^{-1}, in June, July, and August (JJA). (b) Regression of JJA winds, in cms^{-1}, onto AMOC LFC1. (c – d) the same as (a – b) but for December, January, and February (DJF). Red contours in (b) and (d) indicate the significance level of 95% for the longitudinal velocity.

3.5 Simplified model for the freshwater recharge mechanism

Here we propose a conceptual model to summarize the mechanism for centennial variability found in the IPSL-CM6 GCM, and potentially yield some insight into the parameters setting the timescale of the AMOC fluctuations.

As shown in the paper, the key driver of the AMOC strength *AMOC* is the surface salinity in the Nordic Seas and around Greenland *G':*

$$\frac{\partial \mathrm{AMOC}}{\partial t} \sim \mathrm{G}' \tag{3.1}$$

The AMOC being driven by density anomalies at the convection sites downstream of *G'* is consistent with the observed phase relationship between anomalies at the Fram Strait and AMOC. For instance, the occurrence of positive salinity anomalies in the Greenland Sea leads the AMOC by 40 years and lasts from lag -40 to lag 20 (Figure 6 in the article). This is consistent with the freshwater transport through the Fram Strait peaking when leading the AMOC by 40-yr and decreasing until the AMOC leads by 40-yr (Figure 8c in the article). Other impactors, such as stochastic forcing, rainfall, and runoff, can be considered damping terms.

The Greenland Sea salinity anomaly *G'* is in turn driven by different advective terms, which can be expressed as:

$$\frac{\partial G'}{\partial t} \sim V'\overline{\delta S} + \bar{V}A' + \alpha_S\, AMOC \tag{3.2}$$

The first term on the right-hand side represents the anomalous advection of the mean salinity gradient in the Arctic $\overline{\delta S}$ by the anomalous current along Greenland V'. Note that *V'* is taken positive here if the East Greenland current is weak, and $\overline{\delta S}$ is positive. So a weak Greenland current leads to less freshwater export from the Arctic, and salty anomalies *G*'. The second term represents the extension of the central Arctic freshwater anomaly to the Lincoln Sea north of Greenland driven by the transpolar drift (Figure S2 in supplementary and Figure 6 in article). The mean current $\bar{V}$ measures the mean intensity of this transpolar drift, and A' is the salinity anomaly in the central Arctic. Finally, the last term represents the anomalous salinity brought in the Nordic Seas by the anomalous AMOC circulation, the classical AMOC "internal salinity feedback".

We further suppose that the anomalous current around Greenland is in thermal wind balance with the anomalous salinity gradient between the coast and the central Arctic:

$$V' \sim \gamma(G' - A') \tag{3.3}$$

where γ depends on the Coriolis factor f, gravity g (notations same as previous), and the halocline depth.

Finally, the equation for the central Arctic salinity anomaly *A'* is:

$$\frac{\partial A'}{\partial t} \sim -\alpha_T \, AMOC - \bar{V} A' \tag{3.4}$$

where the first term represents the impact of AMOC-related heating on surface freshwater fluxes – mostly due to less sea-ice export – with an intensity α_T, and is driving the freshwater anomaly. The second term is the export by the mean currents (transpolar drift) advecting this anomaly towards Greenland. As there is a large cancellation between the surface freshwater flux and the oceanic transport (Figure 8e in the article), the evolution of *A'* is much smaller than either term. We then have approximately

$$A' \sim -\frac{\alpha_T}{\bar{V}} AMOC \tag{3.5}$$

which is consistent with the observed phase relationship between AMOC intensity and surface freshwater content in the Arctic.

Solving his system for *AMOC,* we find:

$$\frac{\partial^2 \mathrm{AMOC}}{\partial t^2} = \left(\alpha_S + \gamma \overline{\delta S}\right) \frac{\partial \mathrm{AMOC}}{\partial t} - \mathrm{AMOC}\, \alpha_T \left(1 - \frac{\gamma \overline{\delta S}}{\bar{V}}\right). \tag{3.6}$$

We thus have two main feedback loops, corresponding to the two terms on the right-hand side:

- A positive loop given by the first term on the right-hand side, involving *AMOC, G'*, and *V'*, similar to the AMOC internal salinity feedback given by α_S, plus the weakening of the East Greenland current decreasing the Arctic freshwater export.
- A slower, delayed negative loop, given by the second term, involving the buildup of *A'* by the AMOC, and its subsequent discharge by $\bar{V}$.

One key parameter that controls the timescale appears to be $\left(\gamma \overline{\delta S} - \bar{V}\right)$ (second term), that is, given a central Arctic anomaly *A',* the competition between the mean current transporting the anomaly towards Greenland, and the geostrophic anomalous current that maintains the salty anomalies at the Greenland coast. If the two are close, the resulting timescale can be much longer than either mechanism by itself.

While this simple model reproduces some key phase relations between some variables of the GCM, and gives a possible mechanism for the long time-scale of the AMOC variations, it would still need to be validated quantitatively, for example by estimating its different parameters from regressions using the GCM outputs.

Except for the investigation and discussion of the driving mechanism of the AMOC centennial to multicentennial variability, in the article, we also examined its climate impact with

the statistical analysis using the control simulation. The second part of my PhD will be presented in the next chapter: a study of the climate response to the AMOC changes with a series of experiments in the same model.

Chapter 4

Contents

4 EXPERIMENTAL DESIGN TO INVESTIGATE THE INFLUENCE OF LOW-FREQUENCY AMOC VARIABILITY ON CLIMATE 82

4.1 INTRODUCTION 82
4.2 A METHOD TO IMPLEMENT A FLOW FIELD CORRECTION 84
4.3 ADJUSTMENT OF THE PARAMETERS 86
4.3.1 CORRECTION STRENGTH: α 86
4.3.2 LOCALIZATION OF β 90
4.3.3 CUTOFF DEPTH 92
4.4 PERFORMANCE OF CONTROL RUN 94

4 Experimental design to investigate the influence of low-frequency AMOC variability on climate

The proposal of my PhD is to investigate the role of the ocean in the North Atlantic climate variability on long timescales. We have shown in detail the mechanisms driving the Atlantic overturning circulation variability on centennial to multicentennial scales, emerging in the IPSL-CM6A-LR *piControl* simulation. This chapter focuses on the climate response to the AMOC variations.

4.1 Introduction

The investigation of the climate response to the centennial AMOC was studied using regressions in the control simulation in the previous chapter. However, regressions cannot distinguish causality. Furthermore, the AMOC impacts might depend on the mechanism generating the variability. The AMOC impacts related to the multi-centennial variability might not apply to the decadal or multidecadal variability.

Many model studies use water hosing experiments to isolate the impact of the AMOC variations from the fields driving the AMOC changes. Anomalous freshwater flux or equivalent negative salinity flux is applied to some regions of the Atlantic Ocean to generate a weakened

AMOC and explore its impact on the climate (e.g., Hawkins et al., 2011; Jackson and Wood, 2018; Mignot et al., 2007). Jackson et al. (2017) found that the response of AMOC to the input freshwater flux is sensitive to the method by which the freshwater input is compensated. For instance, the compensation can be applied at the surface or throughout the volume. In addition, the application of a large amount of freshwater forcing makes it difficult to disentangle the relative contribution of the dynamical ocean response from the freshening of the Atlantic Ocean itself. Therefore, a method that can better constrain the AMOC and clearly distinguish between forcing and response is needed to better understand the climate response to the AMOC variations.

4.2 A method to implement a flow field correction

Here, we will present the method adopted in the PhD to constrain the AMOC in a fully coupled climate model.

In ocean dynamics, a widely adopted approach is to split the oceanic flow into a depth-independent portion, referred to as the barotropic flow, whose density is only a function of pressure, and the deviation, called the baroclinic flow. In conventional wind-driven ocean circulation theory, barotropic flow is the flow in dynamical balance with the sea surface slope. The baroclinic component is instead generated by the density distribution due to different temperatures and salinity. The AMOC is almost a baroclinic flow with varying density and velocity with the depth, as it is usually measured in the depth-latitude diagram (shown by the zonal mean stream function in Chapter 2). In this work, we control the AMOC by constraining the baroclinic component with prescribed density in the momentum equations.

In the NEMO model, the primitive equation for the local horizontal velocity U_h vector is given by:

$$\frac{d\boldsymbol{U_h}}{dt} = -f\,\boldsymbol{k} \times \boldsymbol{U_h} - \frac{1}{\rho_o}\nabla_h \boldsymbol{p} + D + F, \qquad (4.1)$$

where t is the time, ρ_o is a reference density, p is the pressure, f is the Coriolis acceleration, and k is the local upward vector. D denotes the small-scale physics for momentum and F the surface forcing terms. The first term on the right-hand side is the Coriolis force term, and the second term is the pressure gradient term.

The total pressure at a given depth z is composed of a surface pressure p_s at a reference geopotential surface $(z = 0)$ and a hydrostatic pressure p_h:

$$p = p_s + p_h. \qquad (4.2)$$

The former surface pressure is given by:

$$p_s = \rho g \eta \qquad (4.3)$$

with η denoting the sea surface height and ρ the *in situ* density of the seawater.

The latter depth-dependent pressure is computed as an integral from the depth z to the surface based on the hydrostatic hypothesis:

$$p_h = \int_{\varsigma=z}^{\varsigma=0} g\rho(T,S,\varsigma)d\varsigma \qquad (4.4)$$

where ς is the vertical coordinate. S and T denote the salinity and potential temperature of the seawater, respectively. g is the gravity. p_s is the barotropic part of the pressure and p_h denotes the baroclinic pressure. The corresponding flows are the barotropic and baroclinic flows.

In this study, to explore the influence of the oceanic flow with the same IPSL-CM6A-LR model, we constrain the baroclinic currents in the North Atlantic using the flow-field correction method derived from Drews et al. (2015). The method was initially developed to correct the displacement of the North Atlantic Current by Drews et al. (2015) and Drews and Greatbatch (2016, 2017). It is referred to as the flow-field correction, following the terminology of Drews et al. (2015) and the other two studies.

As shown by Equation 4.4, the density ρ depends on the salinity and potential temperature. The flow field correction is implemented by replacing the *in situ* model density ρ_m in the computation of the pressure gradient and the horizontal component of the flow in Equation (4.1).

The *in situ* model density ρ_m is replaced with a linear combination of ρ_m and input *in situ* density ρ_i:

$$\rho = (1 - \alpha\beta)\rho_m + \alpha\beta\rho_i \qquad (4.5)$$

where α is a fixed scalar parameter. α indicates the percentage of the external input density ρ_i to the total combined density ρ. β is a two-dimensional field indicating the region used for the flow filed correction. This procedure is only applied from the surface to a certain depth. α, β, and the cutoff depth need to be carefully tested to use the flow field correction. It is important to note that the density is only modified when calculating the pressure gradient term and is otherwise not modified in the ocean models.

We aim at constraining the AMOC in the extratropical North Atlantic, where the baroclinic flow is dominant. In the tropics, the wind-driven barotropic flow is likely more important (see Chapter 1.4). To specify the region to which the input density is applied, we use the value β as 1 or 0 to switch on or off the flow field correction. We also build smooth transition zones with β varying from 1 to 0 at the meridional boundaries of the constrained region.

The input density ρ_i is computed from two three-dimensional fields that are read during the integration of the model. These fields are the conservative potential temperature and absolute salinity. The input density is then calculated *on-line* by the state equation in the model. The model used to investigate the influence of AMOC is still IPSL-CM6A-LR (see section 3.2 for more details). To avoid mismatches between the input data and model data when using such flow field correction, the input conservative temperature and absolute salinity are derived from the same model.

4.3 Adjustment of the parameters

For testing purposes, we used an input density calculated with the climatological monthly salinity and temperature computed from the IPSL-CM6A-LR *piControl* simulation. Specifically, we use the first 1200-year of the 2000-year simulation. But we expected only a few differences using the climatology calculated from the whole 2000-yr run.

Sensitivity experiments are used to confirm the choice of three parameters, i.e., the scalar parameter α, the distribution of β, and the cutoff depth. We next compare the results from the sensitivity experiments with the long-term (1200-year) *piControl* run, hereafter referred to as CTL-CM.

4.3.1 Correction strength: α

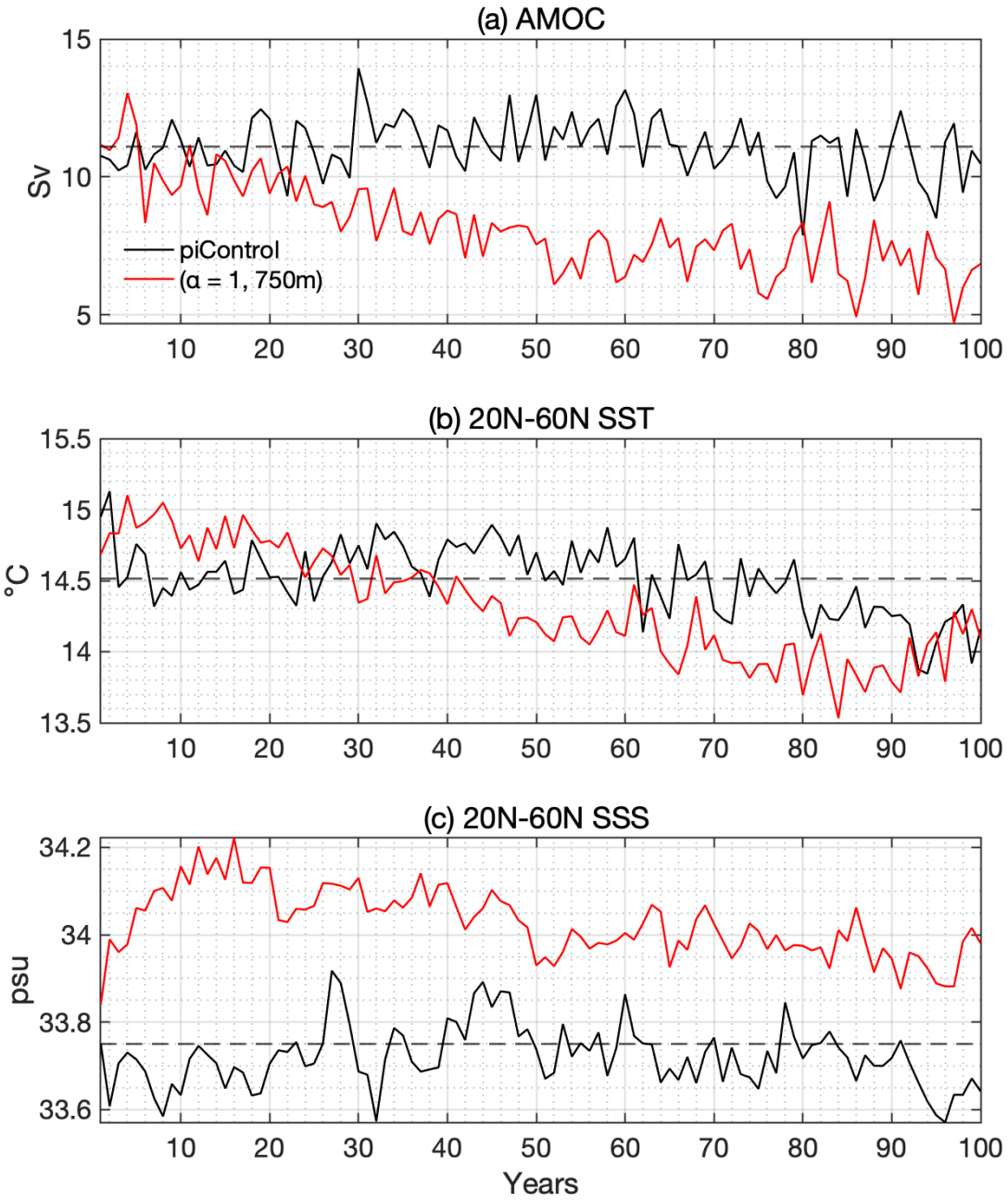

Figure 4.1. Yearly mean (a) AMOC, (b) SST, and (c) SSS averaged over 20°N and 60°N in the Atlantic basin. The solid black lines indict the CTL-CM and red lines show the corrected simulation with α of 1 and a cutoff depth of 750m. Dashed black lines represent the climatology from CTL-CM. The input data is climatology.

We first did a series of tests using a baroclinic flow field fully corrected (α = 1) with a cutoff depth of 750 m. We then focused on the simulated AMOC, the temperature, and salinity in the North Atlantic to evaluate the simulations. The AMOC strength is defined as the maximum streamfunction over the whole depth at 30°N. We compare pairs of runs starting from the same

initial conditions, one fully-coupled run (a portion of the *piControl* control run), and one run including a flow filed correction. In a first simulation, the AMOC decreases from ~11 Sv to ~6 Sv within 100 years (Figure 4.1a). The associated SST in the North Atlantic reduces from 14.7°C to 14.1°C (Figure 4.1b). Apparent drifts exist in the AMOC and SST over the North Atlantic. The SSS shows a swift increase in the first 20 years and then drifts toward a freshening. The simulated salinity is largely higher than the climatology or SSS from CTL-CM in the same period (Figure 4.1c).

We then modified the value of α to see whether such drift toward a weaker AMOC and a warmer North Atlantic Ocean is modified. The values 1, 0.9, 0.7, 0.5, and 0.3 are tested.

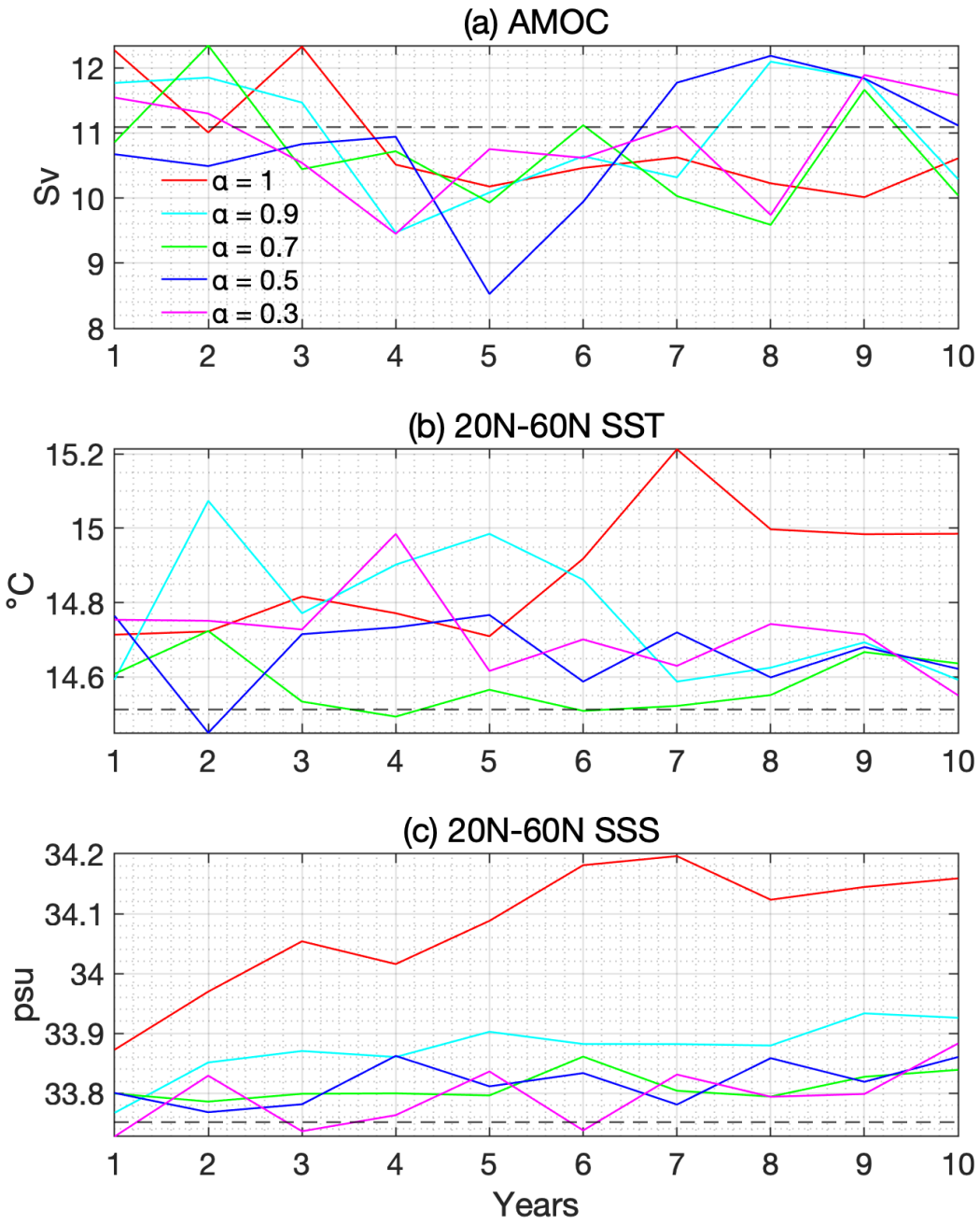

Figure 4.2. Yearly mean (a) AMOC (in Sv), (b) SST in (°C), and (c) SSS (in psu) averaged over 20°N and 60°N in the Atlantic basin, from simulation with α of 1, 0.9, 0.7, 0.5, 0.3 respectively. Dashed black lines represent the climatology from CTL-CM. The cutoff depth is 1000m. The input data is climatology.

Figure 4.2 shows the simulated AMOC, SST, and SSS with different α. Note that the cutoff depth is 1000 m in these five experiments. There are smaller modifications of these three oceanic fields when using small α values, at least in the first 10 years of simulations. Nearly all runs show an increase in SST and SSS compared to the climatologies. When α is 1 and 0.9, the difference

between simulated SST/SSS and climatology is relatively larger than when α is 0.7, 0.5, and 0.3. There is no similar tendency in the AMOC. To maintain an effective correction and constrain the currents to the greatest extent, we choose α = 0.7 because it leads to only a few perturbations of the mean state. In the following (Chapter 4.4), a multi-centennial run has proven that the simulation with α = 0.7 shows negligible drift.

4.3.2 Localization of β

β is used to apply the flow field correction only in the North Atlantic Ocean. Transition zones are set between 10°N and 20°N, and between 60°N and 70°N. Out of this region, the flow is not constrained. However, as the flow field correction might affect the coastal Kelvin wave, which is important for the AMOC equilibration (Zhang, 2010), we tested two different distributions of β with and without smoothing at the western and eastern boundaries (Figure 4.3).

In order to maximize the correction, α is set as 1 here. In this case, the original model density is entirely replaced by the input density. The cutoff depth is 750 m. The two simulations with different β (Figures 4.3a and b) last for 30 years each.

Unfortunately, we misleadingly used the non-conservative temperature and practical salinity rather than conservative temperature and absolute salinity that satisfy the equation of state in the model. Therefore, the results in these two experiments (Figure 4.3) should be interpreted with caution. When the western and eastern boundaries are fully constrained, the simulations using α = 1 and correct input data have been shown previously (see Figures 4.1 and 4.2). The simulated AMOC is weaker when compared to the CTL-CM or the climatology. With the same α but improper data, the AMOC anomaly presents a more massively reduced and extended pattern in the latitude (Figure 4.3d). The negative anomaly extends downward to the 2000 m depth.

When the western and eastern boundaries are smoothed out, the AMOC shows a lighter reduction around 30°N, where the strongest WBC is located, and is more weakened south of 30°N and north of 40°N. The negative anomaly is also shallower, confined to the top 1500 m of the ocean (Figure 4.3c). However, we do not know whether the differences are due to the smoothed boundaries or to the improper data. The choice of β needs further tests.

We decided arbitrarily to fully constrain the flow field in the eastern and western boundaries. The distribution of β shown in Figure 4.3 panel b is used in the following experiments. The input data is only misused in this subsection 4.3.2 and not in the following sections.

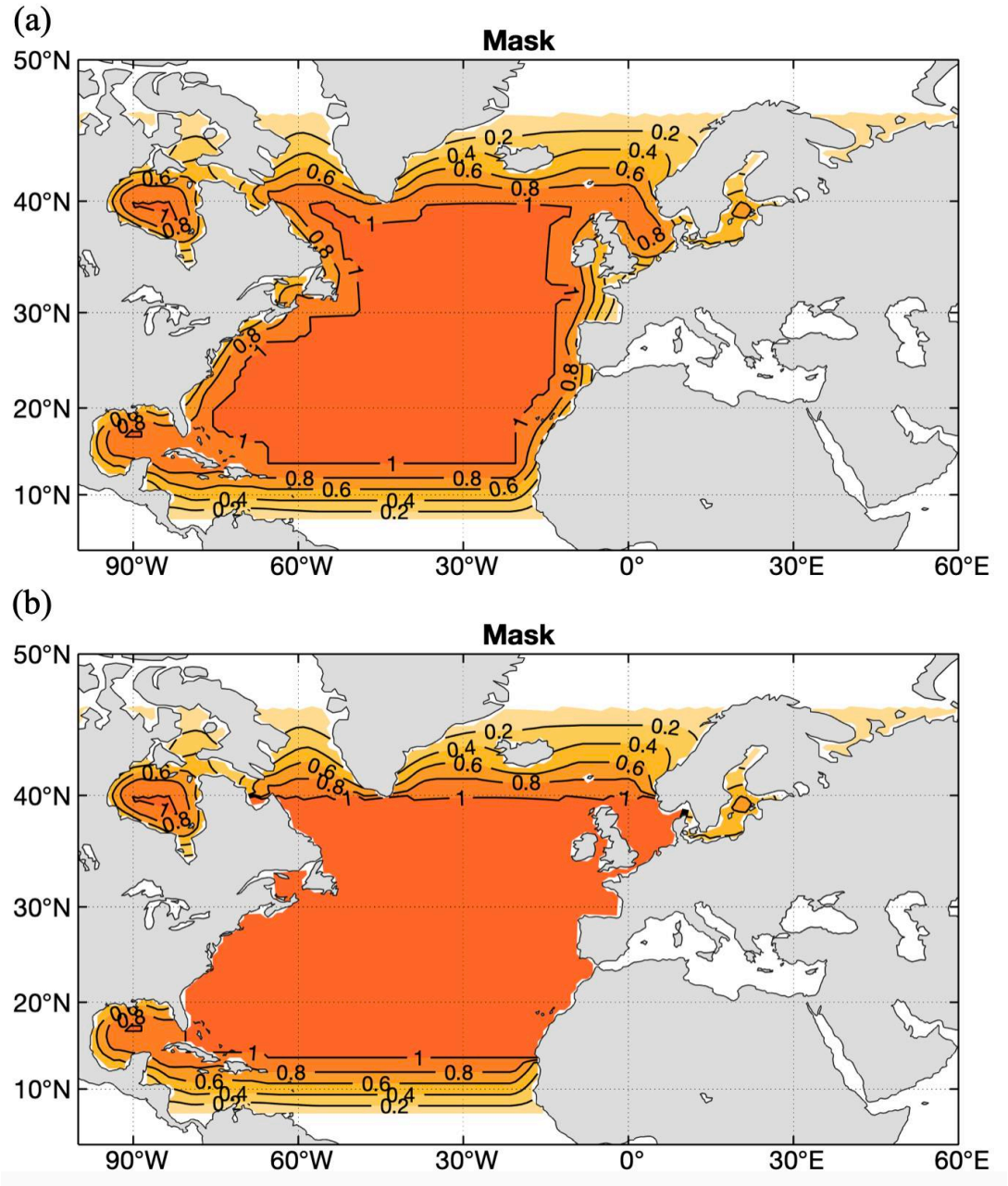
(a)
Mask
50°N
40°N
30°N
20°N
10°N
90°W
60°W
30°W
0°
30°E
60°E
(b)
Mask
50°N
40°N
30°N
20°N
10°N
90°W
60°W
30°W
0°
30°E
60°E

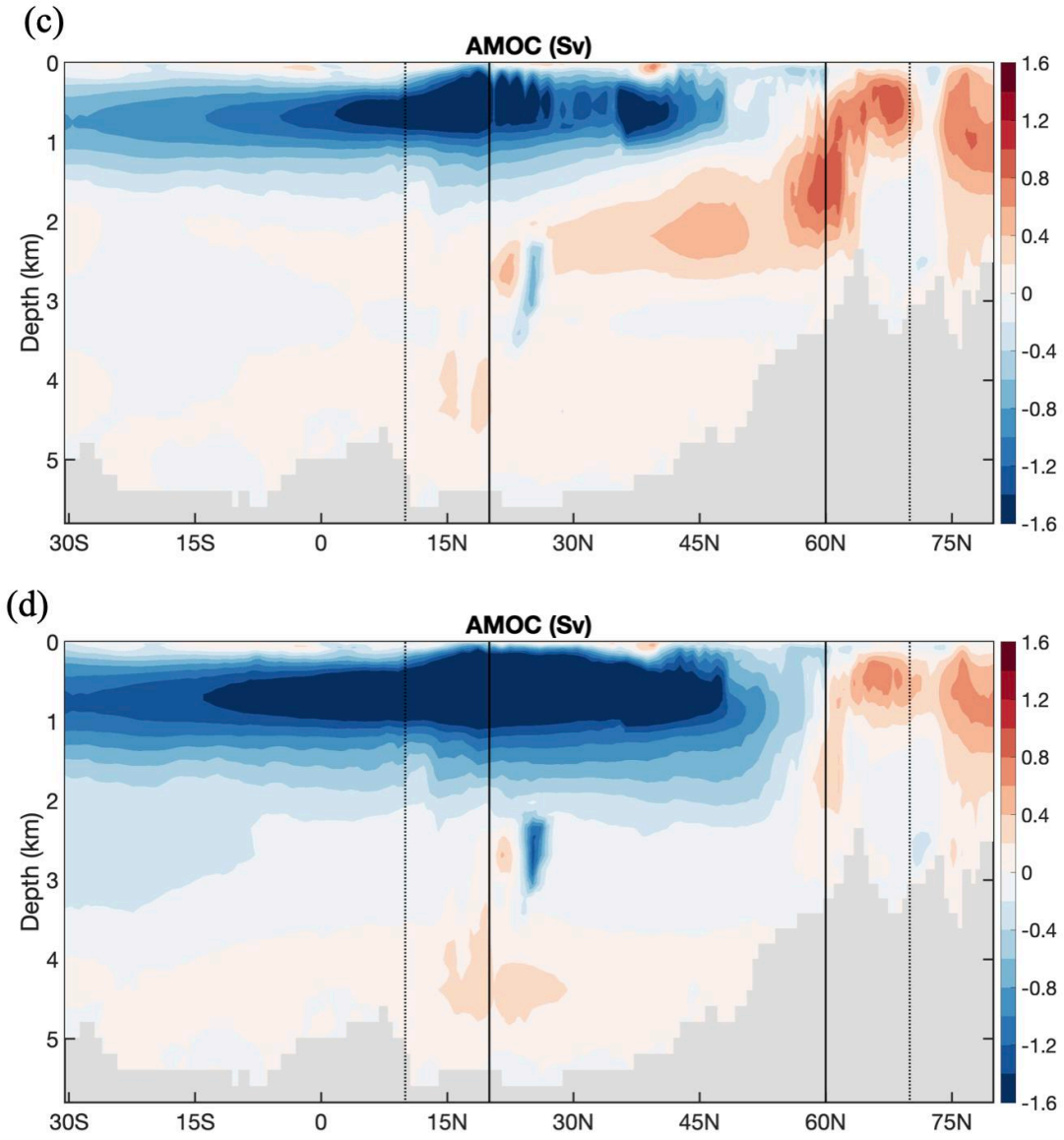

Figure 4.3. (a - b) Distribution of parameter β (a) with and (b) without transition zones at eastern and western boundaries. (c) Departures of the mean AMOC from the 1200-y climatology from CTL-CM in a simulation using β defined as (a). (d) Same as (c) but for a simulation with β as defined in (b). The two solid vertical lines indicate the fully constrained area. Dotted lines show the edge of transition zones.

4.3.3 Cutoff depth

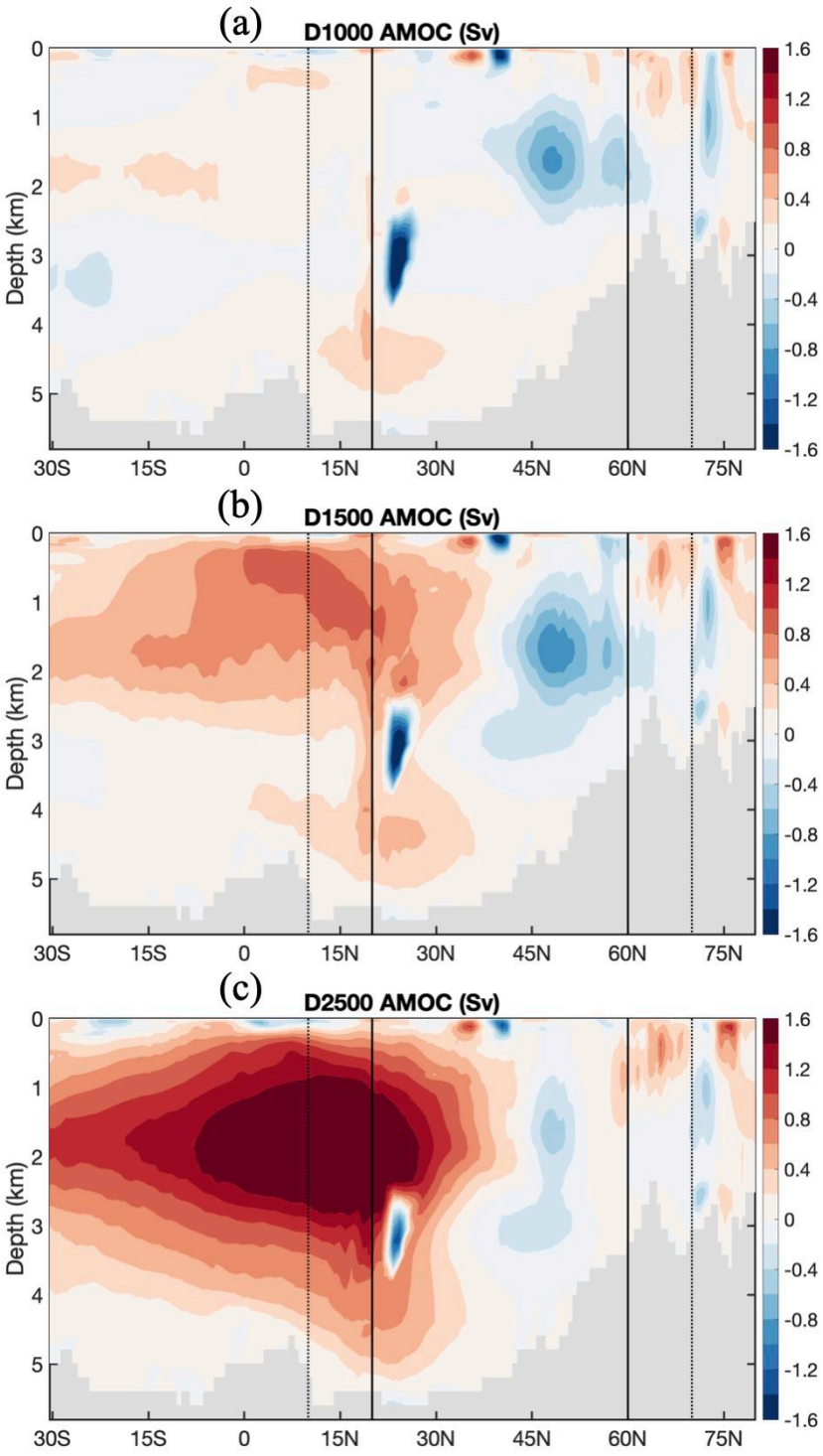

Figure 4.4. The difference between simulated AMOC and the climatology from CTL-CM (the former minus the latter), in Sv, when the cutoff depth is (a) 1000 m, (b) 1500 m, and (c) 2500 m. Each simulation runs for 10 years. Two solid vertical lines indicate the fully constrained area, and dotted lines show the edge of transition zones.

Different cutoff depths were tested with the chosen α (value of 1) and β (no transitions in zonal boundaries). The input density is also calculated from the climatological CTL-CM temperature and salinity. We did 3 runs with a duration of 10 yr with the cutoff depth of 1000 m, 1500 m, and 2500 m, respectively. The meridional streamfunction difference with the CTL-CM simulation is shown in Figure 4.4.

The anomalies are smaller than 1 Sv when the cutoff depth is 1000 m, except for the negative anomalies situated at 3000m and 25°N (Figure 4.4a). Such strong and sharp negative anomalies might result from the slow adjustments of the DWBC to the constraints applied in the upper layer. The flow field correction is applied deeper in the ocean when the cutoff depth increases. Ideally, the correction should only apply to the upper limb of the AMOC, and the lower limb is expected to adjust to the changes imposed on the upper levels. For cutoff depth larger than 1000 m, the AMOC differences with the CRL-CM show a larger amplitude, and the maximum anomaly locates at a deeper depth (Figures 4.4b and c). Moreover, the anomalies concentrate on the tropical to subtropical North Atlantic, where the barotropic flow is important. It may not satisfy our purpose to constrain the AMOC in the extratropical North Atlantic, where the baroclinic current dominates. Considering the amplitude and location of the anomaly, we use the cutoff depth as 1000 m in the following.

4.4 Performance of control run

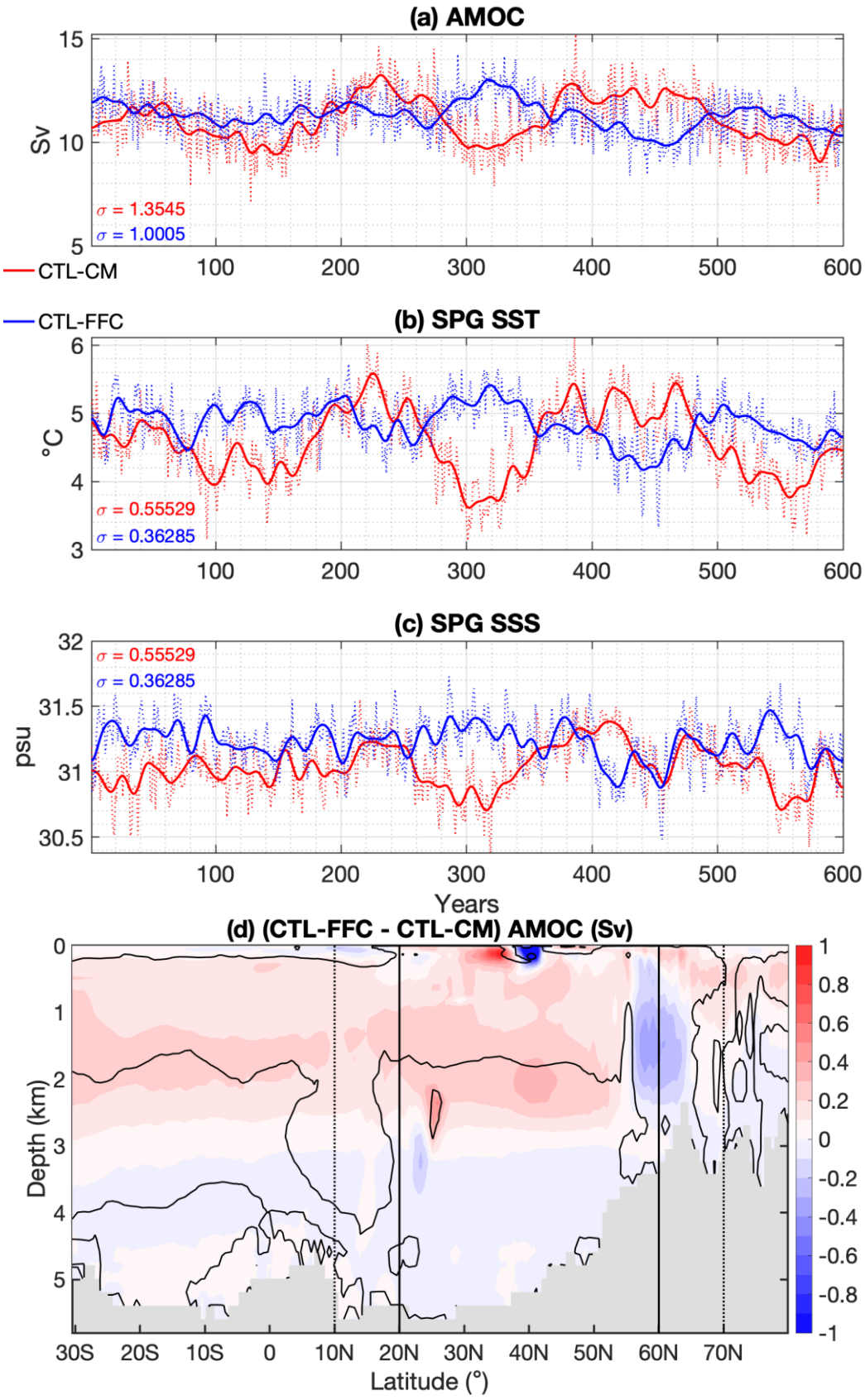
(a) AMOC
Sv
σ = 1.3545
σ = 1.0005
CTL-CM
CTL-FFC
(b) SPG SST
°C
σ = 0.55529
σ = 0.36285
(c) SPG SSS
psu
σ = 0.55529
σ = 0.36285
Years
(d) (CTL-FFC - CTL-CM) AMOC (Sv)
Depth (km)
Latitude (°)
30S
20S
10S
0
10N
20N
30N
40N
50N
60N
70N

Figure 4.5. Comparison between the control simulation with and without flow-field correction. Yearly mean (a) AMOC (in Sv), (b) SST in (°C), and (c) SSS (in psu) averaged over the subpolar gyre between 50°N and 70°N in the North Atlantic, from CTL-CM (in red) and CTL-FFC (in blue). Dotted lines depict yearly time series, and solid lines use 20-y Butterworth lowpass filtered data. Numbers in red and blue indicate the standard deviation of raw timeseries. (d) The difference between simulated AMOC from 600-y control simulation CTL-FFC and the AMOC from CTL-CM (the former minus the latter), in Sv. Black contours indicate the 95% confidence level using student t test assuming equal variance. Two solid vertical lines indicate the fully constrained area, and dotted lines show the edge of transition zones.

As revealed by the test experiments, the smooth transition zones are only set at the northern and southern boundaries to make the important WBC fully constrained. α is chosen as 0.7 to maintain a strong correction and avoid the potential drift when the correction is even stronger. The cutoff depth is 1000 m, in which configuration the simulated AMOC pattern is the most idealized. This set of parameters is adopted in all following experiments. The control simulation with input climatological temperature and salinity is extended to 600 years, referred to as CTL-FFC hereafter.

We assess the performance of CTL-FFC by comparing the key elements to the CTL-CM during the same period. The AMOC shows no apparent drift in CTL-FFC (Figure 4.5a), confirming the choice of α as 0.7 compared to results using α =1. The variability is weaker in CTL-FFC, as the standard deviations in the AMOC are smaller (indicated in the top left corner of Figure 4.5a). SST and SSS in the North Atlantic indicate consistent long-term mean between CTL-FFC and CTL-CM, but these three variables all suggest a modest amplitude of variability with flow fields being constrained to the climatology, which is confirmed by the standard variations (Figures 4.5a-c).

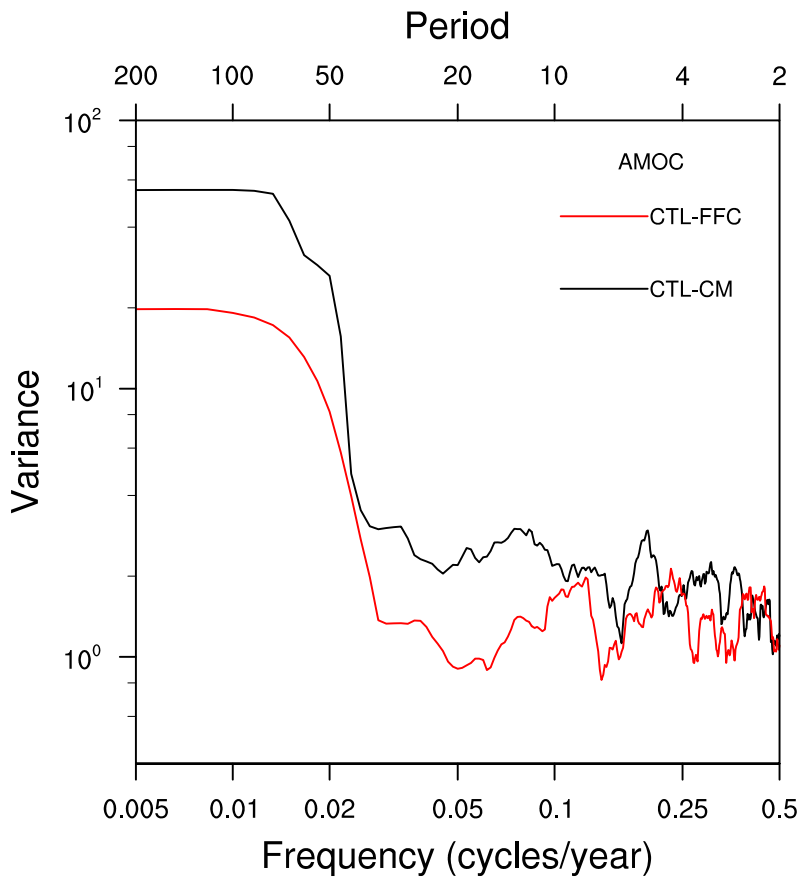

Figure 4.6 The variance-frequency spectrum of AMOC from CTL-CM (in black) and CTL-FFC (in red).

Spectrum analysis of the AMOC indeed shows a clear reduction in the variance for periods longer than 10 years (Figure 4.6). The centennial variations of the AMOC in CTL-FFC are reduced effectively as the currents are corrected by the climatological state. The variability in CTL-FFC is about one-third of that in CTL-CM for a period longer than 100 yr. The analysis of these time series indicates that the decadal to centennial variability is damped in CTL-FFC. But some decadal variability remains in CTL-FFC. This can be linked to the fact that the flow is only partly constrained, as 30% (1- $\alpha = 0.3$) of the original model density is not constrained in calculating the horizontal flow.

We also inspect the AMV here. The AMV index is defined as the 10-y Butterworth lowpass filtered area-weighted average of residual SST anomalies over the North Atlantic from 0 to 65°N and from 80°W to 0°W. The patterns of SST anomalies regressed onto the AMV index in the two simulations are similar, but the amplitude in CTL-FFC is smaller, at 3°C versus 4°C in CTL-CM (Figures 4.7 a and b), likely resulting from the damped variability of AMV in CTL-FFC. As shown in Figure 4.7c, the AMV experiences a similar decrease of variability at the centennial scale, while on periods shorter than 50 years, two simulations exhibit comparable variance. This relatively

unchanged variance on shorter scales may be attituded to feedback through the density and salinity, as the currents are only partially constrained. For instance, the fluctuations in the Arctic sea ice may be linked to the AMV via the anomalous propagation of salinity on multidecadal scales (Frankcombe and Dijkstra, 2011; Jungclaus et al., 2005) and through the atmospheric teleconnections (Castruccio et al., 2019). But a more precise explanation remains established.

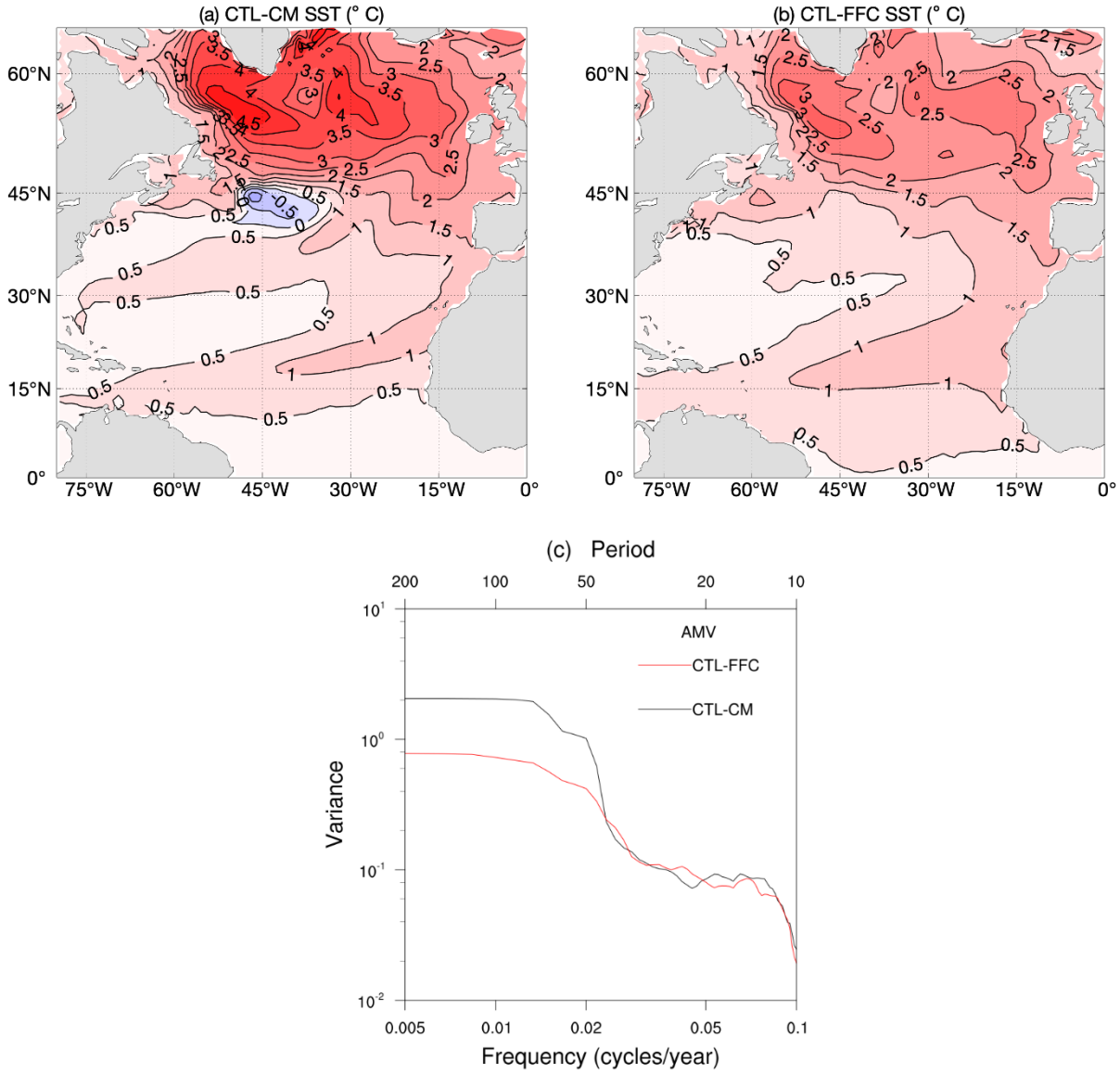

Figure 4.7 SST regressed onto the AMV in (a) CTL-CM and (b) CTL-FFC. AMV is defined as 10-y lowpass filtered SST averaged over the North Atlantic from 0 to 65°N and from 80°W to 0. (c) The variance-frequency spectrum of AMV from CTL-CM (in black) and CTL-FFC (in red).

The AMOC positive anomalies concentrate within the corrected area and extend to the uncorrected regions (Figure 4.5d). The anomaly is ~0.3 Sv, except for a strong dipole anomaly near the surface between 35°N and 45°N. We speculate that this dipole anomaly might be related to the intensified Gulf stream and associated displacement of the eastward North Atlantic Current. The weakened surface current likely leads to the southward extension of the subpolar gyre (Figure 4.7). The weakened AMOC variability is consistent with the reduced amplitude of SST anomalies associated with the AMV as the oceanic circulation is generally considered as part of the cause of the AMV (Figures 4.7a and b; Zhang et al., 2016).

In summary, the flow-field correction method successfully brings the AMOC to the input state, and the simulation runs without drift when 30% of the AMOC is not constrained. We next constrain the AMOC with circulation conditions associated with an intensified or a weakened AMOC computed from the same 1200-y from CTL-CM to produce a corresponding strong or weak AMOC state and study the impacts on climate.

Chapter 5

Contents

5 RESPONSE OF CLIMATE TO AMOC LOW-FREQUENCY VARIATIONS..... 100

5.1 INTRODUCTION 100
5.2 ARTICLE 100
5.3 DISCUSSION 146

5 Response of climate to AMOC low-frequency variations

5.1 Introduction

In Chapter 3, we have presented the driving mechanism of the low-frequency AMOC variability that emerged in the 2000-year IPSL-CM6A-LR *piControl* simulation. The second part of my PhD is to investigate the impacts of this AMOC variability on the climate, using novel sensitivity experiments and diagnostics of the energy flow in the climate system. This study uses the same model as Chapter 3, namely, the IPSL-CM6A-LR model. In the following, I present the main results in a manuscript formatted for future submission to the Journal of Climate or Climate Dynamics.

5.2 Article

We use the *on-line* flow field correction procedure presented in Chapter 4 to constrain the Atlantic overturning circulation and investigate the climate response to the changes in the AMOC. The philosophy of the method is to modify the baroclinic component of the oceanic currents through the horizontal pressure gradient. This horizontal pressure gradient is calculated using a well-chosen input ocean density. Here, to simulate an intensified (a weakened) AMOC, we superpose temperature and salinity anomalies associated with a strong (weak) AMOC to the climatology to produce the input density. The anomalies are computed as regressions of the three-dimensional annual mean fields onto an AMOC index. The AMOC index used is the AMOC LFC1, the first low frequency component of the AMOC introduced in Chapter 3. Before being added to the annual climatological cycle, regression coefficients are multiplied by 1.5 (-1.5) to simulate amplified strong (weak) AMOC changes. Therefore, the input anomalies correspond to those associated with

1.5 AMOC standard deviations. The results show that the enhanced AMOC and northward OMET leads to a warmer Northern Hemisphere and a northward shift of the ITCZ. These climate responses are associated with an abnormal direct Hadley cell in 20°S-20°N that settles to transport MSE southward in its upper branch. This southward AMET compensates for the intensified oceanic transport in the tropics and leads to moisture and heat transport northward in the lower branch of the Hadley cell. The associated trade wind anomaly applies a negative wind stress curl over the tropical ocean and drives an anomalous indirect overturning cell in the upper ocean. This oceanic cell can be understood as an anomalous southward Sverdrup transport in the tropical ocean.

Meanwhile, the AMOC-induced anomalous air-sea heat fluxes in the Atlantic basin found in these flow-field constrained simulations are applied in simulations using a slab ocean model (SOM) coupled to the same atmosphere model LMDz. Such experiments allow us to study the role of ocean dynamics in shaping the AMOC impacts by comparison with the analogous AOGCM experiments. The atmospheric responses are similar in the SOM runs, indicating a relatively minor role of the ocean dynamics. However, we also find several differences. The atmospheric variations are of greater amplitudes in the SOM than in the AOGCM, suggesting that ocean circulations seemingly damp the atmospheric response, especially near the equator, where the amplification in SOM is maximum. It coincides with the southward OMET anomaly in the Indo-Pacific peaking at the equator.

In addition, the tropical changes in the SOM experiment are magnified by positive low cloud feedback. In the tropics, the large-scale atmospheric circulation reorganizes with more subsidence south of the equator and more ascent and atmospheric convection north of the equator. This leads to a decrease (increase) of the low cloud amount north (south) of the equator. Low clouds have a large impact on the planetary albedo, so their changes lead to more (less) incoming shortwave north (south) of the equator. Eventually, the energy transport implied by such changes of the radiative flux at TOA is southward in the tropics, reinforcing the southward AMET anomaly.

Climate response to Atlantic meridional energy transport variations

Weimin Jiang[1], Guillaume Gastineau[1], Francis. Codron[1]

[1] UMR LOCEAN, Sorbonne Université/CNRS/IRD/MNHN, Paris, France

Corresponding author: W. Jiang (weimin.jiang@locean.ipsl.fr)

Key Points

- AMOC anomalies are imposed by constraining the baroclinic component of the North Atlantic Ocean currents in an atmosphere-ocean general circulation model.
- Northward Atlantic meridional energy transport anomaly leads to a compensating southward energy transport split between the atmosphere and the Indo-Pacific Ocean.
- Analogous slab ocean model simulations systematically overestimate the tropical climate response to AMOC anomalies, due to the lack of changes in the Indo-Pacific Ocean and a positive tropical low cloud feedback.

Abstract

The climate impacts of fluctuations of the Atlantic meridional overturning circulation (AMOC) variations are studied in an atmosphere-ocean general circulation model (AOGCM). The baroclinic component of the North Atlantic Ocean currents is modified online in two experiments to reproduce typical strong and weak AMOC conditions deduced from a preindustrial control simulation using the same model. These experiments are compared with slab ocean model (SOM) experiments that use heat flux corrections derived from the coupled model in the Atlantic Ocean.

The major impacts of a strong AMOC include a widespread warming in the Northern Hemisphere and a northward shift of the intertropical convergence zone (ITCZ). Slab ocean model (SOM) experiments exhibit a similar atmospheric response to AMOC-related heat flux anomalies but with a much larger amplitude in the Tropics. The atmospheric changes are driven by an anomalous cross-equatorial Hadley circulation transporting energy southward and moisture and heat northward. In the AOGCM, changes in the Indo-Pacific Ocean circulation and heat transport, driven by the wind stress associated with the abnormal Hadley cell, damp the atmospheric response. In the SOM simulations, the lack of Indo-Pacific transport and of ocean heat storage leads to larger atmospheric changes, that are further amplified by a positive tropical low cloud feedbacks.

1. Introduction

The deep overturning circulation in the Atlantic Ocean plays a unique and active role in the global climate system due to the associated oceanic meridional energy transport (OMET). The surface flow of the Atlantic Meridional Overturning Circulation (AMOC) is northward over the whole basin, while the deep return flow originates at the high latitudes and transports relatively cold North Atlantic Deep Water southward to the Southern Ocean. The resulting heat transport overwhelms the one realized by the wind-driven shallow subtropical cells (STC) in the Tropics (Johns et al. 2011), leading to a total Atlantic OMET oriented northward along the whole latitude range from 30°S to 80°N (Buckley and Marshall, 2016; Ganachaud and Wunsch, 2003; Klinger and Marotzke, 2000; Talley, 2003) and peaking at about 1.1 PW at 20°N (Trenberth et al. 2019).

At the decadal time scale and beyond, if the ocean heat storage can be neglected, the atmospheric meridional energy transport (AMET) should compensate for fluctuations or asymmetries in the global OMET to balance the energy budget at the top of the atmosphere (TOA). This phenomenon is known as the Bjerknes compensation (Bjerknes 1964). As the TOA radiative budget is almost symmetrical about the equator, implying nearly zero total transport across the equator, the northward-oriented OMET associated with the AMOC at the Equator is balanced by a southward-oriented AMET. In the tropics, the atmospheric energy transport is dominated by the Hadley circulation. The net moist static energy (MSE) transport is dominated by the geopotential transport that is in the direction of its upper branch. Such MSE transport is partially balanced by heat and water vapor transports in the lower branch of the Hadley cells. The required southward AMET at the equator thus implies northward heat and water vapor transports near the surface, explaining the mean position of the intertropical convergence zone (ITCZ) north of the Equator (Frierson et al. 2013; Marshall et al. 2014). At higher latitudes, fluctuations of the AMOC and associated heat transport may also contribute to opposite changes in the Arctic and Antarctic regions (Blunier and Brook 2001). Palaeo-proxy evidence suggests a slowdown of the AMOC in the twentieth century (Caesar et al. 2021; Rahmstorf et al. 2015; Thornalley et al. 2018), and the AMOC is projected to further slow down or even shut down in the scenario simulations of global warming (Weijer et al. 2020; Jackson et al. 2022). Considering the essential role of OMET in global climate and the tremendous contribution of AMOC to redistributing heat in the Atlantic Ocean, it is necessary to understand the response of the climate to the associated heat transport (Oldenburg et al. 2021).

Continuous instrumental records of the AMOC and its heat transport exist since 2004 at 26°N provided by the RAPID-MOCHA array (Cunningham et al. 2007; Johns et al. 2011; Kanzow et al. 2010). Other observational arrays have been set up in the subpolar gyre (OSNAP; Lozier et al., 2017) or in the South Atlantic (SAMBA), but such observations are recent and are limited to a few years. The OMET at other latitudes (Trenberth and Caron 2001; Trenberth et al. 2019) is usually

deduced from satellite observations of the TOA radiative budget (Barkstrom 1984; Wielicki et al. 1996) combined with ocean heat content (OHC) and AMET estimations. As the knowledge of OHC is still limited in time and space, and significant uncertainties exist in the satellite observation of the earth radiative budget (Kato et al. 2020), climate models are used to study the impact of the OMET and AMOC on the climate at decadal to centennial time scale.

The climate impacts of the AMOC have previously been investigated using statistical relationships in multi-centennial control simulations of numerous climate models with fixed external forcing (e.g., Delworth and Zeng, 2012; Mahajan et al., 2011; Muir and Fedorov, 2015, 2017). These impacts include a warming of the North Atlantic Ocean surface temperatures, with a local maximum in the subpolar gyre, driven by an anomalously strong AMOC (see Zhang et al., 2019 for a review). A strong AMOC also induces an interhemispheric SST see-saw pattern in CMIP5 models, with cooling in the subtropical Southern Ocean together with North Atlantic warming (Muir and Fedorov 2015). A strong AMOC also shifts the intertropical convergence zone (ITCZ) northward, and, therefore, impacts tropical precipitations (Menary et al., 2012; Moreno-Chamarro et al., 2019; Vellinga and Wu, 2004). Gastineau and Frankignoul (2012) suggested that the anomalous warming in the North Atlantic subpolar gyre decrease the lower tropospheric baroclinity, which induces a negative North Atlantic Oscillation (NAO) – like sea level pressure (SLP) anomalies in winter. The northward heat transport associated with a strong AMOC also lead to Arctic sea ice loss in many models (Day et al., 2012; Delworth and Zeng, 2012; Mahajan et al., 2011; Zhang, 2015). The AMOC was also linked to the main mode of sea surface temperature (SST) variability in the North Atlantic region, known as the Atlantic multidecadal variability (AMV), with positive (negative) AMV phase following a strong (weak) AMOC (Knight 2009; Muir and Fedorov 2015; Ting et al. 2009; Zanchettin et al. 2014; Zhang et al. 2016). Nevertheless, the origin of AMV is debated, as other mechanism are at play, such as the mixed layer response to stochastic atmospheric forcing (Clement et al. 2015), or the influence of aerosol concentration variation (Booth et al., 2012; Watanabe and Tatebe, 2019; Qin et al. 2020).

In this paper, we focus on the results obtained with the IPSL-CM6A-LR model, which exhibits a multi-centennial AMOC variability with important climate impacts (Boucher et al., 2020). This low-frequency variability was found to be driven by the delayed exchanges of salinity between the North Atlantic and the Arctic. In the ascending phase of the AMOC, surface freshwater progressively accumulates in the Arctic Ocean, then reverses the AMOC when it reaches the deep-water formation sites in the North Atlantic (Jiang et al. 2021). During a typical strong AMOC phase, this variability is responsible for mean warming of about 0.4°C in the Northern Hemisphere and 1°C warming in the wintertime Arctic lower troposphere. It also leads to a northward displacement of ITCZ and more summertime rainfall in the Caribbean, African Sahel, and the Indian and Asian monsoon regions and less in Brazil.

Here, we will investigate in more detail the potential mechanisms of the climate response to the AMOC variability through dedicated sensitivity experiments with IPSL-CM6A-LR. Many sensitivity experiments have been analyzed to understand the AMOC climate impacts. Atmospheric experiments using the SST and sea ice anomalies associated with AMOC variability have shown the influence of the subpolar (Gastineau et al., 2016) and tropical Atlantic SST (Montade et al. 2015). However, these experiments do not simulate correct surface or top of the atmosphere fluxes and more generally do not conserve energy, with the ocean acting as an infinite source or sink of heat. Atmospheric experiments coupled with a slab-ocean model (SOM) solve this problem, and have suggested that the global impact of the AMOC anomalies is significant in the tropics (L'Hévéder et al., 2015; Yu and Pritchard, 2019). However, these experiments fail to simulate the oceanic circulation response and overestimate the AMOC impacts (Zhang 2017). Atmosphere-ocean coupled general circulation model (AOGCMs) are therefore needed to understand the AMOC influence through the investigation of meridional energy transports. Many studies implemented "hosing" experiments in which an artificial freshwater flux is applied into the North Atlantic to inhibit deep convection and hence reduce the AMOC strength (e.g., Brunnabend and Dijkstra, 2017; Mignot et al., 2007; Stouffer et al., 2006; Thomas and Fedorov, 2019; Zhang and Delworth, 2005). However, the weakening of the AMOC induced is sensitive to the hosing method adopted (Jackson et al., 2017). These technics also introduce an extra heat/freshwater flux forcing and make it difficult to disentangle the contribution of the dynamical ocean response from the forcing used (Kim et al., 2020; Tandon and Kushner, 2015). A method that can better constrain the AMOC and clearly distinguish between forcing and response is therefore needed to better understand the climate response to the AMOC variations.

In this paper, we constrain the baroclinic currents in the North Atlantic in the AOGCM, using the flow-field correction method derived from Drews et al. (2015). The climate response to the induced AMOC change is investigated and compared to that produced by an equivalent (meaning same OMET in the Atlantic Ocean, the Indo-Pacific being free to evolve) simulation using a SOM. The climate response to an AMOC intensification includes warming in the Northern Hemisphere, a northward shift of the ITCZ, and more precipitation in West Europe and Eastern North America. We found that the anomalous OMET imposed in the Atlantic Ocean is compensated by a southward transport by both the atmosphere and Indo-Pacific Ocean in the AOGCM. In the SOM simulations, the atmospheric response is similar but much stronger as the Indo-Pacific transport remains fixed by construction. Another contribution to the larger tropical response in the SOM is that top-of-the atmosphere radiative feedbacks by clouds and water vapor changes amplify the response.

The paper is organized as follows. Section 2 describes the experimental design for the AOGCM and SOM. The resulting climate response is explored in section 3. Changes in the AMET and

radiative feedback are studied in section 4. Discussion of the results and conclusions are given in section 5.

2. Model and experimental setup

2.1. Coupled model experiments

We use the low resolution coupled model IPSL-CM6A-LR (Boucher et al., 2020), which participated in the CMIP6 experiment (Coupled Model Intercomparison Project Phase 6). Its atmospheric component is LMDZ6, with a horizontal resolution of $1.26° \times 2.5°$ and with 79 levels and a top at 1 Pa. LMDZ6 is coupled to the land surface module ORCHIDEE with the same horizontal grid (Cheruy et al. 2020). The oceanic model is NEMO with the eORCA1 grid with a resolution of about 1°, refined to $1/3°$ in the equatorial and polar regions and 75 levels. The analyses of this study are based on the first 1200-yr of the IPSL-CM6A-LR preindustrial control simulation, hereafter referred to as CTL-CM.

As noted in Boucher et al. (2020), in IPSL-CM6A-LR, the leading deep formation sites are located in the Nordic Seas and the Labrador Sea. The simulated AMOC is slightly weaker than observed, with a strength of 14 Sv, compared to 16.9 ± 4.6 Sv at 26.5°N from the RAPID array observations (McCarthy et al. 2015).

The AMOC represents the zonally-averaged contribution of baroclinic currents in the Atlantic Ocean. Therefore, we constrain the AMOC in IPSL-CM6A-LR simulations by changing the three-dimensional baroclinic current in the North Atlantic. This is realized by replacing in the calculation of the horizontal hydrostatic pressure gradient the raw simulated in-situ density ρ_m with a linear combination of ρ_m and an input in-situ density ρ_i, as presented in Drews et al. (2015) and Drews and Greatbatch (2016, 2017). The baroclinic flow is thus changed by modifying the horizontal pressure gradient force in the model, which then determines the flow in the momentum equations. We only apply this modification from the surface to the depth of 1000 m so that the deep return flow adjusts to the upper ocean changes. The ocean density is only replaced when calculating the pressure gradient force and is not modified elsewhere in the model.

The modified hydrostatic pressure is thus expressed as follows:

$$\frac{\partial p}{\partial z} = -g[(1 - \alpha\beta)\rho_m + \alpha\beta\rho_i]$$

with p, the pressure, z, the depth, and g, the gravity. α is a scalar parameter controlling the intensity to modify the currents, β is a two-dimensional horizontal field with values varying between 0 and 1 to specify the region where the currents will be constrained.

Only currents in the North Atlantic between 20°N to 60°N are constrained (see black contours illustrating β in Figs. S1a-c), with smooth transition zones at the meridional boundaries between 10°N and 20°N, and 60°N and 70°N. Outside of this region, the baroclinic flow is not modified. In the constrained region, α is set to 0.7, so that the baroclinic flow is estimated at 70% by the input density, and the remaining 30% by the model density.

To avoid mismatches between the input data and model data (Drews et al., 2015), we constructed the input density fields using outputs from the CTL-CM simulation of IPSL-CM6A-LR. We calculate the regression of the three dimensional temperature and salinity fields on an AMOC index. The AMOC annual index is the standardized first low-frequency component of the overturning stream-function, called AMOC LFC1 (Fig. S1). The AMOC LFC1 corresponds to a rotation of the truncated AMOC EOFs (empirical orthogonal functions), which explains the maximum low-frequency variability, defined with a cutoff period of 10-yr. This index is associated to a basin-wide AMOC anomalies and shows dominant centennial to multi-centennial variability (see Fig. 1 from Jiang et al. 2021). Similar results are obtained using other indices, such as the lowpass filtered maximum of the meridional overturning streamfunction at 30°N. We regressed the annual time series of the temperature and salinity from all calendar months. These regressions are then multiplied by 1.5 and added or subtracted to the monthly model climatology. The input density used to constrain the AMOC is then calculated on-line by the model's seawater state equation from the temperature and salinity fields.

The run constrained with strong AMOC conditions, referred to as SG, is obtained when adding the anomalies to the climatology of CTL-CM. The run constrained with weak AMOC conditions, called WK, is obtained when subtracting the anomalies to the climatology. All simulations use preindustrial fixed external forcings. To ensure the robustness of the results, WK and SG have three members each and last for 100 yr. The initial states of the three members are sampled in the years 1850, 2000, and 2080 of CTL-CM. It corresponds to neutral, strong, and weak AMOC initial states, respectively (Fig. S1).

The regressions of surface temperature and salinity used to produce AMOC anomalies are shown in Figs. S2a and S2b. Fig. S2c is the corresponding abnormal surface density computed offline from the temperature and salinity. The input sea surface temperature anomaly for SG shows a broad warming in the Atlantic and Arctic Oceans, with a maximum between 0.8°C and 1.4 °C in the subpolar gyre. Similarly, the sea surface salinity anomaly is prominent in the subpolar gyre, as expected due to the intensified northward salt transport. The temperature is locally colder with negative salinity anomalies in the north Atlantic current (NAC), likely associated with the weakening of the North Atlantic subpolar gyre (Zhang 2007). The salinity and density anomalies are largely similar in the deep convection regions of the Labrador and Nordic seas, so that salinity

has a dominant contribution for the density. Significant negative salinity anomalies also occur in the Arctic ocean in the AOGCM. This large freshwater anomaly is linked to sea ice loss and is suggested to play a key role in the AMOC variations in Jiang et al. (2021), but these anomalies in the Arctic are not used here to constrain the currents.

2.2. Slab ocean model experiments

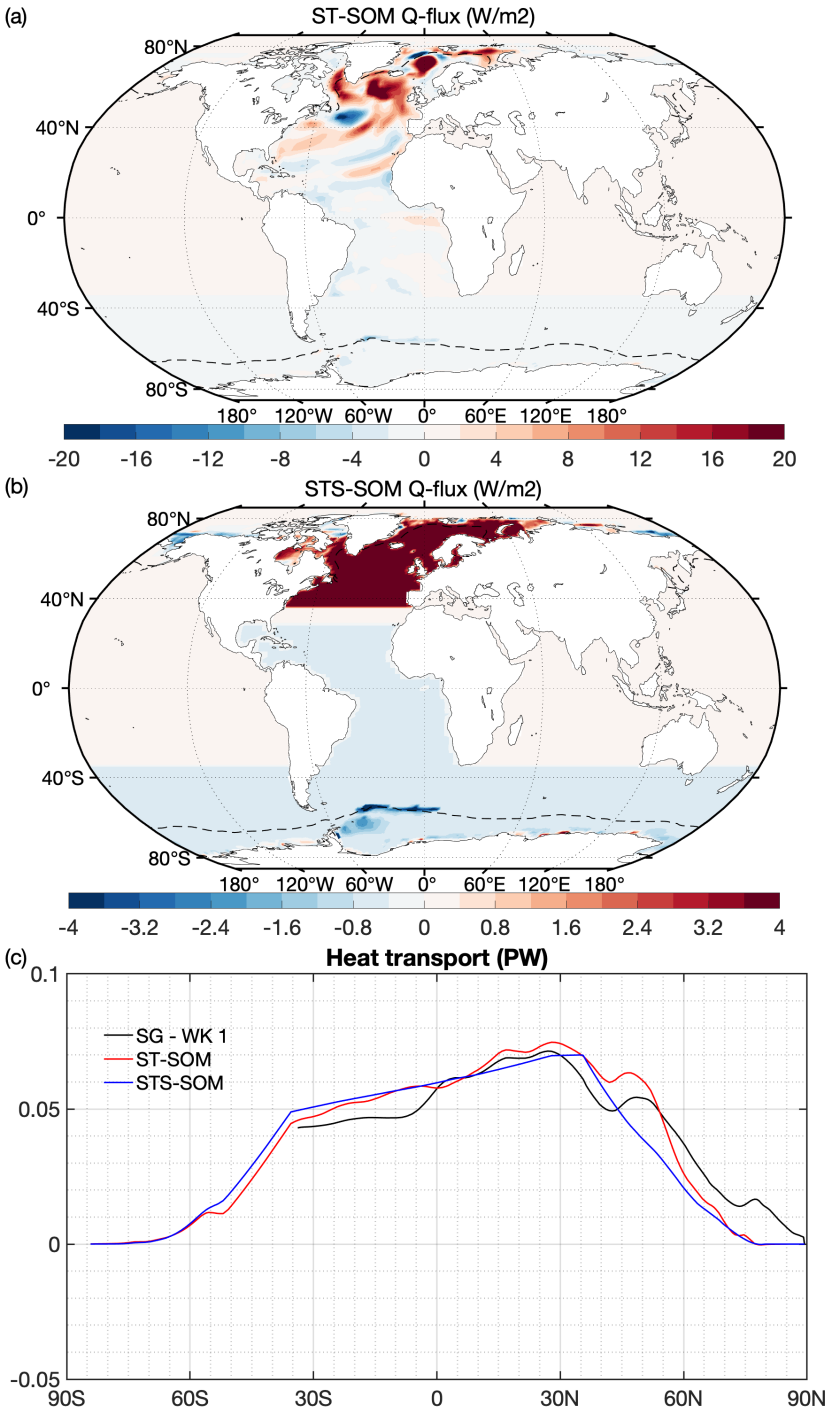

Fig. 1. Distribution of anomalous Q-fluxes (in W m^{-2}) used in (a) ST-SOM and (b) STS-SOM. The dashed black lines indicate the mean 10% sea ice concentration. Note the different color bars used in panels (a) and (b). (c) Anomalous ocean meridional energy transport (OMET) implied by the anomalous Q-flux in ST-SOM (red) and STS-SOM (blue), in PW. These changes in OMET are restricted north of 35°S to the Atlantic, like the corresponding Q-fluxes. The black line indicates for comparison the anomalous Atlantic OMET given by the difference between the first member of SG and WK simulations.

To identify the role of the oceanic dynamical changes, the atmospheric component of IPSL-CM6A-LR is also coupled to a mixed-layer ocean with a depth of 50m. As the capability of using the sea-ice module from NEMO is not implemented, this SOM uses a simplified interactive thermodynamical sea-ice. The sea-ice model only has one ice layer and one snow layer, matching the slab ocean complexity. Once the seawater temperature falls below freezing, the ocean temperature is set to the freezing point, and sea ice forms using the heat content change resulting from the temperature differences. In addition, the ice and snow evolve following surface fluxes, and or ocean-ice fluxes (see Liu et al., 2021 for details). A prescribed annual cycle of additional heat fluxes, hereafter referred to as Q-flux, is added to the oceanic mixed layer to reproduce the pattern of SST and sea ice simulated in CTL-CM. In the control experiment, called CTL-SOM, this mean Q-flux is calculated from the monthly climatology of surface fluxes, SST and sea ice volume from CTL-CM. To study the influence of the AMOC, an anomalous flux is computed by taking the difference of the total surface heat fluxes between the SG and WK runs from 35°S to 80°N in the Atlantic basin (Fig. 1a). The area-weighted average of flux anomaly in the between 35°S and 80°N in the Atlantic basin is non-zero and is about 0.11 W m^{-2}. To avoid any drifts, this net heating of the atmosphere is, therefore, compensated by a uniform cooling in the Southern Ocean south of 35°S. The experiment called SG-SOM is obtained using this Atlantic heat flux compensated in the Southern Ocean added to the Q-flux and corresponds to an intensified AMOC. The anomalous flux was calculated using only the first SG and WK members, but we verified that this taking three members instead leads to a similar anomalous flux.

To examine whether the climate variations are sensitive to the spatial structure of the imposed Q-flux, an additional experiment with uniform anomalous heating over the North Atlantic basin from 35°N to 80°N is performed and called SGS-SOM. The mean area-weighted Atlantic flux anomalies from 35°N to 80°N is calculated in SG-SOM provides the uniform heat flux anomaly used from 35°N to 80°N in SGS-SOM. Similarly, the mean area-weighted Atlantic flux anomalies from 35°S to 35°N from SG-SOM is applied uniformly in that location in SGS-SOM. To avoid any drift, the anomalous flux is also compensated by a uniform cooling in the Southern Ocean south of 35°S. Figure 1b shows resulting the anomalous flux used in SGS-SOM (note the different scales in Figs. 1a and 1b).

Figure 1c shows the meridional energy transport in the Atlantic Ocean implied by the imposed Q-fluxes in SG-SOM and SGS-SOM experiments, as given by the integrated heat flux from the North pole. The implied energy transport matches the Atlantic OMET simulated in flow-constrained simulations, with about 0.07 PW northward at 30°N in both cases. Although the surface fluxes in the Atlantic basin are the same, the heat storage in the AOGCM simulations explains the difference between the Atlantic OMET and the meridional transport implied by the heat flux. In other basins, the Q-flux is identical in ST-SOM and CTL-SOM simulations. Each SOM simulation uses the

same initial conditions as the first member of the simulation in AOGCM and lasts for 50-yr after a spin-up of 10-yr. All SOM simulations use preindustrial fixed external forcings, as in CTL-CM.

2.3. Statistical methods

In the following, we illustrate the differences between the ensemble mean of the SG and WK simulations, denoted SG minus WK. The mean fields are given by the average across the SG and WK experiments. The level of significance for differences in ensemble means is established using a two-sample Student *t*-test, assuming equal variance. The e-folding time scale of the AMOC is 20-yr in the long-term CTL-CM simulation and around 4-yr in the flow field corrected AOGCM simulations. To be conservative, all statistical tests for differences are built using the time series from the three members concatenated and averaged by blocks of 20-yr. The block of 20-yr are then assumed to be independent. Changing the size of the blocks to 4-yr does not modify the results. Meanwhile, the e-folding time scale of surface air temperature is about 2 years in the SOM simulations. To compute statistical significance in SOM runs, all time series are, therefore, averaged by blocks of 2-yr, which are assumed to be independent,

The significance for regression on the AMOC LFC1 in the free-running control simulation CTL-CM is estimated as in Jiang et al. (2021). We create 100 surrogate time series with the same power spectra as the AMOC LFC1 time series but with randomized phases in Fourier space (Ebisuzaki ,1997). The statistical significance level is estimated as the fraction of surrogate time series with a larger correlation then the original correlation. The time series used are averaged over blocks of 10 years to ease the computation, and similar results are obtained when using annual data.

2.4. Evaluation of model performance

We compare the AMOC from the coupled simulations with (SG and WK) and without (CTL-CM) flow field correction. Time-series of the AMOC strength, defined as the maximum of the meridional streamfunction at 30°N, are plotted on Fig. 2a. The AMOC in SG (11.8 Sv) and WK (10.5 Sv) are comparable to the AMOC found in typical strong and weak states in CTL-CM. The standard deviation of the AMOC is 0.52 (0.65) in SG (WK) as given in Fig. 2a (bottom left), which is smaller than that of CTL-CM (1.3 Sv) in SG and WK, likely due to the flow field correction applied toward a fixed AMOC. A lowpass filter with a cutoff period of 7 years removes most of the variability associated with ENSO (El Niño–Southern Oscillation, which has maximum power between 2 and 7 years) and thus reduces the standard deviation in SG and WK. In the last 15 years, the ensemble mean AMOC in WK increases. This increase can be interpreted as driven by the leaking salinity accumulated in the Arctic region through the Fram Strait, leading to more deep water formation in the Nordic Seas and increasing the AMOC, with an approximate time scale of

50-yr. This negative feedback is consistent with the multi-bicentennial variability mechanism found in CTL-CM (Jiang et al., 2021), but is less active in the constrained runs, as only 30% of the baroclinic current is in balance with the actual model density.

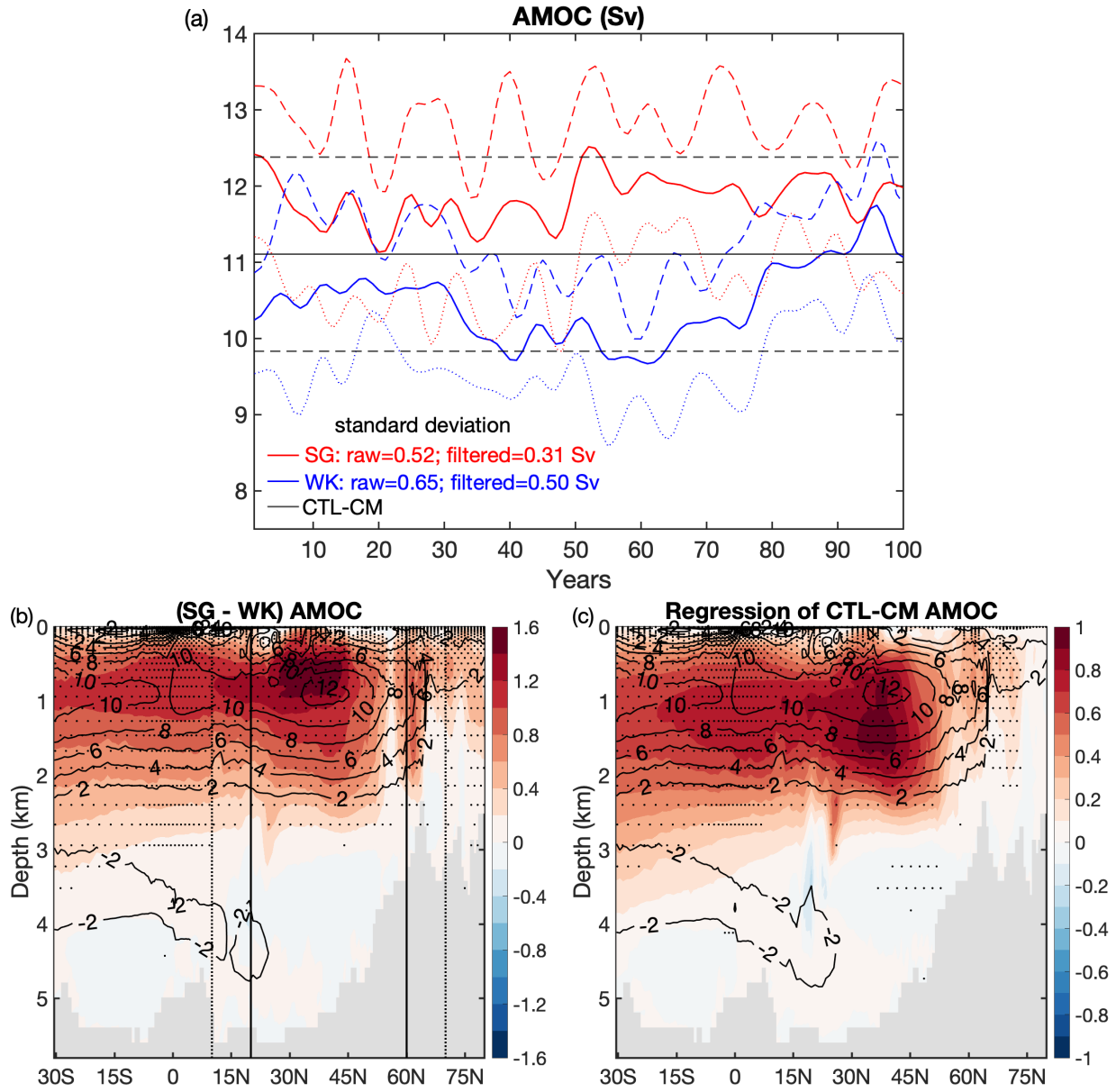

Fig. 2. Comparison of AMOC from the constrained simulations and AMOC from the CTL-CM. (a) Lowpass filtered time series (with a cutoff period of 7-y) of AMOC from SG (red line), WK (blue line), and CTL-CM (black). For SG and WK runs, solid lines represent the ensemble mean of the three members; dotted and dashed lines represent the minimum and maximum values of the three members. For CTL-CM, solid line indicates the mean in the first 100-yr, and dashed lines show the mean plus and minus one standard deviation. The standard deviations of raw and lowpass filtered ensemble mean time series are indicated in the panel. (b) Difference (colors) of AMOC between SG and WK and the mean AMOC average over all runs (contours). The stream function is positive for clockwise rotation. The solid vertical lines indicate the fully constrained area, and dotted vertical lines show the edge of transition zones. (c) Regression of AMOC onto AMOC LFC1 in CTL-CM. The stipples show a significance level of 5%.

The pattern of the Atlantic Meridional streamfunction anomaly given by the difference between SG and WK is similar to the analogous regression on AMOC LFC1 in CTL-CM, even outside of

the region where the flow is constrained. Both anomalies maximize between 30°N and 45°N and gradually decrease below 2500 m. However, the anomalies in the sensitivity experiments are shallower, with a maximum located at 700 m in SG minus WK and at 1300 m in CTL-CM. This difference may be related to the flow field correction cutoff depth at 1000 m (see section 2.1), which explain that the anomalies below 1000 cannot be captured. Besides, SG minus WK shows anomalies of 1.6 Sv maximum (Figs. 2b and c), with a larger amplitude than CTL-CM (0.9 Sv maximum. As the anomalies for SG minus WK correspond to that obtained from (1.5) minus (–1.5) AMOC standard anomalies, the amplitude of SG minus WK should be compared to that obtained with three (1.5 x 2 = 3) AMOC standard deviations. The amplitude of AMOC differences in the constrained simulations (1.6 Sv) are smaller than the three times regression on AMOC LFC1 in CTL-CM (0.9 x 3 = 2.7 Sv). Thus, the AMOC anomaly simulated when using the flow field correction is smaller than the one expected from the density anomaly used. However, this is consistent with the input density only accounting for only 70% of the total density when applying the flow field correction (see section 2.1).

The comparison of SST, SSS, and surface density anomalies also shows a broad agreement between SG minus WK and the analogous regressions on AMOC-LFC1 from CTL-CM (Fig. S2). Within the flow flied correction domain, the pattern of density anomaly resembles that of SSS with positive anomalies in the eastern subtropical gyre and the western subpolar gyre. A local minimum is simulated off Newfoundland in the location of the North Atlantic current. The main difference are located in the eastern subpolar region, where the flow field corrected runs show a negative salinity anomaly, while the regressions from the free runs find positive salinity anomalies.

Moreover, the amplitude of the density salinity in SG minus WK is comparable to, or slightly smaller than that obtained with the regression on the AMOC index in the free run. These anomalies are smaller than that obtained with the regressions multiplied by three, which further agrees with the fact that flow field runs produce smaller anomalies than the one expected from the density anomaly used.

and the dominance of salinity variations on density changes associated with low-frequency AMOC variability are also found in other studies (Ba et al., 2014; Delworth and Zeng, 2012; Jackson and Vellinga, 2013). Regression on CTL-CM presents relatively wide salinization and enhanced convection in the subpolar gyre. In comparison, SG-WK reproduces the essential features of a strong AMOC found in the IPSL-CM6A-LR standard configuration but exhibits an additional freshening and positive buoyancy anomaly along the NAC.

However, the positive freshwater anomaly in the Arctic in SG-WK is much smaller than that in CTL-CM, and the freshening along the NAC in SG-WK is more apparent. This clearly suggests that the anomalous freshwater in the Arctic appears progressively before propagating into the

Atlantic Ocean, consistent with the stronger WK AMOC in the late 15-yr. We have compared the differences between SG-WK using the two halves of the 100-yr available for each simulation. Results are not significantly modified compared to using differences over 100-yr, and thus the latter is adopted to better utilize the samples in the following analysis.

3. Results

3.1. Climate response

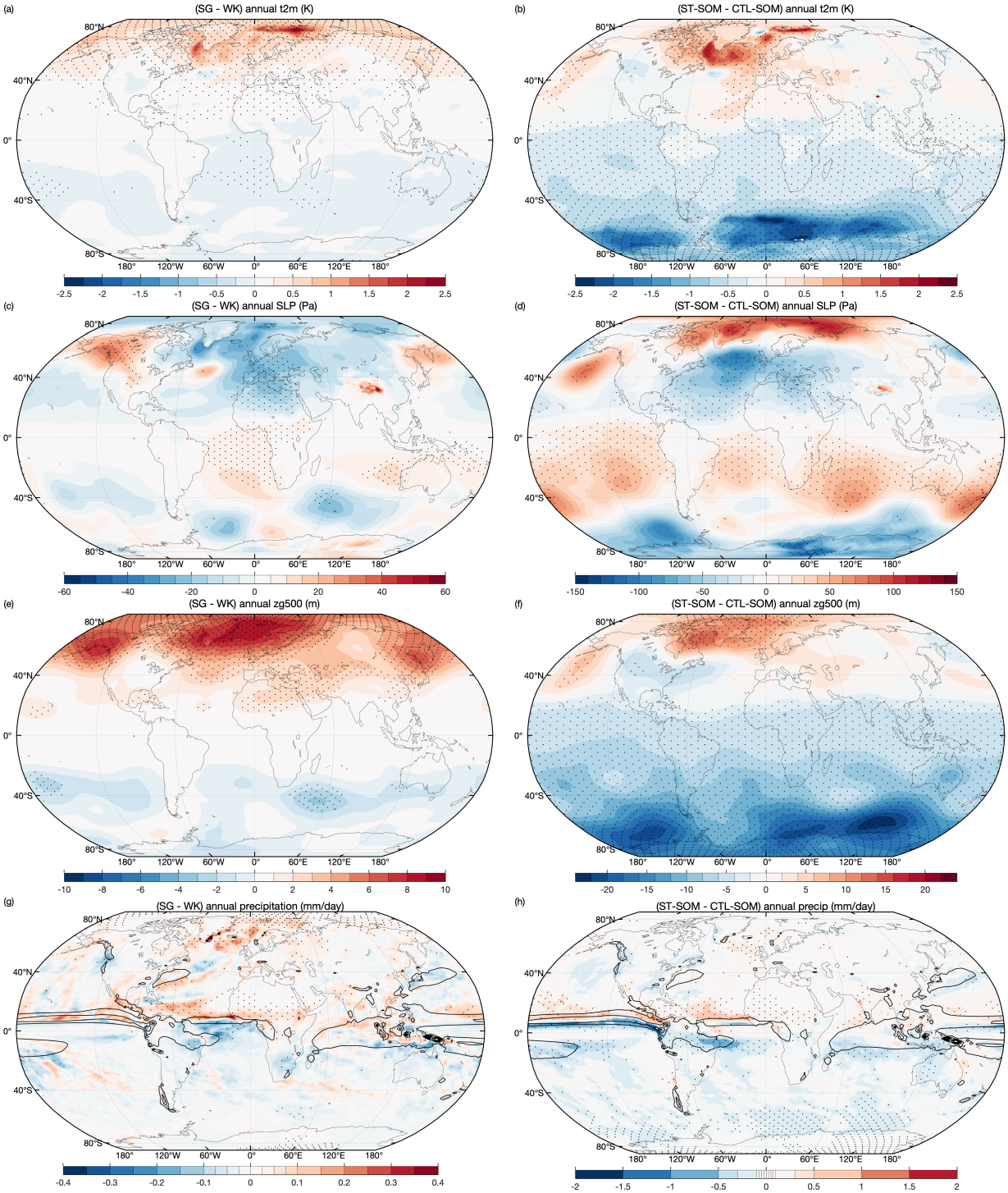

Fig. 3. Anomalous annual (a) air temperature at 2-m (in K), (c) sea level pressure (in Pa), (e) geopotential height at 500 hPa (in m) and (g) precipitation (in mm/day) for SG minus WK. (b), (d), (f), and (h) are the same but for ST-SOM minus CTL-SOM. The black contours in (g) and (h) indicate the mean precipitation every 5 mm/day starting from 5 mm/day. The stipples indicate a significance level of 5%. Note the different scales in the left and right columns.

The difference in AMOC between SG and WK leads to a variety of global climate impacts. The annual mean near-surface air temperature anomalies (Fig. 3a) show widespread warming of ~0.8°C in the high latitude Northern Hemisphere. The warm anomaly reaches up to 1.5°C in the Labrador Sea and 2.5°C at the Arctic sea ice edge, due to the increase in sensible heat from the ocean to the atmosphere associated with Arctic sea ice loss (Mahajan et al. 2011; Moore et al. 2014). The significant warming over the subpolar Atlantic and Arctic extends into the continents with an amplitude between 0.25°C and 0.5°C. Conversely, there is a slight cooling of about 0.1°C above the Southern Hemisphere oceans, visible in the South of the Atlantic, Indian, and Southern Oceans. The negative SLP anomaly and positive geopotential height anomaly above the Arctic, North Atlantic, and Northern Europe indicate a thermal low structure in the lower troposphere (Figs. 3c and e) linked to the warming near the surface. This structure also typically appears as a response to sea ice loss (Deser et al. 2015; Screen et al. 2018). However, these SLP anomalies are hardly statistically significant, except in Northern Africa and Western Europe. Both the SLP and geopotential height anomalies are positive over the Aleutian islands, indicating a barotropic atmospheric anomaly associated with eddy-mean flow interaction. In-phase negative SLP and geopotential height anomalies are also found in the Southern Indian Ocean and, to a lesser extent, in the Southern Pacific. Lastly, positive SLP anomalies are found over the tropical Atlantic and Pacific oceans, suggesting a reorganization of the Walker circulation. The anomalies in summer and winter (not shown) resemble the annual mean results.

The warming in the analogous SOM simulations is more substantial (from 1°C to 1.5°C) than in the constrained AOGCM simulation, and more confined to the North Atlantic subpolar gyre, with little impact on the Arctic Ocean (Fig. 3b), likely because the anomalous Q-flux ends at 80°N (Figs 1a and b) and perhaps because SOM uses a simplified sea ice module (see methods). Meanwhile, the SLP shows a dipolar pattern resembling negative NAO with negative anomalies over the Azores and positive anomalies north of Iceland. This negative NAO is trigged by the subpolar SST warming (Fig. S1a) that corresponds to AMOC-induced positive AMV found in previous studies (Gastineau and Frankignoul, 2015; Peings and Magnusdottir, 2014; Zhang et al., 2019). Nevertheless, the anomalies are different at 500-hPa, with a non-significant negative geopotential height over the East and Central Atlantic, and positive anomalies are found in the North Atlantic and over the Aleutians (Fig. 3f), as in SG-WK.

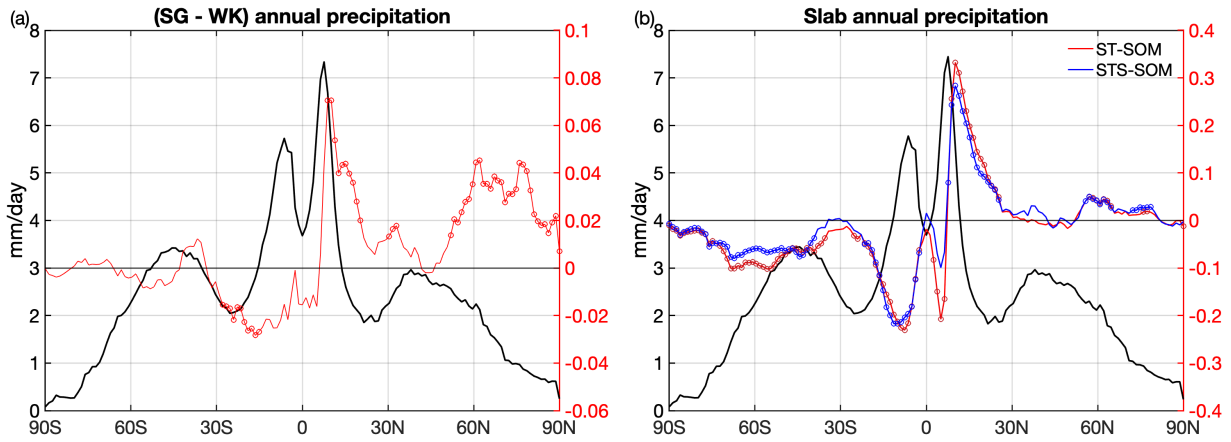

Fig. 4. (a) Climatological (black) and anomalous (red) zonal mean precipitation (in mm/day) in the AOGCM simulations. (b) Same as (a), but for the SOM simulations. Red and blue lines indicate the two different SOM experiments. Circles denote the significance level below 5%. Note the difference in the y-axis in (a) and (b).

The cold anomaly over the Southern Ocean is accompanied by a decrease in the lower-troposphere thickness south of 40°S with negative geopotential height anomalies in the Southern Hemisphere and positive SLP anomalies from 30°S to the Equator. This cooling might result from the negative Q-flux applied in this region of the experimental setup. The cold anomaly is consistent with the negative abnormal rainfall over the Southern Ocean in ST-SOM, which are much weaker in AOGCM simulations (Figs. 3g and h).

The largest rainfall anomalies concentrate in the tropics (Figs. 3g, 3h, and 4). An increase north of the Equator and a decrease south of the Equator indicate a northward shift of the ITCZ, and this displacement of ITCZ has long been recognized as linked to the interhemispheric thermal gradients (e.g., Chiang and Friedman, 2012; Green and Marshall, 2017; Schneider et al., 2014; Sutton and Hodson, 2007). This northward displacement is found in both AOGCM and SOM experiments. One potential mechanism of ITCZ migrations is that the enhanced asymmetry of oceanic heat transport induced by a stronger AMOC leads to a reorganization of the Hadley circulation, with an anomalous near-surface branch transporting moist and warm air northward (Fig. 6). The enhanced precipitation in the north is linked to the poleward shifted ascending branch of the Hadley cell.

The zonal-mean precipitation anomaly at 10°N is 0.32 mm day^{-1} in SOM compared to 0.07 mm day^{-1} in SG-WK (Fig. 4). The tropical rainfall anomaly is therefore four times larger in SOM than that in the AOGCM. Besides, SOM shows a more completed narrow rain-belt anomaly in the Pacific, with opposite anomalies on two sides of the Equator (Fig. 3h). While in the coupled model, rainfall increases in the north but barely decreases in the south (Figs. 3g). In the northern mid-

latitudes, the precipitation shows instead a comparable increase at 0.04 mm day^{-1} in the two models (Fig. 4). In the Atlantic Ocean, more rainfall is found along the Gulf Stream and in the Nordic Seas. In SG-WK, the small-scale dipole anomalies at midlatitudes Atlantic Ocean are likely linked to a shift of the Gulf Stream (Fig. 3g). In the Arctic, SG-WK shows increased precipitation, consistent with the enhanced warming (Fig. 3a).

In summary, SG-WK shows a broad warming in the Northern Hemisphere, while in SOM it is more confined to the Atlantic basin. The baroclinic pressure response and precipitation increase are consistent with these different extents, although the amplitudes are comparable. In the Tropics, both models show a northward shift of ITCZ, but this migration is much larger with the slab model (note the different scales in Figs. 3 and 4). This suggests that the ocean circulation acts to damp the atmospheric response, especially near the Equator. To better understand these different responses to a stronger AMOC/OMET, we next turn to an energy budget perspective to see how the meridional energy transports by the different components of the system reorganize.

3.2. Analysis of the meridional energy transport

The ocean transport OMET is computed using the sum over the x-axis ocean grid of the vertically-integrated meridional heat transport, calculated online in the ocean model at each grid point and time step. This global OMET is further decomposed into transports in the Atlantic and Indo-Pacific basins, using a two-dimensional mask to define each basin. To better understand the redistribution of heat in the ocean, we compute at each latitude a simple energy budget integrated zonally and from the South Pole as follows:

$$\int_{\varphi_s}^{\varphi_n} \frac{\Delta \mathrm{OHC}}{\Delta t} {R_T}^2 \cos\varphi \, \mathrm{d}\varphi + \mathrm{OMET}(\varphi_n) = \int_{\varphi_s}^{\varphi_n} \mathrm{HF} \, {R_T}^2 \cos\varphi \, \mathrm{d}\varphi + R \qquad (1)$$

where φ is the latitude, φ_s is the latitude of the South Pole, and φ_n the northern edge of the region of integration, and R_T is the earth's radius. $\Delta\mathrm{OHC}$ denotes the (zonal-mean) change of ocean heat content during the period Δt (corresponding to the simulation length), estimated by the difference between the last and the first time steps. The OHC is calculated as an integral over the depth of the ocean:

$$\mathrm{OHC} = C_{p,w} \int_{-H}^{0} \rho T \mathrm{d}z \qquad (2)$$

where ρ and T are the density and temperature of the seawater, z is the depth and $C_{p,w}$ is the specific heat capacity of the seawater at constant pressure. HF is the total heat flux entering the ocean (i.e., positive downward). R is a small residue because the integration of the fluxes received by the ocean does not fully account for the OHC variations of the IPSL-CM6-LR. This imbalance

remains weak and unexplained (Mignot et al., 2021). Equation (1) thus expresses that the total surface fluxes entering an ocean region are balanced either by local heat storage, or energy transport out (through the northern edge) of the region.

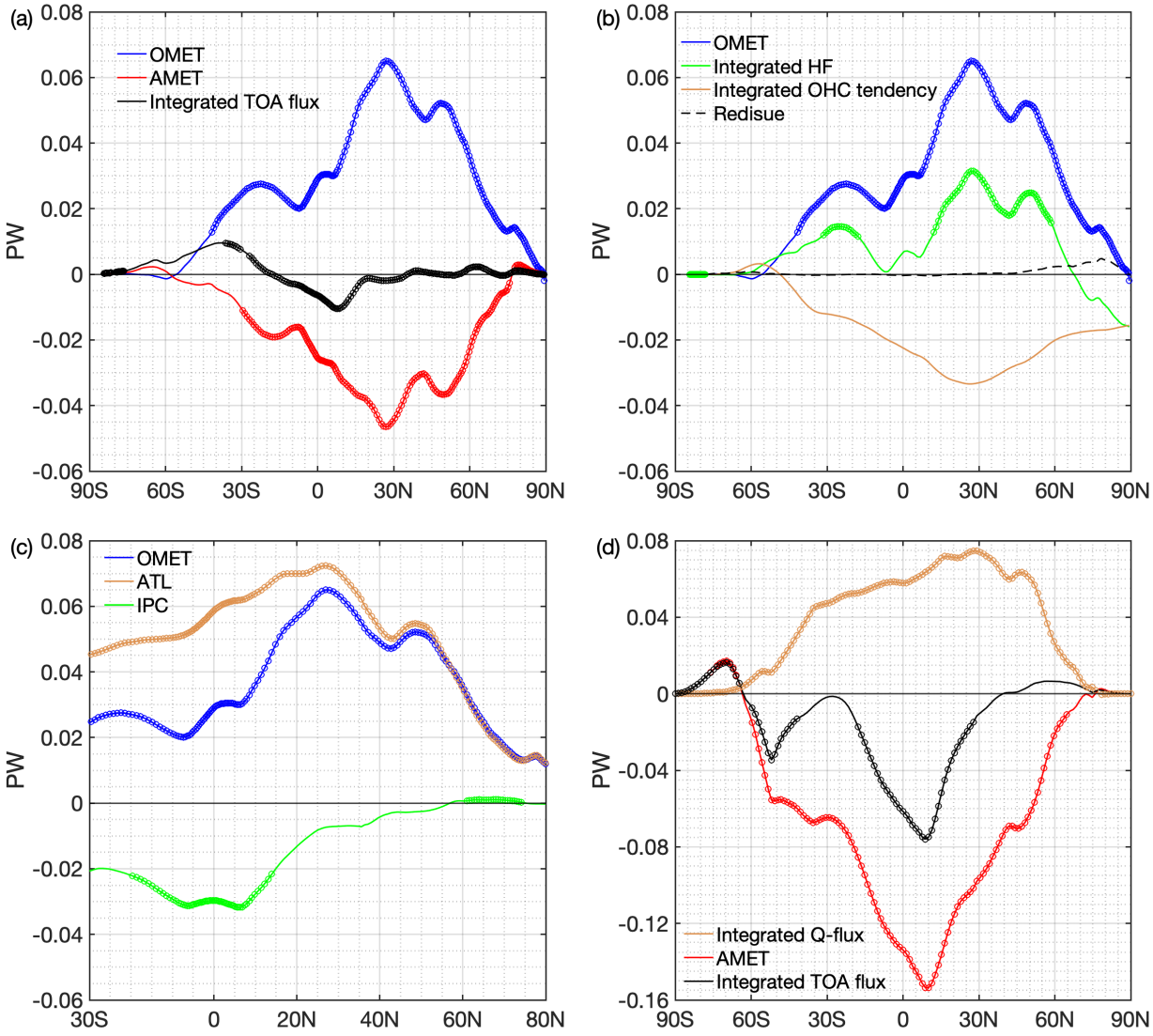

Fig. 5. Anomalous northward energy transports in SG minus WK (a-c) and ST-SOM minus CTL-SOM (d). (a) Atmospheric transport (AMET; red line) and total oceanic transport (OMET; blue line). Black line indicates the total energy transport implied by the net radiative flux at the top of the atmosphere (TOA). (b) Quantification of the terms of equation (1). Brown line depicts cumulated ocean heat content (OHC) changes from the South Pole, and the green line shows the heat transport implied by the total heat flux entering the ocean. The anomalous OMET (same as a) and the residue term are indicated by blue and dashed black lines. (c) global OMET anomaly (blue, same as a,b) and its Atlantic (brown) and Indo-Pacific (green) components. (d) Energy transport implied by the anomalous Q-flux (brown) in ST-SOM, integrated net radiative flux at TOA (black), and AMET in ST-SOM minus CTL-SOM. In all panels, the unit is PW. Circles indicate a significance level below 5%.

The total meridional energy transport implied by top of atmosphere fluxes (i.e. the transport that would exactly balance these fluxes) is computed as the meridional integral from the South Pole of the net TOA fluxes on the atmospheric grid. The global mean TOA value is removed, as it is non-zero due to the potential heat storage in the ocean as well as the small non-conservation in the atmosphere (Hobbs et al. 2016). The AMET is computed similarly but using the difference between the net radiative forcing flux at the TOA and the net air-sea heat fluxes (the storage term is negligible in that case). All computations regarding energy analysis use monthly outputs.

The mean OMET dominates in the tropics with an amplitude of 1.5 PW at 15°N/S, while the AMET peaks at 45°N/S with 5 to 5.5 PW (Fig. S3). The main features are consistent with estimations derived from satellite observations of TOA net forcing and atmospheric reanalysis data (Trenberth et al. 2019), except that the OMET is generally underestimated in the IPSL-CM6A-LR model compared to direct observations (Boucher et al. 2020).

In SG-WK, the stronger AMOC implies an intensified northward OMET in the two hemispheres, with a maximum of 0.065 PW at 30°N (Fig. 5a). The total energy transport implied by the net radiative forcing at TOA remains small, only showing opposite anomalies in the Southern Hemisphere tropics and mid-latitudes (Fig. 3a). The AMET (Fig. 5a, red line) and OMET (blue line) should therefore approximately balance one another (Bjerknes 1964), and indeed the AMET anomaly structure is almost symmetrically opposite to the anomalous OMET. However, their sum is different from zero, with the amplitude of OMET exceeding that of AMET by about -0.02 PW (or 30% of OMET) at 30°N. This discrepancy is due to the storage of heat in the ocean, with a net decrease of 49 ZJ (1 ZJ = 10^{21} J) of the global OHC in SG minus WK over 100 years (Fig. 5b, brown line). The OHC change is dominated by a decrease south of 30°N and compensated by a smaller increase in the Atlantic Ocean between 30°N and 60°N. The AMET is, therefore, smaller than the one expected from Bjerknes compensation, and surface fluxes only balance about half of the northward OMET on average. The residual is minor and negligible.

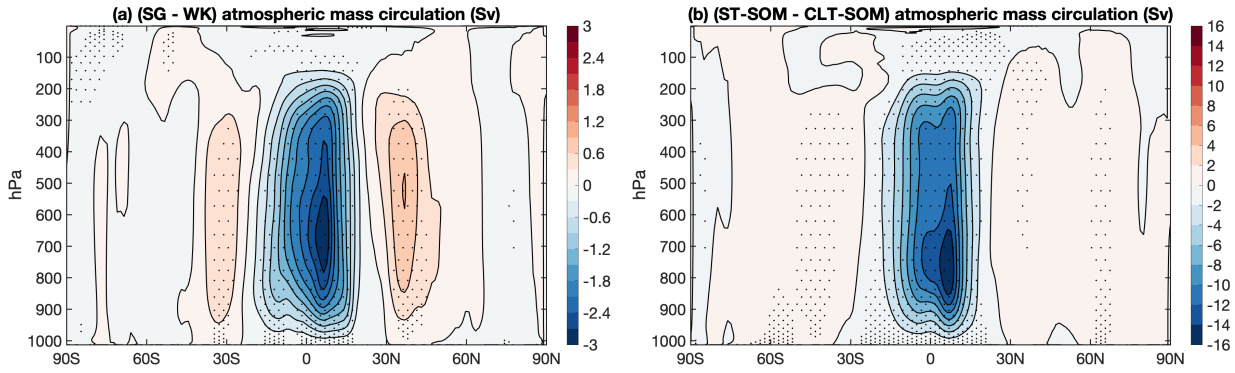

Fig. 6. (a) Mean (black contours) and anomalous (colors) atmospheric overturning mass streamfunction (in Sv) for the difference of SG minus WK. (b) Same as (a) but for the difference of ST-SOM minus CTL-SOM. The stream function is positive for clockwise rotation. Stipples indicate a significance level below 5%.

The AMOC-induced northward OMET anomaly in the Atlantic Ocean (Fig. 5c, brown line) in SG minus WK is also partially balanced by a southward transport in the Indo-Pacific (Fig. 5c, green line), reducing the total OMET. The northward anomalous Atlantic OMET is positive and peaks with 0.07 PW at 30°N, while the anomaly in the Indo-Pacific has an opposite sign and shows a minimum of 0.03 PW in the tropics, or the same amplitude as the southward AMET at the equator.

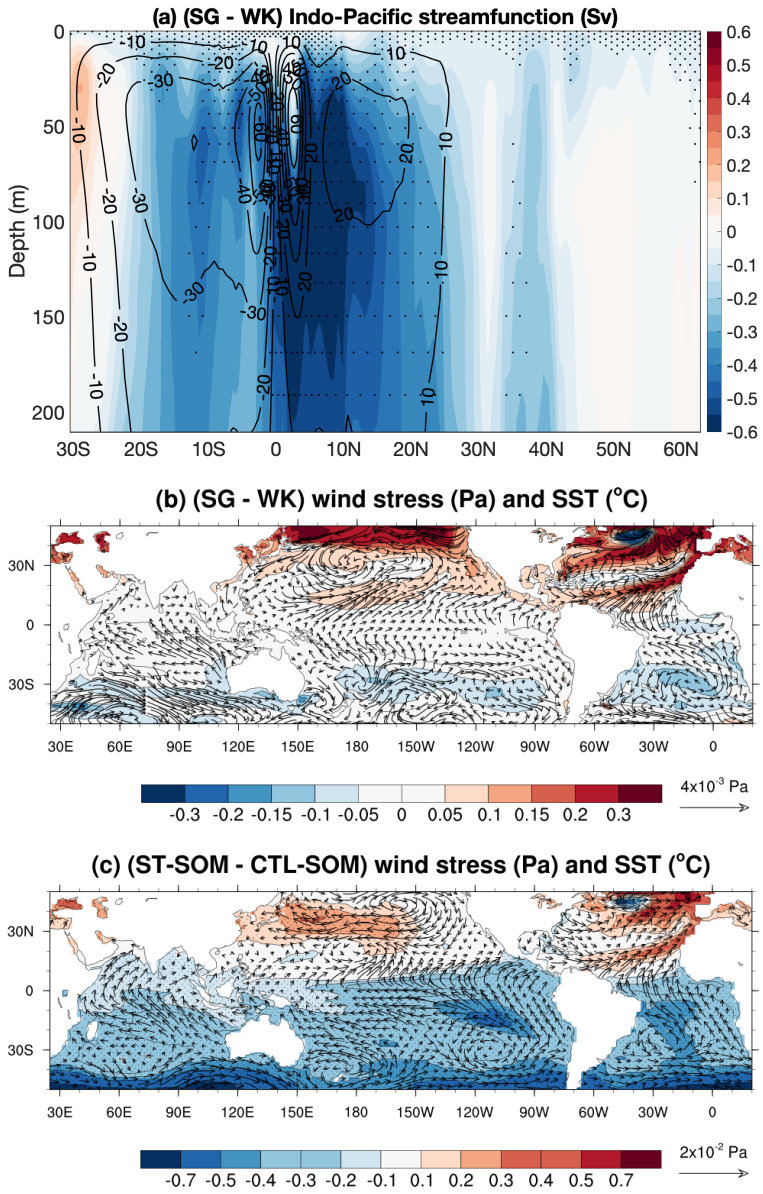

Fig. 7. (a) Anomalous (shading) and mean (contours) Indo-Pacific Ocean overturning streamfunction (in Sv) for the AOGCM (SG minus WK). (b) Anomalous wind stress (vectors, in Pa) and sea surface temperature (SST, shading, in °C) for SG minus WK. (c) Same as (b) but for ST-SOM minus CTL-SOM. Stipples indicate a significance level above 95% for SST.

By construction, the heat transport implied by the anomalous Q-flux in SOM is equal to the Atlantic OMET in SG-WK (brown lines in Figs. 5c and d). Nevertheless, the amplitude of the southward AMET anomaly in ST-SOM reaches twice the implied OMET at the equator, or almost four times that of the AMET anomaly in SG-WK (see the different y-axes for Figs. 5a and 5d). This increased AMET is consistent with the structure of the energy transport implied by the net TOA radiative flux, that shows a large southward component peaking at -0.08 PW just north of

the Equator. This large difference in the AMET response to the same Atlantic transport between the SOM and fully coupled experiments is reflected in the anomalous tropical atmospheric circulation, and more specifically the Hadley cell (Fig. 6).

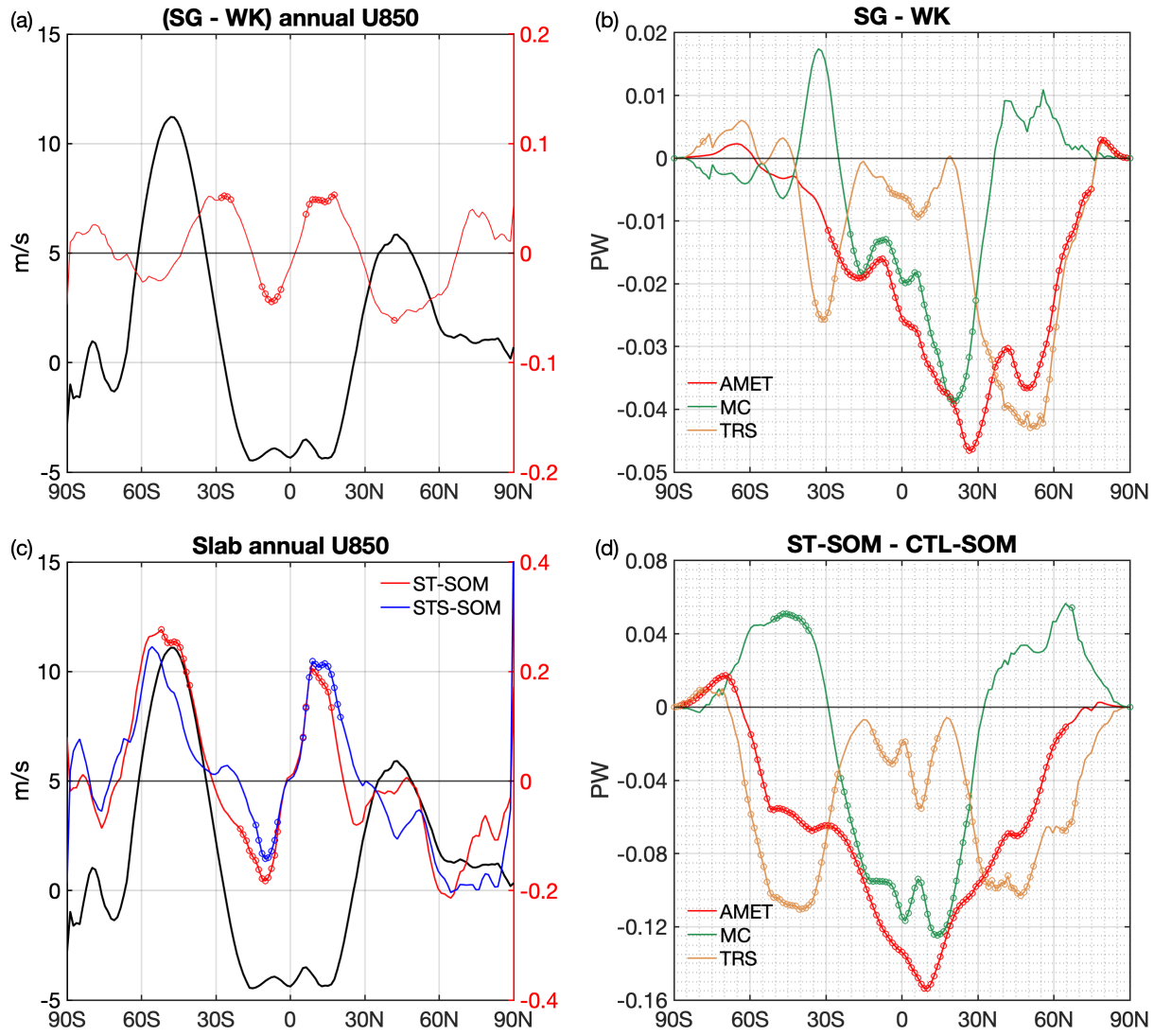

Fig. 8. (a) Mean (black) and anomalous (red) annual zonal wind at 850hPa (in m/s) for SG minus WK. (b) Decomposition of the AMET anomaly (red, in PW) into the contributions of time-mean circulation (MC, green) and transient eddies (TRS, orange). (c) and (d) same as (a) and (b) but for ST-SOM minus CLT-SOM. In (c), STS-SOM minus CTL-SOM is shown in blue line. Circles indicate a significance level above 95%.

Both the ST minus WK and STS – CTL SOM differences show an abnormal cross-equatorial Hadley cell in the tropics between 20°S and 20°N, that would transport energy southward. The corresponding meridional winds in the lower branch are oriented northward, consistent with an increased northward transport of heat and moisture near the surface. This leads to enhanced rainfall (Fig. 4) and weakened trade winds in the Northern Hemisphere tropics, and opposite changes in

the Southern Hemisphere (Fig. 8a,c). The response of the Hadley cell and trade winds is however four times as large in the slab simulations (compare the scales in Figs 6a,b and 8a,c), as is the impact on tropical precipitation (Fig 3,4). Similar associations among the Hadley cell, precipitation, and trade winds anomalies are also found in many other studies (for instance, McGee et al., 2018; Moreno-Chamarro et al., 2019).

The tropical wind stress and the associated wind-driven Ekman transport explain in the mean climate the formation of two antisymmetric shallow circulation cells around the Equator in the tropical ocean, called the STCs. In the Indo-Pacific, the two STCs are well reproduced in IPSL-CM6A-LR, as shown with contours in Fig. 7a. For an intensified AMOC, the anomalous northward cross-equatorial Hadley Cell results in anomalous south-easterlies in the Southern Hemisphere and south-westerlies in the Northern Hemisphere (Figs. 7b and c). The change of direction is located at the Equator and is analogous to that occurring in the Indian Ocean during the summer season because of the change of sign of the Coriolis force when crossing the equator. This change of orientation leads to an anomalous southward Ekman flow on both sides of the equator. At the equator, the Ekman flow is negligible but the negative wind stress curl anomaly leads again to a southward flow in the ocean following the Sverdrup balance. The anomalous cross-equatorial Hadley circulation therefore forces through its associated wind stress an analogous overturning cell in the ocean, apparent on Fig 7a for the Indo-Pacific, that can explain the southward OMET anomaly in the tropics (Fig. 5c).

In the SOM case, the cross-equatorial wind stress anomaly displays a similar structure with a larger amplitude (Fig. 7c). However, the ocean is motionless in that case and the Q-flux in the Indo-Pacific is fixed; there is thus no compensating southward OMET, explaining part of the larger AMET response.

To better distinguish the roles of different dynamical processes in the atmosphere, we further decompose the AMET into contributions from transient eddies (TRS) and mean circulations (MC):

$$AMET(\varphi) = -\frac{2\pi R_T \cos(\varphi)}{g}\int_{p_s}^{0} \underbrace{[\bar{v}][\overline{MSE}] + [v^* MSE^*]}_{MC} + \underbrace{[\overline{v'MSE'}]}_{TRS}\, dp \qquad (3)$$

where p_s is the surface pressure, v is the meridional velocity, g is the gravitational acceleration (Lorenz 1967). Overbar denotes time averages (here, monthly climatologies), and the prime denotes the departure from the time average. Square brackets are zonal averages; the asterisk denotes the departure from the zonal average. MSE denotes the moist static energy, which is computed as the sum of sensible, latent, and potential energy:

$$MSE = C_{p,a}T_a + Lq + gz \qquad (4)$$

where $C_{p,a}$ is the specific heat of the air at constant pressure, T_a is the air temperature, L is the latent heat, q is the specific humidity, and z is the geopotential height.

The MSE transports terms were not saved online, so were reconstructed from the monthly outputs. We first compute the mean meridional circulation terms, i.e., the first and second terms on the right-hand side of Eq. (3), using the monthly climatologies. Then, the TRS component is calculated as the residue of the total AMET calculated previously from the TOA and surface fluxes, minus the MC component.

The mean AMET and its MC and TRS components nearly overlap for the control AOGCM and SOM experiments (Fig. S3), suggesting a good agreement in simulating the mean atmospheric circulation state. The mean circulation includes the contributions of the mean meridional circulation and stationary waves in the conventional decomposition (Lorenz 1967). MC dominates the total transport between 30°S and 30°N, with a maximum of 2.5 PW due to the Hadley cells. The Ferrel cells and stationary eddies have smaller contributions. The TRS component of the AMET is associated with the transport by baroclinic eddies and peaks in mid-latitudes with an amplitude of 4/6 PW at 40°N/S.

In both increased AMOC simulations, the anomalous southward AMET is primarily due to the MC component in the tropics (Fig. 8b,d), consistent with a dominant role of the cross-equatorial Hadley cell. In the mid-latitudes, the eddies (TRS) dominate the transport, opposed by the Ferrel cell (MC).

In the fully coupled case, the TRS anomaly, like the total southward AMET, is much larger in the Northern Hemisphere. This can be understood, as the more intense warming of the atmosphere at higher latitudes (Fig. 3a) leads to a reduced meridional temperature gradient and lower-tropospheric baroclinicity. This results in a reduction of the storm track activity in the mid-latitude North Pacific, North Atlantic and in Northern Europe, as shown by the eddy meridional heat flux $V'T'$ at 850 hPa (Fig. S4), or the standard deviation of the geopotential height at 500-hPa (not shown). The eddy anomalies were calculated from daily outputs using a Lanczos high-pass filter with a window of 21 days and a cutoff period of 10 days. In the SOM case, the AMET and eddy transport changes are more symmetrical around the equator, consistent with the stronger cooling in the Southern Ocean.

The relation between changes in the eddy energy transport and mean westerly winds are not completely straightforward. As seen on Fig 8, a decrease in poleward eddy heat flux generally coincides with lower (westerly) wind speeds, but the amplitude of the response can vary a lot: compare the Northern and Southern Hemisphere responses in Fig 8c,d. Presumably, the anomalous momentum transport caused by these anomalous wave sources depends on details of the mean flow and of the structure of the eddy forcing. For example, the mid-latitude wind anomalies in the

coupled runs SG minus WK correspond to a weaker jet in the Northern Hemisphere, but a northward shift in the Southern Hemisphere.

To sum up, in the coupled simulations, the increased ocean heat transport by the imposed AMOC in the Atlantic Ocean is balanced primarily by a southward AMET by eddies in the midlatitudes; while in the Tropics the anomalous cross-equatorial Hadley cell forces an overturning cell in the Indo-Pacific Ocean that transports a similar amount of energy (AMET and Indo-Pacific OMET are almost equal at the equator). Another factor reducing the atmospheric (and oceanic) response to the Atlantic OMET is the storage of energy in the ocean, with the global heat content decrease south of 30°N during the strong AMOC (Fig. 5b) reducing the "need" for a compensating southward transport.

The absence of a dynamic ocean in the SOM simulations leads to a considerably larger atmospheric response than in the AOGCM, especially in the Tropics (Figs. 3, 6, and 8). First, the global heat content doesn't change, so the compensating southward transport will be larger. Second, the lack of Indo-Pacific Ocean transport means that all of this transport in the Tropics is done by the atmosphere, instead of half of it. Finally, in the SOM simulation, large changes in the tropical top of atmosphere fluxes lead to an additional southward transport across the equator (Fig 5d). We thus turn now to these radiative fluxes at the TOA to better understand their variations in the SOM simulations.

3.3. Radiative feedbacks

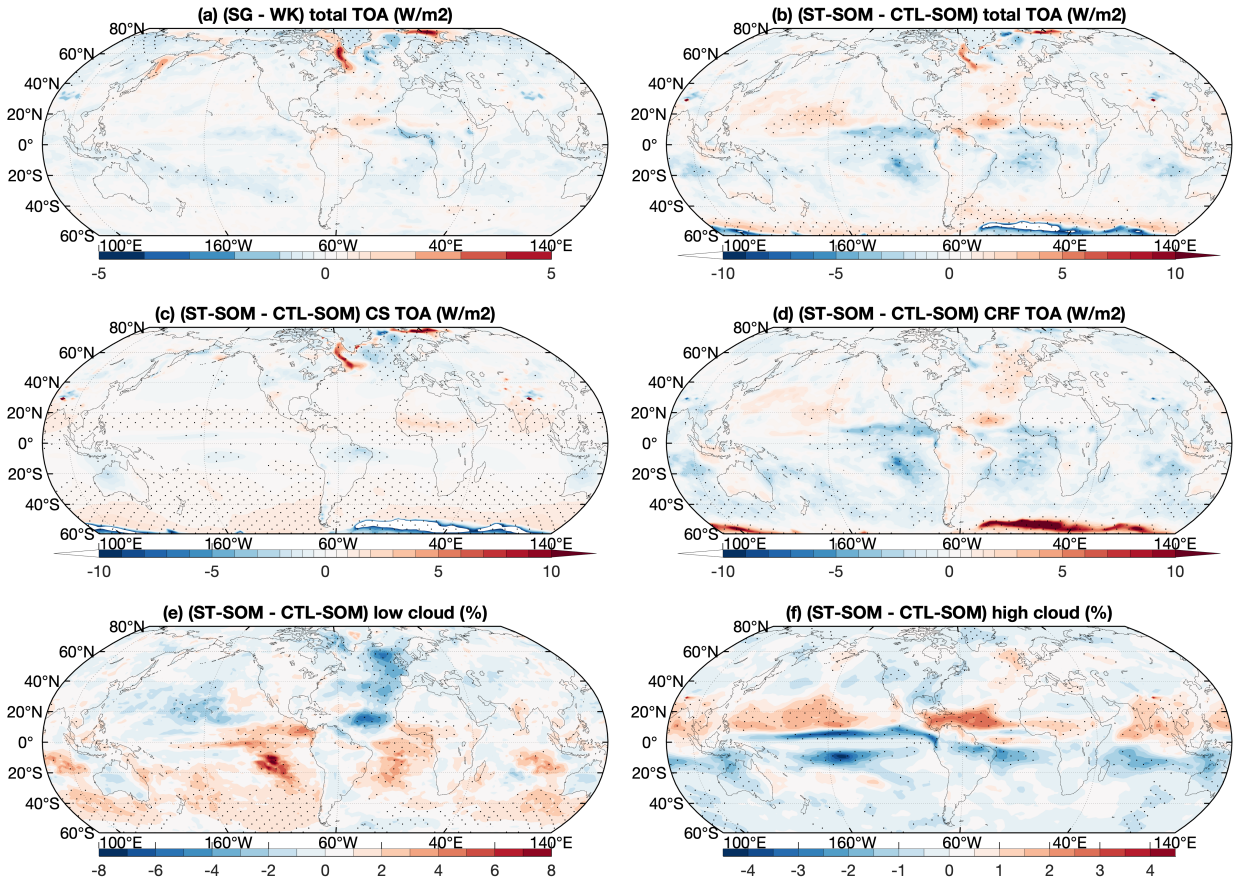

Fig. 9. (a) Anomalous net radiative flux at the top of atmosphere (TOA), in $W\ m^{-2}$, for the AOGCM (SG minus WK) and for slab-ocean model (ST-SOM minus CTL-SOM). The net radiative flux in the slab-ocean model simulations is decomposed into (c) clear-sky (CS) and (d) cloud radiative forcing (CRF), in $W\ m^{-2}$. The flux is positive downward. (e) Low and (f) high cloud anomalies in slab-ocean model, in percentage. Stipples indicate a significance level below 5%.

The response of the net incoming radiative fluxes at the TOA to a stronger AMOC is similar in the North Atlantic Ocean for the AOGCM and SOM experiments (Figs. 9a and b). In both cases, the net TOA flux increases in the Labrador and Kara Seas (Figs. 9a and b), where the sea ice loss is largest, as a result of the decrease in surface albedo. The fluxes decrease slightly in the center of the basin, because the warmer temperature leads to more outgoing infrared radiation.

In the Tropics, the structure is again broadly similar, but the amplitude is much larger in the SOM simulations, and the anomalies more significant: there is a general increase of incoming radiation in a band around 10-20°N north of the ITCZ, and a decrease south of the ITCZ and over the eastern tropical ocean basins of the Southern Hemisphere. To pinpoint the origin of these radiative changes, we compare the TOA net radiative flux for clear sky conditions (Fig. 9c) with the cloud radiative forcing (CRF, Fig 9d). As the AOGCM and SOM experiments show qualitatively similar changes (not shown), we only illustrate the larger anomalies for the SOM experiments. The clear

sky TOA flux shows an increasing downward flux over a band between the Equator and 20°N, with local maxima over the continents: Sahel and western Africa or India. This can be explained by the anomalous Hadley cell bringing more moisture into the Northern Hemisphere, thereby increasing the local greenhouse effect and decreasing the outgoing longwave radiation (OLR). Changes in the mid-latitudes are consistent with changes in surface albedo near the sea-ice edge, and temperature elsewhere.

The net cloud radiative forcing, defined as the difference of the total TOA net flux minus the clear-sky TOA flux, explains most of the changes in the Tropics, especially over the oceans (compare Figs 9b and d). Furthermore, the spatial structure of the CRF coincides with changes in the low cloud cover (Fig. 9e). The amount of low clouds increases widely in the Southern Hemisphere, which is cooler and where the cross-equatorial cell forces a stronger subsidence. The larger albedo of these clouds reflects more solar radiation, increasing the energy deficit of the Southern Hemisphere. The opposite effects occur in the Northern Hemisphere, with warming, decreased subsidence and low clouds, and more incoming energy. The high clouds are also changing as the ITCZ moves northwards (Fig. 9f), consistent with previous model studies and satellite observations (Brachet et al. 2012; McCoy et al. 2017; Minobe et al. 2008). However, the high clouds have a relatively minor influence on the net cloud radiative forcing, as commonly found due to competition between the albedo effect and the greenhouse effect (Harrison et al. 1990; Zhang et al. 2010).

Therefore, the TOA flux changes associated with AMOC anomalies are induced mainly in the tropics by the low cloud changes, with a contribution from clear-sky OLR over the monsoon continents. The asymmetric changes on both sides of the ITCZ as a response to a northward shift will be balanced by more southward AMET and a stronger cross-equatorial cell, thereby providing a positive feedback on ITCZ shifts. A similar feedback was already observed in a slab ocean setting in L'Héveder et al (2015); it also exists in the AOGCM simulations but is weaker in amplitude, just like the AMET and Hadley cell (see Figs. 5a and 5d, black lines).

4. Discussion and conclusions

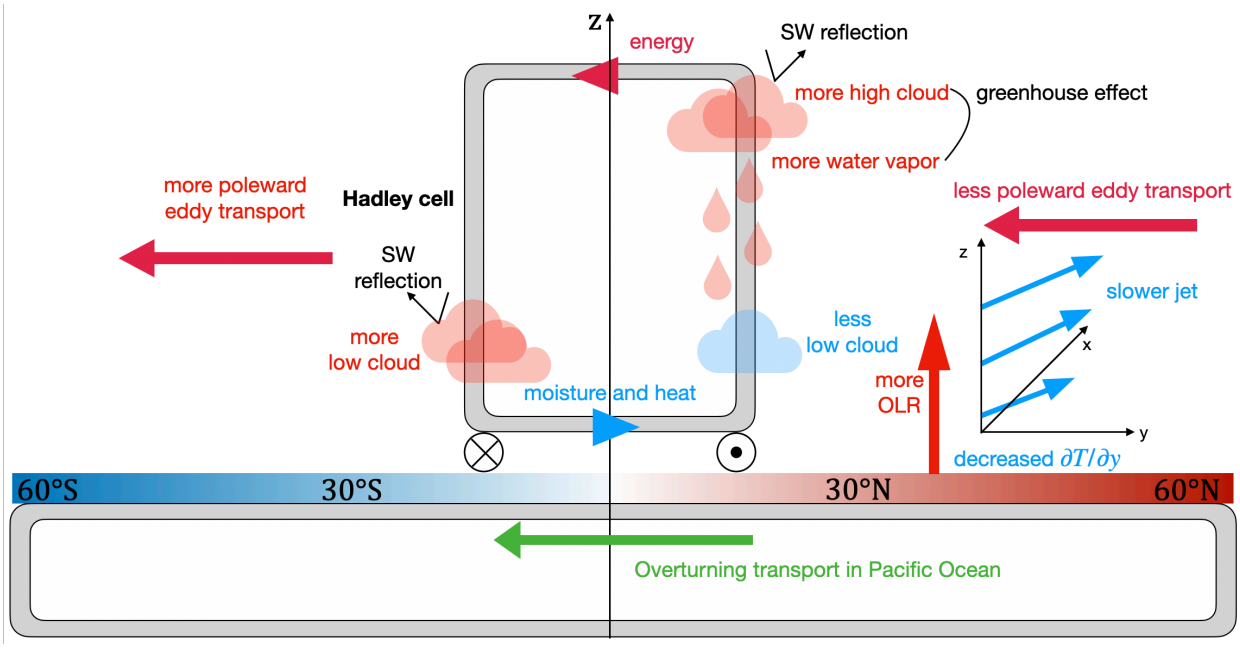

Fig.10. Schematic diagram of the mechanisms that drive the response of the climate to the intensified AMOC and ocean meridional energy transport (OMET). Inspired by Kang (2020).

The climate response to a stronger or weaker AMOC was examined in an atmosphere-ocean general circulation model (AOGCM) by imposing the baroclinic component of oceanic currents in the North Atlantic, hereby controlling the global AMOC intensity. This method has the advantage of not introducing any energy flux corrections, so that the climate response to an intensified AMOC can be investigated with diagnostics of the energy flow in the climate system.

The enhanced AMOC and the associated northward ocean energy transport lead to a broad warming of 0.8°C in the mid- and high-latitude Northern Hemisphere. The ITCZ shows a clear northward shift, as an anomalous direct cross-equatorial Hadley cell develops between 20°S-20°N to offset the increased OMET in the Atlantic Ocean. Consequently, the rainfall presents an intense dipole anomaly of 0.3 mm day^{-1} in low latitudes. The changes in midlatitudes are weak, but show anomalies commonly associated with the AMOC or its SST and sea-ice loss signatures. In particular, the SLP shows a wide negative anomaly over the North Atlantic, while the mid-tropospheric geopotential increases over the polar cap, so that the atmospheric circulation changes are mainly baroclinic. The precipitation also slightly increases by 0.15 mmday^{-1} over the North Atlantic. The anomalies are weaker and opposite in Southern Hemisphere.

To quantify the role of a dynamic ocean, slab ocean model experiments were also performed with an equivalent prescribed OMET in the Atlantic basin, compensated in the Southern Ocean. The climate changes simulated are similar to that of the AOGCM but with much larger amplitudes in the tropics. The comparison between AOGCM and SOM simulation reveals the respective role of

563 the ocean and atmosphere in the climate response to AMOC fluctuations. The underlying
564 mechanisms are summarized in Fig. 10.

565 To compensate for the anomalous northward OMET in the Atlantic Ocean, the anomalous
566 atmospheric meridional energy transport (AMET) is necessary southward. In the mid-latitudes,
567 this atmospheric transport is accomplished by anomalous southward transient eddy fluxes, leading
568 to changes in the storm tracks and eddy-driven jet (here, a reduction in the Northern Hemisphere).
569 In the tropics, the AMET is done by an anomalous cross-equatorial Hadley cell, with ascent in the
570 warmed Northern Hemisphere, and the associated moisture transport shifts the ITCZ northwards.
571 The amplitude of the AMET, Hadley cell, and precipitation changes are however much lower
572 (factor of 4) with the dynamic ocean, for a number of reasons.

573 First, in the AOGCM not all of the increased northward Atlantic OMET is transported back
574 southward: part is stored in the ocean, as the OHC increases in the north and decreases south of
575 30°N. These OHC changes are not balanced, and some of the transported energy is instead lost
576 through larger outgoing top-of-atmosphere fluxes over a broad latitude band from 30°S to the
577 North pole (not shown), reducing the compensating southward transport especially in the Southern
578 Hemisphere. Second, a cross-equatorial shallow overturning cell develops in the Indo-Pacific
579 Ocean between 20°S and 20°N in response to the modified trade winds associated with the cross-
580 equatorial Hadley cell, which transports about the same amount of energy as the atmosphere,
581 hereby reducing by half the latter's amplitude. This mechanism is absent in the inert SOM.

582 In addition, the atmospheric changes are amplified by positive radiative feedbacks in the tropics:
583 the ITCZ shift towards the warmer Northern Hemisphere reduces the low cloud amount and the
584 planetary albedo there and increases the free tropospheric moisture, enhancing the greenhouse
585 effect especially over continents. Conversely, the Southern Tropics have more low clouds and
586 receive less energy. These radiative feedbacks are balanced by a southward energy transport that
587 further enhances the initial southward AMET anomaly. This positive feedback exists in both cases,
588 but is much stronger in the SOM case: because the AMET is larger to start with in that case, and
589 because in the fully coupled case the forcing of the OMET by the Hadley cell means this positive
590 feedback is also cut by half (i.e. half of the extra transport due to the radiative impacts of the ITCZ
591 shift is taken up by the ocean).

592 The role of the ocean in damping ITCZ migrations, because of the robust coupling through the
593 surface wind stress between the energy transports by the Hadley cell and the shallow ocean cells,
594 has been pointed out in other, more idealized, model studies (Green and Marshall, 2017; Kang,
595 Shin, and Xie, 2018). Kang, Shin, and Codron (2018) further inspected the role of Ekman transport
596 by coupling a SOM with parameterized Ekman transport to a gray radiation atmospheric model
597 and found the same damping effect of ocean dynamics in the subtropics (their model did not allow

for cross-equatorial transport), controlled by the ocean stratification. We also find that the climate responses in SOM are not sensitive to the spatial distribution of the heating in the extra-tropics, consistent with the results of L'Hévéder et al. (2015) and Kang et al. (2014).

PNA Anomalies: In the mid-latitudes, both the AOGCM and SOM simulations show a positive PNA-like geopotential height anomaly over the Gulf of Alaska as a response to an intensified AMOC. These anomalies have a barotropic structure, unlike the thermal response over the Arctic. This connection between the AMOC and PNA could result from the midlatitude changes: a global reduction of the storm tracks and the zonal-mean winds. Alternatively, it could be a response to tropical heating anomalies (the northward shift of the ITCZ) through the propagation of Rossby waves, as observed during ENSO (Lau and Nath, 1996, Zhang and Delworth, 2007).

Ocean heat storage: We found that when heat storage is integrated in whole depth, the ocean loses energy to the atmosphere during the strong AMOC phase, with significant impacts on surface fluxes even over 100 years. A strengthening AMOC is more frequently tied to increasing storage in the upper ocean (e.g., Cheng et al., 2021; Latif et al., 2019), and we verified that an increase in OHC indeed occurs in the North Atlantic ocean in the AOGCM, but it is exceeded by decreasing OHC in the Southern Hemisphere, as the northward OMET by the AMOC is not fully compensated by surface fluxes. Further work is needed to better understand this reduction in ocean heat content (OHC), and why the anomalous OMET is not fully compensated and the OHC changes not balanced globally. Nonetheless, this anticorrelation between AMOC and OHC was also found in Pausata et al. (2015), which showed a reduction in global OHC in response to an intensified AMOC induced by high-latitude volcanic eruptions.

Future climate: The slowdown in the AMOC is a robust feature of model projections of global warming; however, the magnitude and impacts of this decline differ in different models. Bellomo et al. (2021) examined 30 idealized abrupt-4xCO_2 climate model simulations. Models with larger AMOC decline were found to result in a southward displacement of ITCZ and a poleward shift of the mid-latitude jet. In models with a more moderate AMOC weakening, the precipitation rather showed a wet-gets-wetter, dry-gets-drier pattern, and there were smaller displacements of the mid-latitude jet. Our study exhibits a distinct displacement of the ITCZ, but the response of the mid-latitude jet is weaker and looks more like a weakening. But future changes in the northern midlatitudes are the result of a number of competing mechanisms such as tropical and Arctic warmings and therefore difficult to predict. To better isolate the role of the AMOC decrease, climate change simulations with constrained baroclinic currents are worth exploring, as well as comparisons of the energy transport changes between different models.

5. References

Ba, J., and Coauthors, 2014: A multi-model comparison of Atlantic multidecadal variability. *Clim. Dyn.*, **43**, 2333–2348, https://doi.org/10.1007/s00382-014-2056-1.

Barkstrom, B. R., 1984: The Earth Radiation Budget Experiment (ERBE). *Bull. Am. Meteorol. Soc.*, **65**, 1170–1185, https://doi.org/10.1175/1520-0477(1984)065<1170:TERBE>2.0.CO;2.

Bellomo, K., M. Angeloni, S. Corti, and J. von Hardenberg, 2021: Future climate change shaped by inter-model differences in Atlantic meridional overturning circulation response. *Nat. Commun.*, **12**, 3659, https://doi.org/10.1038/s41467-021-24015-w.

Bjerknes, J., 1964: Atlantic Air-Sea Interaction. *Advances in Geophysics*, H.E. Landsberg and J. Van Mieghem, Eds., Vol. 10 of, Elsevier, 1–82.

Blunier, T., and E. J. Brook, 2001: Timing of Millennial-Scale Climate Change in Antarctica and Greenland During the Last Glacial Period. *Science*, **291**, 109–112, https://doi.org/10.1126/science.291.5501.109.

Boucher, O., and Coauthors, 2020: Presentation and evaluation of the IPSL-CM6A-LR climate model. *J. Adv. Model. Earth Syst.*, **n/a**, e2019MS002010, https://doi.org/10.1029/2019MS002010.

Brachet, S., F. Codron, Y. Feliks, M. Ghil, H. L. Treut, and E. Simonnet, 2012: Atmospheric Circulations Induced by a Midlatitude SST Front: A GCM Study. *J. Clim.*, **25**, 1847–1853, https://doi.org/10.1175/JCLI-D-11-00329.1.

Brunnabend, S.-E., and H. A. Dijkstra, 2017: Asymmetric response of the Atlantic Meridional Ocean Circulation to freshwater anomalies in a strongly-eddying global ocean model. *Tellus Dyn. Meteorol. Oceanogr.*, **69**, 1299283, https://doi.org/10.1080/16000870.2017.1299283.

Buckley, M. W., and J. Marshall, 2016: Observations, inferences, and mechanisms of the Atlantic Meridional Overturning Circulation: A review. *Rev. Geophys.*, **54**, 5–63, https://doi.org/10.1002/2015RG000493.

Caesar, L., G. D. McCarthy, D. J. R. Thornalley, N. Cahill, and S. Rahmstorf, 2021: Current Atlantic Meridional Overturning Circulation weakest in last millennium. *Nat. Geosci.*, **14**, 118–120, https://doi.org/10.1038/s41561-021-00699-z.

Cheng, L., and Coauthors, 2021: Upper Ocean Temperatures Hit Record High in 2020. *Adv. Atmospheric Sci.*, **38**, 523–530, https://doi.org/10.1007/s00376-021-0447-x.

Cheruy, F., and Coauthors, 2020: Improved Near-Surface Continental Climate in IPSL-CM6A-LR by Combined Evolutions of Atmospheric and Land Surface Physics. *J. Adv. Model. Earth Syst.*, **12**, e2019MS002005, https://doi.org/10.1029/2019ms002005.

Chiang, J. C. H., and A. R. Friedman, 2012: Extratropical Cooling, Interhemispheric Thermal Gradients, and Tropical Climate Change. *Annu. Rev. Earth Planet. Sci.*, **40**, 383–412, https://doi.org/10.1146/annurev-earth-042711-105545.

Cunningham, S. A., and Coauthors, 2007: Temporal Variability of the Atlantic Meridional Overturning Circulation at 26.5°N. *Science*, **317**, 935–938, https://doi.org/10.1126/science.1141304.

Day, J. J., J. C. Hargreaves, J. D. Annan, and A. Abe-Ouchi, 2012: Sources of multi-decadal variability in Arctic sea ice extent. *Environ. Res. Lett.*, **7**, 034011, https://doi.org/10.1088/1748-9326/7/3/034011.

Delworth, T. L., and F. Zeng, 2012: Multicentennial variability of the Atlantic meridional overturning circulation and its climatic influence in a 4000 year simulation of the GFDL CM2.1 climate model: MULTICENTENNIAL CLIMATE VARIABILITY. *Geophys. Res. Lett.*, **39**, n/a-n/a, https://doi.org/10.1029/2012GL052107.

Deser, C., R. A. Tomas, and L. Sun, 2015: The Role of Ocean–Atmosphere Coupling in the Zonal-Mean Atmospheric Response to Arctic Sea Ice Loss. *J. Clim.*, **28**, 2168–2186, https://doi.org/10.1175/JCLI-D-14-00325.1.

Drews, A., R. J. Greatbatch, H. Ding, M. Latif, and W. Park, 2015: The use of a flow field correction technique for alleviating the North Atlantic cold bias with application to the Kiel Climate Model. *Ocean Dyn.*, **65**, 1079–1093, https://doi.org/10.1007/s10236-015-0853-7.

Ebisuzaki, W., 1997: A Method to Estimate the Statistical Significance of a Correlation When the Data Are Serially Correlated. *J. Clim.*, **10**, 2147–2153, https://doi.org/10.1175/1520-0442(1997)010<2147:AMTETS>2.0.CO;2.

Frierson, D. M. W., and Coauthors, 2013: Contribution of ocean overturning circulation to tropical rainfall peak in the Northern Hemisphere. *Nat. Geosci.*, **6**, 940–944, https://doi.org/10.1038/ngeo1987.

Ganachaud, A., and C. Wunsch, 2003: Large-Scale Ocean Heat and Freshwater Transports during the World Ocean Circulation Experiment. *J. Clim.*, **16**, 696–705, https://doi.org/10.1175/1520-0442(2003)016<0696:LSOHAF>2.0.CO;2.

Gastineau, G., and C. Frankignoul, 2012: Cold-season atmospheric response to the natural variability of the Atlantic meridional overturning circulation. *Clim. Dyn.*, **39**, 37–57, https://doi.org/10.1007/s00382-011-1109-y.

——, and ——, 2015: Influence of the North Atlantic SST Variability on the Atmospheric Circulation during the Twentieth Century. *J. Clim.*, **28**, 1396–1416, https://doi.org/10.1175/JCLI-D-14-00424.1.

Green, B., and J. Marshall, 2017: Coupling of Trade Winds with Ocean Circulation Damps ITCZ Shifts. *J. Clim.*, **30**, 4395–4411, https://doi.org/10.1175/JCLI-D-16-0818.1.

Harrison, E. F., P. Minnis, B. R. Barkstrom, V. Ramanathan, R. D. Cess, and G. G. Gibson, 1990: Seasonal variation of cloud radiative forcing derived from the Earth Radiation Budget Experiment. *J. Geophys. Res. Atmospheres*, **95**, 18687–18703, https://doi.org/10.1029/JD095iD11p18687.

Hobbs, W., M. D. Palmer, and D. Monselesan, 2016: An Energy Conservation Analysis of Ocean Drift in the CMIP5 Global Coupled Models. *J. Clim.*, **29**, 1639–1653, https://doi.org/10.1175/JCLI-D-15-0477.1.

Jackson, L., and M. Vellinga, 2013: Multidecadal to Centennial Variability of the AMOC: HadCM3 and a Perturbed Physics Ensemble. *J. Clim.*, **26**, 2390–2407, https://doi.org/10.1175/JCLI-D-11-00601.1.

Jackson, L. C., R. S. Smith, and R. A. Wood, 2017: Ocean and atmosphere feedbacks affecting AMOC hysteresis in a GCM. *Clim. Dyn.*, **49**, 173–191, https://doi.org/10.1007/s00382-016-3336-8.

Jackson, L. C., A. Biastoch, M. W. Buckley, D. G. Desbruyères, E. Frajka-Williams, B. Moat, and J. Robson, 2022: The evolution of the North Atlantic Meridional Overturning Circulation since 1980. *Nat. Rev. Earth Environ.*, **3**, 241–254, https://doi.org/10.1038/s43017-022-00263-2.

Jiang, W., G. Gastineau, and F. Codron, 2021: Multicentennial Variability Driven by Salinity Exchanges Between the Atlantic and the Arctic Ocean in a Coupled Climate Model. *J. Adv. Model. Earth Syst.*, **13**, e2020MS002366, https://doi.org/10.1029/2020MS002366.

Johns, W. E., and Coauthors, 2011: Continuous, Array-Based Estimates of Atlantic Ocean Heat Transport at 26.5°N. *J. Clim.*, **24**, 2429–2449, https://doi.org/10.1175/2010JCLI3997.1.

Kang, S. M., 2020: Extratropical Influence on the Tropical Rainfall Distribution. *Curr. Clim. Change Rep.*, **6**, 24–36, https://doi.org/10.1007/s40641-020-00154-y.

——, I. M. Held, and S.-P. Xie, 2014: Contrasting the tropical responses to zonally asymmetric extratropical and tropical thermal forcing. *Clim. Dyn.*, **42**, 2033–2043, https://doi.org/10.1007/s00382-013-1863-0.

——, Y. Shin, and F. Codron, 2018: The partitioning of poleward energy transport response between the atmosphere and Ekman flux to prescribed surface forcing in a simplified GCM. *Geosci. Lett.*, **5**, 22, https://doi.org/10.1186/s40562-018-0124-9.

Kanzow, T., and Coauthors, 2010: Seasonal Variability of the Atlantic Meridional Overturning Circulation at 26.5°N. *J. Clim.*, **23**, 5678–5698, https://doi.org/10.1175/2010JCLI3389.1.

Kato, S., and Coauthors, 2020: Uncertainty in Satellite-Derived Surface Irradiances and Challenges in Producing Surface Radiation Budget Climate Data Record. *Remote Sens.*, **12**, 1950, https://doi.org/10.3390/rs12121950.

Kim, W. M., S. Yeager, and G. Danabasoglu, 2020: Atlantic Multidecadal Variability and Associated Climate Impacts Initiated by Ocean Thermohaline Dynamics. *J. Clim.*, **33**, 1317–1334, https://doi.org/10.1175/JCLI-D-19-0530.1.

Klinger, B. A., and J. Marotzke, 2000: Meridional Heat Transport by the Subtropical Cell. *J. Phys. Oceanogr.*, **30**, 696–705, https://doi.org/10.1175/1520-0485(2000)030<0696:MHTBTS>2.0.CO;2.

Knight, J. R., 2009: The Atlantic Multidecadal Oscillation Inferred from the Forced Climate Response in Coupled General Circulation Models. *J. Clim.*, **22**, 1610–1625, https://doi.org/10.1175/2008JCLI2628.1.

Latif, M., T. Park, and W. Park, 2019: Decadal Atlantic Meridional Overturning Circulation slowing events in a climate model. *Clim. Dyn.*, **53**, 1111–1124, https://doi.org/10.1007/s00382-019-04772-7.

Lau, N.-C., and M. J. Nath, 1996: The Role of the "Atmospheric Bridge" in Linking Tropical Pacific ENSO Events to Extratropical SST Anomalies. *J. Clim.*, **9**, 2036–2057, https://doi.org/10.1175/1520-0442(1996)009<2036:TROTBI>2.0.CO;2.

L'Hévéder, B., F. Codron, and M. Ghil, 2015: Impact of Anomalous Northward Oceanic Heat Transport on Global Climate in a Slab Ocean Setting. *J. Clim.*, **28**, 2650–2664, https://doi.org/10.1175/JCLI-D-14-00377.1.

Liu, Z., and Coauthors, 2021: Acceleration of western Arctic sea ice loss linked to the Pacific North American pattern. *Nat. Commun.*, **12**, 1519, https://doi.org/10.1038/s41467-021-21830-z.

Lorenz, E. N., 1967: THE NATURE AND THEORY OF THE GENERAL CIRCULATION OF THE ATMOSPHERE. 187.

Lozier, M. S., and Coauthors, 2017: Overturning in the Subpolar North Atlantic Program: A New International Ocean Observing System. *Bull. Am. Meteorol. Soc.*, **98**, 737–752, https://doi.org/10.1175/BAMS-D-16-0057.1.

Mahajan, S., R. Zhang, and T. L. Delworth, 2011: Impact of the Atlantic Meridional Overturning Circulation (AMOC) on Arctic Surface Air Temperature and Sea Ice Variability. *J. Clim.*, **24**, 6573–6581, https://doi.org/10.1175/2011JCLI4002.1.

Marshall, J., A. Donohoe, D. Ferreira, and D. McGee, 2014: The ocean's role in setting the mean position of the Inter-Tropical Convergence Zone. *Clim. Dyn.*, **42**, 1967–1979, https://doi.org/10.1007/s00382-013-1767-z.

McCarthy, G. D., and Coauthors, 2015: Measuring the Atlantic Meridional Overturning Circulation at 26°N. *Prog. Oceanogr.*, **130**, 91–111, https://doi.org/10.1016/j.pocean.2014.10.006.

McCoy, D. T., R. Eastman, D. L. Hartmann, and R. Wood, 2017: The Change in Low Cloud Cover in a Warmed Climate Inferred from AIRS, MODIS, and ERA-Interim. *J. Clim.*, **30**, 3609–3620, https://doi.org/10.1175/JCLI-D-15-0734.1.

McGee, D., E. Moreno-Chamarro, B. Green, J. Marshall, E. Galbraith, and L. Bradtmiller, 2018: Hemispherically asymmetric trade wind changes as signatures of past ITCZ shifts. *Quat. Sci. Rev.*, **180**, 214–228, https://doi.org/10.1016/j.quascirev.2017.11.020.

Menary, M. B., W. Park, K. Lohmann, M. Vellinga, M. D. Palmer, M. Latif, and J. H. Jungclaus, 2012: A multimodel comparison of centennial Atlantic meridional overturning circulation variability. *Clim. Dyn.*, **38**, 2377–2388, https://doi.org/10.1007/s00382-011-1172-4.

Mignot, J., A. Ganopolski, and A. Levermann, 2007: Atlantic Subsurface Temperatures: Response to a Shutdown of the Overturning Circulation and Consequences for Its Recovery. *J. Clim.*, **20**, 4884–4898, https://doi.org/10.1175/JCLI4280.1.

Mignot, J., and Coauthors, 2021: The Tuning Strategy of IPSL-CM6A-LR. *J. Adv. Model. Earth Syst.*, **13**, e2020MS002340, https://doi.org/10.1029/2020MS002340.

Minobe, S., A. Kuwano-Yoshida, N. Komori, S.-P. Xie, and R. J. Small, 2008: Influence of the Gulf Stream on the troposphere. *Nature*, **452**, 206–209, https://doi.org/10.1038/nature06690.

Montade, V., M. Kageyama, N. Combourieu-Nebout, M.-P. Ledru, E. Michel, G. Siani, and C. Kissel, 2015: Teleconnection between the Intertropical Convergence Zone and southern westerly winds throughout the last deglaciation. *Geology*, **43**, 735–738, https://doi.org/10.1130/G36745.1.

Moore, G. w. k., R. s. Pickart, I. a. Renfrew, and K. Våge, 2014: What causes the location of the air-sea turbulent heat flux maximum over the Labrador Sea? *Geophys. Res. Lett.*, **41**, 3628–3635, https://doi.org/10.1002/2014GL059940.

Moreno-Chamarro, E., J. Marshall, and T. L. Delworth, 2019: Linking ITCZ Migrations to the AMOC and North Atlantic/Pacific SST Decadal Variability. *J. Clim.*, **33**, 893–905, https://doi.org/10.1175/JCLI-D-19-0258.1.

Muir, L. C., and A. V. Fedorov, 2015: How the AMOC affects ocean temperatures on decadal to centennial timescales: the North Atlantic versus an interhemispheric seesaw. *Clim. Dyn.*, **45**, 151–160, https://doi.org/10.1007/s00382-014-2443-7.

Muir, L. C., and A. V. Fedorov, 2017: Evidence of the AMOC interdecadal mode related to westward propagation of temperature anomalies in CMIP5 models. *Clim. Dyn.*, **48**, 1517–1535, https://doi.org/10.1007/s00382-016-3157-9.

Oldenburg, D., R. C. J. Wills, K. C. Armour, L. Thompson, and L. C. Jackson, 2021: Mechanisms of Low-Frequency Variability in North Atlantic Ocean Heat Transport and AMOC. *J. Clim.*, **34**, 4733–4755, https://doi.org/10.1175/JCLI-D-20-0614.1.

Pausata, F. S. R., L. Chafik, R. Caballero, and D. S. Battisti, 2015: Impacts of high-latitude volcanic eruptions on ENSO and AMOC. *Proc. Natl. Acad. Sci.*, **112**, 13784–13788, https://doi.org/10.1073/pnas.1509153112.

Peings, Y., and G. Magnusdottir, 2014: Forcing of the wintertime atmospheric circulation by the multidecadal fluctuations of the North Atlantic ocean. *Environ. Res. Lett.*, **9**, 034018, https://doi.org/10.1088/1748-9326/9/3/034018.

Rahmstorf, S., J. E. Box, G. Feulner, M. E. Mann, A. Robinson, S. Rutherford, and E. J. Schaffernicht, 2015: Exceptional twentieth-century slowdown in Atlantic Ocean overturning circulation. *Nat. Clim. Change*, **5**, 475–480, https://doi.org/10.1038/nclimate2554.

Schneider, T., T. Bischoff, and G. H. Haug, 2014: Migrations and dynamics of the intertropical convergence zone. *Nature*, **513**, 45–53, https://doi.org/10.1038/nature13636.

Screen, J. A., and Coauthors, 2018: Consistency and discrepancy in the atmospheric response to Arctic sea-ice loss across climate models. *Nat. Geosci.*, **11**, 155–163, https://doi.org/10.1038/s41561-018-0059-y.

Stouffer, R. J., and Coauthors, 2006: Investigating the Causes of the Response of the Thermohaline Circulation to Past and Future Climate Changes. *J. Clim.*, **19**, 1365–1387, https://doi.org/10.1175/JCLI3689.1.

Sutton, R. T., and D. L. R. Hodson, 2007: Climate Response to Basin-Scale Warming and Cooling of the North Atlantic Ocean. *J. Clim.*, **20**, 891–907, https://doi.org/10.1175/JCLI4038.1.

Talley, L. D., 2003: Shallow, Intermediate, and Deep Overturning Components of the Global Heat Budget. *J. Phys. Oceanogr.*, **33**, 530–560, https://doi.org/10.1175/1520-0485(2003)033<0530:SIADOC>2.0.CO;2.

Tandon, N. F., and P. J. Kushner, 2015: Does External Forcing Interfere with the AMOC's Influence on North Atlantic Sea Surface Temperature? *J. Clim.*, **28**, 6309–6323, https://doi.org/10.1175/JCLI-D-14-00664.1.

Thomas, M. D., and A. V. Fedorov, 2019: Mechanisms and Impacts of a Partial AMOC Recovery Under Enhanced Freshwater Forcing. *Geophys. Res. Lett.*, **46**, 3308–3316, https://doi.org/10.1029/2018GL080442.

Thornalley, D. J. R., and Coauthors, 2018: Anomalously weak Labrador Sea convection and Atlantic overturning during the past 150 years. *Nature*, **556**, 227–230, https://doi.org/10.1038/s41586-018-0007-4.

Ting, M., Y. Kushnir, R. Seager, and C. Li, 2009: Forced and Internal Twentieth-Century SST Trends in the North Atlantic. *J. Clim.*, **22**, 1469–1481, https://doi.org/10.1175/2008JCLI2561.1.

Trenberth, K. E., and J. M. Caron, 2001: Estimates of Meridional Atmosphere and Ocean Heat Transports. *J. Clim.*, **14**, 3433–3443, https://doi.org/10.1175/1520-0442(2001)014<3433:EOMAAO>2.0.CO;2.

——, Y. Zhang, J. T. Fasullo, and L. Cheng, 2019: Observation-Based Estimates of Global and Basin Ocean Meridional Heat Transport Time Series. *J. Clim.*, **32**, 4567–4583, https://doi.org/10.1175/JCLI-D-18-0872.1.

Vellinga, M., and P. Wu, 2004: Low-Latitude Freshwater Influence on Centennial Variability of the Atlantic Thermohaline Circulation. *J. Clim.*, **17**, 4498–4511, https://doi.org/10.1175/3219.1.

Weijer, W., W. Cheng, O. A. Garuba, A. Hu, and B. T. Nadiga, 2020: CMIP6 Models Predict Significant 21st Century Decline of the Atlantic Meridional Overturning Circulation. *Geophys. Res. Lett.*, **47**, e2019GL086075, https://doi.org/10.1029/2019GL086075.

Wielicki, B. A., B. R. Barkstrom, E. F. Harrison, R. B. Lee, G. L. Smith, and J. E. Cooper, 1996: Clouds and the Earth's Radiant Energy System (CERES): An Earth Observing System Experiment. *Bull. Am. Meteorol. Soc.*, **77**, 853–868, https://doi.org/10.1175/1520-0477(1996)077<0853:CATERE>2.0.CO;2.

Yu, S., and M. S. Pritchard, 2019: A Strong Role for the AMOC in Partitioning Global Energy Transport and Shifting ITCZ Position in Response to Latitudinally Discrete Solar Forcing in CESM1.2. *J. Clim.*, **32**, 2207–2226, https://doi.org/10.1175/JCLI-D-18-0360.1.

Zanchettin, D., O. Bothe, W. Müller, J. Bader, and J. H. Jungclaus, 2014: Different flavors of the Atlantic Multidecadal Variability. *Clim. Dyn.*, **42**, 381–399, https://doi.org/10.1007/s00382-013-1669-0.

Zhang, R., 2007: Anticorrelated multidecadal variations between surface and subsurface tropical North Atlantic. *Geophys. Res. Lett.*, **34**, https://doi.org/10.1029/2007GL030225.

——, 2015: Mechanisms for low-frequency variability of summer Arctic sea ice extent. *Proc. Natl. Acad. Sci.*, **112**, 4570–4575, https://doi.org/10.1073/pnas.1422296112.

——, 2017: On the persistence and coherence of subpolar sea surface temperature and salinity anomalies associated with the Atlantic multidecadal variability. *Geophys. Res. Lett.*, **44**, 7865–7875, https://doi.org/10.1002/2017GL074342.

——, and T. L. Delworth, 2005: Simulated Tropical Response to a Substantial Weakening of the Atlantic Thermohaline Circulation. *J. Clim.*, **18**, 1853–1860, https://doi.org/10.1175/JCLI3460.1.

——, S. M. Kang, and I. M. Held, 2010: Sensitivity of Climate Change Induced by the Weakening of the Atlantic Meridional Overturning Circulation to Cloud Feedback. *J. Clim.*, **23**, 378–389, https://doi.org/10.1175/2009JCLI3118.1.

——, R. Sutton, G. Danabasoglu, T. L. Delworth, W. M. Kim, J. Robson, and S. G. Yeager, 2016: Comment on "The Atlantic Multidecadal Oscillation without a role for ocean circulation." *Science*, **352**, 1527–1527, https://doi.org/10.1126/science.aaf1660.

——, ——, ——, Y. Kwon, R. Marsh, S. G. Yeager, D. E. Amrhein, and C. M. Little, 2019: A Review of the Role of the Atlantic Meridional Overturning Circulation in Atlantic Multidecadal Variability and Associated Climate Impacts. *Rev. Geophys.*, **57**, 316–375, https://doi.org/10.1029/2019RG000644.

Supporting Information for

Climate response to the Atlantic meridional energy transport variations

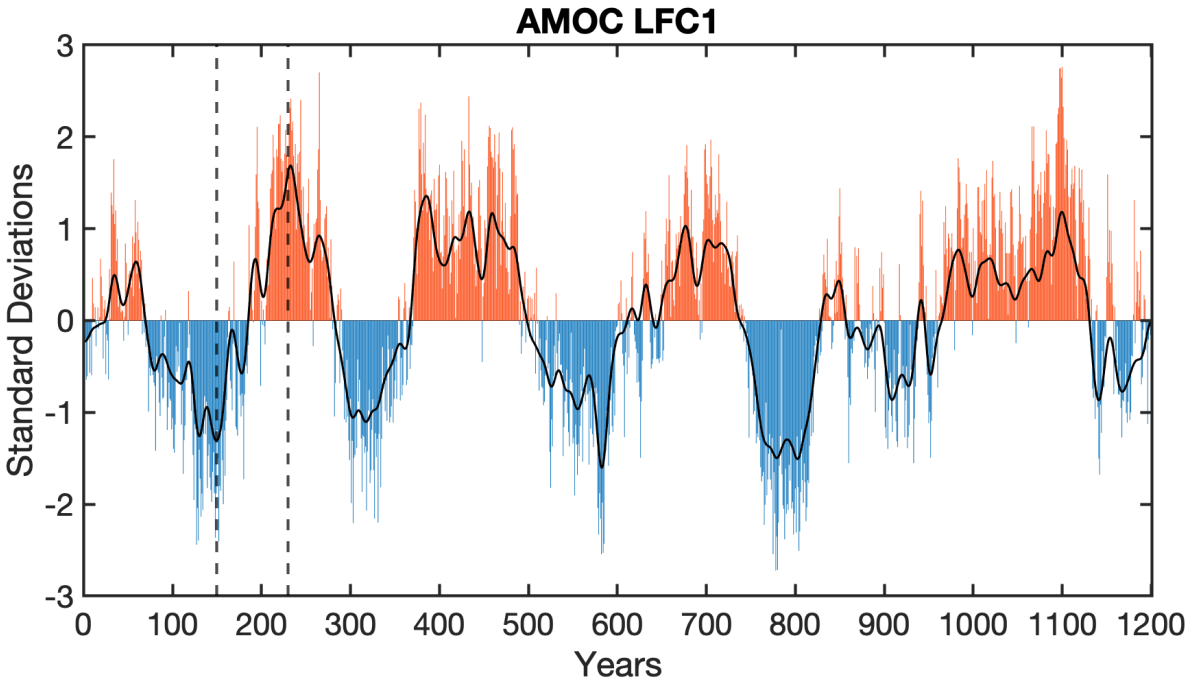

Fig. S1. Standardized first low frequency component (LFC1; in colors) of the Atlantic meridional overturning circulation (AMOC), adapted from Jiang et al. (2021). The solid black line shows the maximum of the Atlantic meridional stream function at 30°N, after applying a third-order Butterworth lowpass filter with a cutoff period of 20 years. The two vertical dashed lines indicate two different initial states for the SG and WK simulations, the third one being year 0.

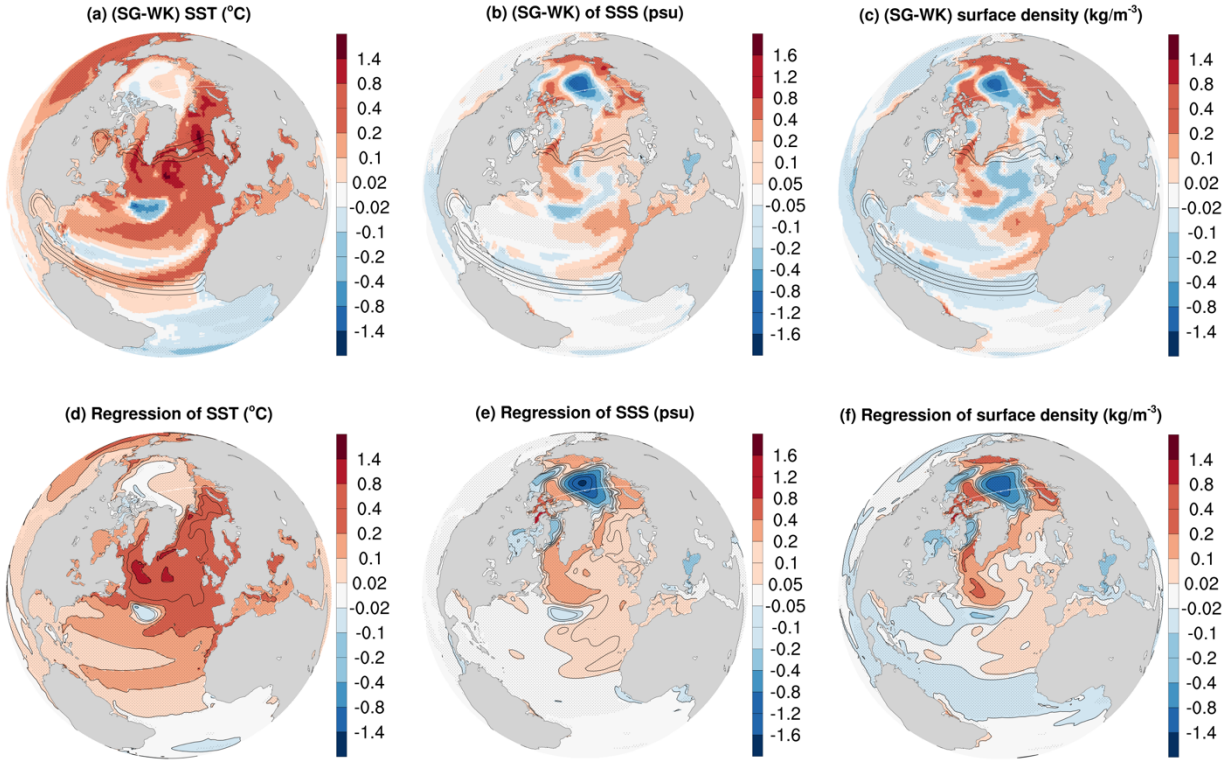

Fig. S2. Differences of input sea surface (a) temperature (in °C), (b) salinity (in psu), and (c) density (in kg m^{-3}) between simulations SG and WK. Black contours in (a)-(c) indicate the spatial mask (varying from 0 to 1) for applying the input data correction. (e) – (f) are the same as (a) – (c) but for regression of the same fields onto the AMOC low-frequency index in CTL-CM. The stipples show the significance level of 5%.

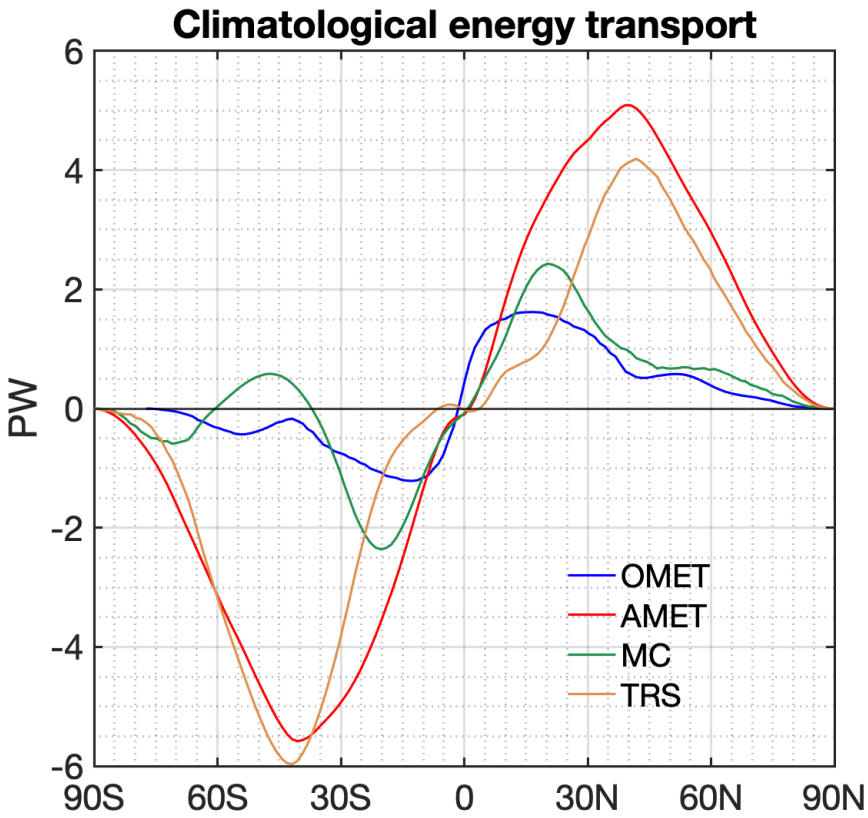

Fig. S3. Mean oceanic meridional energy transport (in blue), atmospheric meridional energy transport (in red) and contributions in the atmosphere from the mean circulation (in green) and transient eddies (in brown). Average from the six runs with the fully coupled model.

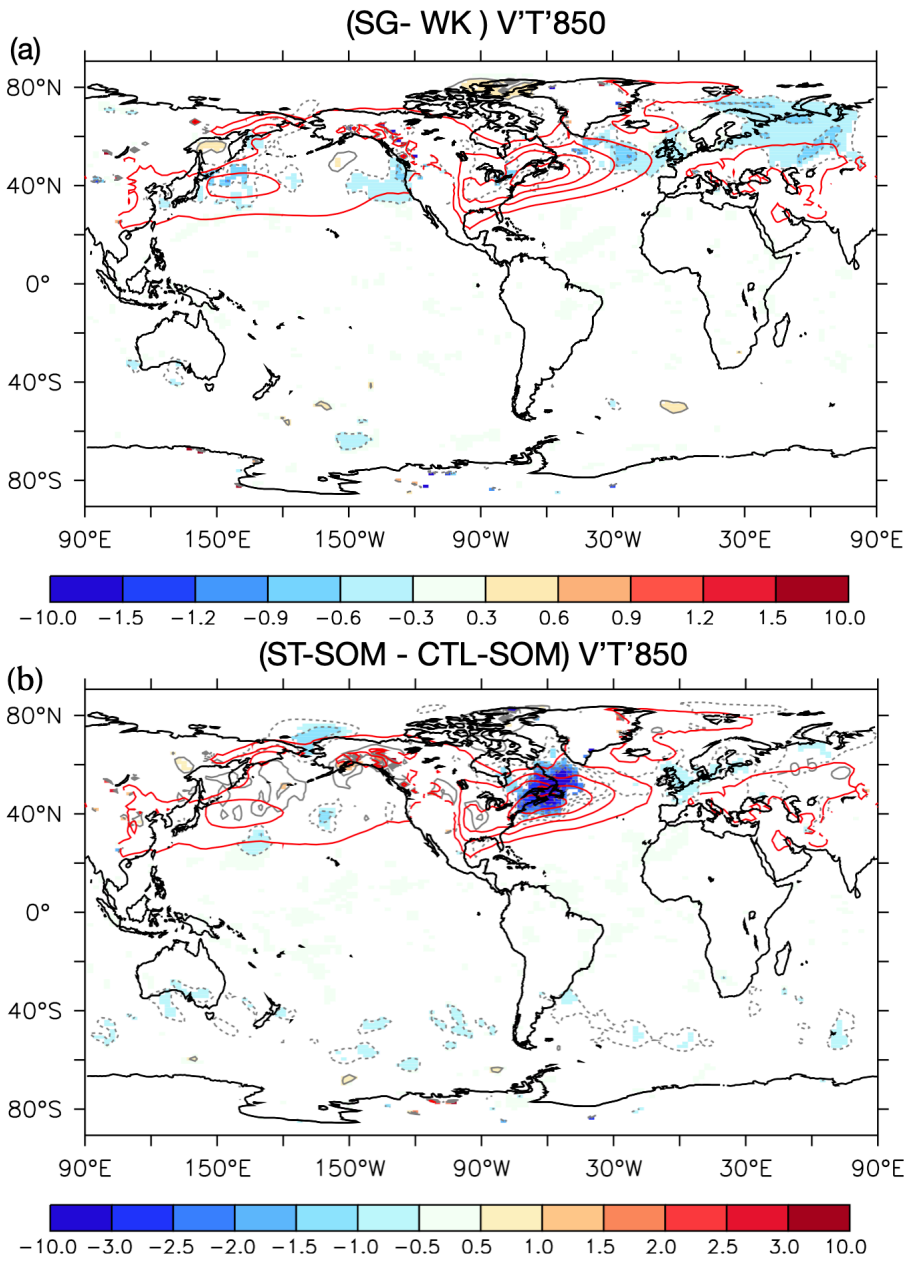

Fig. S4. (a) Mean (red contours) and anomalous (grey dashed contours and shading) eddy meridional heat flux $V'T'$ (in K ms^{-1}) at 850 hPa for coupled runs SG minus WK. (b) Same as (a) but for SOM experiments ST-SOM minus CTL-SOM. $V'T'$ is calculated from daily temperature and meridional velocity at 850 hPa using a Lancos high-pass filter with a window of 21 days and a cutoff period of 10 days. Red contour intervals are 5 K ms^{-1} starting from zero. Grey dashed contours use same interval as shading, but the latter is only shown when the anomalies are significant at the 10% level.

5.3 Discussion

The method used to constrain the flow field is derived initially from the semi-prognostic method developed by Greatbatch et al. (2004) and Sheng et al. (2001). However, Eden et al. (2004) pointed out that some wave dynamics are changed with the application of this semi-prognostic method, for example, reduced Rossby wave speeds and damped eddy activity. Drews et al., 2015 and Eden et al. (2004) thus made the correction non-flow interactive to avoid these impacts, which can presumably affect the ocean dynamics and the resultant climate variability. Therefore, we also did a test to apply a non-interactive flow constraint. To implement it, the seawater density used to calculate the horizontal pressure force is written as:

$$\rho = \rho_m + \Delta\rho \qquad (5.1)$$

The second term on the right-hand side is a density anomaly. This anomaly is given as an input repeated monthly climatological cycle. Such anomaly is independent of the actual *on-line* density. Some preliminary work using this non-flow interactive is discussed in Chapter 6.2.3.

Chapter 6

Contents

6 CONCLUSIONS AND PERSPECTIVES 147

6.1 CONCLUSIONS 147
6.2 PERSPECTIVES 153
6.2.1 REALISM OF MULTI-CENTENNIAL VARIABILITY 153
6.2.2 TOOLS TO UNDERSTAND AMOC VARIABILITY 154
6.2.3 POSSIBLE IMPROVEMENTS IN FLOW-FIELD CONSTRAINT METHOD 157
6.2.4 CONSTRAINING FLOWS TO STUDY CLIMATE CHANGE 158
6.2.5 TELECONNECTIONS WITH OTHER BASINS 159

6 Conclusions and Perspectives

6.1 Conclusions

The AMOC low-frequency variability and its climate impact have been subjects of many model studies. In most studies, the focus is on the multidecadal timescale. In recent years, fluctuations on a centennial to multi-centennial scale have emerged in some AOGCMs since Delworth and Zeng (2012) first found them. On time scales longer than half a century, the AMOC variations are widely found as internal ocean oscillations governed by the salinity changes. There are studies stressing the roles of atmospheric forcing (Jackson and Vellinga, 2013) and oceanic temperatures (Jungclaus et al., 2005). Still, even in these studies, the influence of salinity is dominant. However, there is no agreement on where the salt anomalies originate. For instance, Delworth and Zeng (2012) found that these anomalies are generated in the Southern Ocean in the GFDL CM2.1 model. Vellinga and Wu (2004) suggested that meridional shifts of the ITCZ generate the salinity anomalies in the subtropical Atlantic in the HadCM3 model. Other studies emphasized the Arctic Ocean and the exchanges with the Atlantic Ocean (e.g., Hawkins and Sutton, 2007; Jahn and Holland, 2013; Jungclaus et al., 2005; Pardaens et al., 2008).

When I started my PhD, the latest version of the IPSL model, IPSL-CM6A-LR, was under development. Boucher et al. (2020) pointed out the emergence of low-frequency variability of the AMOC with a period of around 200 years in this model. This variability was called the bicentennial variability. The first work in my PhD was to examine this low-frequency variability. The

variability instead appears to show a broad spectrum with a maximum for periods of 100-yr and longer but no clear peak. This variability is, therefore, called the multi-centennial variability. A statistical method called low-frequency component analysis (LFCA) was used to better isolate the low-frequency variations from high-frequency signals. The LFCA looks for the linear combination of the empirical orthogonal functions that maximize the ratio of low frequency to the total variance (Wills et al., 2018). The LFCA provid es a spatial pattern, called the low-frequency pattern (LFP), which explains most low-frequency variance. The associated time series, called the low-frequency component (LFC), is found by projecting the original unfiltered data onto the LFP. The first LFP shows a meridionally coherent overturning cell, extending from 30°S to 80°N, with a typical variability of 0.8 Sv for one standard deviation between 30°N and 50°N. The associated first LFC shows a clear multicentennial variability. Then lagged regression of other fields onto the first LFC was used to investigate the driving mechanism of this low-frequency variability.

We found that the AMOC intensity is modulated by the delayed freshwater exchanges between the North Atlantic and the Arctic. The influence of the atmospheric forcing is found to be marginal. During a strong AMOC, the intensified northward heat transport leads to a warming surface in the North Atlantic Ocean and heats the lower troposphere. The warmer atmosphere and the increased inflow of North Atlantic water into the Arctic Ocean melt the sea ice. The decreasing sea ice volume diminishes the sea ice export at the Fram straight, which leads to a surface freshwater anomaly in the Central Arctic. In addition, the weakened southward East Greenland Current reduces the liquid freshwater export from the Arctic. The freshwater thus accumulates progressively in the Arctic center, in thermal wind balance with an anomalous anticyclonic circulation that helps maintain it inside the Arctic Ocean. Meanwhile, the inflow of Atlantic water in the subsurface through the Barents Sea results in a positive salinity anomaly in the Eastern Arctic subsurface, specifically in the Laptev and East Siberian seas.

The simulated mean transpolar drift flows from the Laptev and East Siberian seas across the Arctic Ocean towards the Lincoln Sea. It tends to transport the positive salinity in the Eastern Arctic subsurface to the central Arctic and transports the central freshwater anomaly to the Lincoln Sea north of Greenland. At the same time, the abnormal cyclonic circulations and positive salinity anomalies around the coast of Greenland act to maintain the weak state of the East Greenland Current, preventing the export of the freshwater anomaly toward the North Atlantic ocean. This competition leads to the surface freshwater anomaly lasting for four to five decades in the Arctic Ocean until it reaches the Lincoln Sea north of Greenland. The salinity anomalies around the coast of Greenland then become negative, and an anomalous anticyclonic circulation is simulated. The East Greenland Current intensifies, and the anomalous freshwater spreads from the Arctic to the convection sites located in the Nordic and Labrador Seas. The AMOC decreases, and the oscillation shifts to the opposite phase, with positive salinity anomalies occurring on the Central

Arctic surface. In section 3.5, we proposed a simplified model for this freshwater recharge mechanism to explain the long time scale. But accurate quantification of the parameters and their realism remains established.

Our study investigates the driving mechanism of the AMOC low-frequency variability in the preindustrial control simulation. With extended historical simulations (over the 1850-2059 period) in the same IPSL-CM6A-LR model, Bonnet, Boucher, et al. (2021) found that this centennial to multi-centennial variability regulates the global mean surface air temperature trend over the historical period (1850 - 2018) by about ~0.1 K per century. In comparison, the observed global mean surface temperature increased by about 0.7 K from the late 19th century to the year 2000 and warmed continuously at the rate of 0.2 K per decade in the first half decade of the 21st century (Hansen et al., 2006). Bonnet, Swingedouw, et al. (2021) found that in the IPSL-CM6A-LR, historical members simulating a large internally-driven weakening of the AMOC also show the lowest rates of global warming over the past 6 -7 decades. This indicates that the low-frequency internal variability from the Atlantic Ocean may have damped the magnitude of global warming over the historical era. The observations of the recent period may therefore represent only the lower bound of the changes induced by anthropogenic activities. Moreover, the recovery from the internally-driven weak AMOC may lead to increased surface air temperature in the Northern Hemisphere and may increase the risk of near-term global warming.

Moreover, this low-frequency oscillation is not unique to IPSL-CM6A-LR. Two other CMIP6 models, i.e., EC-Earth3 (Döscher et al., 2022) and CNRM-CM6 (Voldoire et al., 2019), display similar centennial to multi-centennial variabilities of the AMOC. These two models also use the NEMO3.6 ocean model with the ORCA1 grid. In addition, among the CMIP6 models, the NEMO3.6-based models were shown to display the largest interdecadal global mean surface temperature variability in their *piControl* simulations. The results are similar to the last-millennium simulations when using the AOGCM simulation with estimated changes in the solar activity and volcanic aerosols since 1850 (Parsons et al., 2020). A careful comparison between the variability of these simulations and the proxies results would be needed to see if such variability is overestimated when using NEMO3.6 and the relatively coarse resolution of the ORCA1 grid (Van Noije et al., 2021). In general, models with increased ocean resolution simulate stronger AMOC (section 2.2). Koenigk et al. (2020) practically pointed out that increasing the ocean resolution from ORCA1 to ORCA025 leads to the intensification of the deep convection in the Labrador Sea in four out of the five models that use NEMO3.6. Nevertheless, the existence of the centennial to multi-centennial variability when using the ORCA025 grid remains to be examined. In addition, it is of interest to investigate whether this low-frequency variability emerges in other CMIP6 climate models using different ocean components such as GFDL CM with isopycnal ocean models (Adcroft et al., 2019). In addition, the IPSL-CM6A model also tested and implemented

configurations similar to IPSL-CM6A-LR but using improved atmospheric resolution (called IPSL-CM6A-MR) or improved resolution in both the ocean and atmosphere (call IPSL-CM6A-ORCA025-MR). Using higher resolution in the Arctic ocean might better simulate the sea ice and liquid freshwater exchanges between the Arctic and the North Atlantic. This will allow exploring if the ocean grid plays a role in this variability.

After investigating the mechanism of the low-frequency variations, we explored the climate impact of this variability through dedicated sensitivity experiments using the IPSL-CM6A-LR model. The novelty is that we directly constrain the AMOC rather than applying imposed freshwater or heat fluxes to induce the targeted circulation changes. We constrain the AMOC by imposing a three-dimensional baroclinic current by replacing the raw model density in the calculation of the horizontal pressure force with a linear combination of the model in-situ density and an input in-situ density. The baroclinic flow is changed by the modified pressure force and the resulting horizontal flow in the momentum equations. We imposed input densities corresponding to strong (weak) AMOC associated with the multi-centennial variability. The input density is obtained with the sum of the salinity and temperature regressions onto the first LFC of AMOC presented previously and the climatology from the long-term preindustrial control simulation. The goal is to generate an intensified (a weakened) AMOC and investigate its climate impact.

Before imposing the abnormal AMOC state, we have analyzed the performance of this method using densities corresponding to the climatological conditions of the preindustrial control simulation. We inspected the simulated AMOC and the North Atlantic SST. A 600-yr control simulation that is constrained toward AMOC control conditions shows only a small drift and reduced variability in all examined fields. The differences between constrained and unconstrained control simulations are relatively small. We conclude that the flow-field correction method is able to bring the AMOC toward a stable state corresponding to that of the preindustrial control simulation.

A global impact of the AMOC variability on the atmosphere is found, with large anomalies located in the tropics and the Northern Hemisphere. An intensified AMOC transports more warm water northward at the surface and carries more cold water southward in its lower limb, leading to an increase in the northward heat transport in the Atlantic Ocean. The resultant warm ocean surface in the North Atlantic heats the atmosphere through the negative heat flux feedback. From an energy budget perspective, the increased northward ocean heat transport needs to be balanced. In response, the atmosphere transports abnormal moist static energy southward, which modifies the tropical Hadley circulations and the activity of mid-latitude eddies. The southward energy in the Hadley cell is accomplished by the geopotential energy in the upper branch. Therefore, the flow in the bottom branch is northward. This cross-equatorial northward branch near the surface applies a negative wind stress curl on the ocean, forming a southward transport in the Pacific Ocean. This

anomalous energy flow can be described with the Sverdrup balance applied in the tropics. The associated anomalous shallow overturning circulation transports heat southward. Without the ocean dynamics, the atmospheric variations present similar patterns with greater amplitudes. It is then concluded that the atmosphere produces most of the responses to a stronger AMOC and associated OMET changes through adjustments within the atmosphere, and the Indo-Pacific Ocean acts to damp the atmospheric variations.

The impacts of the AMOC and associated meridional energy transport variability on climate have been extensively studied in previous studies by statistical relationships in multi-centennial control simulations or by sensitivity experiments. We also explored the climate impact with statistical analyses of the piControl run (Chapter 3.3). However, the cause-effect relationships might not be distinguished well via statistical analysis.

In the atmosphere-ocean model GFDL CM2.1, Zhang et al. (2017) applied NAO-related heat flux to increase the AMOC intensity (NAO-AMOC linkage shown in section 2.3.1) and found a poleward displacement of the westerly jet in the Southern Hemisphere. But in our coupled experiments, the Southern Hemisphere jet tends to intensify on its equatorward side and does not show displacement. Many studies investigated the impacts of a slowdown or collapse of the AMOC through "hosing" experiments by applying an additional freshwater flux into the North Atlantic to inhibit deep convection and hence reduce the AMOC strength (e.g., Jackson et al., 2015; Kageyama et al., 2012; Stouffer et al., 2006; Vellinga and Wood, 2002). Some common features found in these studies include widespread cooling in the Northern Hemisphere, less precipitation in the northern hemisphere midlatitudes, large changes in the tropical rainfall and an intensified North Atlantic storm track. In general, these studies have shown a southward shift of ITCZ over the Atlantic Ocean, but the rainfall anomalies in the tropical Pacific Ocean vary in different studies. These impacts are consistent with our results: a strong AMOC leads to wide warming in the Northern Hemisphere, more precipitation and fewer eddy activities in the Northern Hemisphere midlatitudes, and a northward shift of the ITCZ.

However, in the studies of hosing experiments, the application of an extra heat/freshwater flux forcing makes it difficult to disentangle the contribution of the dynamical ocean response from the effects of the forcing used (Kim et al., 2020; Tandon and Kushner, 2015). In addition, the weakening of the AMOC induced is sensitive to the hosing method adopted (Jackson et al., 2017). Haskins et al. (2020) suggested that the induced freshwater weakens the AMOC, but then a buoyant surface cap forms due to the reduced mixed layer depth, altering the atmospheric fluxes. The resulting warm subsurface layer under the surface cap is the primary driver of the AMOC weakening instead. In this perspective, ideally, our methodology can generate strong or weak AMOC states in a more explicit way without these issues.

Experiments in AGCM with prescribed the global SST and sea ice anomalies associated with the AMOC have revealed that the tropical Atlantic is the key region in promoting relationships between the AMOC and ITCZ (e.g., Montade et al., 2015). These experiments showed a larger ITCZ shift in the Atlantic than in the Pacific, as found in our coupled simulations. As these experiments do not simulate realistic heat fluxes at the air-sea surface, changes in the oceanic and atmospheric energy transport cannot be explored in these studies. Our methodology provides a possibility to investigate the mechanisms driving these connections from an energy perspective.

Regarding energy transport, Yu and Pritchard (2019) used experiments with the CESM AOGCM and pointed out that the ocean circulation response to an interhemispheric radiative imbalance can reduce the migrations of the ITCZ. They suggested that the ocean response acts to reduce the AMET response, consistent with our results. They further investigated the sensitivity to the latitudes of the forcing: the tropics, the subtropics, the mid-latitudes, and the high-latitudes. In the Atlantic Ocean, the cross-equatorial OMET increases with the latitude of forcing and the response of shallow subtropical cells in the Pacific Ocean are not monotonic with latitudes. The increase of energy transport in the Atlantic Ocean induced by forcing is not necessarily associated with the same tendency in the Pacific Ocean.

Thus, more work is needed to test the sensitivity of results to the location of the imposed density anomaly. The imposed modifications can be implemented in the subpolar gyre instead of in the broad North Atlantic Ocean between 20ºN and 60ºN in the current simulations. Moreover, the sensitivity to the model used also needs to be tested. As introduced above, the relatively coarse resolution of ORCA1 might amplify the AMOC low-frequency variability. The response of climates to the AMOC variations might differ in the AOGCM using other ocean models, considering the bias in simulating AMOC mean structure among the coupled models (section 2.2). The improvement of resolution in the atmosphere (IPSL-CM6A-MR) or in both ocean and atmosphere (IPSL-CM6A-ORCA025-MR) may better resolve the air-sea heat fluxes and provide chances to better simulate and understand the changes in total ocean heat content corresponding to an intensified AMOC (section 5.2). Lastly, in our present simulations using the IPSL-CM6A-LR model with nominate 1º oceanic resolution, the AMOC constrained to abnormal conditions tends to recover to the neutral state in the late 100-yr (Figure 2a in the article of section 5.2). We suspect that the time needed to recover from the imposed conditions might be shortened in models with a higher oceanic resolution if the increasing resolution would reduce the low-frequency variations.

We conclude here that the first application of flow-field constraint methodology provides inspiring results in investigating the climate impacts of the low-frequency AMOC variability. Meanwhile, more sensitivity experiments are necessary to further verify its performance and explore more possibilities for utilizing this method.

6.2 Perspectives

A few subjects can be revisited in light of the results presented previously. In particular, the mechanism responsible for the time scale of AMOC variability needs to be further understood. In the following, we briefly discuss the realism of this AMOC multi-centennial variability in comparison to results of paleo-proxy records and introduce two tools that might help to figure out such a mechanism. In terms of the climate response to the Atlantic meridional energy transport changes, the teleconnections between the Atlantic and Pacific Oceans deserve further investigation. Finally, we describe possible applications of the flow-field correction method to understand the response of the climate system to global warming.

6.2.1 Realism of multi-centennial variability

Apart from the numerical modeling, the proxy-derived records are also often used to investigate the long-term climate variations in the past 11,700 years (the Holocene epoch). We have shortly introduced the low-frequency variations of the North Atlantic SST and AMOC found by paleo-proxy studies (section 2.3). More discussion regarding the possible utilization of paleo-proxy records is present here.

There have been several approaches to reconstructing past North Atlantic Ocean circulations. Proxies related to SST and sea surface salinity (SSS) can be used, for instance, inferred by Alkenones, foraminifera assemblages or dinoflagellates cyst. Other methods are based on proxies associated with past changes in the deep limb of the AMOC, using the ^{13}C and ^{18}O of benthic foraminifera. Sortable silts were also proposed to reconstruct the intensity of the deep western boundary current (Caesar et al., 2021). Lastly, the Northern Hemisphere land temperature proxy might also be used.

Ayache et al. (2018) pointed out that inconsistencies among different proxy records remain in the reconstruction of the AMOC variations, while Caesar et al. (2021) suggested a consistency among the AMOC proxies. More work is needed to better understand the uncertainties in each proxy used to reconstruct AMOC and figure out the level of agreement among them. Thus, the direct comparison between reconstructed AMOC and simulated AMOC might be limited by the possible inconsistencies in proxy records. The observational SST data has been available since 1870. We can reconstruct the pseudo-SST multi-centennial variations using the observed SST and simulated AMOC variations through the robust fingerprints of AMOC on the North Atlantic surface temperatures. The comparison between this pseudo-SST and proxy-derived SST may yield insights if this multi-centennial is realistic. However, the investigation of variability may be complicated by the effect of external forcings, as forcing and internal variability cannot be distinguished in the historical record.

6.2.2 Tools to understand AMOC variability

We attempted to use an *off-line* mass preserving Lagrangian diagnostic tool named ARIANE (http://mespages.univ-brest.fr/~grima/Ariane/) to find the advective timescales and explicitly depict the actual pathway of the salt anomaly. ARIANE is a diagnostic tool dedicated to the offline calculation of three-dimensional streamlines in a given velocity field (Blanke and Raynaud, 1997; Döös, 1995). We implemented some qualitative experiments by releasing several salinity particles on the Arctic surface or in the mixed layer and aimed to calculate each individual trajectory. However, the trajectory of salinity originating in the Arctic Ocean either ceased at the margin of the Arctic circle or transported very fast after crossing the Arctic boundary. None of them were consistent with the slow propagation of salinity found with regression. The same situation happened when the backward integration was adopted to trace the sources of the Arctic salinity. A closer look at the definition of the ORCA1 grid with the developer of ARIANE would be necessary to establish the reason for this failure. During the PhD period, we failed to find reasonable and convincing results with the Lagrangian tracking method. An alternative way to use Lagrangian tracking is quantitative experiments in which numerous particles are deployed and move between the initial section (where they are released) and final interception sections. Only the end-point characteristics and the mean statistics and stream functions of the trajectories are then output. But in this mode, the ORCA1 grid still needs to be properly defined and recognized. It would be promising to continue these analyses in future work, either with the help of the developer of ARIANE or using another tool for the Lagrangian ocean analysis.

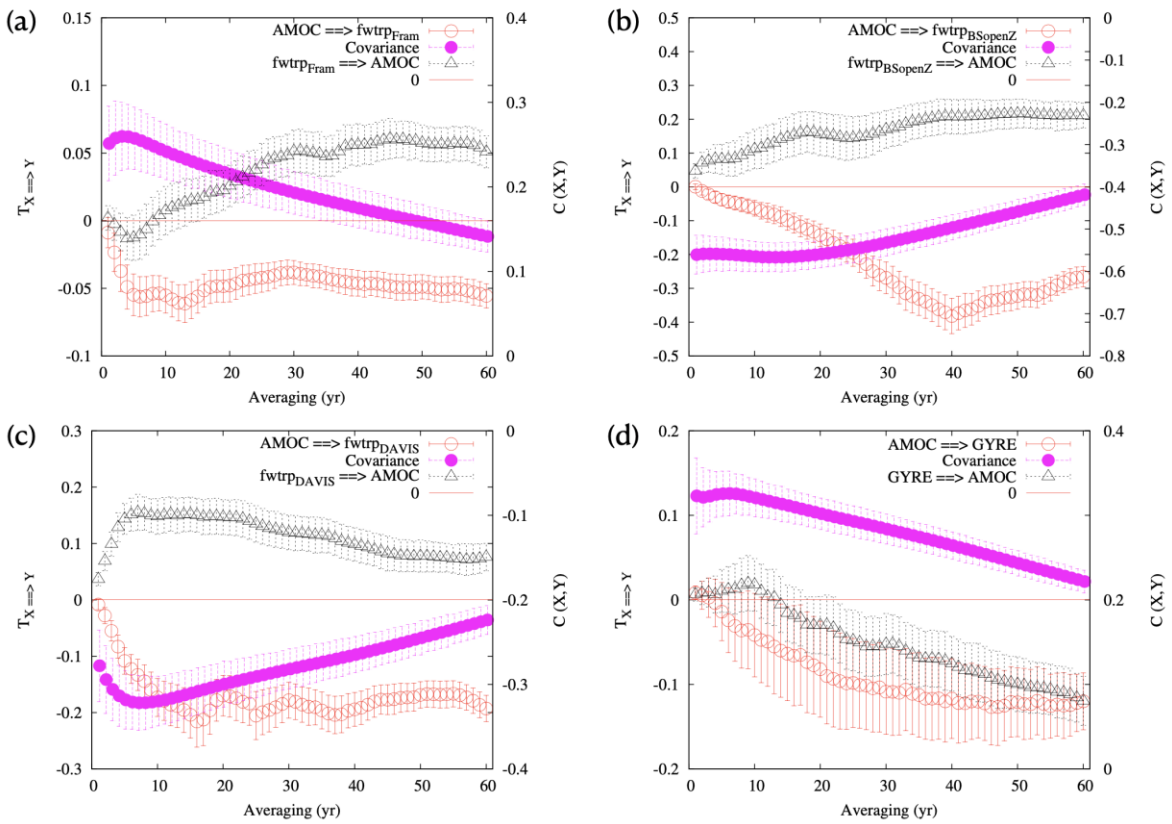

Figure 6.1. (a) Rate of information transfer from AMOC to Fram Strait freshwater transport (red line and empty circles) and from the latter to the former (black line and triangles). The transfer of information is shown as a function of the averaging and measured along the axis on the left. The covariance is measured along the right axis (magenta curve and solid circles). The other three panels are the same as (a) but for (b) freshwater transport through the Barents Opening Sea, (c) through the Davis Strait and (d) the gyre intensity in the Western Arctic. The gyre intensity is given by the area-weighted barotropic stream function. Courtesy of S. Vannistem.

In our study, the connections between AMOC and the liquid or solid freshwater transport were studied with lagged correlation or regression. However, the presence of correlation between two fields does not firmly indicate causality. A causal inference framework called Liang-Kleeman information flow (Liang and Kleeman, 2005) has been recently presented to identify the direction and magnitude of the cause-effect relationships of given variables (Liang, 2014, 2021). This tool has been applied in climate science studies to detect causation in correlated fields. For instance, Stips et al. (2016) found a one-way causality between the total Greenhouse gases and annual global mean surface temperature anomalies. Among the Greenhouse gases, CO_2 is the primary driver of the recent warming. Aerosol makes a smaller contribution, and the influence of volcanic forcings was found in shorter time periods. Another study (https://www.essoar.org/doi/abs/10.1002/essoar.10507846.1; under review) suggested that the

recent and future Arctic sea ice changes are primarily attributed to the air, sea-surface temperatures and OMET. Two-way influences exist, but the impact of the Arctic sea ice on the temperatures and OMET is progressively decreasing in the twenty-first century due to the reduction in sea-ice areas. In contrast, the effect of near-surface air temperature on sea ice stays relatively constant.

We have suggested in Chapter 3 that the AMOC variations are determined by the exchanges of accumulated anomalous freshwater between the central surface Arctic Ocean and the North Atlantic Ocean through the Fram Strait. The surface freshwater anomaly is generated by the sea ice and the liquid transports. The runoff and precipitation make minor contributions. The main deep water formation site related to this oscillation is found located in the Nordic Seas. With the help of Stephane Vannistem (RMI, Belgium), we analyzed a selection of timeseries using the Liang-Kleeman information transfer. We selected the following time series:

- The AMOC LFC1,
- the freshwater transport at the (2) Fram Strait, Davis Strait, and at the Barents Sea opening,
- the salinity in the top 150 m in the Arctic (defined as in Chapter 3.3) and in the Nordic Seas (defined North of the Danmark Straight and the Scotland-Farroé-Iceland ridges, and South of the Arctic region),
- the surface freshwater flux due to exchanges with the atmosphere and runoff, and the surface freshwater flux due to sea ice melting and growth,
- the intensity of the gyre circulation in the Arctic, calculated as the averaged barotropic streamfunction over the Arctic domain (roughly Beaufort gyre),
- the North Atlantic SST (defined between 0°N and 60°N).

To investigate the relationships among the variables at different time scales, the information transfer was calculated after applying a running mean over a time window that varies from 2-yr to 60-yr. The covariance between each variable and the AMOC LFC1 is compared with the information transfer between the two time series in Figures 6.1 and 6.2. In all panels, the information transfer rate is significant between each variable and the AMOC, indicating that all variables and the AMOC influence each other. At the multi-decadal time scale, for the North Atlantic SST, the surface freshwater fluxes, the gyre circulation or the salinity contents, the rate of information transfer from the AMOC to the variable is larger than the rate from the variable to the AMOC. Therefore, the AMOC influence is dominant for all these variables, with a negative rate of information transfer suggesting that the AMOC stabilizes these variables. In addition, freshwater transports have a larger and positive information transfer rate. The Barents Sea Opening (Figure 6.1b) has the strongest influence on the AMOC for time scales larger than 30-yr. Freshwater transport through the Davis Strait (Figure 6.1c) influences AMOC on a shorter time

scale (20-30 yr). The rate of information transfer from the freshwater transport to the AMOC is positive, and they make the AMOC more uncertain. This suggests a dominant influence of the transport at the Barents Sea opening that needs to be better understood. Considering the differences in crucial impactors given by regression analyses and information flow, more work is needed in the future to unravel the drivers of the AMOC low-frequency variability.

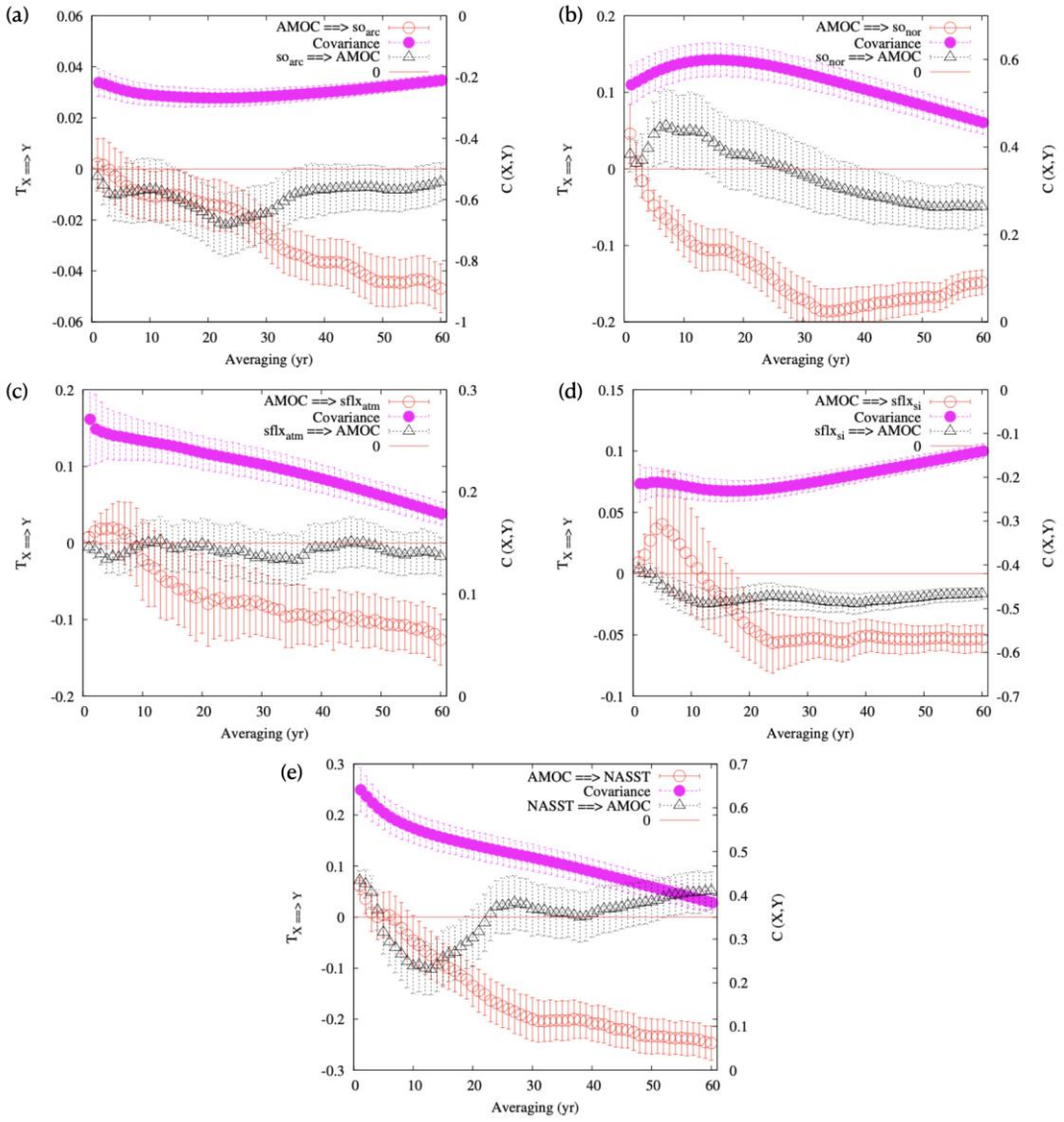

Figure 6.2. Same as Figure 6.1 but for (a) mean salinity in the top 150m in the Arctic Ocean, (b) mean salinity in the top 150m in the Nordic Seas, (c) total freshwater flux at surface in the Arctic due to atmosphere and land, (d) total freshwater flux at surface in the Arctic due to sea ice melting/growth and (e) anomalous mean SST over the Atlantic Ocean (80°W-0 and 0N-60°N). Courtesy of S. Vannistem.

6.2.3 Possible improvements in flow-field constraint method

First, the flow field correction method can be further tested. We have shown an important drift in the AMOC and SST over the North Atlantic when the AMOC is fully constrained, i.e., when the model density is entirely replaced by input density (section 4.3.1). We could investigate if such drift can be removed when using varying cutoff depth and when using a refined design of mask that controls the region to be constrained.

Then, the flow field correction can be modified to build a time-independent flow correction procedure. The method used in this manuscript may lead to reduced wave dynamics (Drews et al., 2015), which are the disadvantages of flow-interactive constraints (see Chapter 5.3). We have shown that it is possible to set up a similar simulation using a non-interactive flow correction. However, a comparison between simulations using different flow field correction settings is needed to reveal the origin of the drift and yield insights for better use of these methods in various applications.

To compute this time-independent density anomaly, we use the simulations presented in section 5.3, using a flow-interactive constraint and lasting for 100-yr. During these simulations, we saved the density correction, calculated online as $\alpha\beta(\rho_i - \rho_m)$ in the model (see Chapter 4 for notations). The annual cycle of this term is calculated from monthly outputs over the 100-yr. This term corresponds to the averaged correction as given in Equation 4.5. We use this term as a fixed correction of the horizontal pressure force, independent of the model flow or density. Such correction is, therefore, non-interactive. We launched a new 50-yr simulation with non-interactive flow correction, using the same initial conditions as the previous runs with the interactive flow correction.

A preliminary analysis of the run suggests no distinct differences compared to the flow-interactive corrected simulations. However, experiments with a longer duration and a larger ensemble are needed to confirm these results. A more careful investigation of the difference and their statistical significance would also be needed. Nevertheless, the non-interactive method might be useful for studying the AMOC in future work. More perspectives are discussed next.

6.2.4 Constraining flows to study climate change

I explored during my PhD the internal variability of the AMOC and its impact on climate. On the other hand, a consensus is achieved that the AMOC is projected to slow down under anthropogenic warming (e.g., Swingedouw et al., 2007; Zhu et al., 2015), affecting the regional and global climates. As shown above, a reduced AMOC intensity is usually accompanied by a cooling in the Northern Hemisphere, less precipitation and more eddies in the northern hemisphere midlatitudes, and presumably a southward displacement of the ITCZ. However, there is a difficulty in

quantifying the exact role of AMOC decline in climate change and separating it from the direct radiative effects of the external forcing.

Recently, sensitivity experiments were used to study the role of the AMOC decline in climate change simulations. Liu et al. (2020) stabilized the AMOC intensity by removing a time-dependent freshwater flux from the subpolar North Atlantic in the CCSM4 model and investigated the impact of AMOC slowdown on climate change in the 21st century. They found that the weakening of AMOC is responsible for ocean cooling south of Greenland, resembling the North Atlantic warming hole. This warming hole was found in both historical observations and IPCC AR5 projections (Drijfhout et al., 2012; Rahmstorf et al., 2015; Sgubin et al., 2017). An alleviated sea ice loss in all seasons was also found, and the emergence of an ice-free Arctic in boreal summer can be delayed for 6 years. An abnormal cooling was found to extend from the lower troposphere in high latitudes to the tropical upper troposphere, and the midlatitude jets thus shifted poleward.

We suggest that the flow-field correction method can also be used in a similar way to stabilize the AMOC strength in historical or scenario simulations. First, we can stabilize the AMOC intensity in anthropogenic warming experiments by constraining the flow field using the input density calculated from the climatology from the preindustrial control simulations. Then the results can be compared to the warming experiments without AMOC corrected. Ideally, in this way, the AMOC climate impacts can be isolated and quantified. This pair of experiments can be implemented in historical simulations, double CO_2 conditions or abrupt-4xCO_2 simulations.

6.2.5 Teleconnections with other basins

Many studies have focused on teleconnections between the North Atlantic and other basins. For instance, the impact of the AMOC on the Pacific SST and sea level pressure is introduced in Chapter 2.4.3. We also found in our work a re-organization of atmospheric circulations and oceanic currents in the upper Indo-Pacific Ocean in response to the AMOC variations. In particular, we found a PNA-like mid-tropospheric geopotential height anomaly and a southward transport in the Sverdrup balance in the tropical Pacific Ocean (section 5.2). We speculate that these changes are likely driven by the mid-latitude storm tracks and Hadley circulation changes, but the relevant mechanism remains further established. Close inspections of the evolution of atmospheric circulations and equatorial SST might be necessary.

In addition, an ensemble of abrupt-AMOC experiments can be used to investigate the time needed for the Pacific Ocean to adjust to the AMOC changes. Other basins, for instance, the South Atlantic, the Pacific Ocean, and the tropical Indian Ocean, are expected to exhibit different sensitivities at different time scales to the AMOC changes. In particular, the accelerated Indian Ocean warming is also a robust feature of anthropogenic warming. A tropical Indian Ocean

warming of 0.1 °C above the mean warming of tropical oceans intensifies the AMOC by ~1 Sv (Hu and Fedorov, 2019). It is of interest to investigate the impact of AMOC intensity variations on the extent of tropical Indian Ocean warming so that the influence of anthropogenic warming can be better isolated from natural variability.

Bibliography

Adcroft, A., Anderson, W., Balaji, V., Blanton, C., Bushuk, M., Dufour, C. O., et al. (2019). The GFDL Global Ocean and Sea Ice Model OM4.0: Model Description and Simulation Features. *Journal of Advances in Modeling Earth Systems*, *11*(10), 3167–3211. https://doi.org/10.1029/2019MS001726

Armour, K. C., Siler, N., Donohoe, A., & Roe, G. H. (2019). Meridional Atmospheric Heat Transport Constrained by Energetics and Mediated by Large-Scale Diffusion. *Journal of Climate*, *32*(12), 3655–3680. https://doi.org/10.1175/JCLI-D-18-0563.1

Årthun, M., Eldevik, T., & Smedsrud, L. H. (2019). The Role of Atlantic Heat Transport in Future Arctic Winter Sea Ice Loss. *Journal of Climate*, *32*(11), 3327–3341. https://doi.org/10.1175/JCLI-D-18-0750.1

Ayache, M., Swingedouw, D., Mary, Y., Eynaud, F., & Colin, C. (2018). Multi-centennial variability of the AMOC over the Holocene: A new reconstruction based on multiple proxy-derived SST records. *Global and Planetary Change*, *170*, 172–189. https://doi.org/10.1016/j.gloplacha.2018.08.016

Ba, J., Keenlyside, N. S., Latif, M., Park, W., Ding, H., Lohmann, K., et al. (2014). A multi-model comparison of Atlantic multidecadal variability. *Climate Dynamics*, *43*(9), 2333–2348. https://doi.org/10.1007/s00382-014-2056-1

Bingham, R. J., & Hughes, C. W. (2009). Signature of the Atlantic meridional overturning circulation in sea level along the east coast of North America. *Geophysical Research Letters*, *36*(2). https://doi.org/10.1029/2008GL036215

Bjerknes, J. (1964). Atlantic Air-Sea Interaction. In H. E. Landsberg & J. Van Mieghem (Eds.), *Advances in Geophysics* (Vol. 10, pp. 1–82). Elsevier. https://doi.org/10.1016/S0065-2687(08)60005-9

Blanke, B., & Raynaud, S. (1997). Kinematics of the Pacific Equatorial Undercurrent: An Eulerian and Lagrangian Approach from GCM Results. *Journal of Physical Oceanography*, *27*(6), 1038–1053. https://doi.org/10.1175/1520-0485(1997)027<1038:KOTPEU>2.0.CO;2

Boccaletti, G., Ferrari, R., Adcroft, A., Ferreira, D., & Marshall, J. (2005). The vertical structure of ocean heat transport. *Geophysical Research Letters*, *32*(10). https://doi.org/10.1029/2005GL022474

Bond, G., Kromer, B., Beer, J., Muscheler, R., Evans, M. N., Showers, W., et al. (2001). Persistent Solar Influence on North Atlantic Climate During the Holocene. *Science*, *294*(5549), 2130–2136. https://doi.org/10.1126/science.1065680

Böning, C. W., Scheinert, M., Dengg, J., Biastoch, A., & Funk, A. (2006). Decadal variability of subpolar gyre transport and its reverberation in the North Atlantic overturning. *Geophysical Research Letters*, *33*(21). https://doi.org/10.1029/2006GL026906

Bonnet, R., Boucher, O., Deshayes, J., Gastineau, G., Hourdin, F., Mignot, J., et al. (2021). Presentation and Evaluation of the IPSL-CM6A-LR Ensemble of Extended Historical

Simulations. *Journal of Advances in Modeling Earth Systems*, *13*(9), e2021MS002565. https://doi.org/10.1029/2021MS002565

Boucher, O., Servonnat, J., Albright, A. L., Aumont, O., Balkanski, Y., Bastrikov, V., et al. (2020). Presentation and evaluation of the IPSL-CM6A-LR climate model. *Journal of Advances in Modeling Earth Systems*, *n/a*(n/a), e2019MS002010. https://doi.org/10.1029/2019MS002010

Brunnabend, S.-E., & Dijkstra, H. A. (2017). Asymmetric response of the Atlantic Meridional Ocean Circulation to freshwater anomalies in a strongly-eddying global ocean model. *Tellus A: Dynamic Meteorology and Oceanography*, *69*(1), 1299283. https://doi.org/10.1080/16000870.2017.1299283

Bryden, H. L., Roemmich, D. H., & Church, J. A. (1991). Ocean heat transport across 24°N in the Pacific. *Deep Sea Research Part A. Oceanographic Research Papers*, *38*(3), 297–324. https://doi.org/10.1016/0198-0149(91)90070-V

Buckley, M. W., & Marshall, J. (2016). Observations, inferences, and mechanisms of the Atlantic Meridional Overturning Circulation: A review. *Reviews of Geophysics*, *54*(1), 5–63. https://doi.org/10.1002/2015RG000493

Caesar, L., McCarthy, G. D., Thornalley, D. J. R., Cahill, N., & Rahmstorf, S. (2021). Current Atlantic Meridional Overturning Circulation weakest in last millennium. *Nature Geoscience*, *14*(3), 118–120. https://doi.org/10.1038/s41561-021-00699-z

Cassou, C., Kushnir, Y., Hawkins, E., Pirani, A., Kucharski, F., Kang, I.-S., & Caltabiano, N. (2018). Decadal Climate Variability and Predictability: Challenges and Opportunities. *Bulletin of the American Meteorological Society*, *99*(3), 479–490. https://doi.org/10.1175/BAMS-D-16-0286.1

Castruccio, F. S., Ruprich-Robert, Y., Yeager, S. G., Danabasoglu, G., Msadek, R., & Delworth, T. L. (2019). Modulation of Arctic Sea Ice Loss by Atmospheric Teleconnections from Atlantic Multidecadal Variability. *Journal of Climate*, *32*(5), 1419–1441. https://doi.org/10.1175/JCLI-D-18-0307.1

Cheruy, F., Ducharne, A., Hourdin, F., Musat, I., Vignon, É., Gastineau, G., et al. (2020). Improved Near-Surface Continental Climate in IPSL-CM6A-LR by Combined Evolutions of Atmospheric and Land Surface Physics. *Journal of Advances in Modeling Earth Systems*, *12*(10), e2019MS002005. https://doi.org/10.1029/2019ms002005

Chidichimo, M. P., Kanzow, T., Cunningham, S. A., Johns, W. E., & Marotzke, J. (2010). The contribution of eastern-boundary density variations to the Atlantic meridional overturning circulation at 26.5° N. *Ocean Science*, *6*(2), 475–490. https://doi.org/10.5194/os-6-475-2010

Chylek, P., Folland, C. K., Lesins, G., & Dubey, M. K. (2010). Twentieth century bipolar seesaw of the Arctic and Antarctic surface air temperatures. *Geophysical Research Letters*, *37*(8). https://doi.org/10.1029/2010GL042793

Clark, P. U. (2009). *Abrupt Climate Change: Final Report, Synthesis and Assessment Product 3. 4*. DIANE Publishing.

Clement, A., Bellomo, K., Murphy, L. N., Cane, M. A., Mauritsen, T., Rädel, G., & Stevens, B. (2015). The Atlantic Multidecadal Oscillation without a role for ocean circulation. *Science*, *350*(6258), 320–324. https://doi.org/10.1126/science.aab3980

Cunningham, S. A., Kanzow, T., Rayner, D., Baringer, M. O., Johns, W. E., Marotzke, J., et al. (2007). Temporal Variability of the Atlantic Meridional Overturning Circulation at 26.5°N. *Science*, *317*(5840), 935–938. https://doi.org/10.1126/science.1141304

Danabasoglu, G., Yeager, S. G., Kwon, Y.-O., Tribbia, J. J., Phillips, A. S., & Hurrell, J. W. (2012). Variability of the Atlantic Meridional Overturning Circulation in CCSM4. *Journal of Climate*, *25*(15), 5153–5172. https://doi.org/10.1175/JCLI-D-11-00463.1

Danabasoglu, G., Yeager, S., Bailey, D., Behrens, E., Bentsen, M., Bi, D., et al. (2014). North Atlantic simulations in Coordinated Ocean-ice Reference Experiments phase II (CORE-II). Part I: Mean states. *Ocean Modelling*, *73*, 76–107. https://doi.org/10.1016/j.ocemod.2013.10.005

Danabasoglu, G., Yeager, S. G., Kim, W. M., Behrens, E., Bentsen, M., Bi, D., et al. (2016). North Atlantic simulations in Coordinated Ocean-ice Reference Experiments phase II (CORE-II). Part II: Inter-annual to decadal variability. *Ocean Modelling*, *97*, 65–90. https://doi.org/10.1016/j.ocemod.2015.11.007

Darelius, E., Fer, I., Rasmussen, T., Guo, C., & Larsen, K. M. H. (2015). On the modulation of the periodicity of the Faroe Bank Channel overflow instabilities. *Ocean Science*, *11*(5), 855–871. https://doi.org/10.5194/os-11-855-2015

Davini, P., Hardenberg, J. von, & Corti, S. (2015). Tropical origin for the impacts of the Atlantic Multidecadal Variability on the Euro-Atlantic climate. *Environmental Research Letters*, *10*(9), 094010. https://doi.org/10.1088/1748-9326/10/9/094010

Day, J. J., Hargreaves, J. C., Annan, J. D., & Abe-Ouchi, A. (2012). Sources of multi-decadal variability in Arctic sea ice extent. *Environmental Research Letters*, *7*(3), 034011. https://doi.org/10.1088/1748-9326/7/3/034011

Dee, D. P., Uppala, S. M., Simmons, A. J., Berrisford, P., Poli, P., Kobayashi, S., et al. (2011). The ERA-Interim reanalysis: configuration and performance of the data assimilation system. *Quarterly Journal of the Royal Meteorological Society*, *137*(656), 553–597. https://doi.org/10.1002/qj.828

Delworth, T. L., & Zeng, F. (2012). Multicentennial variability of the Atlantic meridional overturning circulation and its climatic influence in a 4000 year simulation of the GFDL CM2.1 climate model: MULTICENTENNIAL CLIMATE VARIABILITY. *Geophysical Research Letters*, *39*(13), n/a-n/a. https://doi.org/10.1029/2012GL052107

Delworth, T. L., & Zeng, F. (2016). The Impact of the North Atlantic Oscillation on Climate through Its Influence on the Atlantic Meridional Overturning Circulation. *Journal of Climate*, *29*(3), 941–962. https://doi.org/10.1175/JCLI-D-15-0396.1

Delworth, T. L., Zeng, F., Vecchi, G. A., Yang, X., Zhang, L., & Zhang, R. (2016). The North Atlantic Oscillation as a driver of rapid climate change in the Northern Hemisphere. *Nature Geoscience*, *9*(7), 509–512. https://doi.org/10.1038/ngeo2738

Deshayes, J., & Frankignoul, C. (2008). Simulated Variability of the Circulation in the North Atlantic from 1953 to 2003. *Journal of Climate*, *21*(19), 4919–4933. https://doi.org/10.1175/2008JCLI1882.1

Dines, W. H. (1917). The heat balance of the atmosphere. *Quarterly Journal of the Royal Meteorological Society*, *43*(182), 151–158. https://doi.org/10.1002/qj.49704318203

Dong, C., McWilliams, J. C., Liu, Y., & Chen, D. (2014). Global heat and salt transports by eddy movement. *Nature Communications*, *5*(1), 3294. https://doi.org/10.1038/ncomms4294

Döös, K. (1995). Interocean exchange of water masses. *Journal of Geophysical Research: Oceans*, *100*(C7), 13499–13514. https://doi.org/10.1029/95JC00337

Döscher, R., Acosta, M., Alessandri, A., Anthoni, P., Arsouze, T., Bergman, T., et al. (2022). The EC-Earth3 Earth system model for the Coupled Model Intercomparison Project 6. *Geoscientific Model Development*, *15*(7), 2973–3020. https://doi.org/10.5194/gmd-15-2973-2022

Drews, A., & Greatbatch, R. J. (2016). Atlantic Multidecadal Variability in a model with an improved North Atlantic Current: AMV IN MODEL WITH IMPROVED NAC. *Geophysical Research Letters*, *43*(15), 8199–8206. https://doi.org/10.1002/2016GL069815

Drews, A., & Greatbatch, R. J. (2017). Evolution of the Atlantic Multidecadal Variability in a Model with an Improved North Atlantic Current. *Journal of Climate*, *30*(14), 5491–5512. https://doi.org/10.1175/JCLI-D-16-0790.1

Drews, A., Greatbatch, R. J., Ding, H., Latif, M., & Park, W. (2015). The use of a flow field correction technique for alleviating the North Atlantic cold bias with application to the Kiel Climate Model. *Ocean Dynamics*, *65*(8), 1079–1093. https://doi.org/10.1007/s10236-015-0853-7

Drijfhout, S. (2015). Competition between global warming and an abrupt collapse of the AMOC in Earth's energy imbalance. *Scientific Reports*, *5*(1), 14877. https://doi.org/10.1038/srep14877

Drijfhout, S., van Oldenborgh, G. J., & Cimatoribus, A. (2012). Is a Decline of AMOC Causing the Warming Hole above the North Atlantic in Observed and Modeled Warming Patterns? *Journal of Climate*, *25*(24), 8373–8379. https://doi.org/10.1175/JCLI-D-12-00490.1

Drinkwater, K. F., Miles, M., Medhaug, I., Otterå, O. H., Kristiansen, T., Sundby, S., & Gao, Y. (2014). The Atlantic Multidecadal Oscillation: Its manifestations and impacts with special emphasis on the Atlantic region north of 60°N. *Journal of Marine Systems*, *133*, 117–130. https://doi.org/10.1016/j.jmarsys.2013.11.001

Eden, C., Greatbatch, R. J., & Böning, C. W. (2004). Adiabatically Correcting an Eddy-Permitting Model Using Large-Scale Hydrographic Data: Application to the Gulf Stream and the North Atlantic Current. *Journal of Physical Oceanography*, *34*(4), 701–719. https://doi.org/10.1175/1520-0485(2004)034<0701:ACAEMU>2.0.CO;2

Escudier, R., Mignot, J., & Swingedouw, D. (2013). A 20-year coupled ocean-sea ice-atmosphere variability mode in the North Atlantic in an AOGCM. *Climate Dynamics*, *40*(3), 619–636. https://doi.org/10.1007/s00382-012-1402-4

Eyring, V., Bony, S., Meehl, G. A., Senior, C. A., Stevens, B., Stouffer, R. J., & Taylor, K. E. (2016). Overview of the Coupled Model Intercomparison Project Phase 6 (CMIP6) experimental design and organization. *Geoscientific Model Development*, *9*(5), 1937–1958. https://doi.org/10.5194/gmd-9-1937-2016

Farmer, E. J., Chapman, M. R., & Andrews, J. E. (2008). Centennial-scale Holocene North Atlantic surface temperatures from Mg/Ca ratios in Globigerina bulloides. *Geochemistry, Geophysics, Geosystems*, *9*(12). https://doi.org/10.1029/2008GC002199

Farneti, R., & Vallis, G. K. (2013). Meridional Energy Transport in the Coupled Atmosphere–Ocean System: Compensation and Partitioning. *Journal of Climate*, *26*(18), 7151–7166. https://doi.org/10.1175/JCLI-D-12-00133.1

Fasullo, J. T., & Trenberth, K. E. (2008). The Annual Cycle of the Energy Budget. Part I: Global Mean and Land–Ocean Exchanges. *Journal of Climate*, *21*(10), 2297–2312. https://doi.org/10.1175/2007JCLI1935.1

Frajka-Williams, E. (2015). Estimating the Atlantic overturning at 26°N using satellite altimetry and cable measurements. *Geophysical Research Letters*, *42*(9), 3458–3464. https://doi.org/10.1002/2015GL063220

Frankcombe, L. M., & Dijkstra, H. A. (2011). The role of Atlantic-Arctic exchange in North Atlantic multidecadal climate variability. *Geophysical Research Letters*, *38*(16). https://doi.org/10.1029/2011GL048158

Frankignoul, C., Gastineau, G., & Kwon, Y.-O. (2015). Wintertime Atmospheric Response to North Atlantic Ocean Circulation Variability in a Climate Model. *Journal of Climate*, *28*(19), 7659–7677. https://doi.org/10.1175/JCLI-D-15-0007.1

Frierson, D. M. W., Hwang, Y.-T., Fučkar, N. S., Seager, R., Kang, S. M., Donohoe, A., et al. (2013). Contribution of ocean overturning circulation to tropical rainfall peak in the Northern Hemisphere. *Nature Geoscience*, *6*(11), 940–944. https://doi.org/10.1038/ngeo1987

Ganachaud, A., & Wunsch, C. (2003). Large-Scale Ocean Heat and Freshwater Transports during the World Ocean Circulation Experiment. *Journal of Climate*, *16*(4), 696–705. https://doi.org/10.1175/1520-0442(2003)016<0696:LSOHAF>2.0.CO;2

Gastineau, G., L'Hévéder, B., Codron, F., & Frankignoul, C. (2016). Mechanisms Determining the Winter Atmospheric Response to the Atlantic Overturning Circulation. *Journal of Climate*, *29*(10), 3767–3785. https://doi.org/10.1175/JCLI-D-15-0326.1

Gastineau, Guillaume, & Frankignoul, C. (2012). Cold-season atmospheric response to the natural variability of the Atlantic meridional overturning circulation. *Climate Dynamics*, *39*(1), 37–57. https://doi.org/10.1007/s00382-011-1109-y

Gastineau, Guillaume, & Frankignoul, C. (2015). Influence of the North Atlantic SST Variability on the Atmospheric Circulation during the Twentieth Century. *Journal of Climate*, *28*(4), 1396–1416. https://doi.org/10.1175/JCLI-D-14-00424.1

Gastineau, Guillaume, D'Andrea, F., & Frankignoul, C. (2013). Atmospheric response to the North Atlantic Ocean variability on seasonal to decadal time scales. *Climate Dynamics*, *40*(9), 2311–2330. https://doi.org/10.1007/s00382-012-1333-0

Gastineau, Guillaume, Mignot, J., Arzel, O., & Huck, T. (2018). North Atlantic Ocean Internal Decadal Variability: Role of the Mean State and Ocean-Atmosphere Coupling. *Journal of Geophysical Research: Oceans*, *123*(8), 5949–5970. https://doi.org/10.1029/2018JC014074

Greatbatch, R. J., Sheng, J., Eden, C., Tang, L., Zhai, X., & Zhao, J. (2004). The semi-prognostic method. *Continental Shelf Research*, *24*(18), 2149–2165. https://doi.org/10.1016/j.csr.2004.07.009

Grist, J. P., Josey, S. A., New, A. L., Roberts, M., Koenigk, T., & Iovino, D. (2018). Increasing Atlantic Ocean Heat Transport in the Latest Generation Coupled Ocean-Atmosphere Models: The Role of Air-Sea Interaction. *Journal of Geophysical Research: Oceans*, *123*(11), 8624–8637. https://doi.org/10.1029/2018JC014387

Gulev, S. K., Latif, M., Keenlyside, N., Park, W., & Koltermann, K. P. (2013). North Atlantic Ocean control on surface heat flux on multidecadal timescales. *Nature*, *499*(7459), 464–467. https://doi.org/10.1038/nature12268

Haar, T. H. V., & Oort, A. H. (1973). New Estimate of Annual Poleward Energy Transport by Northern Hemisphere Oceans. *Journal of Physical Oceanography*, *3*(2), 169–172. https://doi.org/10.1175/1520-0485(1973)003<0169:NEOAPE>2.0.CO;2

Häkkinen, S., Rhines, P. B., & Worthen, D. L. (2011). Atmospheric Blocking and Atlantic Multidecadal Ocean Variability. *Science*, *334*(6056), 655–659. https://doi.org/10.1126/science.1205683

Hall, I. R., Bianchi, G. G., & Evans, J. R. (2004). Centennial to millennial scale Holocene climate-deep water linkage in the North Atlantic. *Quaternary Science Reviews*, *23*(14), 1529–1536. https://doi.org/10.1016/j.quascirev.2004.04.004

Hall, M. M., & Bryden, H. L. (1982). Direct estimates and mechanisms of ocean heat transport. *Deep Sea Research Part A. Oceanographic Research Papers*, *29*(3), 339–359. https://doi.org/10.1016/0198-0149(82)90099-1

Hansen, J., Nazarenko, L., Ruedy, R., Sato, M., Willis, J., Genio, A. D., et al. (2005). Earth's Energy Imbalance: Confirmation and Implications. *Science*. https://doi.org/10.1126/science.1110252

Hansen, J., Sato, M., Ruedy, R., Lo, K., Lea, D. W., & Medina-Elizade, M. (2006). Global temperature change. *Proceedings of the National Academy of Sciences*, *103*(39), 14288–14293. https://doi.org/10.1073/pnas.0606291103

Hartmann, D. L. (2015). *Global Physical Climatology*. Newnes.

Haskins, R. K., Oliver, K. I. C., Jackson, L. C., Wood, R. A., & Drijfhout, S. S. (2020). Temperature domination of AMOC weakening due to freshwater hosing in two GCMs. *Climate Dynamics*, *54*(1), 273–286. https://doi.org/10.1007/s00382-019-04998-5

Hawkins, E., Smith, R. S., Allison, L. C., Gregory, J. M., Woollings, T. J., Pohlmann, H., & de Cuevas, B. (2011). Bistability of the Atlantic overturning circulation in a global climate

model and links to ocean freshwater transport. *Geophysical Research Letters*, *38*(10). https://doi.org/10.1029/2011GL047208

Hawkins, Ed, & Sutton, R. (2007). Variability of the Atlantic thermohaline circulation described by three-dimensional empirical orthogonal functions. *Climate Dynamics*, *29*(7–8), 745–762. https://doi.org/10.1007/s00382-007-0263-8

Held, I. M. (2001). The Partitioning of the Poleward Energy Transport between the Tropical Ocean and Atmosphere. *Journal of the Atmospheric Sciences*, *58*(8), 943–948. https://doi.org/10.1175/1520-0469(2001)058<0943:TPOTPE>2.0.CO;2

Hirschi, J. J.-M., Barnier, B., Böning, C., Biastoch, A., Blaker, A. T., Coward, A., et al. (2020). The Atlantic Meridional Overturning Circulation in High-Resolution Models. *Journal of Geophysical Research: Oceans*, *125*(4), e2019JC015522. https://doi.org/10.1029/2019JC015522

Hourdin, F., Rio, C., Grandpeix, J.-Y., Madeleine, J.-B., Cheruy, F., Rochetin, N., et al. (2020). LMDZ6A: The Atmospheric Component of the IPSL Climate Model With Improved and Better Tuned Physics. *Journal of Advances in Modeling Earth Systems*, *12*(7), e2019MS001892. https://doi.org/10.1029/2019MS001892

Hsiung, J. (1985). Estimates of Global Oceanic Meridional Heat Transport. *Journal of Physical Oceanography*, *15*(11), 1405–1413. https://doi.org/10.1175/1520-0485(1985)015<1405:EOGOMH>2.0.CO;2

Hu, S., & Fedorov, A. V. (2019). Indian Ocean warming can strengthen the Atlantic meridional overturning circulation. *Nature Climate Change*, *9*(10), 747–751. https://doi.org/10.1038/s41558-019-0566-x

Hunt, G. E., Kandel, R., & Mecherikunnel, A. T. (1986). A history of presatellite investigations of the Earth's Radiation Budget. *Reviews of Geophysics*, *24*(2), 351–356. https://doi.org/10.1029/RG024i002p00351

Jackson, L., & Vellinga, M. (2013). Multidecadal to Centennial Variability of the AMOC: HadCM3 and a Perturbed Physics Ensemble. *Journal of Climate*, *26*(7), 2390–2407. https://doi.org/10.1175/JCLI-D-11-00601.1

Jackson, L. C., Kahana, R., Graham, T., Ringer, M. A., Woollings, T., Mecking, J. V., & Wood, R. A. (2015). Global and European climate impacts of a slowdown of the AMOC in a high resolution GCM. *Climate Dynamics*, *45*(11), 3299–3316. https://doi.org/10.1007/s00382-015-2540-2

Jackson, L. C., Smith, R. S., & Wood, R. A. (2017). Ocean and atmosphere feedbacks affecting AMOC hysteresis in a GCM. *Climate Dynamics*, *49*(1), 173–191. https://doi.org/10.1007/s00382-016-3336-8

Jackson, Laura C., & Wood, R. A. (2018). Timescales of AMOC decline in response to fresh water forcing. *Climate Dynamics*, *51*(4), 1333–1350. https://doi.org/10.1007/s00382-017-3957-6

Jackson, Laura C., Peterson, K. A., Roberts, C. D., & Wood, R. A. (2016). Recent slowing of Atlantic overturning circulation as a recovery from earlier strengthening. *Nature Geoscience*, *9*(7), 518–522. https://doi.org/10.1038/ngeo2715

Jahn, A., & Holland, M. M. (2013). Implications of Arctic sea ice changes for North Atlantic deep convection and the meridional overturning circulation in CCSM4-CMIP5 simulations. *Geophysical Research Letters*, *40*(6), 1206–1211. https://doi.org/10.1002/grl.50183

Jayne, S. R., & Marotzke, J. (2002). The Oceanic Eddy Heat Transport. *Journal of Physical Oceanography*, *32*(12), 3328–3345. https://doi.org/10.1175/1520-0485(2002)032<3328:TOEHT>2.0.CO;2

Jiang, W., Gastineau, G., & Codron, F. (2021). Multicentennial Variability Driven by Salinity Exchanges Between the Atlantic and the Arctic Ocean in a Coupled Climate Model. *Journal of Advances in Modeling Earth Systems*, *13*(3), e2020MS002366. https://doi.org/10.1029/2020MS002366

Johns, W. E., Beal, L. M., Baringer, M. O., Molina, J. R., Cunningham, S. A., Kanzow, T., & Rayner, D. (2008). Variability of Shallow and Deep Western Boundary Currents off the Bahamas during 2004–05: Results from the 26°N RAPID–MOC Array. *Journal of Physical Oceanography*, *38*(3), 605–623. https://doi.org/10.1175/2007JPO3791.1

Johns, W. E., Baringer, M. O., Beal, L. M., Cunningham, S. A., Kanzow, T., Bryden, H. L., et al. (2011). Continuous, Array-Based Estimates of Atlantic Ocean Heat Transport at 26.5°N. *Journal of Climate*, *24*(10), 2429–2449. https://doi.org/10.1175/2010JCLI3997.1

Jungclaus, J. H., Haak, H., Latif, M., & Mikolajewicz, U. (2005). Arctic–North Atlantic Interactions and Multidecadal Variability of the Meridional Overturning Circulation. *Journal of Climate*, *18*(19), 4013–4031. https://doi.org/10.1175/JCLI3462.1

Kageyama, M., Merkel, U., Otto-Bliesner, B., Prange, M., Abe-Ouchi, A., Lohmann, G., et al. (2012). *Climatic impacts of fresh water hosing under Last Glacial Maximum conditions: a multi-model study* (preprint). Climate Modelling/Modelling only/Millenial/D-O. https://doi.org/10.5194/cpd-8-3831-2012

Kalnay, E., Kanamitsu, M., Kistler, R., Collins, W., Deaven, D., Gandin, L., et al. (1996). The NCEP/NCAR 40-Year Reanalysis Project. *Bulletin of the American Meteorological Society*, *77*(3), 437–472. https://doi.org/10.1175/1520-0477(1996)077<0437:TNYRP>2.0.CO;2

Kang, I.-S., No, H., & Kucharski, F. (2014). ENSO Amplitude Modulation Associated with the Mean SST Changes in the Tropical Central Pacific Induced by Atlantic Multidecadal Oscillation. *Journal of Climate*, *27*(20), 7911–7920. https://doi.org/10.1175/JCLI-D-14-00018.1

Kanzow, T., Cunningham, S. A., Johns, W. E., Hirschi, J. J.-M., Marotzke, J., Baringer, M. O., et al. (2010). Seasonal Variability of the Atlantic Meridional Overturning Circulation at 26.5°N. *Journal of Climate*, *23*(21), 5678–5698. https://doi.org/10.1175/2010JCLI3389.1

Kerr, R. A. (2000). A North Atlantic Climate Pacemaker for the Centuries. *Science*, *288*(5473), 1984–1985. https://doi.org/10.1126/science.288.5473.1984

Kiehl, J. T., & Trenberth, K. E. (1997). Earth's Annual Global Mean Energy Budget. *Bulletin of the American Meteorological Society*, *78*(2), 197–208. https://doi.org/10.1175/1520-0477(1997)078<0197:EAGMEB>2.0.CO;2

Kilbourne, K. H., Wanamaker, A. D., Moffa-Sanchez, P., Reynolds, D. J., Amrhein, D. E., Butler, P. G., et al. (2022). Atlantic circulation change still uncertain. *Nature Geoscience*, *15*(3), 165–167. https://doi.org/10.1038/s41561-022-00896-4

Kim, H., & Lee, S. (2001). Hadley Cell Dynamics in a Primitive Equation Model. Part II: Nonaxisymmetric Flow. *Journal of the Atmospheric Sciences*, *58*(19), 2859–2871. https://doi.org/10.1175/1520-0469(2001)058<2859:HCDIAP>2.0.CO;2

Kim, W. M., Yeager, S., & Danabasoglu, G. (2020). Atlantic Multidecadal Variability and Associated Climate Impacts Initiated by Ocean Thermohaline Dynamics. *Journal of Climate*, *33*(4), 1317–1334. https://doi.org/10.1175/JCLI-D-19-0530.1

Kissel, C., Van Toer, A., Laj, C., Cortijo, E., & Michel, E. (2013). Variations in the strength of the North Atlantic bottom water during Holocene. *Earth and Planetary Science Letters*, *369–370*, 248–259. https://doi.org/10.1016/j.epsl.2013.03.042

Klinger, B. A., & Marotzke, J. (2000). Meridional Heat Transport by the Subtropical Cell. *Journal of Physical Oceanography*, *30*(4), 696–705. https://doi.org/10.1175/1520-0485(2000)030<0696:MHTBTS>2.0.CO;2

Koenigk, T., Fuentes-Franco, R., Meccia, V., Gutjahr, O., Jackson, L. C., New, A. L., et al. (2020). Deep water formation in the North Atlantic Ocean in high resolution global coupled climate models. *Ocean Science Discussions*, 1–39. https://doi.org/10.5194/os-2020-41

Kuhlbrodt, T., Griesel, A., Montoya, M., Levermann, A., Hofmann, M., & Rahmstorf, S. (2007). On the driving processes of the Atlantic meridional overturning circulation. *Reviews of Geophysics*, *45*(2). https://doi.org/10.1029/2004RG000166

Kwon, Y.-O., & Frankignoul, C. (2012). Stochastically-driven multidecadal variability of the Atlantic meridional overturning circulation in CCSM3. *Climate Dynamics*, *38*(5), 859–876. https://doi.org/10.1007/s00382-011-1040-2

Laepple, T., & Huybers, P. (2013). Reconciling discrepancies between Uk37 and Mg/Ca reconstructions of Holocene marine temperature variability. *Earth and Planetary Science Letters*, *375*, 418–429. https://doi.org/10.1016/j.epsl.2013.06.006

Levine, A. F. Z., Frierson, D. M. W., & McPhaden, M. J. (2018). AMO Forcing of Multidecadal Pacific ITCZ Variability. *Journal of Climate*, *31*(14), 5749–5764. https://doi.org/10.1175/JCLI-D-17-0810.1

Levitus, S. (1987). Meridional Ekman Heat Fluxes for the World Ocean and Individual Ocean Basins. *Journal of Physical Oceanography*, *17*(9), 1484–1492. https://doi.org/10.1175/1520-0485(1987)017<1484:MEHFFT>2.0.CO;2

Levitus, S., Antonov, J. I., Boyer, T. P., & Stephens, C. (2000). Warming of the World Ocean. *Science*. https://doi.org/10.1126/science.287.5461.2225

Li, F., Lozier, M. S., Bacon, S., Bower, A. S., Cunningham, S. A., de Jong, M. F., et al. (2021). Subpolar North Atlantic western boundary density anomalies and the Meridional Overturning Circulation. *Nature Communications*, *12*(1), 3002. https://doi.org/10.1038/s41467-021-23350-2

Li, Feili, Lozier, M. S., & Johns, W. E. (2017). Calculating the Meridional Volume, Heat, and Freshwater Transports from an Observing System in the Subpolar North Atlantic: Observing System Simulation Experiment. *Journal of Atmospheric and Oceanic Technology*, *34*(7), 1483–1500. https://doi.org/10.1175/JTECH-D-16-0247.1

Liang, X. S. (2014). Unraveling the cause-effect relation between time series. *Physical Review E*, *90*(5), 052150. https://doi.org/10.1103/PhysRevE.90.052150

Liang, X. S. (2021). Normalized multivariate time series causality analysis and causal graph reconstruction. *ArXiv:2104.11360 [Cs]*. Retrieved from http://arxiv.org/abs/2104.11360

Liang, X. S., & Kleeman, R. (2005). Information Transfer between Dynamical System Components. *Physical Review Letters*, *95*(24), 244101. https://doi.org/10.1103/PhysRevLett.95.244101

Little, C. M., Piecuch, C. G., & Ponte, R. M. (2017). On the relationship between the meridional overturning circulation, alongshore wind stress, and United States East Coast sea level in the Community Earth System Model Large Ensemble. *Journal of Geophysical Research: Oceans*, *122*(6), 4554–4568. https://doi.org/10.1002/2017JC012713

Liu, W., Fedorov, A. V., Xie, S.-P., & Hu, S. (2020). Climate impacts of a weakened Atlantic Meridional Overturning Circulation in a warming climate. *Science Advances*, *6*(26), eaaz4876. https://doi.org/10.1126/sciadv.aaz4876

Liu, Y., Attema, J., Moat, B., & Hazeleger, W. (2020). Synthesis and evaluation of historical meridional heat transport from midlatitudes towards the Arctic. *Earth System Dynamics*, *11*(1), 77–96. https://doi.org/10.5194/esd-11-77-2020

Loeb, N. G., Wielicki, B. A., Doelling, D. R., Smith, G. L., Keyes, D. F., Kato, S., et al. (2009). Toward Optimal Closure of the Earth's Top-of-Atmosphere Radiation Budget. *Journal of Climate*, *22*(3), 748–766. https://doi.org/10.1175/2008JCLI2637.1

Lorenz, E. N. (1967). THE NATURE AND THEORY OF THE GENERAL CIRCULATION OF THE ATMOSPHERE, 187.

Lozier, M. S., Li, F., Bacon, S., Bahr, F., Bower, A. S., Cunningham, S. A., et al. (2019). A sea change in our view of overturning in the subpolar North Atlantic. *Science*, *363*(6426), 516–521. https://doi.org/10.1126/science.aau6592

Lozier, M. Susan. (1997). Evidence for Large-Scale Eddy-Driven Gyres in the North Atlantic. *Science*, *277*(5324), 361–364. https://doi.org/10.1126/science.277.5324.361

Lozier, M. Susan, Bacon, S., Bower, A. S., Cunningham, S. A., Jong, M. F. de, Steur, L. de, et al. (2017). Overturning in the Subpolar North Atlantic Program: A New International Ocean Observing System. *Bulletin of the American Meteorological Society*, *98*(4), 737–752. https://doi.org/10.1175/BAMS-D-16-0057.1

Lumpkin, R., & Speer, K. (2007). Global Ocean Meridional Overturning. *Journal of Physical Oceanography*, *37*(10), 2550–2562. https://doi.org/10.1175/JPO3130.1

Lutsko, N. J., Marshall, J., & Green, B. (2019). Modulation of Monsoon Circulations by Cross-Equatorial Ocean Heat Transport. *Journal of Climate*, *32*(12), 3471–3485. https://doi.org/10.1175/JCLI-D-18-0623.1

Lyu, K., Yu, J.-Y., & Paek, H. (2017). The Influences of the Atlantic Multidecadal Oscillation on the Mean Strength of the North Pacific Subtropical High during Boreal Winter. *Journal of Climate*, *30*(1), 411–426. https://doi.org/10.1175/JCLI-D-16-0525.1

Mahajan, S., Zhang, R., & Delworth, T. L. (2011). Impact of the Atlantic Meridional Overturning Circulation (AMOC) on Arctic Surface Air Temperature and Sea Ice Variability. *Journal of Climate*, *24*(24), 6573–6581. https://doi.org/10.1175/2011JCLI4002.1

Mann, M. E., Park, J., & Bradley, R. S. (1995). Global interdecadal and century-scale climate oscillations during the past five centuries. *Nature*, *378*(6554), 266–270. https://doi.org/10.1038/378266a0

Mann, M. E., Steinman, B. A., Brouillette, D. J., & Miller, S. K. (2021). Multidecadal climate oscillations during the past millennium driven by volcanic forcing. *Science*, *371*(6533), 1014–1019. https://doi.org/10.1126/science.abc5810

Marshall, J., Donohoe, A., Ferreira, D., & McGee, D. (2014). The ocean's role in setting the mean position of the Inter-Tropical Convergence Zone. *Climate Dynamics*, *42*(7), 1967–1979. https://doi.org/10.1007/s00382-013-1767-z

Marshall, John, & Speer, K. (2012). Closure of the meridional overturning circulation through Southern Ocean upwelling. *Nature Geoscience*, *5*(3), 171–180. https://doi.org/10.1038/ngeo1391

Marshall, John, Johnson, H., & Goodman, J. (2001). A Study of the Interaction of the North Atlantic Oscillation with Ocean Circulation. *Journal of Climate*, *14*(7), 1399–1421. https://doi.org/10.1175/1520-0442(2001)014<1399:ASOTIO>2.0.CO;2

Mayer, M., & Haimberger, L. (2012). Poleward Atmospheric Energy Transports and Their Variability as Evaluated from ECMWF Reanalysis Data. *Journal of Climate*, *25*(2), 734–752. https://doi.org/10.1175/JCLI-D-11-00202.1

McCarthy, G., Frajka-Williams, E., Johns, W. E., Baringer, M. O., Meinen, C. S., Bryden, H. L., et al. (2012). Observed interannual variability of the Atlantic meridional overturning circulation at 26.5°N. *Geophysical Research Letters*, *39*(19). https://doi.org/10.1029/2012GL052933

McCarthy, G. D., Smeed, D. A., Johns, W. E., Frajka-Williams, E., Moat, B. I., Rayner, D., et al. (2015). Measuring the Atlantic Meridional Overturning Circulation at 26°N. *Progress in Oceanography*, *130*, 91–111. https://doi.org/10.1016/j.pocean.2014.10.006

McCreary, J. P., & Lu, P. (1994). Interaction between the Subtropical and Equatorial Ocean Circulations: The Subtropical Cell. *Journal of Physical Oceanography*, *24*(2), 466–497. https://doi.org/10.1175/1520-0485(1994)024<0466:IBTSAE>2.0.CO;2

Medhaug, I., Langehaug, H. R., Eldevik, T., Furevik, T., & Bentsen, M. (2012). Mechanisms for decadal scale variability in a simulated Atlantic meridional overturning circulation. *Climate Dynamics*, *39*(1), 77–93. https://doi.org/10.1007/s00382-011-1124-z

Menary, M. B., Jackson, L. C., & Lozier, M. S. (2020). Reconciling the Relationship Between the AMOC and Labrador Sea in OSNAP Observations and Climate Models. *Geophysical Research Letters*, *47*(18), e2020GL089793. https://doi.org/10.1029/2020GL089793

Messori, G., & Czaja, A. (2013). On the sporadic nature of meridional heat transport by transient eddies. *Quarterly Journal of the Royal Meteorological Society*, *139*(673), 999–1008. https://doi.org/10.1002/qj.2011

Messori, G., Geen, R., & Czaja, A. (2017). On the Spatial and Temporal Variability of Atmospheric Heat Transport in a Hierarchy of Models. *Journal of the Atmospheric Sciences*, *74*(7), 2163–2189. https://doi.org/10.1175/JAS-D-16-0360.1

Meyssignac, B., Boyer, T., Zhao, Z., Hakuba, M. Z., Landerer, F. W., Stammer, D., et al. (2019). Measuring Global Ocean Heat Content to Estimate the Earth Energy Imbalance. *Frontiers in Marine Science*, *6*. https://doi.org/10.3389/fmars.2019.00432

Mignot, J., Ganopolski, A., & Levermann, A. (2007). Atlantic Subsurface Temperatures: Response to a Shutdown of the Overturning Circulation and Consequences for Its Recovery. *Journal of Climate*, *20*(19), 4884–4898. https://doi.org/10.1175/JCLI4280.1

Montade, V., Kageyama, M., Combourieu-Nebout, N., Ledru, M.-P., Michel, E., Siani, G., & Kissel, C. (2015). Teleconnection between the Intertropical Convergence Zone and southern westerly winds throughout the last deglaciation. *Geology*, *43*(8), 735–738. https://doi.org/10.1130/G36745.1

Moreno-Chamarro, E., Marshall, J., & Delworth, T. L. (2019). Linking ITCZ Migrations to the AMOC and North Atlantic/Pacific SST Decadal Variability. *Journal of Climate*, *33*(3), 893–905. https://doi.org/10.1175/JCLI-D-19-0258.1

Morrow, R., Coleman, R., Church, J., & Chelton, D. (1994). Surface Eddy Momentum Flux and Velocity Variances in the Southern Ocean from Geosat Altimetry. *Journal of Physical Oceanography*, *24*(10), 2050–2071. https://doi.org/10.1175/1520-0485(1994)024<2050:SEMFAV>2.0.CO;2

Msadek, R., & Frankignoul, C. (2009). Atlantic multidecadal oceanic variability and its influence on the atmosphere in a climate model. *Climate Dynamics*, *33*(1), 45–62. https://doi.org/10.1007/s00382-008-0452-0

Msadek, R., Frankignoul, C., & Li, L. Z. X. (2011). Mechanisms of the atmospheric response to North Atlantic multidecadal variability: a model study. *Climate Dynamics*, *36*(7), 1255–1276. https://doi.org/10.1007/s00382-010-0958-0

Muir, L. C., & Fedorov, A. V. (2015). How the AMOC affects ocean temperatures on decadal to centennial timescales: the North Atlantic versus an interhemispheric seesaw. *Climate Dynamics*, *45*(1), 151–160. https://doi.org/10.1007/s00382-014-2443-7

Muir, Les C., & Fedorov, A. V. (2017). Evidence of the AMOC interdecadal mode related to westward propagation of temperature anomalies in CMIP5 models. *Climate Dynamics*, *48*(5), 1517–1535. https://doi.org/10.1007/s00382-016-3157-9

Nakamura, H. (1992). Midwinter Suppression of Baroclinic Wave Activity in the Pacific. *Journal of the Atmospheric Sciences*, *49*(17), 1629–1642. https://doi.org/10.1175/1520-0469(1992)049<1629:MSOBWA>2.0.CO;2

van Noije, T., Bergman, T., Le Sager, P., O'Donnell, D., Makkonen, R., Gonçalves-Ageitos, M., et al. (2021). EC-Earth3-AerChem: a global climate model with interactive aerosols and

atmospheric chemistry participating in CMIP6. *Geoscientific Model Development*, *14*(9), 5637–5668. https://doi.org/10.5194/gmd-14-5637-2021

Nummelin, A., Li, C., & Hezel, P. J. (2017). Connecting ocean heat transport changes from the midlatitudes to the Arctic Ocean. *Geophysical Research Letters*, *44*(4), 1899–1908. https://doi.org/10.1002/2016GL071333

Nyberg, J., Malmgren, B. A., Kuijpers, A., & Winter, A. (2002). A centennial-scale variability of tropical North Atlantic surface hydrography during the late Holocene. *Palaeogeography, Palaeoclimatology, Palaeoecology*, *183*(1), 25–41. https://doi.org/10.1016/S0031-0182(01)00446-1

Oka, A., & Niwa, Y. (2013). Pacific deep circulation and ventilation controlled by tidal mixing away from the sea bottom. *Nature Communications*, *4*(1), 2419. https://doi.org/10.1038/ncomms3419

Omrani, N.-E., Keenlyside, N. S., Bader, J., & Manzini, E. (2014). Stratosphere key for wintertime atmospheric response to warm Atlantic decadal conditions. *Climate Dynamics*, *42*(3), 649–663. https://doi.org/10.1007/s00382-013-1860-3

Oort, A. H., & Haar, T. H. V. (1976). On the Observed Annual Cycle in the Ocean-Atmosphere Heat Balance Over the Northern Hemisphere. *Journal of Physical Oceanography*, *6*(6), 781–800. https://doi.org/10.1175/1520-0485(1976)006<0781:OTOACI>2.0.CO;2

O'Reilly, C. H., Huber, M., Woollings, T., & Zanna, L. (2016). The signature of low-frequency oceanic forcing in the Atlantic Multidecadal Oscillation. *Geophysical Research Letters*, *43*(6), 2810–2818. https://doi.org/10.1002/2016GL067925

d'Orgeville, M., & Peltier, W. R. (2007). On the Pacific Decadal Oscillation and the Atlantic Multidecadal Oscillation: Might they be related? *Geophysical Research Letters*, *34*(23). https://doi.org/10.1029/2007GL031584

Ortega, P., Mignot, J., Swingedouw, D., Sévellec, F., & Guilyardi, E. (2015). Reconciling two alternative mechanisms behind bi-decadal variability in the North Atlantic. *Progress in Oceanography*, *137*, 237–249. https://doi.org/10.1016/j.pocean.2015.06.009

Pardaens, A., Vellinga, M., Wu, P., & Ingleby, B. (2008). Large-Scale Atlantic Salinity Changes over the Last Half-Century: A Model–Observation Comparison. *Journal of Climate*, *21*(8), 1698–1720. https://doi.org/10.1175/2007JCLI1988.1

Park, T., Park, W., & Latif, M. (2016). Correcting North Atlantic sea surface salinity biases in the Kiel Climate Model: influences on ocean circulation and Atlantic Multidecadal Variability. *Climate Dynamics*, *47*(7), 2543–2560. https://doi.org/10.1007/s00382-016-2982-1

Park, W., & Latif, M. (2008). Multidecadal and multicentennial variability of the meridional overturning circulation. *Geophysical Research Letters*, *35*(22). https://doi.org/10.1029/2008GL035779

Parsons, L. A., Brennan, M. K., Wills, R. C. J., & Proistosescu, C. (2020). Magnitudes and Spatial Patterns of Interdecadal Temperature Variability in CMIP6. *Geophysical Research Letters*, *47*(7), e2019GL086588. https://doi.org/10.1029/2019GL086588

Peings, Y., & Magnusdottir, G. (2014). Forcing of the wintertime atmospheric circulation by the multidecadal fluctuations of the North Atlantic ocean. *Environmental Research Letters*, *9*(3), 034018. https://doi.org/10.1088/1748-9326/9/3/034018

Peters, M. E., Kuang, Z., & Walker, C. C. (2008). Analysis of Atmospheric Energy Transport in ERA-40 and Implications for Simple Models of the Mean Tropical Circulation. *Journal of Climate*, *21*(20), 5229–5241. https://doi.org/10.1175/2008JCLI2073.1

Peterson, I. K., Pettipas, R., & Rosing-Asvid, A. (2015). Trends and Variability in Sea Ice and Icebergs off the Canadian East Coast. *Atmosphere-Ocean*, *53*(5), 582–594. https://doi.org/10.1080/07055900.2015.1057684

Polo, I., Martin-Rey, M., Rodriguez-Fonseca, B., Kucharski, F., & Mechoso, C. R. (2015). Processes in the Pacific La Niña onset triggered by the Atlantic Niño. *Climate Dynamics*, *44*(1), 115–131. https://doi.org/10.1007/s00382-014-2354-7

Rahmstorf, S., Box, J. E., Feulner, G., Mann, M. E., Robinson, A., Rutherford, S., & Schaffernicht, E. J. (2015). Exceptional twentieth-century slowdown in Atlantic Ocean overturning circulation. *Nature Climate Change*, *5*(5), 475–480. https://doi.org/10.1038/nclimate2554

Rimbu, N., Lohmann, G., & Ionita, M. (2014). Interannual to multidecadal Euro-Atlantic blocking variability during winter and its relationship with extreme low temperatures in Europe. *Journal of Geophysical Research: Atmospheres*, *119*(24), 13,621-13,636. https://doi.org/10.1002/2014JD021983

Roberts, M. J., Hewitt, H. T., Hyder, P., Ferreira, D., Josey, S. A., Mizielinski, M., & Shelly, A. (2016). Impact of ocean resolution on coupled air-sea fluxes and large-scale climate. *Geophysical Research Letters*, *43*(19), 10,430-10,438. https://doi.org/10.1002/2016GL070559

Roemmich, D., & Wunsch, C. (1985). Two transatlantic sections: meridional circulation and heat flux in the subtropical North Atlantic Ocean. *Deep Sea Research Part A. Oceanographic Research Papers*, *32*(6), 619–664. https://doi.org/10.1016/0198-0149(85)90070-6

Ruprich-Robert, Y., & Cassou, C. (2015). Combined influences of seasonal East Atlantic Pattern and North Atlantic Oscillation to excite Atlantic multidecadal variability in a climate model. *Climate Dynamics*, *44*(1), 229–253. https://doi.org/10.1007/s00382-014-2176-7

Ruprich-Robert, Y., Msadek, R., Castruccio, F., Yeager, S., Delworth, T., & Danabasoglu, G. (2017). Assessing the Climate Impacts of the Observed Atlantic Multidecadal Variability Using the GFDL CM2.1 and NCAR CESM1 Global Coupled Models. *Journal of Climate*, *30*(8), 2785–2810. https://doi.org/10.1175/JCLI-D-16-0127.1

Sévellec, F., & Fedorov, A. V. (2013). The Leading, Interdecadal Eigenmode of the Atlantic Meridional Overturning Circulation in a Realistic Ocean Model. *Journal of Climate*, *26*(7), 2160–2183. https://doi.org/10.1175/JCLI-D-11-00023.1

Sgubin, G., Swingedouw, D., Drijfhout, S., Mary, Y., & Bennabi, A. (2017). Abrupt cooling over the North Atlantic in modern climate models. *Nature Communications*, *8*(1), 14375. https://doi.org/10.1038/ncomms14375

Sheng, J., Greatbatch, R. J., & Wright, D. G. (2001). Improving the utility of ocean circulation models through adjustment of the momentum balance. *Journal of Geophysical Research: Oceans*, *106*(C8), 16711–16728. https://doi.org/10.1029/2000JC000680

Shrestha, S., Babel, M. S., & Pandey, V. P. (2014). *Climate Change and Water Resources*. CRC Press.

Sicre, M.-A., Yiou, P., Eiríksson, J., Ezat, U., Guimbaut, E., Dahhaoui, I., et al. (2008). A 4500-year reconstruction of sea surface temperature variability at decadal time-scales off North Iceland. *Quaternary Science Reviews*, *27*(21), 2041–2047. https://doi.org/10.1016/j.quascirev.2008.08.009

Sillmann, J., Croci-Maspoli, M., Kallache, M., & Katz, R. W. (2011). Extreme Cold Winter Temperatures in Europe under the Influence of North Atlantic Atmospheric Blocking. *Journal of Climate*, *24*(22), 5899–5913. https://doi.org/10.1175/2011JCLI4075.1

Skinner, L. C., Elderfield, H., & Hall, M. (2007). Phasing of Millennial Climate Events and Northeast Atlantic Deep-Water Temperature Change Since 50 Ka Bp. In *Ocean Circulation: Mechanisms and Impacts—Past and Future Changes of Meridional Overturning* (pp. 197–208). American Geophysical Union (AGU). https://doi.org/10.1029/173GM14

Smeed, D. A., McCarthy, G. D., Cunningham, S. A., Frajka-Williams, E., Rayner, D., Johns, W. E., et al. (2014). Observed decline of the Atlantic meridional overturning circulation 2004–2012. *Ocean Science*, *10*(1), 29–38. https://doi.org/10.5194/os-10-29-2014

Smirnov, D., & Vimont, D. J. (2012). Extratropical Forcing of Tropical Atlantic Variability during Boreal Summer and Fall. *Journal of Climate*, *25*(6), 2056–2076. https://doi.org/10.1175/JCLI-D-11-00104.1

Song, Z., Latif, M., & Park, W. (2019). East Atlantic Pattern Drives Multidecadal Atlantic Meridional Overturning Circulation Variability During the Last Glacial Maximum. *Geophysical Research Letters*, *46*(19), 10865–10873. https://doi.org/10.1029/2019GL082960

Stephens, G. L., Li, J., Wild, M., Clayson, C. A., Loeb, N., Kato, S., et al. (2012). An update on Earth's energy balance in light of the latest global observations. *Nature Geoscience*, *5*(10), 691–696. https://doi.org/10.1038/ngeo1580

Stips, A., Macias, D., Coughlan, C., Garcia-Gorriz, E., & Liang, X. S. (2016). On the causal structure between CO2 and global temperature. *Scientific Reports*, *6*(1), 21691. https://doi.org/10.1038/srep21691

Stouffer, R. J., Yin, J., Gregory, J. M., Dixon, K. W., Spelman, M. J., Hurlin, W., et al. (2006). Investigating the Causes of the Response of the Thermohaline Circulation to Past and Future Climate Changes. *Journal of Climate*, *19*(8), 1365–1387. https://doi.org/10.1175/JCLI3689.1

Straneo, F., & Heimbach, P. (2013). North Atlantic warming and the retreat of Greenland's outlet glaciers. *Nature*, *504*(7478), 36–43. https://doi.org/10.1038/nature12854

Sutton, R. T., McCarthy, G. D., Robson, J., Sinha, B., Archibald, A. T., & Gray, L. J. (2018). Atlantic Multidecadal Variability and the U.K. ACSIS Program. *Bulletin of the American Meteorological Society*, *99*(2), 415–425. https://doi.org/10.1175/BAMS-D-16-0266.1

Swingedouw, D., Braconnot, P., Delecluse, P., Guilyardi, E., & Marti, O. (2007). Quantifying the AMOC feedbacks during a 2×CO2 stabilization experiment with land-ice melting. *Climate Dynamics*, *29*(5), 521–534. https://doi.org/10.1007/s00382-007-0250-0

Talandier, C., Deshayes, J., Treguier, A.-M., Capet, X., Benshila, R., Debreu, L., et al. (2014). Improvements of simulated Western North Atlantic current system and impacts on the AMOC. *Ocean Modelling*, *76*, 1–19. https://doi.org/10.1016/j.ocemod.2013.12.007

Talley, L. D. (2003). Shallow, Intermediate, and Deep Overturning Components of the Global Heat Budget. *Journal of Physical Oceanography*, *33*(3), 530–560. https://doi.org/10.1175/1520-0485(2003)033<0530:SIADOC>2.0.CO;2

Talley, L. D., PICKARD, GEORGE L., EMERY, WILLIAM J., & SWIFT, JAMES H. (2011). *Descriptive physical oceanography: an introduction* (6. ed). Amsterdam Heidelberg: Elsevier, AP.

Tandon, N. F., & Kushner, P. J. (2015). Does External Forcing Interfere with the AMOC's Influence on North Atlantic Sea Surface Temperature? *Journal of Climate*, *28*(16), 6309–6323. https://doi.org/10.1175/JCLI-D-14-00664.1

Thornalley, D. J. R., Oppo, D. W., Ortega, P., Robson, J. I., Brierley, C. M., Davis, R., et al. (2018). Anomalously weak Labrador Sea convection and Atlantic overturning during the past 150 years. *Nature*, *556*(7700), 227–230. https://doi.org/10.1038/s41586-018-0007-4

Trenberth, K. E., & Caron, J. M. (2001). Estimates of Meridional Atmosphere and Ocean Heat Transports. *Journal of Climate*, *14*(16), 3433–3443. https://doi.org/10.1175/1520-0442(2001)014<3433:EOMAAO>2.0.CO;2

Trenberth, K. E., & Fasullo, J. T. (2013). Regional Energy and Water Cycles: Transports from Ocean to Land. *Journal of Climate*, *26*(20), 7837–7851. https://doi.org/10.1175/JCLI-D-13-00008.1

Trenberth, K. E., & Fasullo, J. T. (2018). Applications of an Updated Atmospheric Energetics Formulation. *Journal of Climate*, *31*(16), 6263–6279. https://doi.org/10.1175/JCLI-D-17-0838.1

Trenberth, K. E., & Stepaniak, D. P. (2003). Seamless Poleward Atmospheric Energy Transports and Implications for the Hadley Circulation. *Journal of Climate*, *16*(22), 3706–3722. https://doi.org/10.1175/1520-0442(2003)016<3706:SPAETA>2.0.CO;2

Trenberth, K. E., & Stepaniak, D. P. (2004). The flow of energy through the earth's climate system. *Quarterly Journal of the Royal Meteorological Society*, *130*(603), 2677–2701. https://doi.org/10.1256/qj.04.83

Trenberth, K. E., Fasullo, J. T., & Kiehl, J. (2009). Earth's Global Energy Budget. *Bulletin of the American Meteorological Society*, *90*(3), 311–324. https://doi.org/10.1175/2008BAMS2634.1

Trenberth, K. E., Fasullo, J. T., & Mackaro, J. (2011). Atmospheric Moisture Transports from Ocean to Land and Global Energy Flows in Reanalyses. *Journal of Climate*, *24*(18), 4907–4924. https://doi.org/10.1175/2011JCLI4171.1

Trenberth, K. E., Zhang, Y., Fasullo, J. T., & Cheng, L. (2019). Observation-Based Estimates of Global and Basin Ocean Meridional Heat Transport Time Series. *Journal of Climate*, *32*(14), 4567–4583. https://doi.org/10.1175/JCLI-D-18-0872.1

Uppala, S. M., KÅllberg, P. W., Simmons, A. J., Andrae, U., Bechtold, V. D. C., Fiorino, M., et al. (2005). The ERA-40 re-analysis. *Quarterly Journal of the Royal Meteorological Society*, *131*(612), 2961–3012. https://doi.org/10.1256/qj.04.176

Vellinga, M., & Wood, R. A. (2002). Global Climatic Impacts of a Collapse of the Atlantic Thermohaline Circulation, 17.

Vellinga, M., & Wu, P. (2004). Low-Latitude Freshwater Influence on Centennial Variability of the Atlantic Thermohaline Circulation. *Journal of Climate*, *17*(23), 4498–4511. https://doi.org/10.1175/3219.1

Voldoire, A., Saint-Martin, D., Sénési, S., Decharme, B., Alias, A., Chevallier, M., et al. (2019). Evaluation of CMIP6 DECK Experiments With CNRM-CM6-1. *Journal of Advances in Modeling Earth Systems*, *11*(7), 2177–2213. https://doi.org/10.1029/2019MS001683

Volkov, D. L., Lee, T., & Fu, L.-L. (2008). Eddy-induced meridional heat transport in the ocean. *Geophysical Research Letters*, *35*(20). https://doi.org/10.1029/2008GL035490

Wang, C., Zhang, L., Lee, S.-K., Wu, L., & Mechoso, C. R. (2014). A global perspective on CMIP5 climate model biases. *Nature Climate Change*, *4*(3), 201–205. https://doi.org/10.1038/nclimate2118

Warren, B. A. (1999). Approximating the energy transport across oceanic sections. *Journal of Geophysical Research: Oceans*, *104*(C4), 7915–7919. https://doi.org/10.1029/1998JC900089

Wills, R. C., Schneider, T., Wallace, J. M., Battisti, D. S., & Hartmann, D. L. (2018). Disentangling Global Warming, Multidecadal Variability, and El Niño in Pacific Temperatures. *Geophysical Research Letters*, *45*(5), 2487–2496. https://doi.org/10.1002/2017GL076327

Winton, M. (2003). On the Climatic Impact of Ocean Circulation. *Journal of Climate*, *16*(17), 2875–2889. https://doi.org/10.1175/1520-0442(2003)016<2875:OTCIOO>2.0.CO;2

Woollings, T., Hoskins, B., Blackburn, M., & Berrisford, P. (2008). A New Rossby Wave–Breaking Interpretation of the North Atlantic Oscillation. *Journal of the Atmospheric Sciences*, *65*(2), 609–626. https://doi.org/10.1175/2007JAS2347.1

Woollings, T., Hannachi, A., Hoskins, B., & Turner, A. (2010). A Regime View of the North Atlantic Oscillation and Its Response to Anthropogenic Forcing. *Journal of Climate*, *23*(6), 1291–1307. https://doi.org/10.1175/2009JCLI3087.1

Wunsch, C. (2005). The Total Meridional Heat Flux and Its Oceanic and Atmospheric Partition. *Journal of Climate*, *18*(21), 4374–4380. https://doi.org/10.1175/JCLI3539.1

Wunsch, C., & Ferrari, R. (2004). Vertical Mixing, Energy, and the General Circulation of the Oceans. *Annual Review of Fluid Mechanics*, *36*(1), 281–314. https://doi.org/10.1146/annurev.fluid.36.050802.122121

Xu, X., Hurlburt, H. E., Schmitz Jr., W. J., Zantopp, R., Fischer, J., & Hogan, P. J. (2013). On the currents and transports connected with the atlantic meridional overturning circulation in the subpolar North Atlantic. *Journal of Geophysical Research: Oceans*, *118*(1), 502–516. https://doi.org/10.1002/jgrc.20065

Xu, Xiaobiao, Chassignet, E. P., & Wang, F. (2019). On the variability of the Atlantic meridional overturning circulation transports in coupled CMIP5 simulations. *Climate Dynamics*, *52*(11), 6511–6531. https://doi.org/10.1007/s00382-018-4529-0

Yang, H., Li, Q., Wang, K., Sun, Y., & Sun, D. (2015). Decomposing the meridional heat transport in the climate system. *Climate Dynamics*, *44*(9), 2751–2768. https://doi.org/10.1007/s00382-014-2380-5

Yang, T., & Xu, Y. (2015). Estimation of the time series of the meridional heat transport across 15°N in the Pacific Ocean from Argo and satellite data. *Journal of Geophysical Research: Oceans*, *120*(4), 3043–3060. https://doi.org/10.1002/2015JC010752

Yao, Y., & Luo, D. (2015). Do European blocking events precede North Atlantic Oscillation events? *Advances in Atmospheric Sciences*, *32*(8), 1106–1118. https://doi.org/10.1007/s00376-015-4209-5

Yeager, S., & Danabasoglu, G. (2014). The Origins of Late-Twentieth-Century Variations in the Large-Scale North Atlantic Circulation. *Journal of Climate*, *27*(9), 3222–3247. https://doi.org/10.1175/JCLI-D-13-00125.1

Yu, J.-Y., Kao, P., Paek, H., Hsu, H.-H., Hung, C., Lu, M.-M., & An, S.-I. (2015). Linking Emergence of the Central Pacific El Niño to the Atlantic Multidecadal Oscillation. *Journal of Climate*, *28*(2), 651–662. https://doi.org/10.1175/JCLI-D-14-00347.1

Yu, S., & Pritchard, M. S. (2019). A Strong Role for the AMOC in Partitioning Global Energy Transport and Shifting ITCZ Position in Response to Latitudinally Discrete Solar Forcing in CESM1.2. *Journal of Climate*, *32*(8), 2207–2226. https://doi.org/10.1175/JCLI-D-18-0360.1

Yuan, T., Oreopoulos, L., Zelinka, M., Yu, H., Norris, J. R., Chin, M., et al. (2016). Positive low cloud and dust feedbacks amplify tropical North Atlantic Multidecadal Oscillation. *Geophysical Research Letters*, *43*(3), 1349–1356. https://doi.org/10.1002/2016GL067679

Zanna, L., Heimbach, P., Moore, A. M., & Tziperman, E. (2011). Optimal Excitation of Interannual Atlantic Meridional Overturning Circulation Variability. *Journal of Climate*, *24*(2), 413–427. https://doi.org/10.1175/2010JCLI3610.1

Zhang, D., Johns, W. E., & Lee, T. N. (2002). The seasonal cycle of meridional heat transport at 24°N in the North Pacific and in the global ocean. *Journal of Geophysical Research: Oceans*, *107*(C7), 20-1-20–24. https://doi.org/10.1029/2001JC001011

Zhang, L., & Wang, C. (2013). Multidecadal North Atlantic sea surface temperature and Atlantic meridional overturning circulation variability in CMIP5 historical simulations. *Journal of Geophysical Research: Oceans*, *118*(10), 5772–5791. https://doi.org/10.1002/jgrc.20390

Zhang, L., Delworth, T. L., & Zeng, F. (2017). The impact of multidecadal Atlantic meridional overturning circulation variations on the Southern Ocean. *Climate Dynamics*, *48*(5), 2065–2085. https://doi.org/10.1007/s00382-016-3190-8

Zhang, R. (2007). Anticorrelated multidecadal variations between surface and subsurface tropical North Atlantic. *Geophysical Research Letters*, *34*(12). https://doi.org/10.1029/2007GL030225

Zhang, R. (2008). Coherent surface-subsurface fingerprint of the Atlantic meridional overturning circulation. *Geophysical Research Letters*, *35*(20). https://doi.org/10.1029/2008GL035463

Zhang, R. (2010). Latitudinal dependence of Atlantic meridional overturning circulation (AMOC) variations. *Geophysical Research Letters*, *37*(16). https://doi.org/10.1029/2010GL044474

Zhang, R. (2015). Mechanisms for low-frequency variability of summer Arctic sea ice extent. *Proceedings of the National Academy of Sciences*, *112*(15), 4570–4575. https://doi.org/10.1073/pnas.1422296112

Zhang, R. (2017). On the persistence and coherence of subpolar sea surface temperature and salinity anomalies associated with the Atlantic multidecadal variability. *Geophysical Research Letters*, *44*(15), 7865–7875. https://doi.org/10.1002/2017GL074342

Zhang, R., & Delworth, T. L. (2007). Impact of the Atlantic Multidecadal Oscillation on North Pacific climate variability. *Geophysical Research Letters*, *34*(23). https://doi.org/10.1029/2007GL031601

Zhang, R., Sutton, R., Danabasoglu, G., Delworth, T. L., Kim, W. M., Robson, J., & Yeager, S. G. (2016). Comment on "The Atlantic Multidecadal Oscillation without a role for ocean circulation." *Science*, *352*(6293), 1527–1527. https://doi.org/10.1126/science.aaf1660

Zhang, R., Sutton, R., Danabasoglu, G., Kwon, Y., Marsh, R., Yeager, S. G., et al. (2019). A Review of the Role of the Atlantic Meridional Overturning Circulation in Atlantic Multidecadal Variability and Associated Climate Impacts. *Reviews of Geophysics*, *57*(2), 316–375. https://doi.org/10.1029/2019RG000644

Zhang, W., Vecchi, G. A., Murakami, H., Villarini, G., Delworth, T. L., Yang, X., & Jia, L. (2018). Dominant Role of Atlantic Multidecadal Oscillation in the Recent Decadal Changes in Western North Pacific Tropical Cyclone Activity. *Geophysical Research Letters*, *45*(1), 354–362. https://doi.org/10.1002/2017GL076397

Zhang, Z., Zhong, Y., Tian, J., Yang, Q., & Zhao, W. (2014). Estimation of eddy heat transport in the global ocean from Argo data. *Acta Oceanologica Sinica*, *33*(1), 42–47. https://doi.org/10.1007/s13131-014-0421-x

Zheng, Y., & Giese, B. S. (2009). Ocean heat transport in Simple Ocean Data Assimilation: Structure and mechanisms. *Journal of Geophysical Research: Oceans*, *114*(C11). https://doi.org/10.1029/2008JC005190

Zhu, J., Liu, Z., Zhang, J., & Liu, W. (2015). AMOC response to global warming: dependence on the background climate and response timescale. *Climate Dynamics*, *44*(11–12), 3449–3468. https://doi.org/10.1007/s00382-014-2165-x